


*Raman Heterodyne Detected
Magnetic Resonance of the
Nitrogen-Vacancy Centre in Diamond*

By
Xing-Fei He



A Thesis Submitted for the Degree of Doctor of Philosophy at
The Australian National University

July 1991

Manuscript prepared by  Macintosh™

MacWrite 4.6, MacDraw 1.9.5 and PowerDraw 3.0

US Letter / Times 12 Point / Reduce 14%

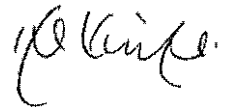
DECLARATION

The research described in this thesis is my own work except where indicated. The work was carried out while I was a full time postgraduate student at the Australian National University.

This thesis has never been submitted to another university or similar institution.

Canberra, July 1991

Xing-Fei He

A handwritten signature in black ink, appearing to read 'Xing-Fei He', written in a cursive style.

ACKNOWLEDGEMENTS

I wish to express my sincere thanks to Dr. Neil B. Manson and Dr. Peter T.H. Fisk for their help, encouragement and supervision throughout the course of this work. I also wish to thank Dr. Zameer Hasan and Dr. Keith Holliday for their help during the initial stages of this study, and Dr. John P.D. Martin for his illuminating discussions and critical reading of this manuscript.

In particular, I wish to thank Professor Lewis T. Chadderton for his help, encouragement and so many invaluable discussions, from which I learnt the art and practice of basic science.

The technical assistance from Mr. Ian McRae and Mr. John Rimmel is gratefully acknowledged. Thanks are also due to Ms. Dianne Hodges for her kindly help in many aspects, to Mr. Wolfgang Boehm for supplying liquid helium and to all other members of the Laser Physics Centre for their help and advice given to me.

Finally, I wish to thank the Australian National University for the financial assistance of an ANU PhD Scholarship.

ABSTRACT

This thesis describes the Raman heterodyne detection of magnetic resonance in the 3A ground state of the nitrogen-vacancy (N-V) centre in diamond. The recently developed theory of Raman heterodyne spectroscopy was tested and compared with the spectra measured on the N-V centre. Among those results, the electron-nuclear double resonance (ENDOR), nuclear-nuclear double resonance (double NMR), Autler-Townes effect, coherence transfer and Zeeman quantum beat were observed for the first time using such techniques. Raman heterodyne techniques were also used to investigate the level anticrossing, hyperfine and nuclear quadrupole interactions, and spin relaxations of the N-V centre with high sensitivity and precision.

This thesis is comprised of three parts. Part one includes Chapters 1 to 3, providing introductory accounts. Chapter 1 is an introduction to the N-V colour centre, which describes the defect configuration, the spin Hamiltonian and the calculations of energy levels and wave functions of the 3A ground state. Chapter 2 briefly describes the theory of Raman heterodyne spectroscopy - a coherent optical radio-frequency (RF) double resonance technique, in particular the Raman heterodyne signals at weak and intense RF fields. Chapter 3 deals with experimental details and techniques utilized in the studies.

Part two consists of Chapters 4 and 5, where the Raman heterodyne theory is compared with experimental results. Chapter 4 presents the Raman heterodyne detected nuclear magnetic resonance (NMR) and electron paramagnetic resonance (EPR) lineshapes compared with theoretical results at various RF power levels, laser intensities and laser frequencies within the 6380\AA zero-phonon line. The double resonance spectra obtained by Raman heterodyne techniques are discussed in Chapter 5, where attention is paid to the analysis of their spectral

profiles depending on the detection scheme.

The application of Raman heterodyne techniques to the studies of magnetic resonance of the N-V centre is described in part three, consisting of Chapters 6 to 9. The EPR measurements are described in Chapter 6, which were used to study various interactions near the level anticrossing, in particular the spin alignment. The hyperfine and nuclear quadrupole interactions probed by the NMR, ENDOR and hole burning measurements are described in Chapter 7. From these measurements, the hyperfine and quadrupole parameters in the spin Hamiltonian were fully determined. Chapter 8 deals with the Autler-Townes effect in the NMR and EPR transitions. By measuring the Autler-Townes splittings, the magnitudes of matrix elements of the NMR transitions were examined and compared. Chapter 9 presents the coherent spin transient properties, including nutations, echoes, Zeeman beating and coherence transfer. The dephasing time and homogeneous linewidths of the NMR and EPR transitions were then determined from the echo measurements.

Finally, the thesis is summarized in Chapter 10.

CONTENTS

Declaration

Acknowledgements

Abstract

<i>Chapter 1</i>	<i>The Nitrogen-Vacancy Colour Centre in Diamond</i>	1
1-1.	Introduction	1
1-2.	Defect Configuration	3
1-3.	Electronic States and Energy Levels	3
	1-3-1. 3A Ground State	6
	1-3-2. 3E Excited State	13
1-4.	Optical and Magnetic Transitions	14
<i>Chapter 2</i>	<i>Raman Heterodyne Detection of Magnetic Resonance</i>	18
2-1.	Introduction	18
2-2.	Raman Heterodyne Signal	22
	2-2-1. Weak RF Fields	25
	2-2-2. RF Fields of Arbitrary Strengths	27
	2-2-3. Optical Pumping Effects	29
2-3.	Symmetry and Interference	29

Chapter 3	<i>Experimental Details</i>	32
3-1.	Sample and Equipment	32
3-2.	Experimental Configuration	37
3-2-1.	Amplitude and Phase Detections	37
3-2-2.	CW Measurements	40
3-2-3.	Transient Measurements	42
3-3.	Linewidth and Inhomogeneity of the Laser and RF Fields	43
Chapter 4	<i>NMR and EPR Lineshape Analysis</i>	46
4-1.	Inhomogeneous Lineshapes at Weak RF Fields	47
4-1-1.	NMR Transition	47
4-1-2.	EPR Transition	51
4-2.	RF Power Broadening and Saturating Effects	55
4-2-1.	NMR	55
4-2-2.	EPR	61
4-3.	Laser Power Dependence	66
4-4.	Laser Detuning within the 6380Å Zero-Phonon Line	71
4-5.	Conclusions	75
Chapter 5	<i>ENDOR and Double NMR Spectra</i>	77
5-1.	ENDOR: Dependence on RF Power	79
5-2.	ENDOR Measured in Different EPR Phase Components	81
5-3.	ENDOR Measured at Different EPR Resonances	81
5-4.	Double NMR	84
5-5.	Conclusions	86

Chapter 6	<i>Level Anticrossing Study</i>	87
6-1.	EPR Lineshape and Spin Alignment	87
6-2.	EPR in the Level Anticrossing Region	90
	6-2-1. Lineshape: Dependence on Magnetic Field Strength	90
	6-2-2. Lineshape: Dependence on Magnetic Field Orientation	92
6-3.	Collapse of EPR at the Level Anticrossing	93
6-4.	Zero-Field Splitting D	101
6-5.	Conclusions	103
Chapter 7	<i>Hyperfine and Nuclear Quadrupole Interactions</i>	105
7-1.	NMR and ENDOR Measurements	106
	7-1-1. Determination of Hyperfine and Quadrupole Parameters	112
	7-1-2. Transition Intensity	119
7-2.	Hole Burning	120
7-3.	Interference Effects	123
7-4.	Spin Density Distribution	127
7-5.	Quadrupole Interaction and Local Electric Field	129
7-6.	Energy Levels and Wave Functions of the 3A Ground State	130
7-7.	Conclusions	136
Chapter 8	<i>The Autler-Townes Effect</i>	138
8-1.	The Autler-Townes Effect in NMR and EPR Transitions	140
8-2.	Doublet Splitting	148
8-3.	Matrix Elements of the $m_J=0 \leftrightarrow \pm 1 (m_S=0)$ Transitions	151
8-4.	Conclusions	156

Chapter 9	Coherent Spin Transients	157
9-1.	Nutation	158
9-2.	Spin Echo and Homogeneous Linewidth 161	
9-2-1.	NMR Transition	165
9-2-2.	EPR Transition	168
9-3.	Coherence Transfer in ENDOR	171
9-4.	Zeeman Quantum Beat	174
9-5.	Conclusions	177
Chapter 10	Summary	181
	References	183

Chapter 1

THE NITROGEN-VACANCY COLOUR CENTRE IN DIAMOND

1-1. INTRODUCTION

Diamond has long been a subject of interest (see *e.g.* Owen 1965, Loubser and van Wyk 1978, Walker 1979). It has the following characteristics that make it particularly worthwhile to study.

(1) The tetrahedral symmetry about each lattice site and the simplicity of the lattice have facilitated the theoretical treatments of optical and magnetic resonances and provided a testing ground for the calculations on defects or impurities.

(2) The covalent nature of the tetrahedrally directed bonds result purely from the sp^3 hybridisation of the carbon atoms, and

(3) It has unique properties such as hardness (10 on Mohs scale), high Debye temperature (2230 K) and large forbidden gap (5.4 eV).

On the other hand, a further understanding of the colour centres is practically important for diamond characterization and applications. Compared with silicon, germanium and other related element or compound semiconductors (see *e.g.* Watkins 1975), diamond has been studied in less detail, mainly due to the inability of selective doping techniques.

The nitrogen-vacancy (N-V) colour centre is found in electron or neutron irradiated and annealed type Ib diamond (du Preez 1965). It is considered to arise from a substitutional nitrogen accompanied by a vacancy at a nearest neighbour site (Davies and Hamer 1976).

Various experiments have been carried out on the N-V centre:

Photoluminescence (Clark and Norris 1971),

Uniaxial stress (Davies and Hamer 1976),

Electron spin resonance (Loubser and van Wyk 1977),

Optical hole burning (Harley *et al.* 1984, Reddy *et al.* 1987),

RF-optical excitation (Bloch *et al.* 1985b),

Spin coherence (van Oort *et al.* 1988, van Oort and Glasbeek 1990a, b),

Cross relaxation dynamics (van Oort and Glasbeek 1989), and

Raman heterodyne spectroscopy (Holliday *et al.* 1990, Manson *et al.* 1990, He *et al.* 1991a, this work).

The optical characteristic of the N-V centre is a strong zero-phonon line at 6380\AA (Davies and Hamer 1976). The argument in some of the earlier papers concerning the electronic states involved in the optical transition has become clear recently and it has been shown that the ground state is a 3A (Reddy *et al.* 1987). Of particular interest for the N-V centre is the inversion of spin population in the 3A state at field strengths greater than the level anticrossing, as observed in the EPR spectra under optical illumination (Loubser and van Wyk 1977). This has led to the suggestion of constructing a maser without microwave pumping.

This chapter describes the N-V defect configuration, the spin Hamiltonian, and the calculations of energy levels, wave functions, and magnetic transition matrix elements, providing an introductory account of the colour centre. The Raman heterodyne technique is introduced in subsequent chapters and is used in the present work to study various interactions of the N-V centre (Holliday *et al.* 1990, Manson *et al.* 1990, He *et al.* 1991a), as will be discussed in detail in Chapters 6 to 9. Because of its simple spectral structure, the centre provides an ideal system for testing the theory of Raman heterodyne spectroscopy (Wong *et al.* 1983, Fisk *et al.* 1990), particularly for analyzing the spectral lineshapes at various RF power levels, as will be presented in Chapters 4 and 5.

1-2. DEFECT CONFIGURATION

The N-V centre used in this study was created by 1 MeV electron irradiation and subsequent annealing at about 650°C. Considering that the vacancies in diamond become mobile at this temperature, Davies and Hamer (1976) have suggested that the defect consists of a substitutional nitrogen atom next to a carbon atom vacancy capturing one extra electron (Fig.1-1). Their optical experiments showed that the centre has trigonal symmetry of point group C_{3v} , where the C_3 major principal axis is along the nitrogen-vacancy pair, which is the crystallographic [111] direction.

There are four orientations of trigonal centres in the cubic lattice (the centres related by spatial inversion are magnetically indistinguishable). Figure 1-2 illustrates the C_3 main axes of four ensembles of the N-V centres, labeled I, II, III and IV respectively (van Oort and Glasbeek 1989). Ensemble I is defined as those whose main axes are along the [111] direction. When an external magnetic field H is applied along the [111] direction, ensemble I is aligned. Only these aligned centres are considered in this study. In this case, ensembles II, III and IV are magnetically equivalent and their energy levels become degenerate. In general, the DC magnetic field direction is aligned in the (110) plane to the [111] direction at a small angle θ ($-1^\circ \leq \theta \leq 1^\circ$), as indicated in Fig.1-2. Angular dependence of resonance spectra can thus be obtained by changing θ . In this case, ensembles II, III and IV are no longer magnetically equivalent and their degeneracy is lifted. The degeneracy reflected in the optical hole bleaching spectra in the 6380Å zero-phonon line is used to judge the crystal alignment (see Chapter 3).

1-3. ELECTRONIC STATES AND ENERGY LEVELS

The uniaxial stress measurements by Davies and Hamer (1976) showed that the 6380Å zero-phonon line results from an A to E transition. It was proposed that the states involved in

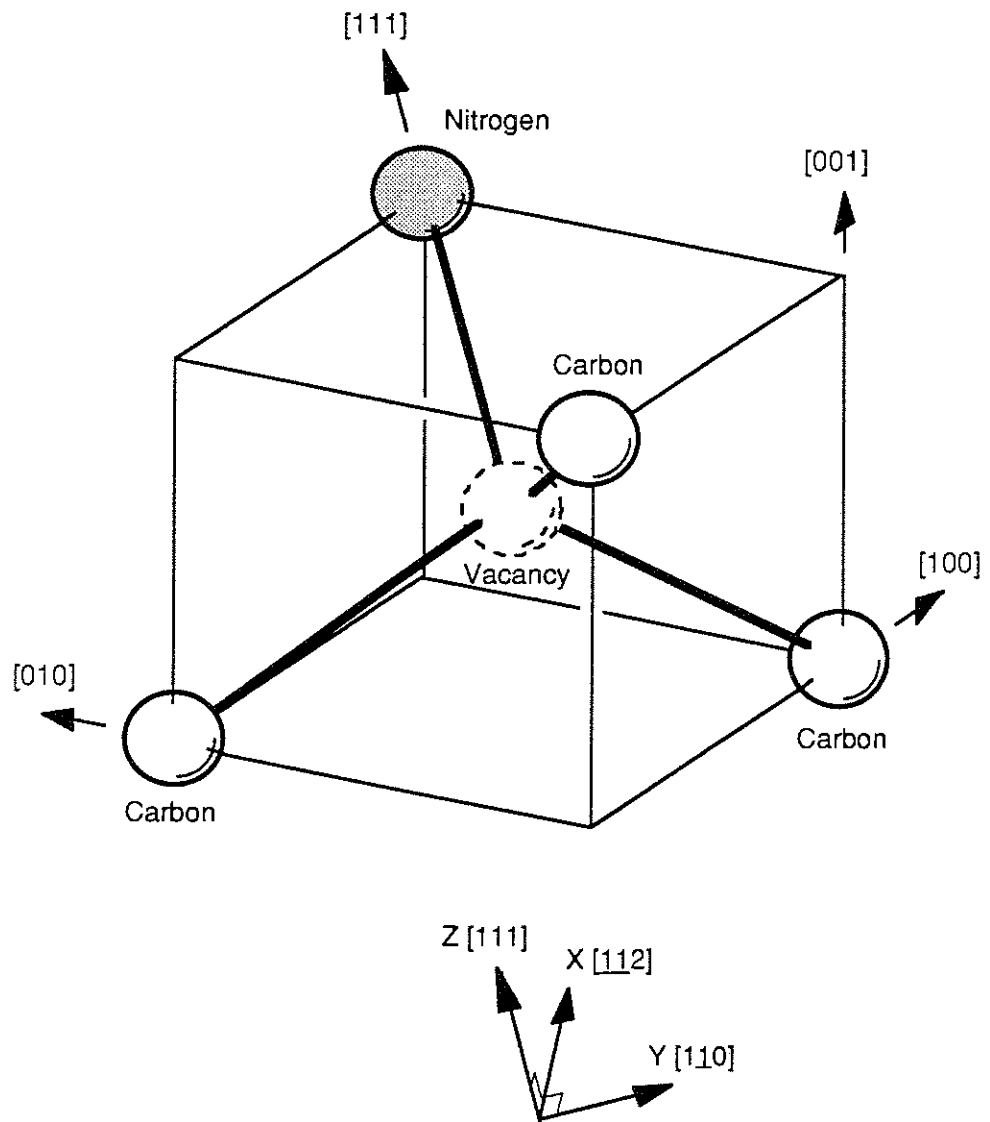


FIG. 1-1 Crystallographic symmetry of the N-V colour centre in diamond. The defect has C_{3v} symmetry and the major principal C_3 axis is along the N-V pair in the $[111]$ direction. The principal coordinate system (X,Y,Z) chosen in the calculations is also shown.

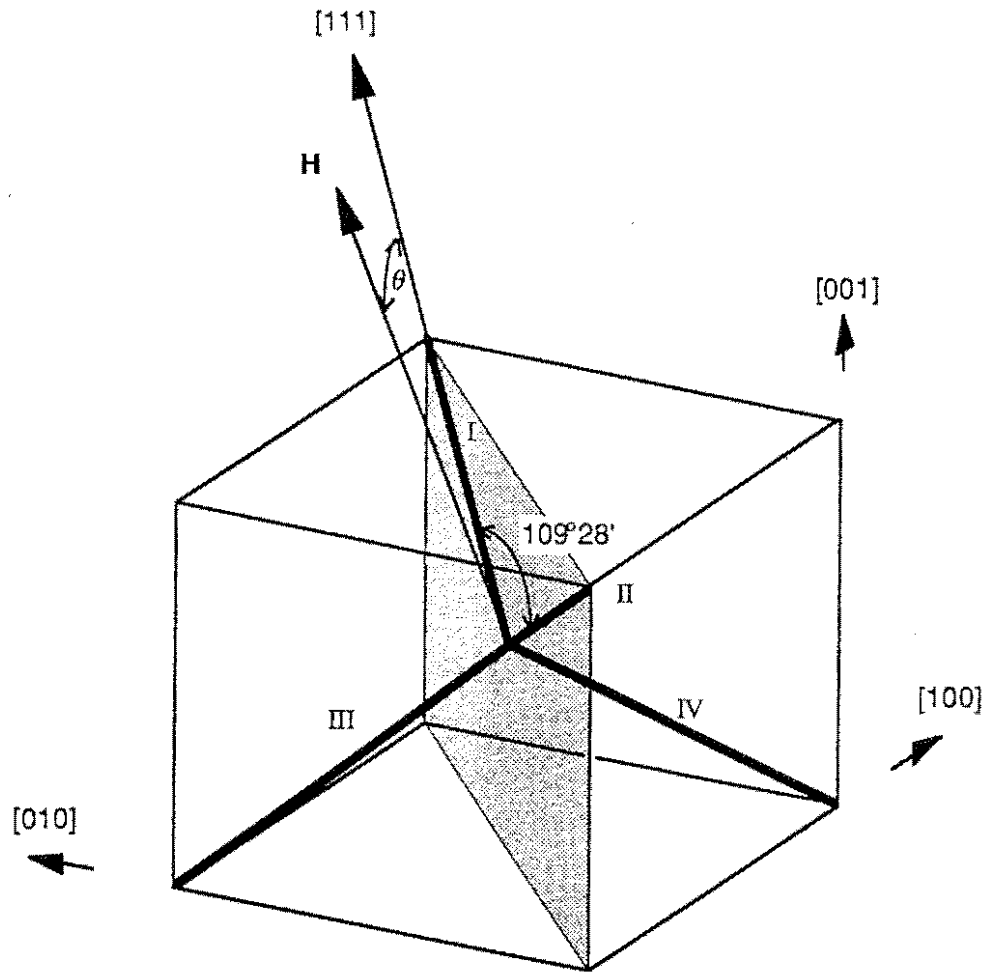


FIG. 1-2 Four orientations of the N-V centres in diamond, where their major principal axes (N-V pairs) are labeled I, II, III and IV respectively. In the experiments a static magnetic field H is applied in the X-Z or $(1\bar{1}0)$ plane (shaded area) to the major principal axis of ensemble I at a small angle θ ($-1^{\circ} \leq \theta \leq 1^{\circ}$).

the optical transition were spin singlets, *i.e.* $^1A \leftrightarrow ^1E$, and that the EPR signals observed under optical illumination arise from an intermediate 3A state (Loubser and van Wyk 1977, Bloch *et al.* 1985a). This conclusion was solely based on the enhancement of the EPR signals upon the illumination of light at about 6380\AA . However, recent experiments have shown the existence of EPR signals at room temperature without optical illumination (Nisida *et al.* 1989, Holliday 1989). Two-laser hole burning measurements by Reddy *et al.* (1987) suggested that the centre has a 3A ground state as the triplets are not excluded from the linear combination of atomic orbitals (LCAO) calculation (Stoneham 1975, Reddy 1989). This was later confirmed by the experiments using spin coherence (van Oort *et al.* 1988, van Oort and Glasbeek 1990a, b), cross relaxation (van Oort and Glasbeek 1989) and Raman heterodyne techniques (Holliday *et al.* 1990, Manson *et al.* 1990, He *et al.* 1991a), which gave unambiguous evidence that the zero-phonon line originates from a $^3A \leftrightarrow ^3E$ transition and that the ground state is indeed a 3A . The enhanced EPR signals reported previously could be interpreted as arising from optical pumping, which favors the population difference in the triplet. This was substantiated by the appearance of emissive EPR signals at high fields (Loubser and van Wyk 1977).

1-3-1. 3A Ground State

It has been demonstrated (Loubser and van Wyk 1977, 1978) that the 3A state is split by the crystal field into a doublet and a singlet separated by $|D|=2.88\text{GHz}$ at zero field and that the EPR spectra are associated with three hyperfine lines 0.8G apart when the DC field is parallel to the [111] axis. The electronic spin triplet ($S=1$) results from two unpaired electrons and the hyperfine structure is associated with the nitrogen (^{14}N), the only atom having non-zero nuclear spin ($I=1$) in the centre. Other weak satellite patterns were also found in previous EPR measurements, which were considered to arise from the 1.1% abundant ^{13}C ($I=1/2$).

As mentioned above, when the magnetic field H is applied along the [111] direction, one

of four ensembles of the N-V centres is aligned. Its Hamiltonian, eigenvalues and wave functions are treated here.

The magnetic field lifts the degeneracy of the $m_S = \pm 1$ states and the two levels split linearly with increasing field strength (Fig.1-3). At 1028G the $m_S = 0$ and $m_S = -1$ levels (assuming $D > 0$, see Chapter 6) approach the same energy but do not cross due to the hyperfine interaction and the slight misalignment of the [111] axis to the field direction in the experiments. This is generally referred to as level anticrossing (LAC). In this anticrossing region, the wave function is an admixture of the $m_S = 0$ and $m_S = -1$ states.

The eigenvalues E_n and wave functions $|n\rangle$, where $n=1, 2, \dots, 6$ denotes the spin levels of the 3A state (the $m_S = 1$ state is not included in this study) in the order of increasing energy, are described by the Schrödinger equation (see *e.g.* Schiff 1968),

$$\mathcal{H}_0 |n\rangle = E_n |n\rangle, \quad (1-1)$$

where \mathcal{H}_0 is the spin Hamiltonian in the presence of a magnetic field H . By solving Eq.(1-1) the energy levels and wave functions at various field strengths and orientations are obtained.

Let $|S m_S\rangle$ be the eigenstates of the electronic spin operators S^2 and S_z and, similarly, $|I m_I\rangle$ be those of the nuclear spin operators I^2 and I_z , where $S=1$ and $m_S = 0, \pm 1$ being the quantum numbers of electronic spin, and $I=1$ and $m_I = 0, \pm 1$ being those of nuclear spin. The direct product expansion,

$$|S m_S\rangle |I m_I\rangle \equiv |S I m_S m_I\rangle \equiv |m_S m_I\rangle, \quad m_S = 0, \pm 1, m_I = 0, \pm 1 \quad (1-2)$$

forms an orthogonal and complete basis, satisfying the usual relationships (see *e.g.* Poole and Farach 1972).

At a magnetic field strength far away from the anticrossing (1028G), the electronic spin (S, m_S) and the nuclear spin (I, m_I) may be good quantum numbers and therefore the eigenstates of the 3A are $|m_S m_I\rangle$ to a fair approximation. In the anticrossing region, however, the eigenstates

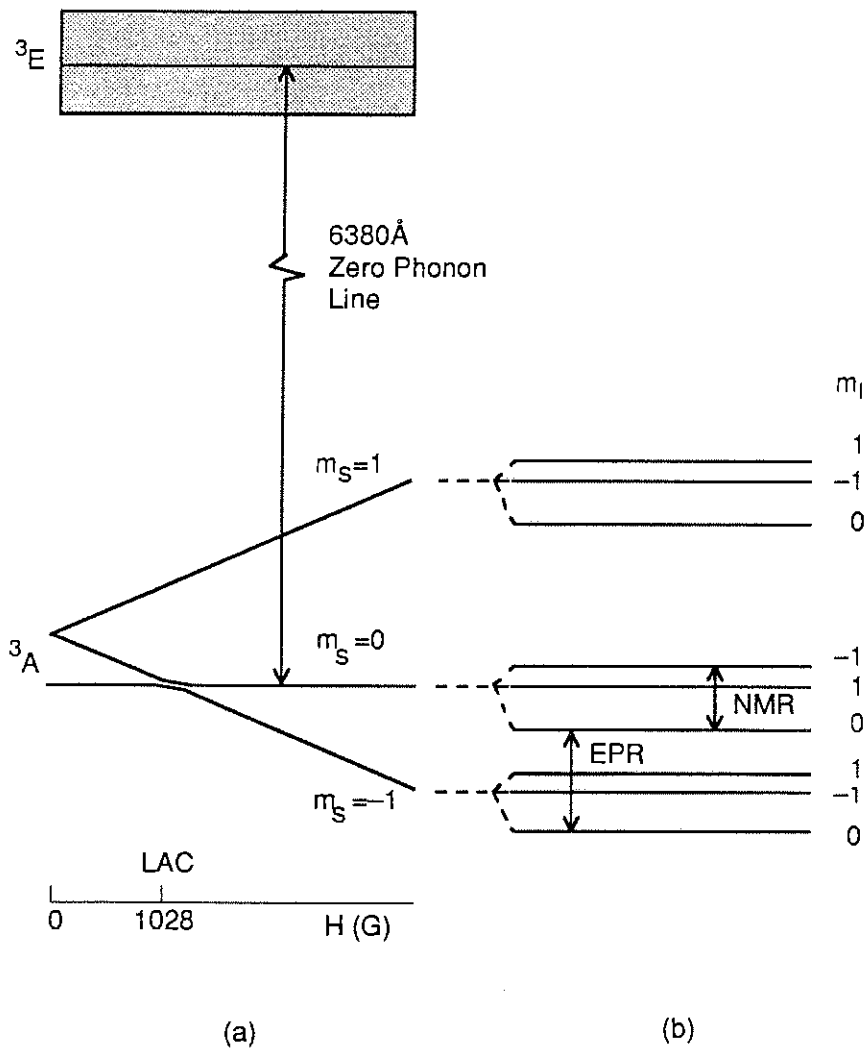


FIG. 1-3 A schematic of energy levels for the $^3A \leftrightarrow ^3E$ zero-phonon optical transition and the magnetic transitions within the 3A ground state of the N-V centre. The broad 3E excited state is shown by a shaded area. (a) Energy level splitting in a static magnetic field $H//[111]$, where the hyperfine structure is ignored. (b) Hyperfine sub-levels due to ^{14}N nuclear spin at a field strength greater than the level anticrossing value (1028G).

are in general the linear combinations of the $|m_S m_I\rangle$ basis,

$$|n\rangle = \sum_{m_S m_I} a_n(m_S m_I) |m_S m_I\rangle, \quad (1-3)$$

where

$$a_n(m_S m_I) = \langle m_S m_I | n \rangle, \quad m_S = 0, -1, m_I = 0, \pm 1$$

are coefficients, which form a representation of the wave function $|n\rangle$ in the $|m_S m_I\rangle$ basis. The $m_S=1$ state is ignored here as it lies much higher in energy (~ 5.8 GHz above the $m_S=0$ state) in the level anticrossing region. The wave function $|n\rangle$ can be written as a column matrix,

$$[|n\rangle] = \begin{bmatrix} a_n(-) \\ a_n(-0) \\ a_n(-+) \\ a_n(0-) \\ a_n(00) \\ a_n(0+) \end{bmatrix} \quad (1-4)$$

where + represents +1 and - represents -1. The quantity

$$|a_n(m_S m_I)|^2 = a_n^*(m_S m_I) a_n(m_S m_I)$$

gives the probability of the wave function $|n\rangle$ being in the $|m_S m_I\rangle$ state (see *e.g.* Schiff 1968). As $|m_S m_I\rangle$ forms a complete basis, observables can be calculated by solving the eigen problem in such a space.

The spin Hamiltonian in the presence of a magnetic field is given by (see *e.g.* Poole and Farach 1972),

$$\mathcal{H}_0 = \mathcal{H}_Z + \mathcal{H}_{CF} + \mathcal{H}_{HF} + \mathcal{H}_{Zn} + \mathcal{H}_Q, \quad (1-5)$$

where terms in the right hand side represent, respectively, the electronic Zeeman, the second-order crystal field, the magnetic hyperfine, the nuclear Zeeman and the nuclear electric quadrupole interactions. These terms can be expressed in terms of electron and nuclear spin operators and they have simple forms in the principal coordinate system.

For the trigonal N-V centre, it is convenient to define the coordinate system in terms of the crystallographic principal axes, where,

X-axis: $[1\bar{1}2]$

Y-axis: $[1\bar{1}0]$

Z-axis: $[111]$,

as shown in Fig. 1-1. The static magnetic field \mathbf{H} is applied in the X-Z or $(1\bar{1}0)$ plane to the Z-axis at an angle θ (Fig.1-2), and therefore its components are

$$\mathbf{H} = H(\sin\theta, 0, \cos\theta),$$

where H is the magnitude of the magnetic field strength.

It has been demonstrated (Loubser and van Wyk 1977) that the electronic g -tensor \mathbf{g} is isotropic with $g_{||} = g_{\perp} = g = 2.0028$. The electronic Zeeman term is therefore (see *e.g.* Poole and Farach 1972),

$$\begin{aligned} \mathcal{H}_Z &= \beta \mathbf{H} \cdot \mathbf{g} \cdot \mathbf{S} \\ &= (\gamma/2\pi) H [S_z \cos\theta + (S^+ + S^-) \sin\theta / 2], \end{aligned} \quad (1-6)$$

where S^+ and S^- are respectively the electronic spin raising and lowering operators, β is the electronic Bohr magneton ($\beta=1.40$ MHz/G), $\gamma=g\beta/\hbar$ is the electron gyromagnetic ratio and the Hamiltonian (energy) has units of Hz. For the N-V centre, $\gamma/2\pi=2.80$ MHz/G.

In the principal coordinate system, the D-tensor D is diagonal and the crystal field term for a trigonal centre can be simplified to,

$$\begin{aligned}\mathcal{H}_{CF} &= S.D.S \\ &= D[S_z^2 - S(S+1)/3],\end{aligned}\quad (1-7)$$

where the zero-field splitting D is related to the D-tensor matrix element by $D=3D_{zz}/2$ and it has been determined previously that $|D|=2.88$ GHz (Loubser and van Wyk 1977).

The hyperfine tensor A for the trigonal centre can be expressed by the parameters $A_{||}$ and A_{\perp} and the interaction is given by,

$$\begin{aligned}\mathcal{H}_{HF} &= S.A.I \\ &= A_{||}S_zI_z + A_{\perp}(S^-I^+ + S^+I^-)/2,\end{aligned}\quad (1-8)$$

where I^+ and I^- are respectively the nuclear spin raising and lowering operators. $|A_{||}|=2.3$ MHz was given by a conventional EPR measurement (Loubser and van Wyk 1977).

As is in most cases, the nuclear spin is less affected by the surrounding lattice and its g-tensor g_n can be assumed to be isotropic. Therefore, similarly to Eq.(1-6) the nuclear Zeeman term is,

$$\begin{aligned}\mathcal{H}_{Zn} &= -\beta_n H \cdot g_n \cdot I \\ &= -(\gamma_n/2\pi)H [I_z \cos\theta + (I^+ + I^-) \sin\theta / 2],\end{aligned}\quad (1-9)$$

where β_n is the nuclear Bohr magneton ($\beta_n=0.762$ kHz/G) and $\gamma_n=g_n\beta_n/\hbar$ is the nuclear gyromagnetic ratio. For ^{14}N the values are $g_n=0.4036$ and $\gamma_n/2\pi=0.307$ kHz/G (Pople, Schneider and Bernstein 1959). These values are taken in the calculations of magnetic resonance

of the N-V centre.

The nuclear electric quadrupole interaction is of the same form as Eq.(1-7),

$$\begin{aligned} \mathcal{H}_Q &= I.P.I \\ &= P[I_z^2 - I(I+1)/3], \end{aligned} \quad (1-10)$$

where the quadrupole parameter P is related to the matrix element of P-tensor P by $P=3P_{zz}/2$.

In the above expressions, it has been assumed that the principal axes of the tensors A , D and P coincide as they do in most cases for diamond (Loubser and van Wyk 1978). However, their anisotropies may not be the same (Abragam 1961, Abragam and Bleaney 1970).

In the $|m_S m_I\rangle$ basis, the spin Hamiltonian is a 6x6 matrix (Poole and Farach 1972),

$$\langle m_S m_I | \mathcal{H}_0 | m_S m_I \rangle, \quad m_S=0, -1, \quad m_I=0, \pm 1,$$

which is represented below corresponding to the order of the $|m_S m_I\rangle$ basis indicated.

$$[\mathcal{H}_0] = \begin{bmatrix} \begin{matrix} | \rightarrow & | -0 \rangle & | + \rangle & | 0 \rangle & | 00 \rangle & | 0+ \rangle \end{matrix} \\ \begin{matrix} (-k+k_n)\eta + \frac{D}{3} + A_{//} + \frac{P}{3} & -\frac{k_n\zeta}{\sqrt{2}} & 0 & \frac{k\zeta}{\sqrt{2}} & 0 & 0 \\ -\frac{k_n\zeta}{\sqrt{2}} & -k\eta + \frac{D}{3} - \frac{2P}{3} & -\frac{k_n\zeta}{\sqrt{2}} & A_{\perp} & \frac{k\zeta}{\sqrt{2}} & 0 \\ 0 & -\frac{k_n\zeta}{\sqrt{2}} & (-k-k_n)\eta + \frac{D}{3} - A_{//} + \frac{P}{3} & 0 & A_{\perp} & \frac{k\zeta}{\sqrt{2}} \\ \frac{k\zeta}{\sqrt{2}} & A_{\perp} & 0 & k_n\eta - \frac{2D}{3} + \frac{P}{3} & -\frac{k_n\zeta}{\sqrt{2}} & 0 \\ 0 & \frac{k\zeta}{\sqrt{2}} & A_{\perp} & -\frac{k_n\zeta}{\sqrt{2}} & -\frac{2D}{3} - \frac{2P}{3} & -\frac{k_n\zeta}{\sqrt{2}} \\ 0 & 0 & \frac{k\zeta}{\sqrt{2}} & 0 & -\frac{k_n\zeta}{\sqrt{2}} & -k_n\eta - \frac{2D}{3} + \frac{P}{3} \end{matrix} \end{bmatrix}$$

(1-11)

The parameters in Eq.(1-11) are, $k=(\gamma 2\pi)H$, $k_n=(\gamma_n/2\pi)H$, $\eta=\cos\theta$ and $\zeta=\sin\theta$.

By diagonalizing the Hamiltonian matrix, Eq.(1-11), the energy levels E_n (in Hz) and the wave functions $|n\rangle$ of the triplet, where $n=1,2,\dots,6$, can be obtained as a function of either H or θ . Thus the $|n\rangle\leftrightarrow|m\rangle$ transition frequencies, $\nu_{nm}=|E_n-E_m|$ ($n\neq m$, $n,m=1,2,\dots,6$), are obtained. Conversely, by fitting the experimental data of resonance frequencies to the Hamiltonian, the parameters D , $A_{//}$, A_{\perp} and P are determined. This, in general, can only be done numerically.

When H is set far away from the level anticrossing (1028 G), one of $a_n(m_S m_I)$ dominates in each eigenstate $|n\rangle$. In the anticrossing region, however, the states are strongly mixed such that each $|n\rangle$ consists of several significant $a_n(m_S m_I)$ components.

1-3-2. 3E Excited State

The first excited state 3E is 1.945eV (6380Å) above the ground state and has a radiative lifetime of 13ns (Collins *et al.* 1983). Its orbital g-value and spin-orbit parameter have been determined to be $g=0.10$ and $\lambda=30\text{GHz}$ (Reddy *et al.* 1987). With zero stress, the triplet splits into three two-fold degenerate levels separated by λ . However, few centres are free from stress in diamond and it is likely that there is large internal stress which will lift the symmetry of the centre. The total inhomogeneous width of the 6380Å zero-phonon line is about 1THz and there can be large strain splittings of the 3E state, as shown in the two-laser spectral hole burning spectra (Reddy *et al.* 1987).

The detailed treatment of the spin levels in the 3E excited state requires a consideration of the strain distribution inside the crystal (Reddy *et al.* 1987, Reddy 1989). Nevertheless, their actual positions are not a concern for the studies of magnetic resonances in the 3A ground state. For Raman heterodyne experiments and calculations in this study, the $^3A\leftrightarrow^3E$ zero-phonon transition driven by a single mode laser can be simply treated as a selective excitation between the ground state and the excited state of a particular subgroup of N-V centres in the broad

inhomogeneous distribution. The energy level of the subgroup in the 3E state associated with the ${}^3A \leftrightarrow {}^3E$ transition is indicated by a line in a shaded area in Fig.1-3.

Although the Raman heterodyne technique is capable of measuring magnetic resonances either in a ground state or in an optically excited state, we have been unable to detect such signals in the 3E state. This may be attributed to the very short radiative lifetime (13 ns), which prevents an appreciable population factor in the excited levels from being obtained.

1-4. OPTICAL AND MAGNETIC TRANSITIONS

The 6380Å zero-phonon optical transition and the magnetic transitions within the 3A ground state are illustrated in Fig.1-3. The optical transition induced by the interaction between the electric dipole moment μ_E and the laser field $E_L(r,t)$ is represented by the Hamiltonian as (see *e.g.* Yariv 1975),

$$\mathcal{H}_1(t) = -\mu_E \cdot E_L(r,t).$$

The transition matrix element for the 6380Å zero-phonon line $\mu_{23} = \langle 2 | \mu_E | 3 \rangle$ is determined by the symmetry of wave functions of both the 3A ground and 3E excited states, where μ_E is the component of the electric dipole moment μ_E in the direction of the laser polarization, and $|2\rangle$ and $|3\rangle$ are two spin levels in the 3A and 3E states, respectively. In Raman heterodyne measurements, the laser was polarized along the X-axis or the $[112]$ direction. Because of the spin-orbit coupling in the 3E state, the optical transition $|2\rangle \leftrightarrow |3\rangle$ connecting any spin level $|2\rangle$ in the 3A state is active and significant. This condition is important for obtaining a non-zero Raman heterodyne signal (see Chapter 2).

The magnetic transitions are induced by the interaction between the magnetic dipole moment μ_H and the RF field, $H_{RF}(t)$, described by (see e.g. Slichter 1990),

$$\mathcal{H}_1(t) = -\mu_H \cdot H_{RF}(t).$$

In Raman heterodyne experiments, the RF field was polarized along Y-axis, or the $[1\bar{1}0]$ direction. The magnetic dipole moment of the N-V centre comprises contributions from the electronic and nuclear spins,

$$\mu_H = (-\gamma S + \gamma_n I) / 2\pi, \quad (1-12)$$

where its units have been transformed into Hz/G, consistent with the units of Hamiltonian (in Hz). Its component in the direction of RF field polarization is given by,

$$\mu_H = [-\gamma(S^+ - S^-) + \gamma_n(I^+ - I^-)] / 4\pi i. \quad (1-13)$$

The magnetic dipole transition matrix element or coupling strength between $|1\rangle$ and $|2\rangle$, where $|1\rangle$ and $|2\rangle$ are two spin levels in the 3A state, is given by $\mu_{12} = \langle 1 | \mu_H | 2 \rangle$, which determines the transition intensity.

In the $|m_S m_I\rangle$ representation, the magnetic dipole moment operator (Poole and Farach 1972),

$$\langle m_S m_I | \mu_H | m_S m_I \rangle, \quad m_S = 0, -1, m_I = 0, \pm 1, \quad .$$

is a 6x6 matrix, which is given below corresponding to the order of $|m_S m_I\rangle$ basis indicated.

$$\begin{array}{cccccc}
| \rightarrow & | \rightarrow 0 & | \rightarrow + & | 0 \rightarrow & | 00 \rightarrow & | 0+ \rightarrow \\
\left[\mu_H \right] = & \begin{bmatrix}
0 & \frac{\sqrt{2}\gamma_n}{4\pi_i} & 0 & -\frac{\sqrt{2}\gamma}{4\pi_i} & 0 & 0 \\
-\frac{\sqrt{2}\gamma_n}{4\pi_i} & 0 & \frac{\sqrt{2}\gamma_n}{4\pi_i} & 0 & -\frac{\sqrt{2}\gamma}{4\pi_i} & 0 \\
0 & -\frac{\sqrt{2}\gamma_n}{4\pi_i} & 0 & 0 & 0 & -\frac{\sqrt{2}\gamma}{4\pi_i} \\
\frac{\sqrt{2}\gamma}{4\pi_i} & 0 & 0 & 0 & \frac{\sqrt{2}\gamma_n}{4\pi_i} & 0 \\
0 & \frac{\sqrt{2}\gamma}{4\pi_i} & 0 & -\frac{\sqrt{2}\gamma_n}{4\pi_i} & 0 & \frac{\sqrt{2}\gamma_n}{4\pi_i} \\
0 & 0 & \frac{\sqrt{2}\gamma}{4\pi_i} & 0 & -\frac{\sqrt{2}\gamma_n}{4\pi_i} & 0
\end{bmatrix} & (1-14)
\end{array}$$

The transition matrix element between any two levels, $\mu_{nm} = \langle n | \mu_H | m \rangle$ ($n \neq m$, $n, m = 1, 2, \dots, 6$), in the 3A state at various magnetic field strengths and orientations can be calculated by transforming Eq.(1-14) into the representation in which the Hamiltonian Eq.(1-11) is diagonal.

In usual circumstances, γ is much larger than γ_n ($\gamma/\gamma_n \sim 10^3$) and therefore the EPR transition is much stronger than the NMR transition. In the level anticrossing region, however, both the electron and nuclear spin states are strongly mixed such that the NMR transition are greatly enhanced, giving rise to significant NMR signals comparable to EPR transitions. In this region, many normally "forbidden" transitions appear and the spectra are complicated.

It is worth noting that the NMR or EPR intensity measured by conventional techniques is proportional to μ_{12}^2 , while the Raman heterodyne detected signal intensity in the weak RF field regime is proportional to μ_{12} , as will be discussed in Chapter 2.

Though in the level anticrossing region m_S and m_I are no longer good quantum numbers, theoretical calculations show that one of the $a_n(m_S m_I)$ components still dominates (>80%) in each eigenstate $|n\rangle$ unless H is very close to the anticrossing where $1023\text{G} < H < 1033\text{G}$ (see Chapter 7). As most measurements in this study were carried out at field values outside this

regime, we will use the following notations to label spin transitions,

$$\begin{aligned} m_S=m_S' \leftrightarrow m_S''(m_I=m_I') & \text{ or } m_S' \leftrightarrow m_S''(m_I') && \text{for an EPR transition} \\ m_I=m_I' \leftrightarrow m_I''(m_S=m_S') & \text{ or } m_I' \leftrightarrow m_I''(m_S') && \text{for an NMR transition,} \end{aligned}$$

instead of using the symbol $|n\rangle \leftrightarrow |m\rangle$. The former is more convenient and also physically clear.

Chapter 2

RAMAN HETERODYNE DETECTION OF MAGNETIC RESONANCE

2-1. INTRODUCTION

Raman heterodyne detection of magnetic resonance was first reported by Mlynek *et al.* (1983) and its detail theoretical description was later provided by Wong *et al.* (1983). The technique was developed as a new way for optically detecting magnetic resonance using a coherent optical radio-frequency (RF) induced Raman effect and is capable of monitoring CW magnetic resonances or coherent spin transients in both ground and optically excited states with high sensitivity and precision. The method surpasses previous optically detected magnetic resonance (ODMR) techniques and allows the sensitive detection of nuclear magnetic resonance (NMR) (Mlynek *et al.* 1983 and Wong *et al.* 1983), electron paramagnetic resonance (EPR) (Fisk *et al.* 1990, Holliday *et al.* 1990, Manson *et al.* 1990) and possibly infrared transitions. This method has been demonstrated in the following impurity and defect systems:

$\text{LaF}_3:\text{Pr}^{3+}$ (Mlynek *et al.* 1983, Wong *et al.* 1983, Takahashi *et al.* 1987 and 1988, Erickson 1989),

$\text{YAlO}_3:\text{Pr}^{3+}$ (Taylor 1984, Misunaga *et al.* 1984 and 1985, Kintzer *et al.* 1985, Erickson 1990),

$\text{LiYF}_4:\text{Pr}^{3+}$ (Erickson 1985),

$\text{YAG}:\text{Pr}^{3+}$ (Bloch *et al.* 1985a)

$\text{YAlO}_3:\text{Eu}^{3+}$ (Erickson 1987),

$\text{KEu}(\text{WO}_4)_2$ (Manson and Silversmith 1987),

$\text{Al}_2\text{O}_3:\text{Cr}^{3+}$ (Szabo *et al.* 1988 and 1990), and diamond N-V centre (Fisk *et al.* 1990, Holliday *et al.* 1990, Manson *et al.* 1990, He *et al.* 1991b, this work).

Figure 2-1 is a simplified schematic of the experimental arrangement for the Raman heterodyne detection of magnetic resonance of the N-V centre in diamond in this study. A static magnetic field H is applied such that the system is in the level anticrossing region. A laser field E_L at frequency ω_L and an RF field H_{RF} at frequency ω_{RF} resonantly drive two coupled optical and magnetic transitions sharing a common level, which combine in a two-photon process to generate coherent Raman fields at frequencies $\omega_R = \omega_L \pm \omega_{RF}$ (Fig. 2-2). The two optical fields ω_L and ω_R produce a heterodyne beat signal of frequency $\omega_{RF} = |\omega_R - \omega_L|$ detected by a photodiode. Unlike the usual stimulated Raman effect (see *e.g.* Levenson 1982), this is a resonant process in which all three transitions are either electric or magnetic dipole allowed (Wong *et al.* 1983). By sweeping the RF field through the resonance, the spectral lineshape of this magnetic transition can be displayed in a spectrum analyzer with kilohertz precision, enabling one to test the line broadening theory and to analyze the hyperfine interaction. Spin transients can also be measured with appropriate RF switching techniques, allowing observation of spin relaxation behaviour.

This chapter describes the theory of Raman heterodyne spectroscopy, including the Raman heterodyne signals at weak and intense RF fields, and the interference effect due to the crystal or site symmetry. The theory will be tested and compared with the experimental results measured on the N-V centre in diamond (Chapters 4 and 5). In this study, the Raman heterodyne technique is employed to measure the magnetic resonances, including the NMR, EPR, electron-nuclear double resonance (ENDOR), nuclear-nuclear double resonance (double NMR), Autler-Townes splitting and hole burning effect in the 3A ground state under CW or transient conditions. From these measurements, important properties such as the hyperfine and quadrupole interaction parameters and the spin-spin relaxation times are determined (Chapters 6-9).

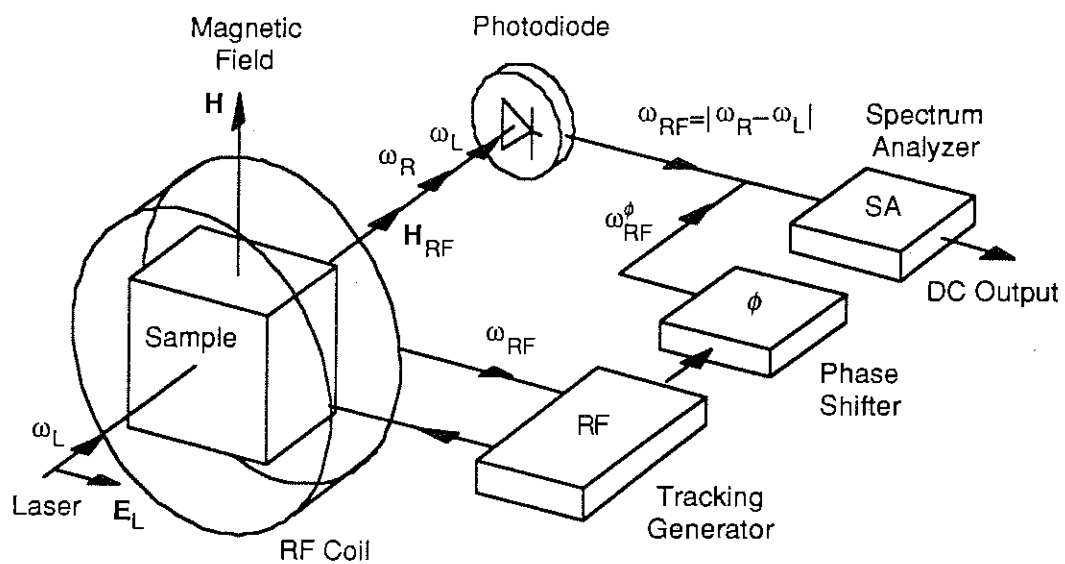


FIG. 2-1 A basic schematic of the experimental arrangement for the Raman heterodyne detection of magnetic resonance of the N-V centre in diamond.

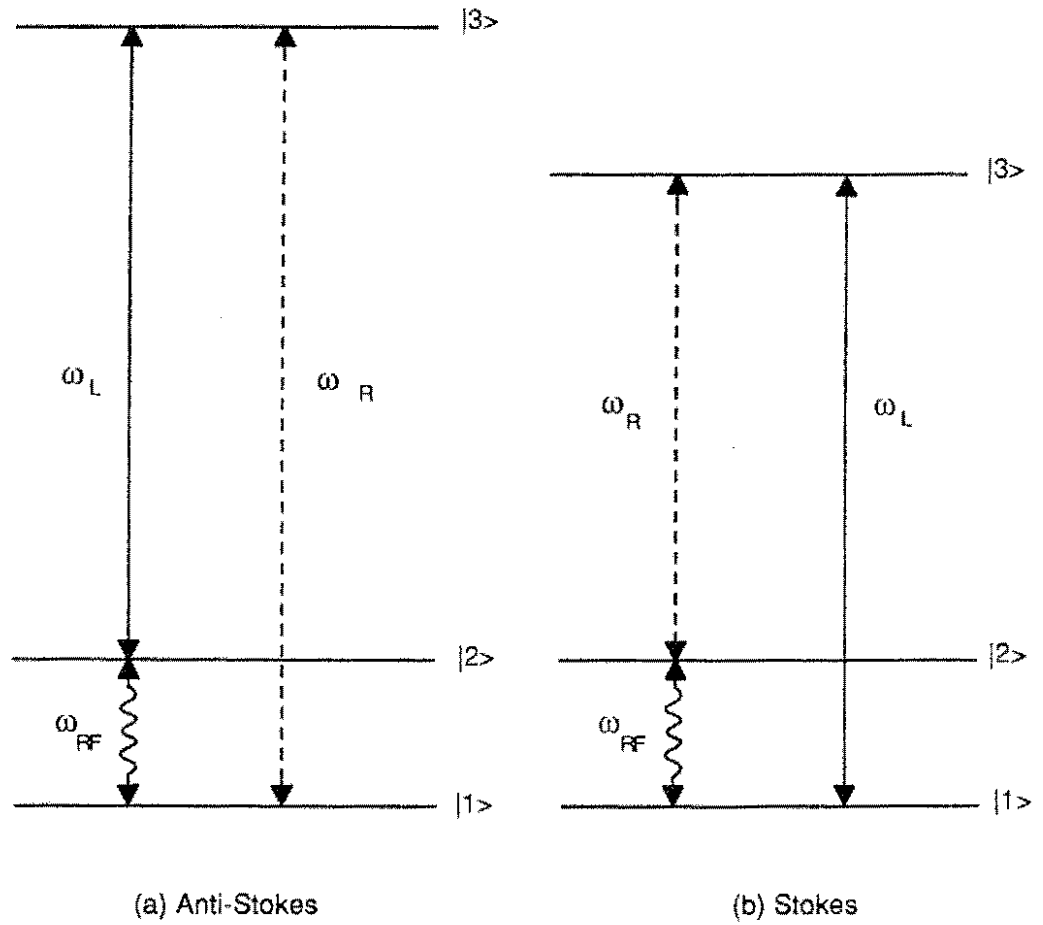


FIG. 2-2 The three level systems for the Raman heterodyne detection of magnetic resonance, where both anti-Stokes $\omega_R = \omega_L + \omega_{RF}$ (a) and Stokes $\omega_R = \omega_L - \omega_{RF}$ (b) processes are shown. The energy levels in (a) and (b) are related to two different subgroups of N-V centres.

2-2. RAMAN HETERODYNE SIGNAL

A detailed theoretical treatment of Raman heterodyne spectroscopy at weak RF fields was provided by Wong *et al.* (1983) using a density matrix perturbation method. Recently, a theoretical description based on the Bloch equations applicable to arbitrary RF field strengths was given by Fisk *et al.* (1990), complementing the previous theory for the weak RF field regime. Their theories are outlined below.

The Raman heterodyne technique applies to any three level system $|i\rangle$ where all three transitions $|i\rangle \leftrightarrow |j\rangle$, where $i \neq j$, $i, j = 1, 2, 3$, are dipole allowed (Fig.2-2). For the N-V centre, this requirement is satisfied because of the spin-orbit coupling in the 3E state (Reddy *et al.* 1987). The magnetic dipole transition $|1\rangle \leftrightarrow |2\rangle$ is driven by an RF field at frequency ω_{RF} (in angular frequency units),

$$H_{RF}(t) = H_{RF} \cos(\omega_{RF} t), \quad (2-1)$$

where the spatial dependence is ignored because the RF wavelength is much larger than the interaction region. The electric dipole transition $|2\rangle \leftrightarrow |3\rangle$ is driven by a laser field at frequency ω_L (in angular frequency units),

$$E_L(r, t) = E_L \cos(\omega_L t - \mathbf{k}_L \cdot \mathbf{r}), \quad (2-2)$$

where \mathbf{k}_L is the wavevector of the laser. The frequencies of laser and RF field satisfy the condition $\omega_L \gg \omega_{RF}$.

The density matrix equations of motion are given by (Wong *et al.* 1983),

$$i\hbar \frac{\partial \rho(t)}{\partial t} = [\mathcal{H}(t), \rho(t)] + \text{relaxation terms}, \quad (2-3)$$

where the square bracket denotes the commutation, \hbar is Planck's constant divided by 2π , $\rho(t)$ is the density matrix and the Hamiltonian $\mathcal{H}(t)=\mathcal{H}_0+\mathcal{H}_1(t)$ consists of the field free Hamiltonian \mathcal{H}_0 and the dipole interactions,

$$\mathcal{H}_1(t) = -\boldsymbol{\mu}_E \cdot \mathbf{E}_L(\mathbf{r},t) - \boldsymbol{\mu}_H \cdot \mathbf{H}_{RF}(t),$$

where $\boldsymbol{\mu}_E$ and $\boldsymbol{\mu}_H$ are the electric and magnetic dipole moment operators, respectively.

The electric field magnitude of the Raman signal $E_S(\mathbf{r},t)$ results from the polarization $P_S(\mathbf{r},t)$ induced in the sample by the applied laser and RF fields, where

$$\tilde{P}_S(t) = N [\mu_{31} \langle \tilde{\rho}_{13}(t) \rangle + \mu_{32} \langle \tilde{\rho}_{23}(t) \rangle] \quad (2-4)$$

and for an optically thin sample from Maxwell's wave equations,

$$\frac{\partial \tilde{E}_S}{\partial y} = -2\pi i k_S \tilde{P}_S, \quad (2-5)$$

where N is the number density of the centres, k_S is the wave number of the induced Raman field, μ_{ij} ($i \neq j$, $i,j=1,2,3$) are the dipole moments of transitions $|i\rangle \leftrightarrow |j\rangle$, ρ_{ij} are the optical coherences (off-diagonal density matrix elements) and y is the distance along the sample. The angular bracket in Eq.(2-4) denotes averaging over the Gaussian optical and RF inhomogeneous profiles. The tilde indicates that oscillations at optical frequencies have been removed by a suitable transformation (Wong *et al.* 1983, Whitley and Stroud 1976).

The Raman signal field $E_S(\mathbf{r},t)$ and the input laser field $E_L(\mathbf{r},t)$ give rise to the total field,

$$E_T(\mathbf{r},t) = E_L(\mathbf{r},t) + E_S(\mathbf{r},t).$$

From the total optical intensity $I_T = E_T \cdot E_T^*$ one obtains the observable heterodyne beat signal,

$$I_S(t) = \text{Re} [\vec{E}_S(t) E_L] . \quad (2-6)$$

The optical coherences can be calculated by solving Eq.(2-3) with relevant conditions and approximations. Thus the Raman field and the heterodyne signal can be obtained by integrating over the inhomogeneous distributions.

For a weak laser field, an optically thin sample and the condition that the optical inhomogeneous linewidth is much larger than that of the magnetic transition, which is valid for the N-V centre in diamond, the resulting Raman heterodyne signal intensity, $I_S(t)$, can be described as follows (Wong *et al.* 1983, Fisk *et al.* 1990),

$$I_S(t) = C e^{-\left(\frac{\Delta_L}{\sigma_E}\right)^2} \left[A_I(\omega_{RF}) \cos(\omega_{RF}t) + A_O(\omega_{RF}) \sin(\omega_{RF}t) \right] , \quad (2-7)$$

where C is a constant of proportionality, $\Delta_L = \omega_L - \omega_{23}$ is the laser frequency detuning, ω_{23} and σ_E are respectively the centre frequency and linewidth of the inhomogeneous optical profile, and $A_I(\omega_{RF})$ and $A_O(\omega_{RF})$ are the spectral lineshapes of the in-phase and the 90° out-of-phase components.

Equation (2-7) indicates that the Raman heterodyne signal consists of two different phases. Using appropriate detection techniques, either the in-phase $A_I(\omega_{RF})$ or the out-of-phase $A_O(\omega_{RF})$ components can be selected (see Chapter 3).

The total beat signal, $I_T(t)$, is the vector sum of two phase components,

$$I_T(t) = C e^{-\left(\frac{\Delta_L}{\sigma_E}\right)^2} A_T(\omega_{RF}) \cos(\omega_{RF}t + \phi) , \quad (2-8)$$

where

$$A_T(\omega_{RF}) = \sqrt{A_I(\omega_{RF})^2 + A_O(\omega_{RF})^2} \quad (2-9)$$

is the total amplitude lineshape and ϕ is a phase constant. In Eq.(2-9), the information on the phase of the individual components is lost. This scheme is referred to as amplitude detection.

Equations (2-7) and (2-8) also indicate that the optical Gaussian profile, $\exp[-(\Delta_I/\sigma_E)^2]$, is preserved in the Raman heterodyne lineshape if the condition $\sigma_E \gg \sigma_H$ is satisfied. This is a result of the weak laser field approximation.

2-2-1. Weak RF Fields

In the case of weak excitation fields, Eq.(2-3) can be solved using a perturbation technique (Wong *et al.* 1983) to give a perturbative stationary solution to the equations of motion to various orders. Wong *et al.* (1983) have calculated the second order solutions of the density matrix, which reflect the two-quantum transitions. In the weak field regime, they showed that the Raman heterodyne lineshapes are given by,

$$A_I(\omega_{RF}) = \text{Im} w \left(\frac{\Delta_{RF} + i \Gamma_2}{\sigma_H} \right) \quad (2-10a)$$

and

$$A_O(\omega_{RF}) = \text{Re} w \left(\frac{\Delta_{RF} + i \Gamma_2}{\sigma_H} \right) , \quad (2-10b)$$

where $\Delta_{RF} = \omega_{RF} - \omega_{I2}$ is the RF frequency detuning, ω_{I2} and σ_H are respectively the centre frequency and linewidth (in angular frequency units) of the inhomogeneous RF transition, Γ_2 is the transverse or spin-spin decay rate (in angular frequency units) and $w(z)$ is the w -function (Abramowitz and Stegun 1972) defined as follows,

$$\begin{aligned}
w(z) &= \frac{i}{\pi} \int_{-\infty}^{\infty} \frac{e^{-t^2}}{z-t} dt \quad (\text{Im } z > 0) \\
&= e^{-z^2} [1 + \text{erf}(iz)] ,
\end{aligned}$$

which is related to the error function $\text{erf}(z)$. The prefactor in Eq.(2-7) or (2-8) is,

$$C = \pi^2 k_L L N \mu_{12} \mu_{23} \mu_{31} (P_2 - P_1) E_L^2 H_{RF} / \hbar^2 \sigma_E \sigma_H,$$

where P_i ($i=1,2$) are the field-free populations of state $|i\rangle$ and L is the thickness of the sample.

Wong *et al.* (1983) demonstrated that for a large magnetic inhomogeneous linewidth $\sigma_H \gg \Gamma_2$ the Raman heterodyne lineshapes of Eqs.(2-10a) and (2-10b) reduce to,

$$A_I(\omega_{RF}) = \frac{2}{\sqrt{\pi}} \left(\frac{\Delta_{RF}}{\sigma_H} \right) e^{-\left(\frac{\Delta_{RF}}{\sigma_H} \right)^2} \quad (2-11a)$$

and

$$A_O(\omega_{RF}) = e^{-\left(\frac{\Delta_{RF}}{\sigma_H} \right)^2} , \quad (2-11b)$$

which are the differential Gaussian (dispersive) and Gaussian (absorptive) profiles, respectively.

The theory for weak RF fields predicts that the Raman heterodyne signal amplitude of both phase components is proportional to:

- (1) The laser power, $\sim E_L^2$,
- (2) The square root of the RF power, $\sim H_{RF}$,
- (3) The product of the three dipole moments $\mu_{12} \mu_{23} \mu_{31}$, and

(4) The field-free population difference $P_2 - P_1$.

The relationship (3) shows that the effect is a three-wave mixing process and that no Raman heterodyne signal is observable unless all the three transitions are dipole allowed. The relationship (4) indicates that a population difference between the levels coupled by the RF field is required in order to have a non-zero signal. For the resonance where the energy level separation is smaller than the Boltzmann factor, the population difference is determined, to a large extent, by optical pumping effects.

2-2-2. RF Fields of Arbitrary Strengths

The theory of Raman heterodyne spectroscopy with an RF field of arbitrary power level was recently treated by Fisk *et al.* (1990) using the Bloch equations. The density matrix for a three level system consists of a 9x9 set of first order linear differential equations. For the diamond N-V centre, the laser field can be treated as a weak perturbation while the RF field is allowed to saturate the magnetic transitions. With this approximation the 9x9 set is reduced to a 3x3 system and the solution could be found analytically. In this case, only the centres close to the resonance with the laser light contribute to the signal and this simplifies the optical integration. The resulting Raman heterodyne lineshapes are found to be,

$$A_I(\omega_{RF}) = \text{Im} w \left(\frac{\Delta_{RF} + i\sqrt{1+S}\Gamma_2}{\sigma_H} \right) \quad (2-12a)$$

and

$$A_O(\omega_{RF}) = \frac{1}{\sqrt{1+S}} \text{Re} w \left(\frac{\Delta_{RF} + i\sqrt{1+S}\Gamma_2}{\sigma_H} \right) , \quad (2-12b)$$

where S is a saturation factor defined as follows,

$$S = \frac{I}{I_0} = 2 \left(\frac{\beta_{RF}}{\Gamma_2} \right)^2, \quad (2-13)$$

where I and I_0 are respectively the RF intensity and RF saturation intensity, and β_{RF} is the Rabi frequency (in angular frequency units) of the transition $|1\rangle \leftrightarrow |2\rangle$, which is related to the magnetic dipole moment μ_{12} by, $\beta_{RF} = \mu_{12} H_{RF} / \hbar$. It should be noted that S depends not only on the RF power but also on the magnetic dipole moment and the dephasing time.

If the RF field is weak, $S=0$ and Eqs.(2-12a) and (2-12b) reduce to their counterparts Eqs.(2-10a) and (2-10b).

When the RF power increases, the Raman heterodyne signal is broadened and saturated. With an arbitrary RF field strength, the lineshapes are described by the w -function and characterized by the saturation factor S . In this case, no simple relationship exists between the signal amplitude and the RF power. If S is sufficiently large such that $(1+S)^{1/2} \Gamma_2$ is much greater than the RF detuning, Δ_{RF} , it can be proved using the rational approximation of error function (Abramowitz and Stegun 1972) that the in-phase signal amplitude is approximately a constant while the out-of-phase signal is inversely proportional to the square root of RF power, *i.e.*

$$A_I(\omega_{RF})_{p-p} \sim \text{constant}$$

and

$$A_O(\omega_{RF})_0 \sim \frac{1}{\sqrt{S}},$$

where subscripts $p-p$ and 0 denote the peak-to-peak value and the peak height of the corresponding spectral lineshape.

Although the Bloch equations seem to be a reasonable approximation to the steady state

problem, it is found (Fisk 1991) that they may not hold if the RF power is sufficiently high. In this case, the dephasing time can not be assumed to be a constant and, in fact, it may depend on the RF power as well. The model could be possibly improved by taking into account such effects using the Redfield theories (Redfield 1955 and 1965).

2-2-3. Optical Pumping Effects

In the theoretical treatments discussed above, optical pumping effects are not taken into account partly because of the complexity in modeling them, but also because they occur on a much longer time scale than that of the coherence processes. When the separation of NMR or EPR levels is smaller than the Boltzmann factor, optical pumping is essential to Raman heterodyne measurements as it creates the population difference required for an observable signal. However, the details of these optical pumping effects are rarely fully understood (Wong *et al.* 1983, Erickson 1990, Manson *et al.* 1991) and the methods of obtaining improved Raman heterodyne signals require a level of experience.

2-3. SYMMETRY AND INTERFERENCE

As can be seen above, the Raman heterodyne signal depends on the product of the three dipole moments as a consequence of three wave mixing, *i.e.* $I_S \sim \mu_{12}\mu_{23}\mu_{31}$. Since each dipole matrix element is phase dependent and appears linearly, destructive interference in the Raman heterodyne signal may occur.

It has been shown that two effects may lead to complete interference resulting in no Raman heterodyne signal being observed (Mitsunaga *et al.* 1985). Firstly, the phenomenon arises from two inequivalent spins that generate Raman heterodyne signals of opposite sign and thus interfere destructively when their frequencies match (Taylor 1984, Mitsunaga *et al.* 1984). Symmetry analyses of the interference between different sites in solids have been presented from simple

group theoretical considerations (Taylor 1984, Kintzer *et al.* 1985) in terms of the laser, RF field and Raman signal polarizations and the crystal axes. Secondly, the interference can also occur in a single spin system among Zeeman hyperfine transitions (Mitsunaga *et al.* 1985) when the Zeeman levels are degenerate.

Taking into account the symmetry, the Raman heterodyne signal can be written as (Kintzer *et al.* 1985),

$$I_S = \sum_{ijk} \chi_{ijk} E_i E_j H_k, \quad (i,j,k = x,y,z) \quad (2-14)$$

where the nonlinear susceptibility χ is a third-rank tensor, which is a function of RF frequency *etc.* The macroscopic nonlinear susceptibility must be invariant under the symmetry operations of the point group. Consequently, certain components may be zero and relationships exist among those remaining. For example, for the C_{3v} symmetry the Raman heterodyne signal for the applied laser and RF fields of

$$\begin{aligned} E_L &= (E_x, E_y, E_z) \\ H_{RF} &= (H_x, H_y, H_z) \end{aligned}$$

can be expressed as follows,

$$I_S = \chi_{xxx} [(E_x^2 - E_y^2)H_x - 2E_x E_y H_y] + (\chi_{xyx} + \chi_{zyx})(E_x H_y - E_y H_x)E_z, \quad (2-15)$$

where the coordinate system (x,y,z) is such that the z direction coincides with the C_3 axis. For the ${}^3A_1 \leftrightarrow {}^3E$ transition at a site of C_{3v} symmetry, the transition is allowed only when the fields are polarized in the (x,y) plane. Therefore only the first term in Eq.(2-15) remains.

For the diamond N-V centre in a magnetic field along the [111] direction, the EPR level separations of the 3A state for the aligned centres (ensemble I, see Chapter 1) under study are different from those of the unaligned centres (ensembles II, III and IV) except at some particular values of field strengths, *e.g.* 0 and 600 G (van Oort and Glasbeek 1989). Since these field values are not included in the present experiments, cancellation of the Raman heterodyne EPR signal due to the inequivalent spins is not expected. Also, because the applied magnetic field lifts the degeneracy of electron and nuclear spin states, destructive interference due to the Zeeman levels does not occur.

As the static magnetic field selects only one ensemble of the N-V centres, the local symmetry rather than the crystal symmetry determines whether the Raman heterodyne signal can be observed. The N-V centre has C_{3V} symmetry and for several field configurations the Raman heterodyne signals are observable (see Eq.(2-15)). This will be described in detail in Chapter 3.

Chapter 3

EXPERIMENTAL DETAILS

A simplified schematic of the experimental arrangement is shown in Fig.2-1. Described in this chapter are the experimental details for the CW and transient measurements of the magnetic resonances of the N-V centre in diamond using Raman heterodyne techniques. This includes the sample and equipment, the experimental configurations, and the effect of linewidth and inhomogeneity of the laser and RF fields.

3-1. SAMPLE AND EQUIPMENT

The diamond sample used in this study was a 1mm cube with the (110), (1 $\bar{1}$ 0) and (001) crystallographic faces. It was mounted, stress free, at the centre of the RF coil located in an *Oxford Instruments* 3T helium exchange gas cryostat and cooled to about 4 K within the bore of a superconducting magnet (see Fig.3-1). The crystal could be rotated about both axes perpendicular to the direction of the static magnetic field.

The static magnetic field was applied by the superconducting magnet, which could be steadily varied from zero to several tesla (inhomogeneity better than 1 part in 10^5 in a volume of 3mm^3) and set to the magnitude corresponding to the anticrossing region of the N-V centre (900~1200 G in this study). In this region, the separation between the $m_S=0$ and $m_S=-1$ levels in the 3A state is less than 1 GHz, enabling the RF field to be applied and the EPR signals to be probed without technical difficulty with the available equipment. The factor which results in the

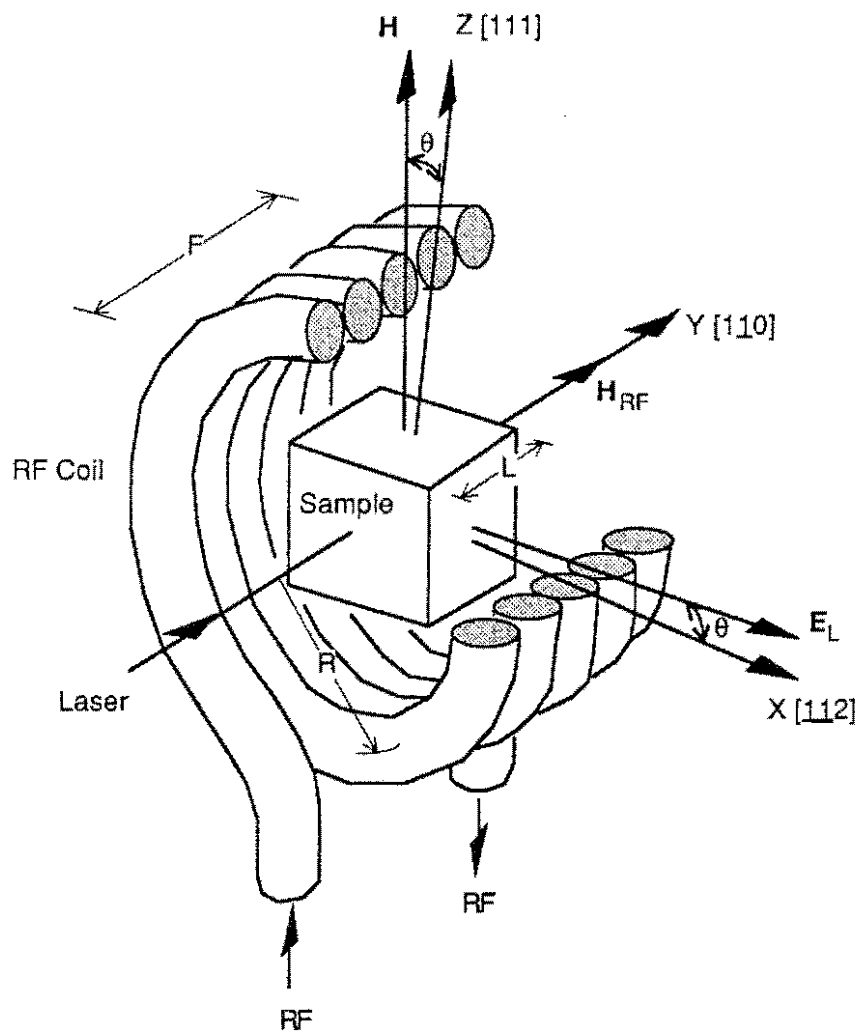


FIG. 3-1 The experimental geometry and the directions of laser field E_L , RF field H_{RF} , and static magnetic field H chosen for Raman heterodyne measurements. The parameters are $L=1\text{mm}$, $F=5\text{mm}$ and $R=5\text{mm}$.

upper frequency limits is mainly the frequency response of the RF coil and the photodetector system. Raman heterodyne signals at higher frequencies are expected to be detectable when these limitations are overcome.

The crystal alignment along the DC field direction was carried out using an optical hole bleaching phenomenon in the 6380Å line. Hole bleaching occurs due to cross relaxation between different orientation ensembles of N-V centres (van Oort and Glasbeek 1989, Holliday 1989). As discussed in Section 1-2, there are four orientations of N-V centres in the crystal. When the [111] axis is aligned along the field direction, ensemble II, III and IV (see Fig.1-2) become degenerate. If the field is at such a value that the resonance frequency of ensemble I matches that of others, cross relaxation occurs. This results in a decrease of the optical hole depth as shown in Fig.3-2. When the crystal [111] axis is aligned not exactly along the field direction, the degeneracy is lifted and therefore three lines appear. By examining the line patterns crystal alignment could be optimized.

A *Coherent* CR 599-21 standing wave dye laser was used (with DCM dye), which had an RMS linewidth of approximately 1 MHz. The laser could scan automatically over 30 GHz or mode-hop manually by 200 GHz each step, and was used to explore the Raman heterodyne signal over the large region of the 6380Å zero-phonon line and to modify the population distribution within the ground state through optical pumping. This could improve the Raman heterodyne signal significantly due to the strong hole burning effect in the optical transition.

An RF field was supplied by a *Hewlett Packard* HP 8443 tracking generator (linewidth 200Hz) and applied by winding a 5-turn coil (10mm diameter and 5mm length) of copper wire around the crystal with its axis along the direction of the laser propagation (Fig.3-1). The coil had a broadband frequency response and a second RF could be applied to the same coil, making double resonance measurements feasible. The RF generated by the tracking generator was amplified by an *Amplifier Research* model 5W1000 RF amplifier. In the case where a second RF field was needed, an additional RF generator (*Hewlett Packard* HP 8601) was used.

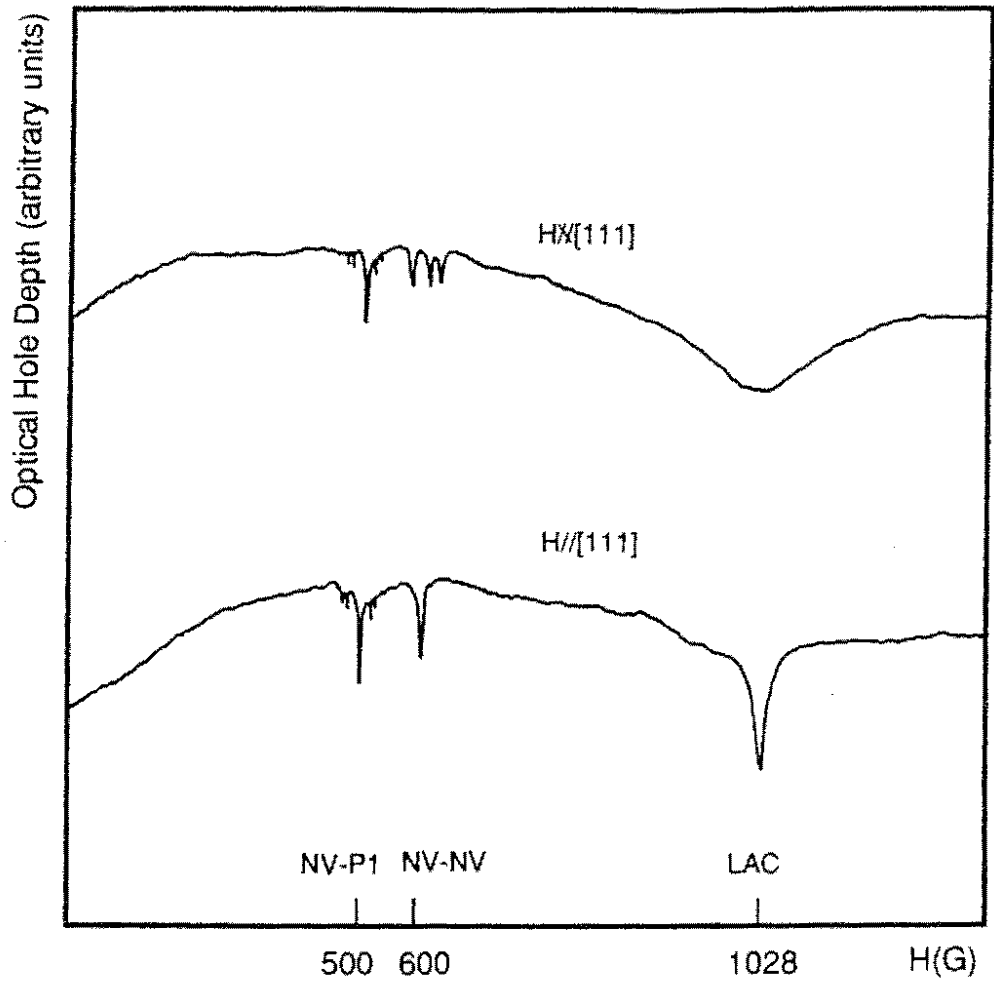


FIG. 3-2 The depth of optical hole in the 6380\AA zero-phonon line as a function of magnetic field strength. The three features result from the NV-P1(substitutional nitrogen impurity) cross relaxation, the NV-NV cross relaxation and the level anticrossing, respectively.

The magnetic field amplitude of the RF field produced by the coil at the centre of the coil is given by (Anderson 1989),

$$H_{RF} = \frac{2\pi}{5} \frac{F}{\sqrt{F^2 + 4R^2}} n I_{RF} \quad (3-1)$$

where H_{RF} has the units of G, n is turns per cm, I_{RF} is the RF current in A, and F and R are respectively the length and radius of the coil. Taking into account the geometry of the coil, the RF field strength at the centre of the coil in the experiment is,

$$H_{RF} \approx 5.62 I_{RF}, \quad (3-2)$$

where the units are the same as those for Eq.(3-1). The RF field strength is determined when the RF current through the coil is known.

When the output power level of the tracking generator was set to 0dBm and the RF amplifier was used, the magnetic field amplitude of the RF field at the centre of the coil was typically ~3 G at an RF frequency of 5.5MHz. However, the output RF power from the tracking generator was found to be dependent on the RF frequency. We have not reliably established the RF current in the coil due to the accuracy of available equipment, therefore only relative power levels were recorded in the experiments (labeled by dB) using an RF attenuator.

The light transmitted through the crystal was detected by an *Electrooptics* PD-15 or *RCA* 30902E photodiode. The photodiode measured the light intensity, which oscillates at the RF frequency as a result of the coherent Raman heterodyne effect. The Raman heterodyne signal was displayed on a *Hewlett Packard* HP 8553 spectrum analyzer (resolution 0.1~300kHz). In some measurements a pre-amplifier was used. For phase detection, a home-made RF phase-shifter was used to adjust the phase of the reference RF field. The output from the spectrum analyzer was averaged and stored by a *Data Precision* DATA 6000 or *Princeton Applied Research* model 4202 waveform averager.

For the coherent transient measurements, a locally built RF switching unit was employed

which was capable of producing RF pulses of variable widths from 0.1 to 100 μ s, digitally adjustable. In most transient experiments, a *Watkins-Johnson* MIA-11 double balanced mixer (DBM) was used for phase-sensitive detection in place of the spectrum analyzer.

3-2. EXPERIMENTAL CONFIGURATION

As discussed in Section 2-3, taking into account the crystal or site symmetry, certain experimental conditions must be met so that the Raman heterodyne signal can be observed. The application of a static magnetic field to the N-V centre causes the Raman heterodyne signal to be determined by the local symmetry. For the C_{3v} symmetry, several field configurations can be used, for which a non-zero Raman heterodyne signal is expected (see Eq.(2-15)) (Kintzer *et al.* 1985). As the ${}^3A \leftrightarrow {}^3E$ transition of the N-V centre is forbidden when the laser polarization is parallel to the C_3 principal axis, the laser and RF fields must be perpendicular to the C_3 axis and the orientations shown in Fig. 3-1 were chosen. The laser propagated along the $[1\bar{1}0]$ direction. The E-vector of the laser E_L , and the direction of the magnetic field, H , were at an angle θ ($-1^\circ \leq \theta \leq 1^\circ$) relative to the $X[\bar{1}12]$ and $Z[111]$ axes, respectively. The angle θ could be changed by rotating the sample about the Y-axis. The H-vector of the RF field, H_{RF} , was set in the $[1\bar{1}0]$ direction. In the experiment, E_L , H_{RF} and H were mutually perpendicular.

3-2-1. Amplitude and Phase Detections

Most of the Raman heterodyne measurements were carried out using phase detection. In CW measurements, a portion of the RF from the tracking generator was added to the photocurrent from the photodiode and then sent to the spectrum analyzer. This reference RF selected one phase component of the Raman heterodyne signal that is of the same phase while suppressed the other that is 90° out of phase. Therefore different phase components could be chosen. In transient measurements, however, the DBM was used and the usual phase-sensitive

detection was achieved.

The principle of phase detection in CW measurements is now described. Let $A_I(\omega_{RF})$ and $A_O(\omega_{RF})$ be two phase components of the Raman heterodyne signal, and the reference RF have an amplitude A_R , independent of frequency. The phase of the reference is set to be the same as that of $A_I(\omega_{RF})$ (Fig.3-3).

In amplitude detection, no reference RF is added and the detected signal $|A_T(\omega_{RF})|$ is thus the vector sum of the two phase components,

$$|A_T(\omega_{RF})| = \sqrt{A_I(\omega_{RF})^2 + A_O(\omega_{RF})^2} \quad (3-3)$$

In this case, the spectral lineshape depends on the magnitude of both phase components and their phase information is lost.

In phase detection, the reference RF A_R , where

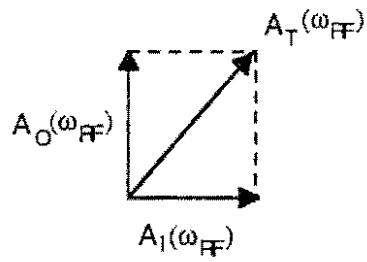
$$A_R \gg |A_I(\omega_{RF})| \text{ and } |A_O(\omega_{RF})|$$

is added to the resulting signal from the photodiode. With the above condition, the signal $|A_T(\omega_{RF})|$ detected by the spectrum analyzer is then,

$$\begin{aligned} |A_T(\omega_{RF})| &= \sqrt{[A_R + A_I(\omega_{RF})]^2 + A_O(\omega_{RF})^2} \\ &\approx A_R \left[1 + 2A_I(\omega_{RF}) / A_R \right]^{1/2} \\ &\approx A_R + A_I(\omega_{RF}) , \end{aligned} \quad (3-4)$$

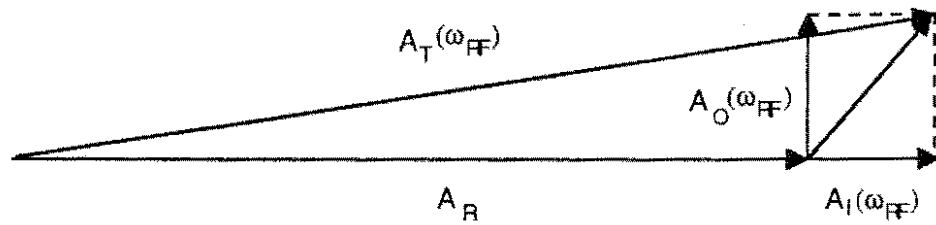
which reflects the in-phase lineshape $A_I(\omega_{RF})$ and is insensitive to $A_O(\omega_{RF})$. The lineshape $A_I(\omega_{RF})$ can therefore be displayed on the spectrum analyzer by choosing an appropriate offset.

We found that this is a very simple and convenient technique for selecting phase components and this technique enables one to compare and analyze both the Raman heterodyne



Detected Signal $|A_T(\omega_{FF})| = \sqrt{A_I(\omega_{FF})^2 + A_O(\omega_{FF})^2}$

(a) Amplitude Detection



Detected Signal $|A_T(\omega_{FF})| \approx A_R + A_I(\omega_{FF})$

(b) Phase Detection

FIG. 3-3 Phase diagram showing the relationships among the Raman heterodyne signals and the detected signals in amplitude (a) and phase (b) detection schemes.

phase and amplitude profiles. In the NMR measurements, an RF phase shifter was used to adjust the phase of the reference RF such that it matched the phase of one components.

In the EPR measurements, however, phase adjustment was achieved by changing the position of the photodiode rather than using the RF phase shifter, which was not usable for an RF frequency greater than 30 MHz. This is equivalent to changing the relative phase between the Raman heterodyne signal and the reference RF. A change in distance ΔL corresponds to a change in the RF phase,

$$\Delta\phi = (\omega_{RF}/c) \Delta L, \quad (3-5)$$

where c is the speed of light. With an RF frequency of 100 MHz, the required distance for changing the Raman heterodyne signal from the in-phase component to the 90° out-of-phase component is 75 cm (a quarter of the wavelength). Speed of light in co-axial cable is $\frac{2}{3}c$ and, therefore, distance is 50cm.

3-2-2. CW Measurements

The experimental configuration for CW measurements is shown in Fig.3-4. The linearly polarized CW laser at 6380\AA excited the $^3A \leftrightarrow ^3E$ zero-phonon transition. The laser had a beam diameter of approximately 0.1 mm and an output power of 120mW. The laser power could be changed in the range of 10 ~ 120 mW using neutral density filters. Lenses were used to focus the laser beam onto the sample and the photodiode. The RF field in the range of 0 ~ 1GHz (0~10 MHz for NMR and 20 MHz~1GHz for EPR) generated by the tracking generator and applied by the coil excited the magnetic transition in the 3A ground state. A $50\ \Omega$ load connected in series to the coil was used to dissipate the RF energy. In the hole burning, Autler-Townes effect and ENDOR measurements, an additional RF produced by the second RF generator was put into the same coil. The Raman heterodyne signal detected by the photodiode was amplified and then displayed by the spectrum analyzer, in either phase or amplitude lineshape, as discussed in

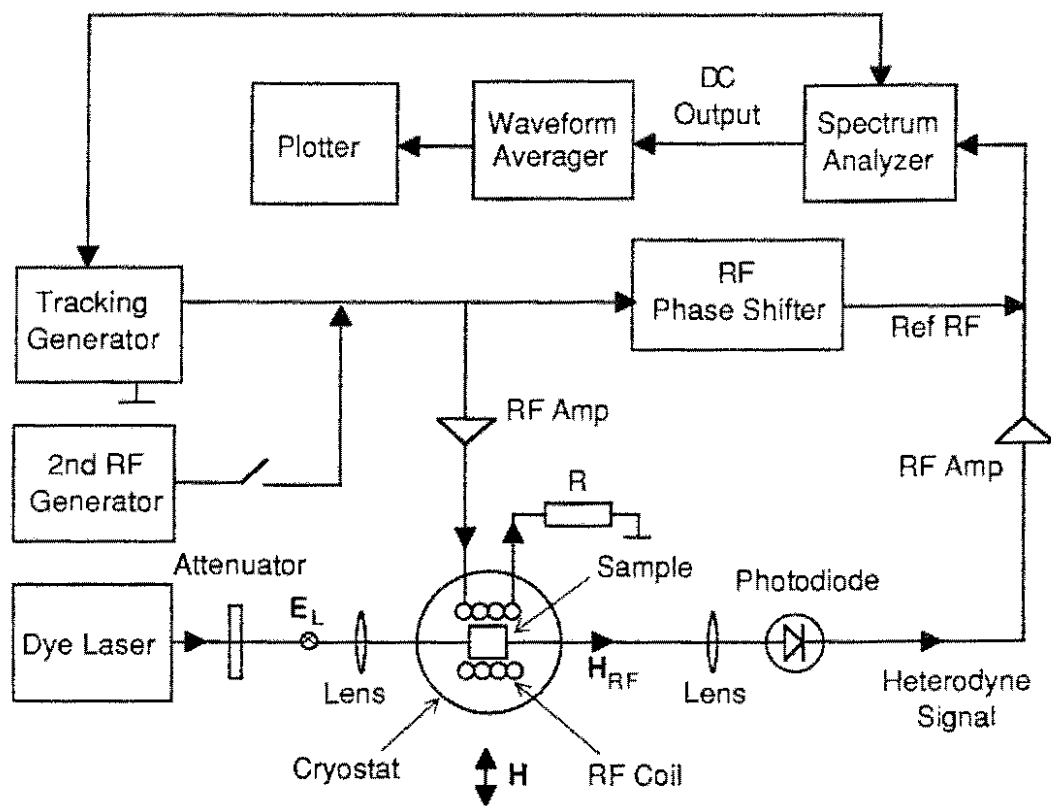


FIG. 3-4 Experimental configuration for the CW Raman heterodyne measurements of magnetic resonance of the N-V centre.

Section 3-2-1. Finally the DC output from the spectrum analyzer was averaged by the waveform averager and plotted out.

In cases where it was necessary to achieve high accuracy for the spectral lineshape analysis, an optical power as low as 10 mW was employed. Saturation of the RF transition was avoided by attenuating the RF power by 30~50 dB, so that the field was in the low power regime. Even under these conditions, the Raman heterodyne signals were easily detected without averaging.

A strong background signal was sometimes observed in the NMR measurements, which came from the EPR transitions when the [111] crystal axis was very well aligned along the magnetic field direction. This was overcome by slightly altering the crystal orientation until the background was sufficiently reduced, allowing the study of the pure NMR spectral lineshapes.

In the EPR measurements, by sweeping either the RF frequency or the static magnetic field, the lineshapes were determined. Because of the effects of RF pickup, it was preferable to sweep the magnetic field rather than to sweep the RF frequency. In the former case any background signal due to the RF pickup was then constant and did not affect the EPR profiles. When sweeping the magnetic field, the output from the spectrum analyzer was directly plotted out and a sweep rate of $0.1\sim 1\text{G s}^{-1}$ was used. The low sweep rate was chosen to avoid possible hysteresis effects in the magnet.

For phase detection of ENDOR, the in-phase or the 90° out-of-phase EPR signal was achieved first, then the EPR signal amplitude at a particular resonance line was recorded as a function of the second RF frequency. In amplitude detection, the ENDOR signal reflected the total change in the two EPR phase components.

3-2-3. Transient Measurements

Most of the arrangement remained the same for the coherent transient measurements except

for the RF system (Fig.3-5). The RF switch unit was used to pulse the CW RF field produced by the RF generator, while the laser remained CW. A trigger signal (generated inside the RF switch unit) controlled the RF switching and the waveform averager with a repetition rate of typically 10ms. A portion of the CW RF from the generator was sent to the DBM as a local oscillator. The signal detected by the photodiode was amplified by a broadband and low noise RF amplifier before being sent to the DBM, where it was mixed with the local oscillator. The DC output from the DBM was then connected to the waveform averager, again after being amplified.

For the transient ENDOR measurements, an additional RF generator was needed (not shown in Fig.3-5). The RF driving the EPR transition was kept CW while the one driving the NMR transition was pulsed (Chapter 9). The signal amplitude monitored at a particular EPR line was then recorded as a function of time. In this way, the response of the EPR signal due to the transient NMR could be examined.

3-3. LINEWIDTH AND INHOMOGENEITY OF THE LASER AND RF FIELDS

The radiative lifetime of the 3E state is 13ns (Collins *et al.* 1983) and the optical dephasing time may be shorter (see *e.g.* Bartola 1968). Therefore the relevant coherence among the three levels in the Raman heterodyne scheme (Fig. 2-2) is established by the optical field over a time scale of ns. With a linewidth of 1MHz, the laser has a coherence time much longer than a few ns. As a consequence, the frequency jitter will not add significantly to the noise of the Raman signal due to the loss of optical coherence. On the other hand, with a lifetime of ~ns, the optical homogeneous linewidth is expected to be ~100MHz or greater, much larger than the laser linewidth. This implies that the laser selectively excites a subgroup of centres during a CW measurement and no significant fluctuations are expected owing to the involvement of different resonance frequencies.

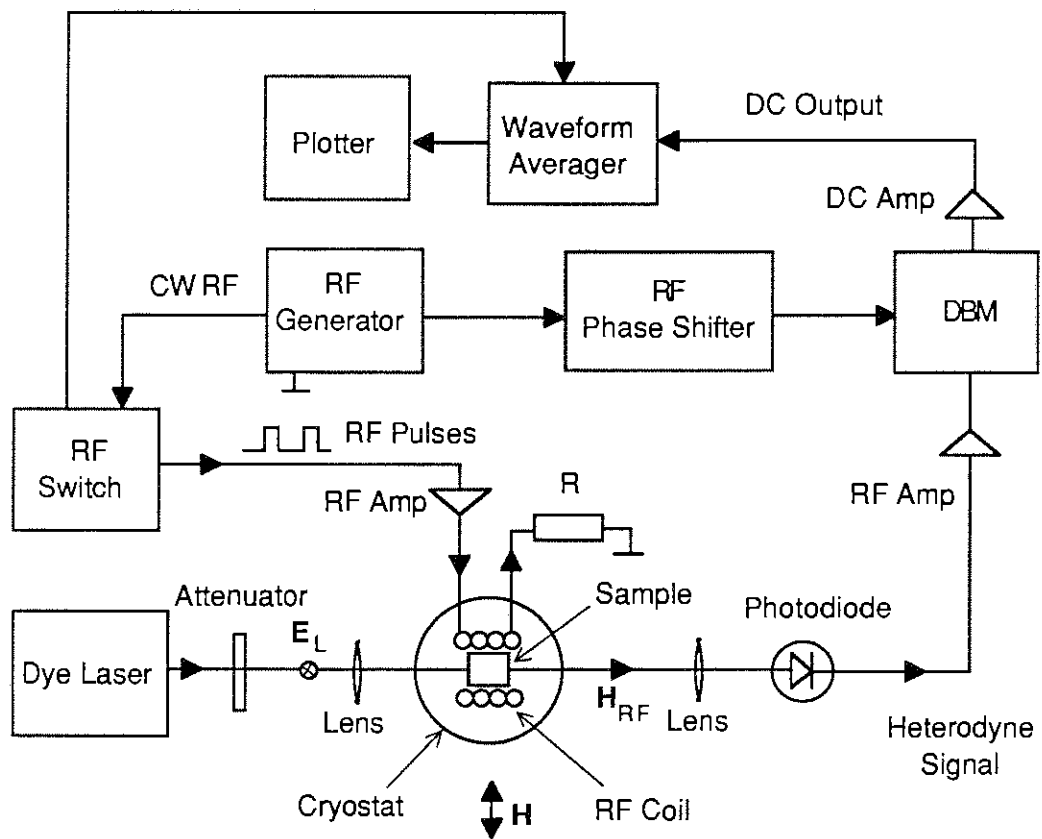


FIG. 3-5 Experimental configuration for the coherent spin transient measurements using Raman heterodyne techniques.

Due to the Gaussian spatial distribution of the laser intensity, the active centres located in the laser path experience different optical field strengths. However, providing the laser is in the low power regime, such difference does not affect the Raman heterodyne lineshape except the signal magnitude, which is proportional to the laser power.

The CW RF produced by the tracking generator was very sharp in frequency (linewidth 200Hz) compared with the homogeneous linewidth of the magnetic transition (~kHz). With the broadband response of the RF coil, the RF field can be considered as a highly stable coherent source.

The dimensions of the diamond crystal (1mm cube) located in a 5-turn coil (10mm diameter and 5 mm length), however, may give rise to the inhomogeneity of RF field strength inside the sample as the active centres located at different parts of the sample receive different RF field strengths. The difference between the field strength at the centre of the sample and that at the edges is estimated with the experimental geometry to be,

$$\Delta H_{RF} \approx 0.031 H_{RF}, \quad (3-6)$$

which is about 3 percent of the value at the centre of the sample. In the low RF power regime, such difference is negligible. However, at high power levels, the inhomogeneity may be significant. This inhomogeneity causes additional broadening in the magnetic transitions, where the observable signal depends on the RF power level as in the nutation and the Autler-Townes splitting measurements.

Chapter 4

NMR AND EPR LINESHAPE ANALYSIS

The following assumptions made in the theoretical treatment of Raman heterodyne detected magnetic resonance (Wong *et al.* 1983) are all satisfied for the N-V centre:

(1) All the three transitions in the Raman heterodyne scheme are dipole allowed due to the spin-orbit coupling in the 3E state.

(2) The optical transition frequency ($\sim 10^{14}$ Hz) is much greater than the magnetic transition frequency ($10^6\sim 10^9$ Hz).

(3) The strain broadening of the optical transition (\sim THz) is large compared with the RF inhomogeneous linewidth (kHz~MHz), and

(4) Although our diamond sample is 100% absorbing in white light absorption at 6380Å, the hole burning effect substantially reduces the absorption when exposed to a focussed laser beam, such that the optical signal field can be described by Maxwell's wave equation.

Therefore, the N-V centre provides an appropriate system for testing the theory of Raman heterodyne spectroscopy (Wong *et al.* 1983, Fisk *et al.* 1990), particularly for analyzing the spectral lineshapes at various RF power levels. All the NMR resonances are well separated and one can study an individual non-degenerate transition. Consequently, the lineshapes can be analyzed and compared with theoretical results in detail. Compared with the NMR, the EPR spectra are complicated due to the hyperfine interaction associated with the nitrogen nuclei (^{14}N). Three allowed transitions are prominent. Forbidden transitions also arise when the magnetic field magnitude is close to the level anticrossing.

This chapter presents the Raman heterodyne detected NMR and EPR lineshapes and the theoretical results at various RF power levels, laser intensities, and laser frequencies within the

6380Å zero-phonon line.

The coherence processes involved in the Raman heterodyne detection of NMR and EPR in the 3A ground state is shown schematically in Fig.4-1. The static magnetic field along the [111] crystallographic direction is of such a magnitude that the system is close to the level anticrossing. It is near this anticrossing that the NMR and EPR were found to be detectable. In the measurements, the magnetic transition $|1\rangle \leftrightarrow |2\rangle$, either an NMR or an EPR in the 3A state, was driven by an RF field, ω_{RF} , while the 6380Å $^3A \leftrightarrow ^3E$ optical transition $|2\rangle \leftrightarrow |3\rangle$ was driven by a laser field, ω_L . The NMR or EPR signal at the frequency $\omega_{RF} = |\omega_L - \omega_R|$ was detected as discussed in Chapter 2.

4-1. INHOMOGENEOUS LINESHAPES AT WEAK RF FIELDS

4-1-1. NMR Transition

Figures 4-2 and 4-3 show two typical Raman heterodyne detected NMR signals associated with the $m_f=0 \leftrightarrow -1$ ($m_s=0$) transition in the 3A ground state in dispersion (in-phase component) and absorption (90° out-of-phase component) measured at a magnetic field of 1058 G. Phase detection scheme described in Chapter 3 was used, where the probing RF power was attenuated such that no power broadening effect occurred. The laser powers were also set in the low power regime. The detected signal lineshape was found to be very sensitive to the phase of the reference RF and by carefully adjusting the phase either the in-phase or the out-of-phase component could be easily selected. In the experiment, the output from the spectrum analyzer was directly plotted out without averaging, and the trace indicates the signal-to-noise ratio as well.

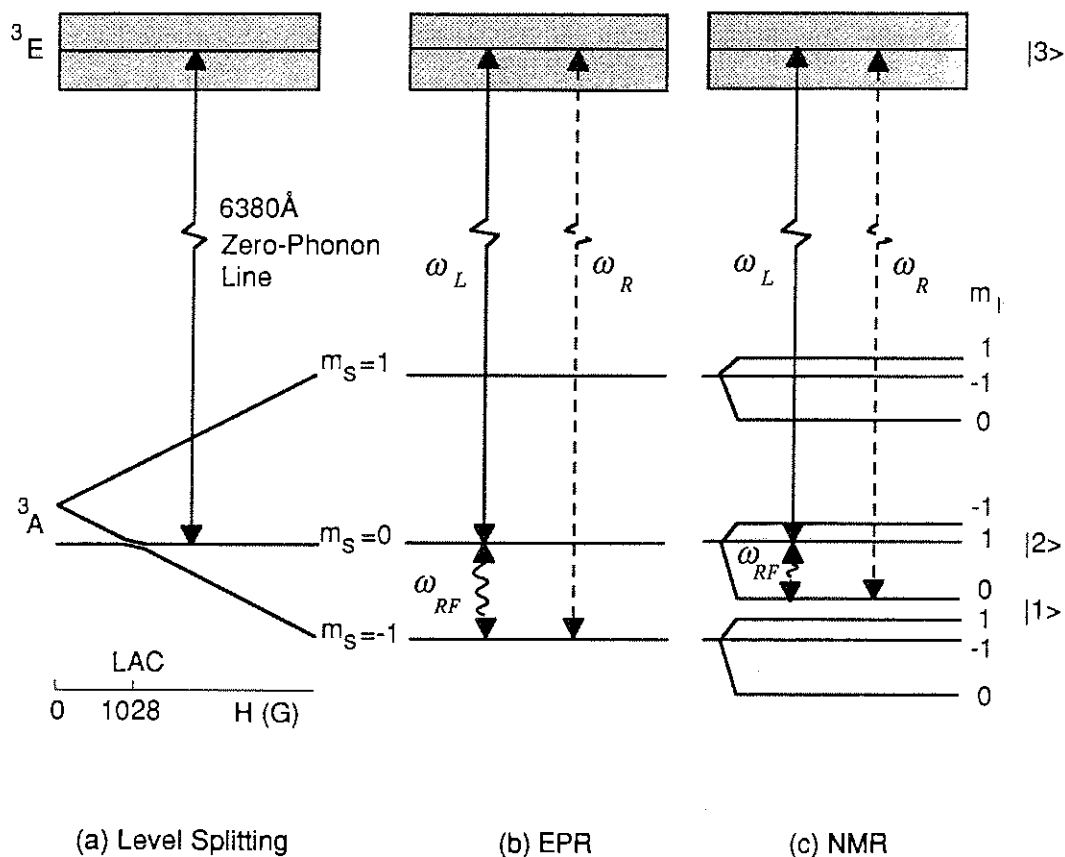


FIG.4-1 Level splitting in the magnetic field (a) and the energy levels and coherence processes involved in the Raman heterodyne detection of EPR (b) and NMR (c) in the 3A ground state of the diamond N-V centre. Only the anti-Stokes processes $\omega_R = \omega_{RF} + \omega_L$ are illustrated. In (a) and (b) the hyperfine sub-levels are not shown.

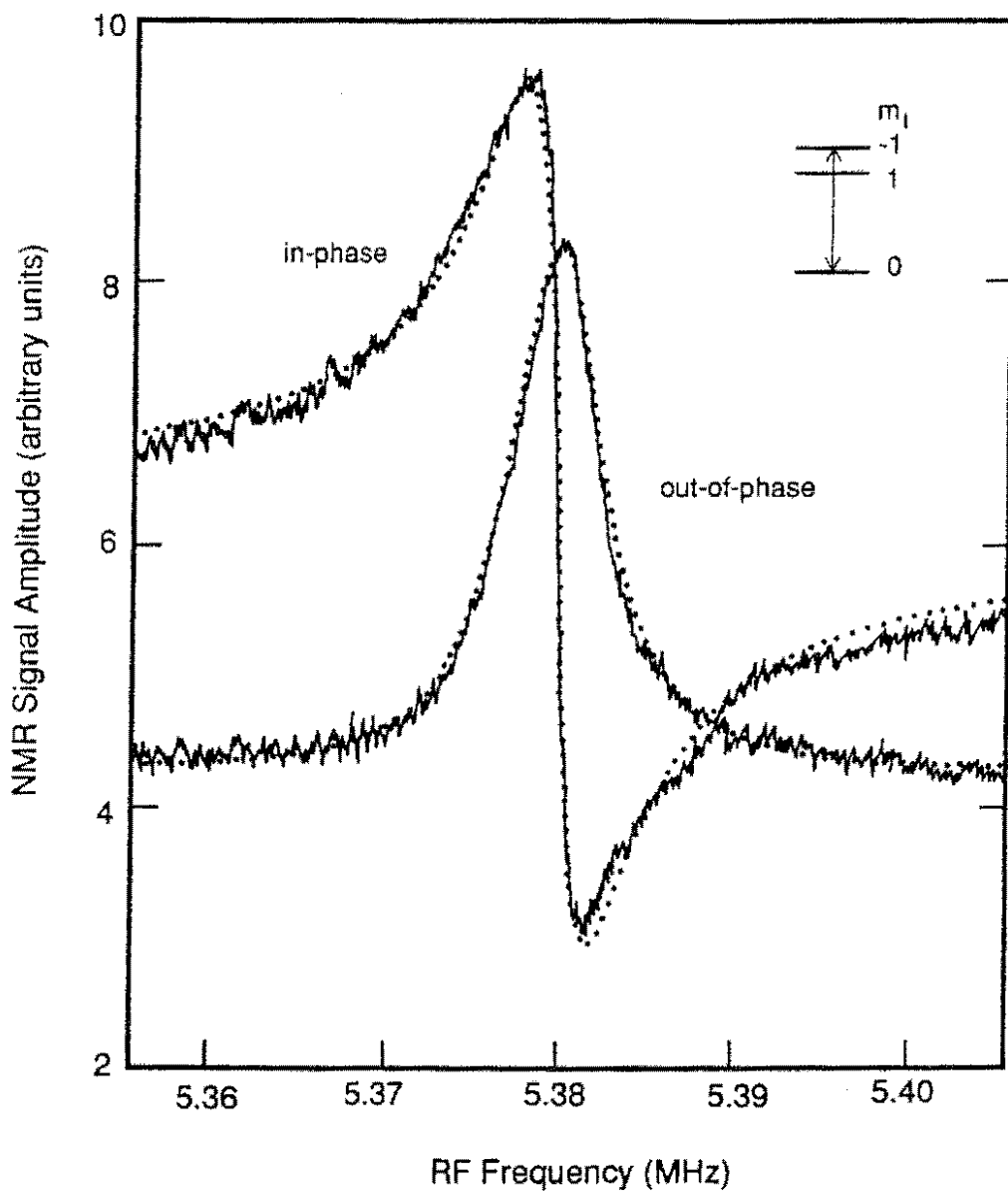


FIG.4-2 The Raman heterodyne detected NMR lineshapes associated with the $m_l=0 \leftrightarrow -1 (m_s=0)$ transition in the 3A ground state, where the laser power was 60 mW. The signal is compared with the w -function of Eqs.(2-10a) and (2-10b) (dots).

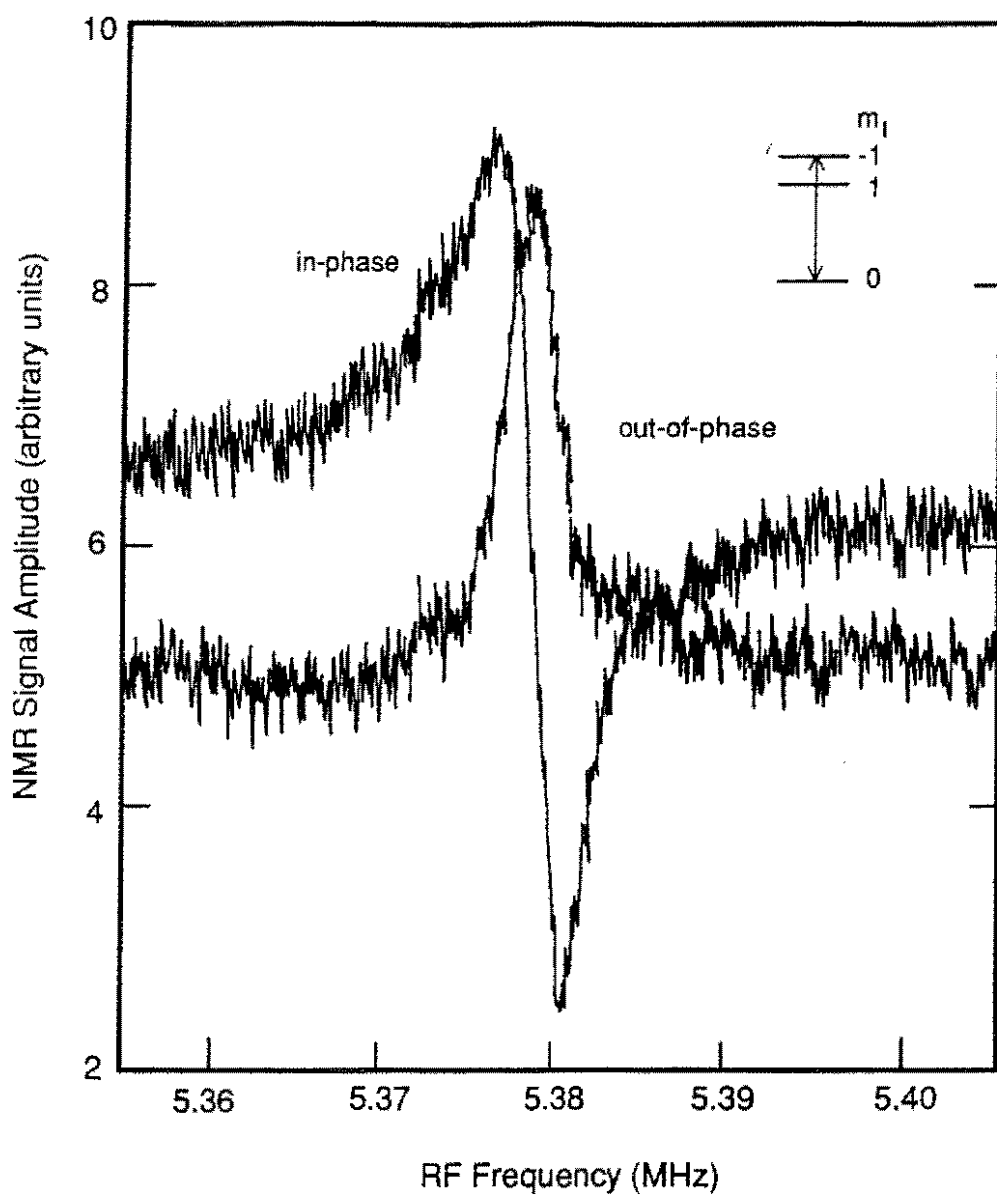


FIG. 4-3 The same NMR signal as in Fig. 4-2 but with a laser power of 10mW.

Data-fitting to the theoretical expressions shows that the NMR lineshapes are well described by the w -function of Eqs.(2-10a) and (2-10b), with a linewidth (FWHM) as narrow as 3.4 kHz. The observed spectral lineshapes are in good agreement with the Raman heterodyne theory in the low RF power regime (Wong *et al.* 1983). However, the NMR lineshapes measured here were found not to have Gaussian profiles, in contrast to the previous results (Mlynec *et al.* 1983, Wong *et al.* 1983). This is due to the fact that the homogeneous linewidth for the $m_f=0 \leftrightarrow -1$ ($m_s=0$) transition (1.2kHz) (see Chapter 9) is almost the same as the inhomogeneous linewidth therefore the Voigt convolution profile does not have Gaussian characteristics.

Experimentally, the NMR signal size could be improved significantly (by a factor of 2~8) by dithering the laser frequency within the 6380Å zero-phonon line. Increasing laser intensity also improved the NMR signal magnitude as well as the signal-to-noise ratio. Neither of these modifications to the experiments was found to affect the spectral lineshapes.

4-1-2. EPR Transition

Figure 4-4 illustrates the Raman heterodyne detected EPR signals associated with the $m_s=-1 \leftrightarrow 0$ ($m_f=0, \pm 1$) transitions at a magnetic field of 995 G observed by scanning the RF frequency, where the background signal due to the RF pickup has been subtracted. In the experiment, both the RF and the laser were in the low power regime. Phase detection was employed and the dispersive and absorptive components were obtained by adjusting the position of the photodiode as discussed in Chapter 3.

The alternative way of measuring the EPR is sweeping the magnetic field while keeping the RF frequency constant (Holliday *et al.* 1990). The result obtained using this method is shown in Fig.4-5, where the signal is due to the same transitions as in Fig.4-4 and the RF frequency was 95 MHz. Other settings were the same as those in Fig.4-4.

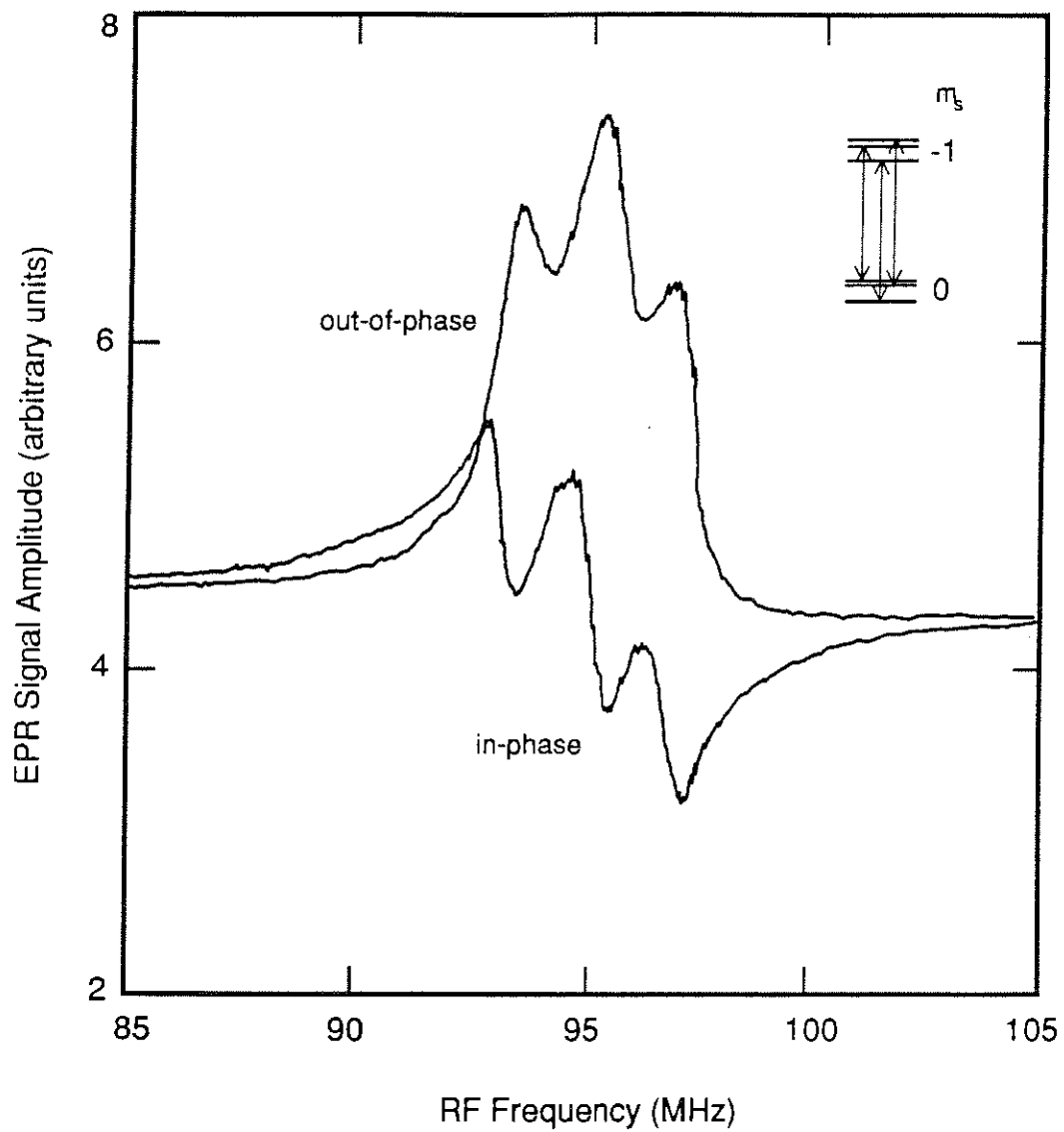


FIG.4-4 The Raman heterodyne detected EPR lineshapes associated with the $m_s=0 \leftrightarrow -1$ ($m_f=0, \pm 1$) transitions in the 3A state at a magnetic field of 995 G by sweeping the RF frequency.

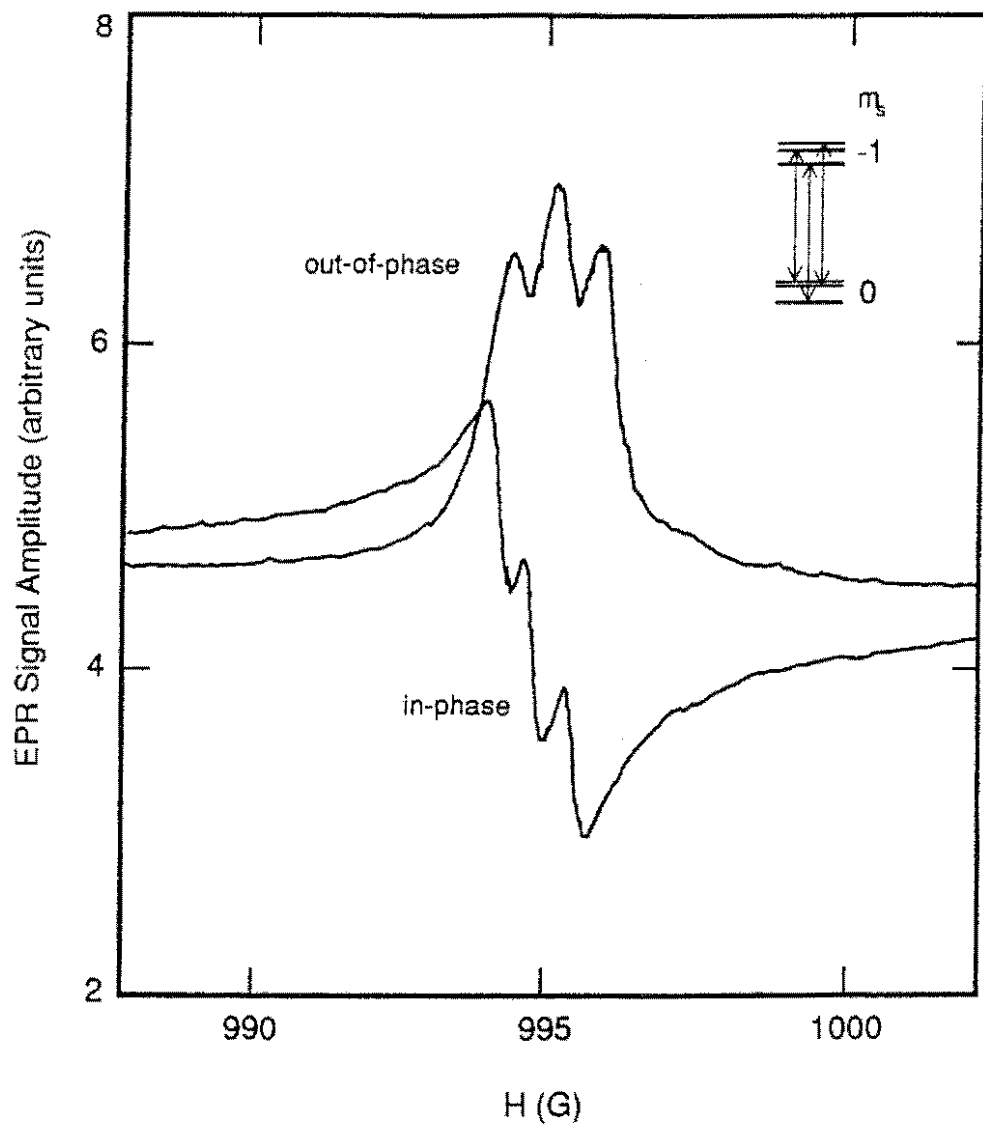


FIG.4-5 The same EPR signals as in Fig.4-4, but by sweeping the magnetic field while keeping the RF frequency at 95 MHz.

In either Fig.4-4 or 4-5, three hyperfine components are clearly resolved in both dispersive and absorptive lineshapes, which correspond to the allowed transitions $m_s = -1 \leftrightarrow 0$ for each of the nuclear spin orientations $m_I = -1, 0$ and $+1$. The hyperfine splitting measured here is 2.2 MHz or 0.78 G, compared with 2.3 MHz or 0.83 G obtained by conventional EPR technique at the microwave frequency of 9.4 GHz (Loubser and van Wyk 1977). The difference is due to the state-mixing near the level anticrossing (see Chapters 6 and 7), which causes small changes in the energies of hyperfine sub-levels. Comparison with the theoretical lineshapes indicates that each hyperfine component in the EPR spectra has profiles described by Eqs.(2-10a) and (2-10b), as expected for the inhomogeneously broadened transition probed by a weak RF field (Wong *et al.* 1983). The linewidth (FWHM) of each component is ~ 2 MHz, compared with \sim kHz for the NMR. This is because the electron wave function has a much larger spatial extent and therefore the crystal irregularity gives rise to a much broader inhomogeneous linewidth (Abragam and Bleaney 1970).

The two detection schemes (RF frequency sweeping and magnetic field sweeping) yield the same signal, which are related to each other by the relationship, $\omega_{RF} \sim \gamma H$, where γ is the electron gyromagnetic ratio ($\gamma/2\pi = 2.80$ MHz/G). In practice, better phase profiles were obtained by sweeping the static magnetic field, as any background signal due to RF pickup was constant and therefore did not affect the lineshape. When sweeping the RF frequency, the EPR signal was displayed in real time and consequently it was convenient for phase adjustment. However, when sweeping the magnetic field, the lineshape could only be assessed after a slow sweep taking more than a minute and it was much more time consuming to make appropriate adjustment to the phase.

4-2. RF POWER BROADENING AND SATURATING EFFECTS

The RF power received by the active centres located in the sample with a cross section area A perpendicular to the axis of the coil can be estimated by (see *e.g.* Jackson 1975),

$$P_{RF} = \frac{cA}{8\pi n} H_{RF}^2, \quad (4-1)$$

where c is the speed of light and n is the refractive index of the sample. The RF power is proportional to the square of the RF magnetic field amplitude. In Raman heterodyne experiments, the RF power was varied by changing the RF current in the coil, which is proportional to the magnitude of the RF magnetic field (see Eq.(3-2)), and the relative power level was labeled by dB.

4-2-1. NMR

The 5.38 MHz NMR associated with the $m_f=0 \leftrightarrow -1$ ($m_s=0$) transition at a magnetic field of 1055 G was measured at various RF power levels from 0dB to -60 dB while the laser was kept in the low power regime. In Fig. 4-6, some of the experimental lineshapes (higher traces) are plotted and compared with theoretical calculations (lower traces).

At low powers, the signals have profiles described by Eqs.(2-10a) and (2-10b), as have been analyzed in Section 4-1. When the RF power is increased, the linewidth is broadened and the signal magnitude is saturated. The saturation characteristics of the in-phase and out-of-phase components are totally different. This results in anomalous lineshapes using

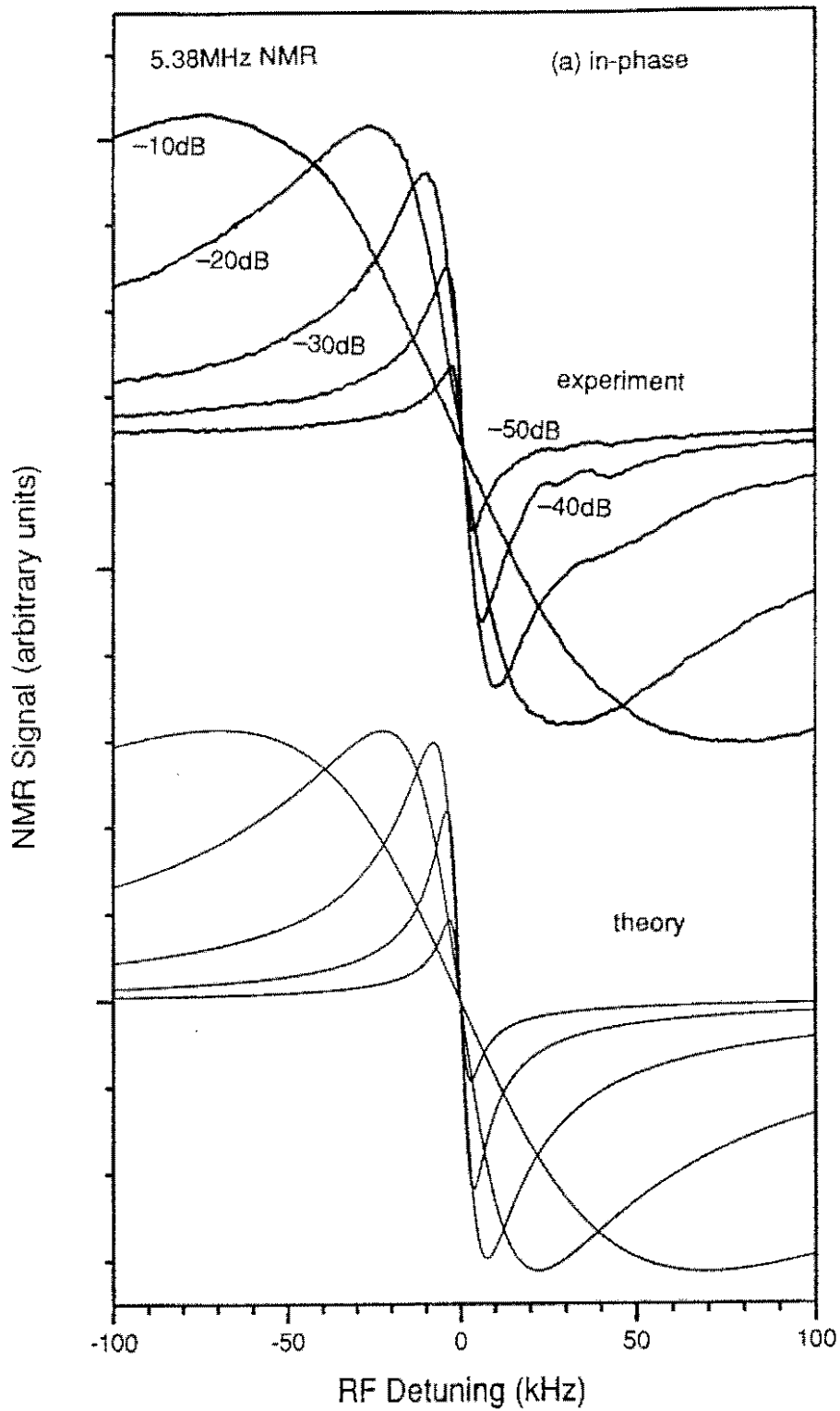


FIG.4-6 The saturation effects in the 5.38MHz (0kHz) NMR signal at various RF powers.
 (a) Dispersive, (b)absorptive and (c) amplitude lineshapes.

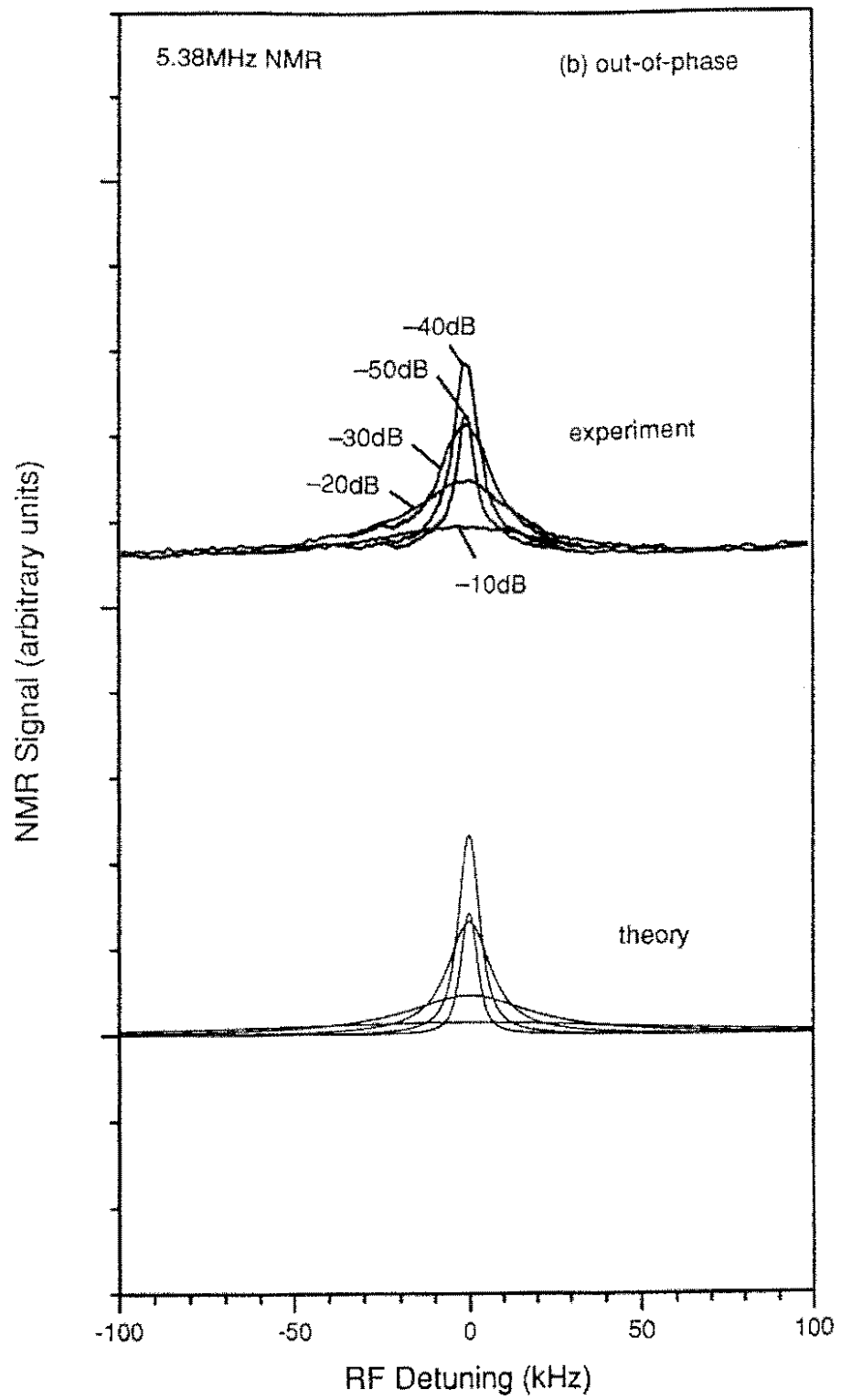


FIG. 4-6 (Continued)

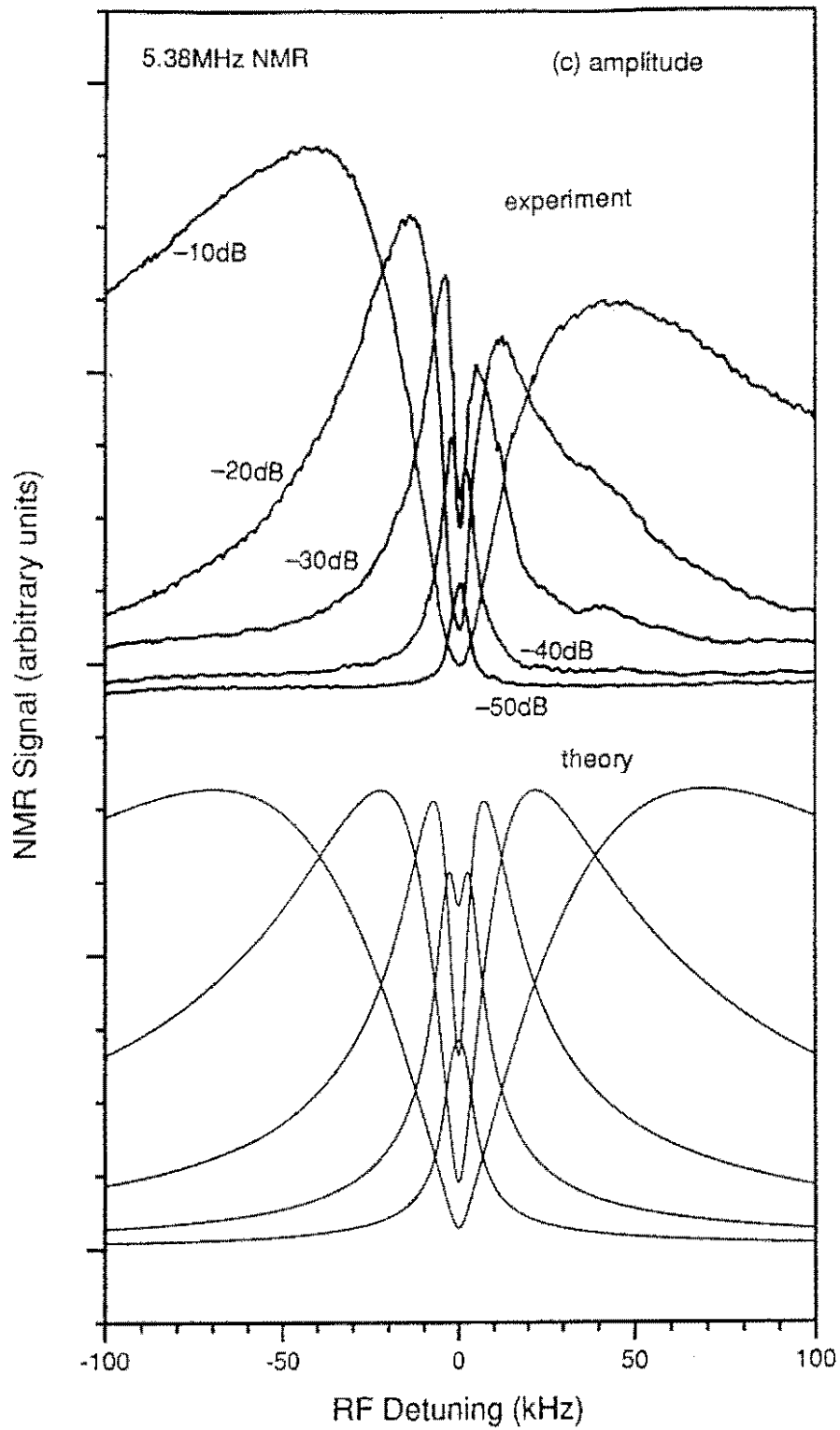


FIG. 4-6 (Continued)

amplitude detection, where a "hole" appears in the middle of the line at high powers. In amplitude detection, the lineshapes are obviously asymmetric at high powers due to the interference effect between the NMR and the background signal, which arose from the EPR when the crystal was well aligned.

Theoretical profiles were calculated using Eqs.(2-9) and (2-12). In the calculations, the parameters $\Gamma_2=0.6$ kHz and $\sigma_H=2$ kHz were used as determined by the spin echo (Chapter 9) and the weak field NMR (Section 4-1) measurements. The saturation factor S in Eqs.(2-12a) and (2-12b) was considered as a free parameter. Its values used in the calculations were 0.15, 1.5, 15, 150 and 1500, respectively, increasing by 10dB for each trace, corresponding to the -50, -40, -30, -20, and -10 dB power settings in the measurements. From Fig. 4-6 one finds a good agreement between theory and experiment. However, comparison of the amplitude lineshapes with the theoretical traces is less satisfactory at higher powers due to the interference effect.

Figure 4-7 shows the dependence of the NMR signal amplitude, peak height in the absorptive component or peak-to-peak value in the dispersive component on the RF power level compared with theoretical predictions. Below -50dB the NMR signal increases with the square root of RF power, being in agreement with the theoretical relationship,

$$I_S \propto H_{RF} \propto (\text{RF power})^{1/2}, \quad (4-2)$$

predicted for the weak RF field regime (Wong *et al.* 1983). This indicates that for the NMR the RF power below -50dB can be treated as a low power level for the experimental setups. Above -50 dB, the signal begins to be saturated. For strong RF fields, the in-phase peak signal size is unchanged while the other phase signal size drops, approximately with $(\text{RF power})^{-1/2}$. The saturation behaviors are found to be well described by Eqs.(2-12a) and (2-12b) (Fisk *et al.* 1990) as indicated by the solid curves in Fig. 4-7.

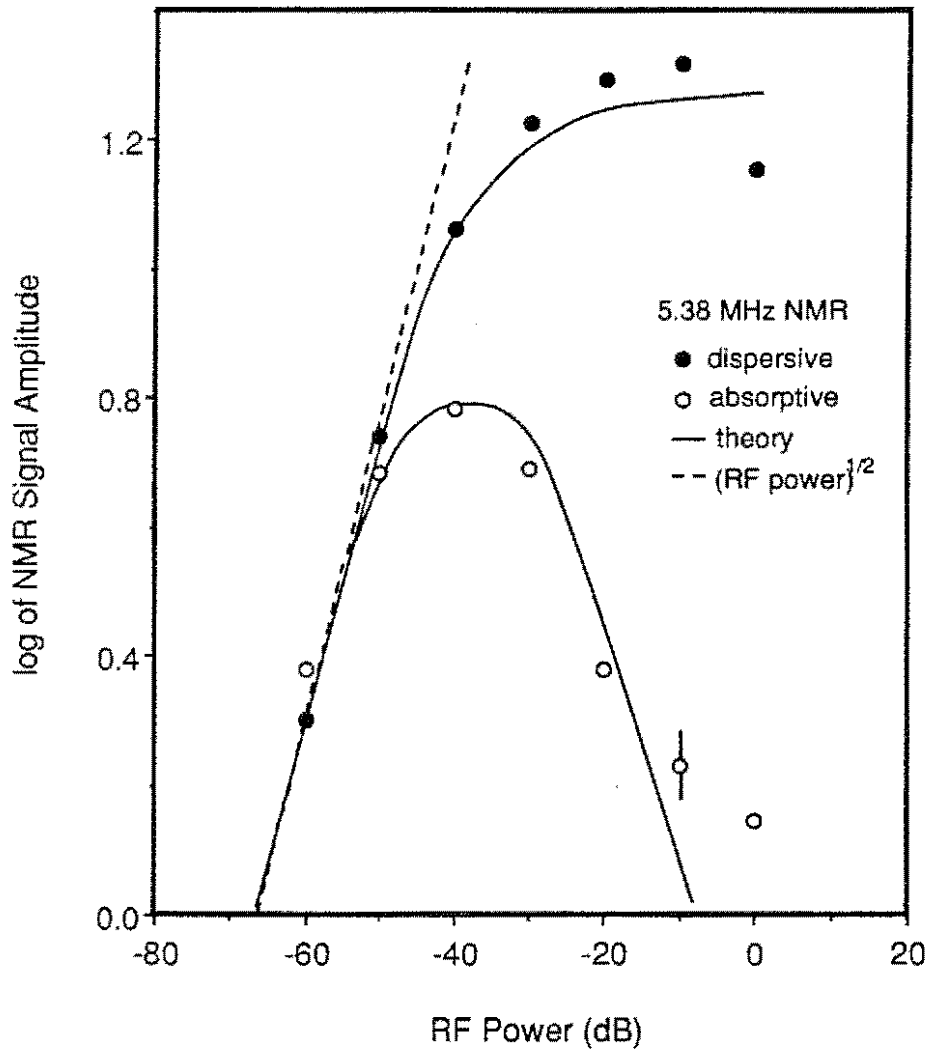


FIG.4-7 The 5.38 MHz NMR signal amplitude (dots) as a function of RF power compared with theoretical predictions (solid curves). The square root dependence in the low power regime is also indicated (dashed line).

For the lineshapes of Eqs.(2-10a) and (2-10b), the linewidth (FWHM) of the absorptive profile, $\Delta\omega_{1/2}$, is related to the peak-to-peak width in the dispersive profile, $\Delta\omega_{p-p}$, by

$$\Delta\omega_{1/2} \approx 1.5 \Delta\omega_{p-p}, \quad (4-3)$$

therefore the linewidth can also be obtained from the dispersive phase components. The measured NMR linewidth (FWHM) and the corresponding theoretical predictions are plotted as a function of RF power in Fig. 4-8. One can see that the linewidths obtained from both phase components are approximately the same and unchanged below -50 dB, but increase drastically when the power is above -50 dB. This power level coincides with the one below which the NMR signal size depends linearly on the RF power. At high powers, the linewidth is found to increase with the square root of the RF power. A good agreement between theory and experiment is evident for the NMR linewidth over the power range of 0~-60 dB.

It should be noted that at high powers the lineshapes are no longer those described by Eqs.(2-10a) and (2-10b) therefore the linewidth calculated from the dispersive component using Eq.(4-3) differs from that of the absorptive component.

4-2-2. EPR

The EPR lineshapes were also measured at various RF power levels (-5dB~-50dB), where similar to the NMR measurements the laser was kept in the low power regime. Some of the results are illustrated and compared with theory in Fig.4-9, where the RF frequency was 95 MHz and the centre magnetic field was 995 G.

As can be seen in Fig. 4-9, at low RF powers, the three hyperfine components clearly appear. At higher powers, however, the transitions are broadened such that the individual lineshape can no longer be distinguished. Similar to the NMR case, one finds that the

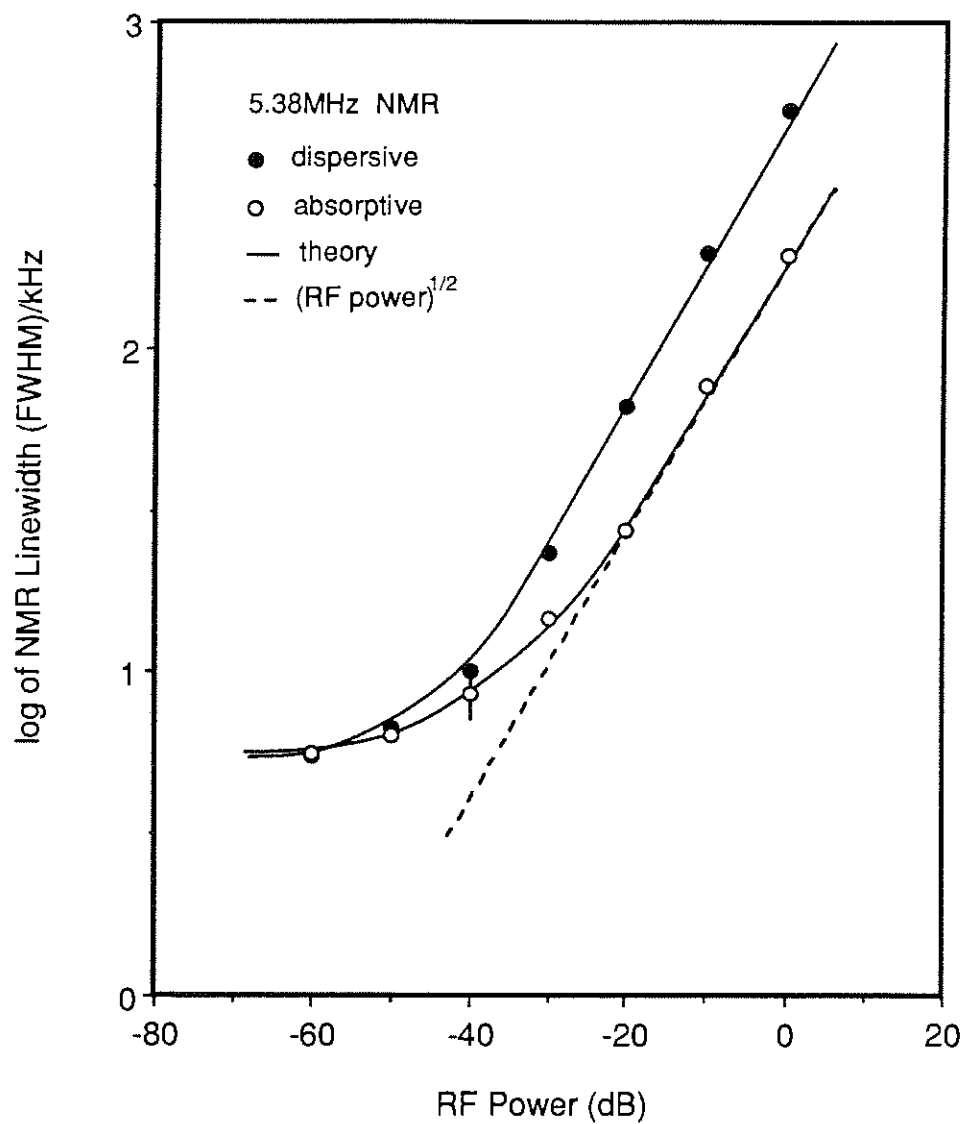


FIG. 4-8 The 5.38 MHz NMR linewidth (FWHM) (dots) as a function of RF power compared with theoretical predictions (solid curves).

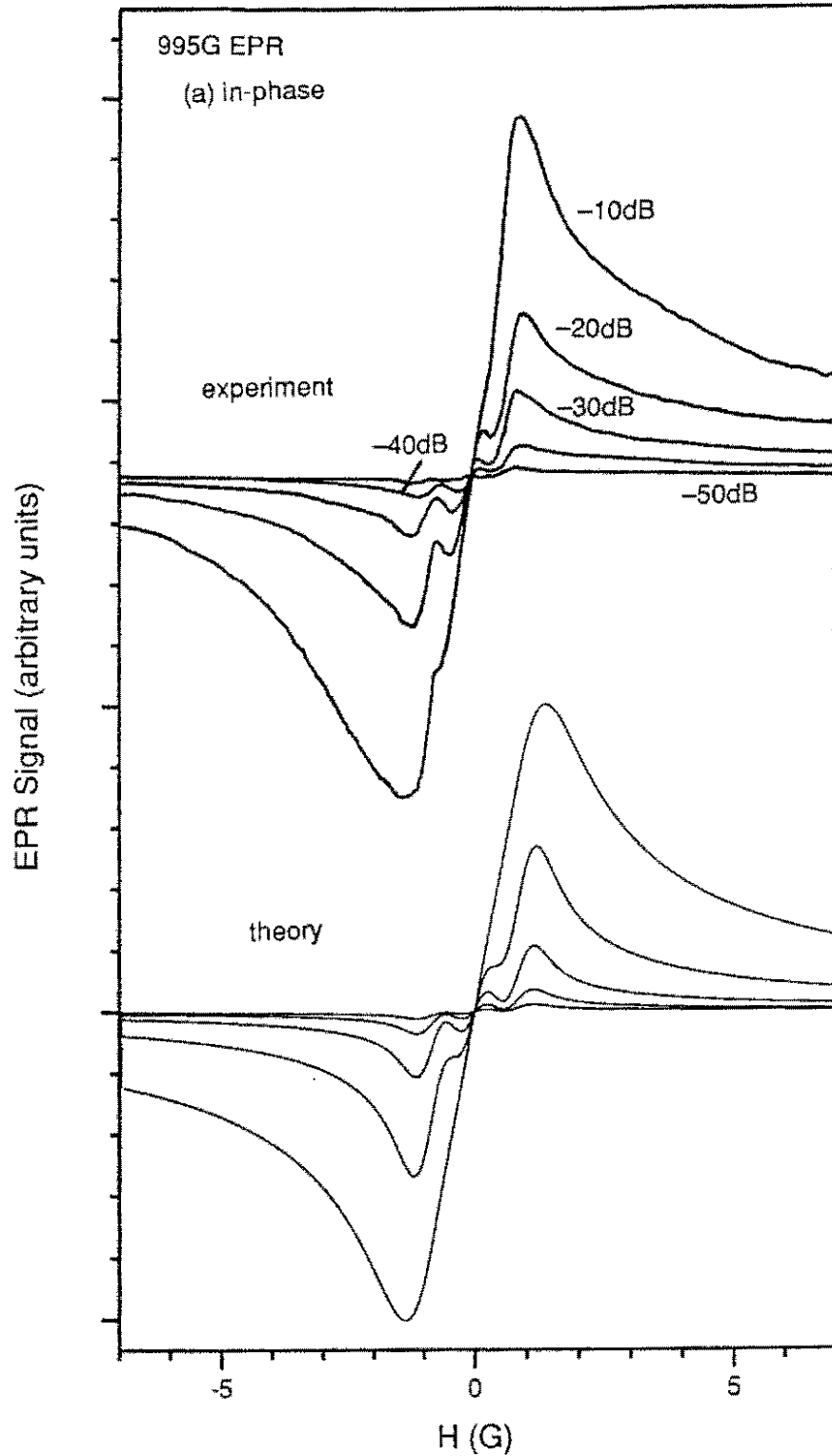


FIG.4-9 Saturation effects in the 995G (0G) EPR signal at various RF power levels.
 (a)Dispersive, (b)absorptive and (c)amplitude lineshapes.

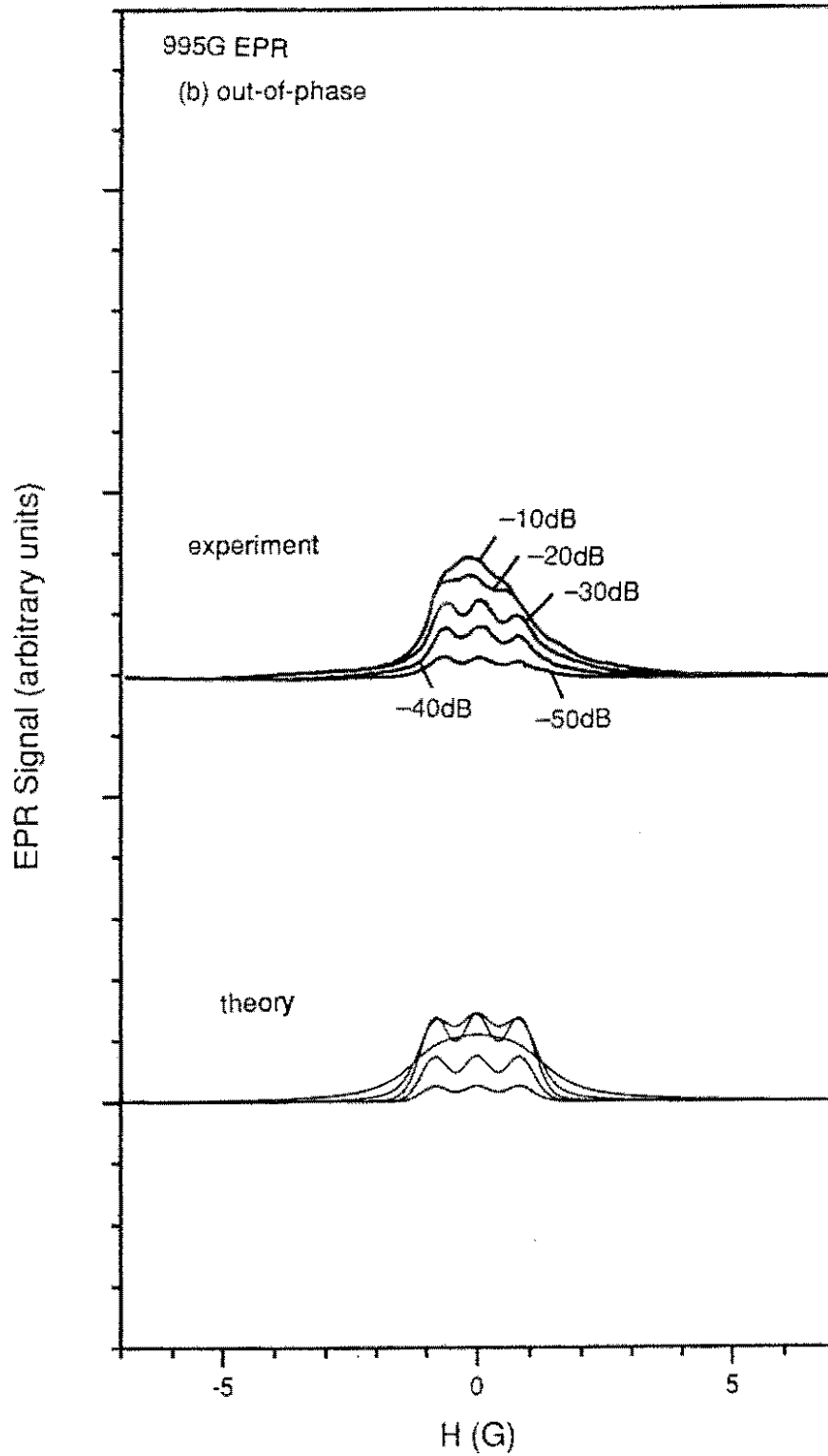


FIG. 4-9 (Continued)

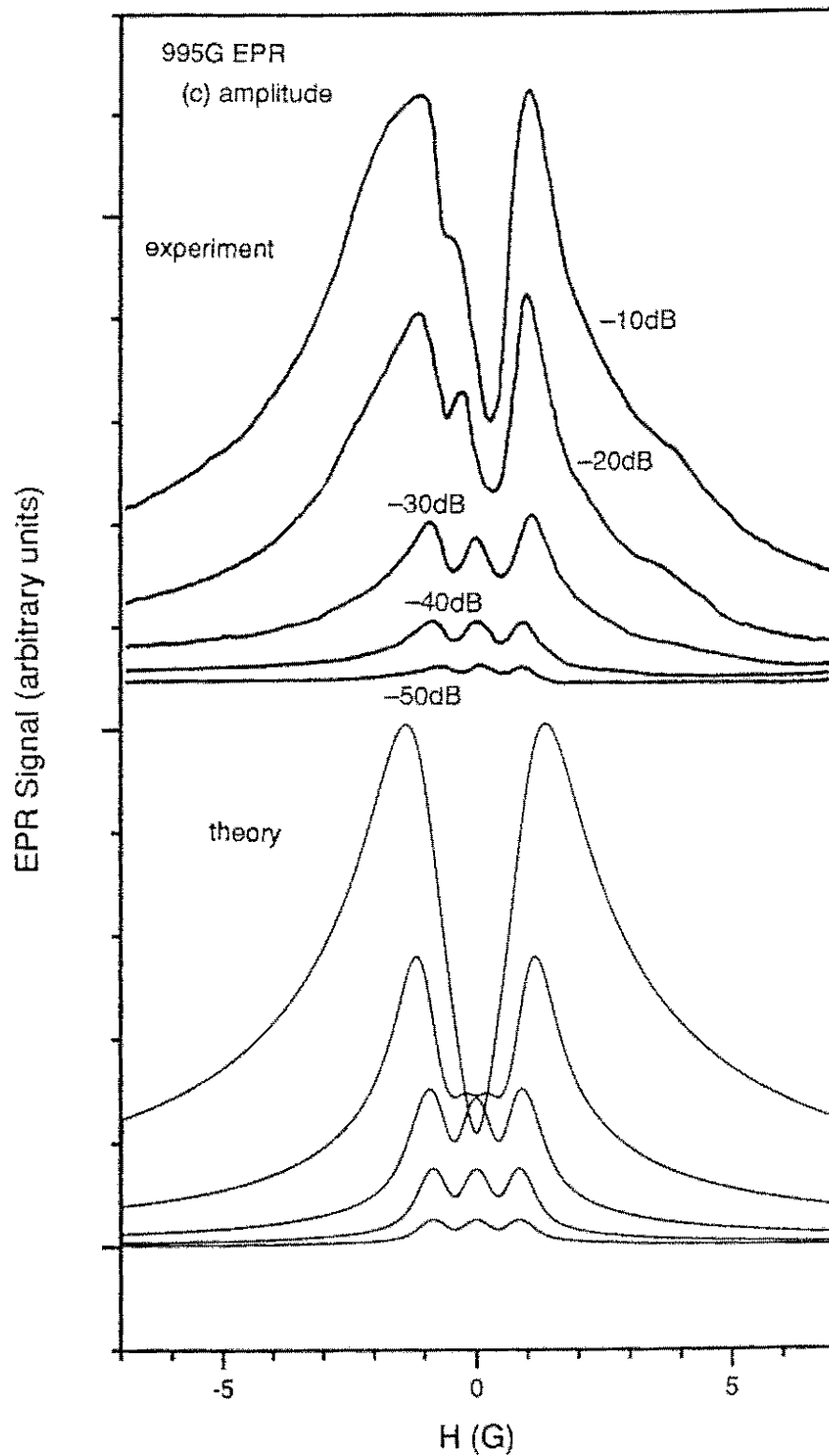


FIG. 4-9 (Continued)

dispersive component continues to grow while the absorptive component reaches a maximum then at higher powers decreases, resulting in a "hole" in the middle of the amplitude spectra (Fisk *et al.* 1990). Despite the hyperfine structure, the anomalous lineshapes are similar to those observed in the NMR. The lineshapes obtained using absorptive phase detection at high powers are less reliable due to the experimental difficulties in phase adjustment.

In the theoretical calculations, the EPR signal was considered as the sum of three independent hyperfine components separated by 0.78G. The in-phase and the out-of-phase lineshapes were calculated first using Eqs.(2-12a) and (2-12b). The total amplitude lineshape was then obtained by adding the two phases using Eq.(2-9). Parameters used in the calculations were $\Gamma_2=0.02$ MHz and $\sigma_H=1.0$ MHz, again determined from the spin echo (Chapter 9) and the weak field EPR (Section 4-1) measurements. The saturation factor S was taken to be 0.02, 0.2, 2, 20 and 200, corresponding to the -50, -40, -30, -20 and -10 dB power settings. As can be seen in Fig.4-9, a reasonable agreement is clear between theory and experiment.

Figure 4-10 plots the measured EPR signal amplitude as a function of RF power compared with theoretical predictions. The signal size here is the total contribution from the three hyperfine transitions. It is clear that below -35 dB the signal amplitude increases with (RF power)^{1/2}, again being consistent with the prediction for the low RF field regime (Wong *et al.* 1983). At higher powers there is an indication of saturation. Unlike the NMR, however, the critical RF power level, at which the absorptive signal begins to drop and the dispersive signal reaches a maximum has not been reached. This is a consequence of the limited power available and as a result the RF saturation dependency at higher powers for the EPR could not be studied.

4-3. LASER POWER DEPENDENCE

Similar to RF, the laser power received by the active centres inside the sample is proportional to E_L^2 and the cross section area of the laser beam A (Jackson 1975),

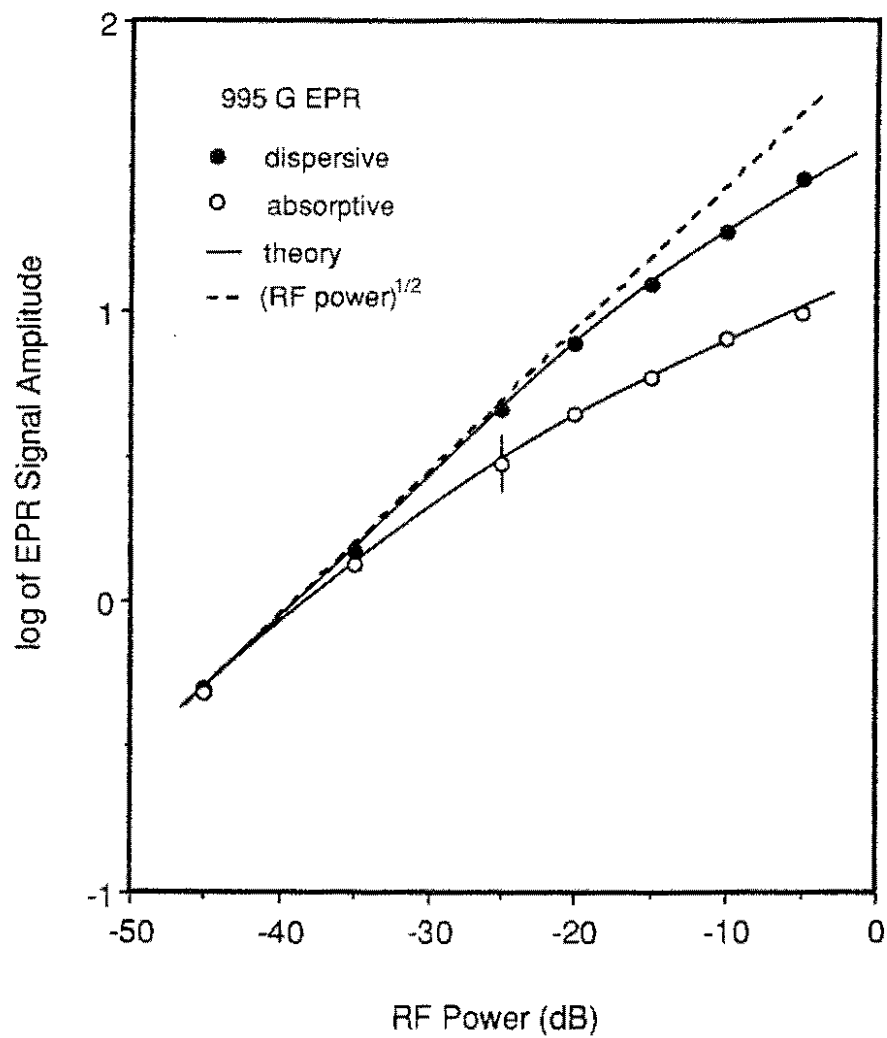


FIG.4-10 The 995 G EPR signal amplitudes (dots) compared with theoretical predictions (solid curves) as a function of RF power. Square root dependence in the weak RF field regime is also indicated (dashed line).

$$P_L = \frac{cnA}{8\pi} E_L^2 \quad , \quad (4-4)$$

In the experiments, the laser power could be changed using various neutral density filters and measured by a power meter.

The 5.38 MHz NMR signal amplitude and linewidth (FWHM) are plotted against the laser power in Fig.4-11 and 4-12, respectively. In the measurements, the RF was set in the low power regime and the magnetic field strength was 1058 G. Increasing laser power improved the signal size in both the dispersive and absorptive components. The signal amplitude was found to be linear in the laser power initially but tended to be saturated when the power was greater than 60 mW. The linear dependence is in agreement with theoretical prediction (Wong *et al.*1983),

$$I_S \propto E_L^2 \propto \text{laser power}, \quad (4-5)$$

for the weak laser field approximation. Also, there is no appreciable change in the linewidth below 60 mW. The power levels below 60mW can thus be considered as being in the weak laser power regime. Therefore, in all other measurements, the laser power was kept below 60 mW.

Several mechanisms can evidently affect the Raman heterodyne signal size at high laser powers. One is the strong hole burning effect in the 6380Å zero-phonon line, which reduces the optical absorption. Another is the population distribution within the spin levels of the 3A state, which can be affected significantly by optical pumping. Consequently, the field-free population difference $P_1 - P_2$ is disturbed. Such optical pumping effects will be discussed in Chapters 6 and 7. Another possible mechanism affecting the Raman heterodyne signal may be the population storage *e.g.* in the $m_s=1$ state through inter-system crossing. This may reduce the number of centres as the laser power increases.

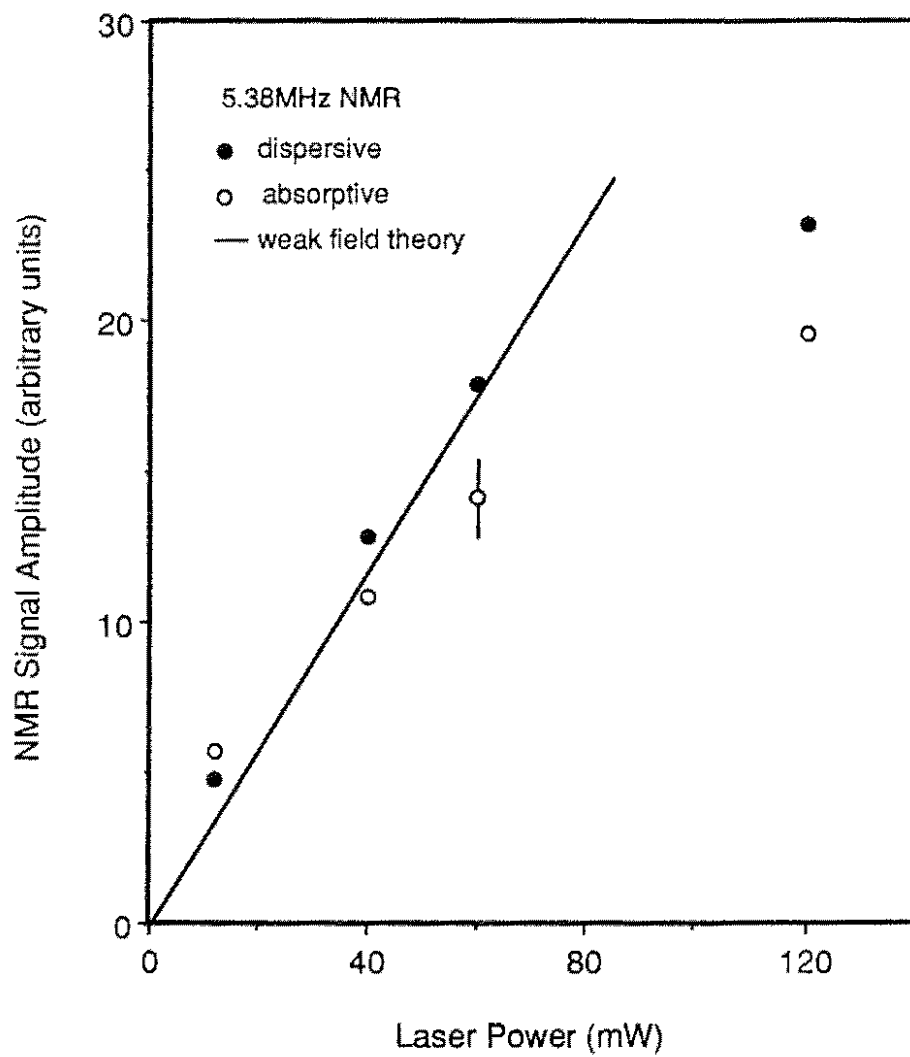


FIG. 4-11 The 5.38 MHz NMR signal amplitude as a function of laser power.

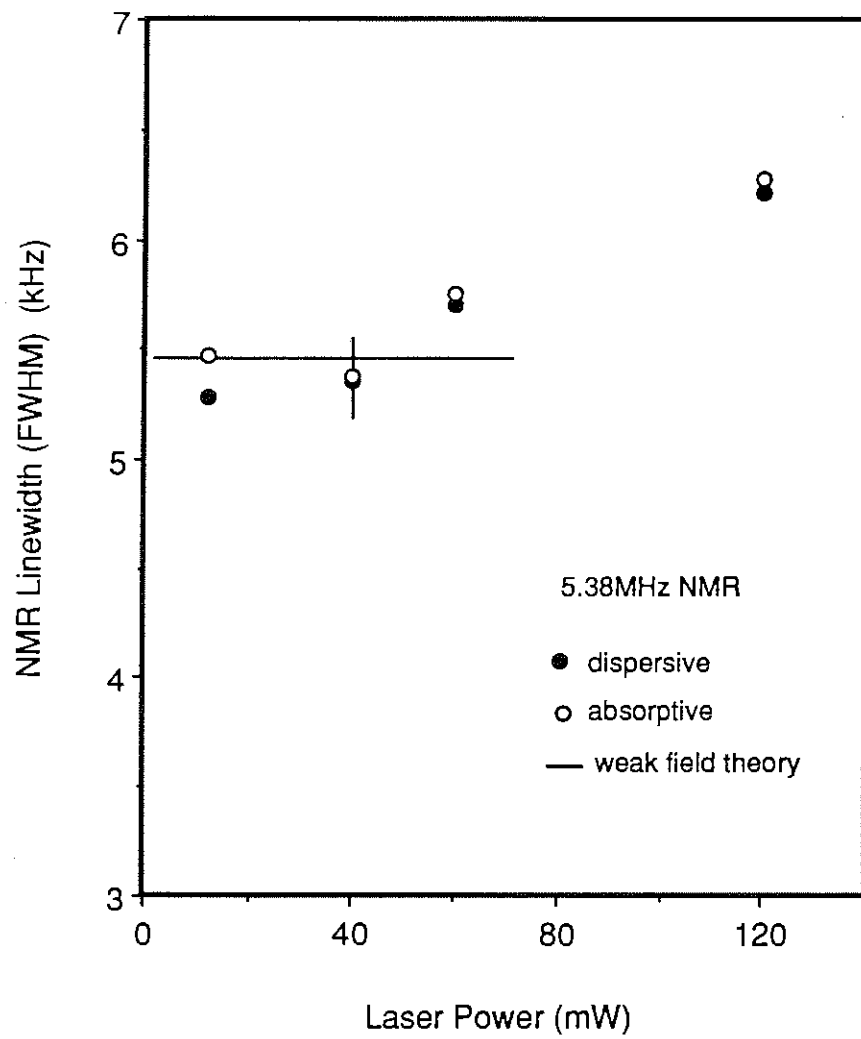


FIG.4-12 The 5.38 MHz NMR linewidth as a function of laser power.

4-4. LASER DETUNING WITHIN THE 6380Å ZERO-PHONON LINE

The 6380 Å zero-phonon line is inhomogeneously broadened due to crystal strain. By manually mode-hopping the laser by 200 GHz in each step, the Raman heterodyne NMR and EPR signals can be explored within the inhomogeneous line. The NMR lineshapes measured at various laser frequency detunings within the zero-phonon line are plotted in Fig.4-13. It was found that the laser detuning did not affect the spectral profiles except for a decrease of the signal size. This implies that there is no appreciable difference among different subgroups of N-V centres in the inhomogeneous distribution contributing to the Raman process except via their number densities, which determine the signal amplitude.

The theory for weak laser fields predicts that the Raman heterodyne signal amplitude changes with the laser detuning Δ_L with, $\sim \exp[-(\Delta_L/\sigma_E)^2]$, (see Eqs.(2-7) and (2-8)), where σ_E is the optical inhomogeneous linewidth. For our sample we found that the NMR and EPR signal size dropped appreciably when the laser was detuned from the 6380Å line centre, as shown in Fig. 4-14, where the envelope of the best-fit is assumed to be a Gaussian profile. The linewidth (FWHM) determined from the envelope (~ 320 GHz) is narrower by a factor of 3 compared with the inhomogeneous linewidth (FWHM) measured by excitation spectroscopy (~ 1000 GHz) (Reddy 1989).

The reason for the difference is not completely clear. It is possibly due to optical pumping and relaxations, which affect the population factor, P_1-P_2 , and thus affect the detected signal. As the Raman heterodyne signal is proportional to,

$$I_S \sim (P_1-P_2) \exp[-(\Delta_L/\sigma_E)^2],$$

any change in the population factor will alter the NMR or EPR signal amplitude. For our diamond sample, the hole burning effect substantially reduces the optical absorption when exposed to a focussed 6380Å laser beam, particularly when the laser frequency is in the wings of

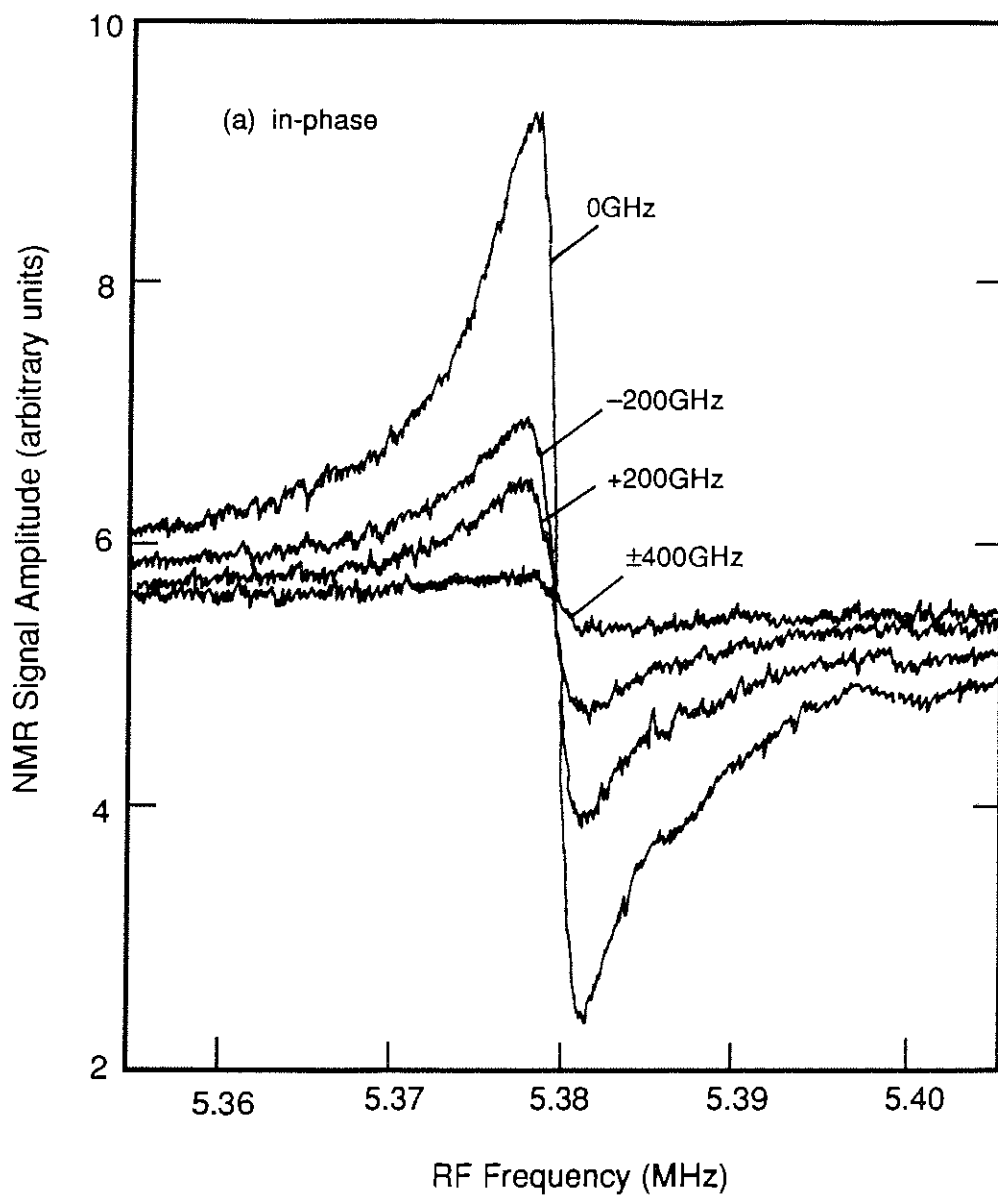


FIG. 4-13 The Raman heterodyne detected NMR lineshapes as the laser is detuned within the 6380\AA zero-phonon line. (a) The in-phase and (b) the out-of-phase components.

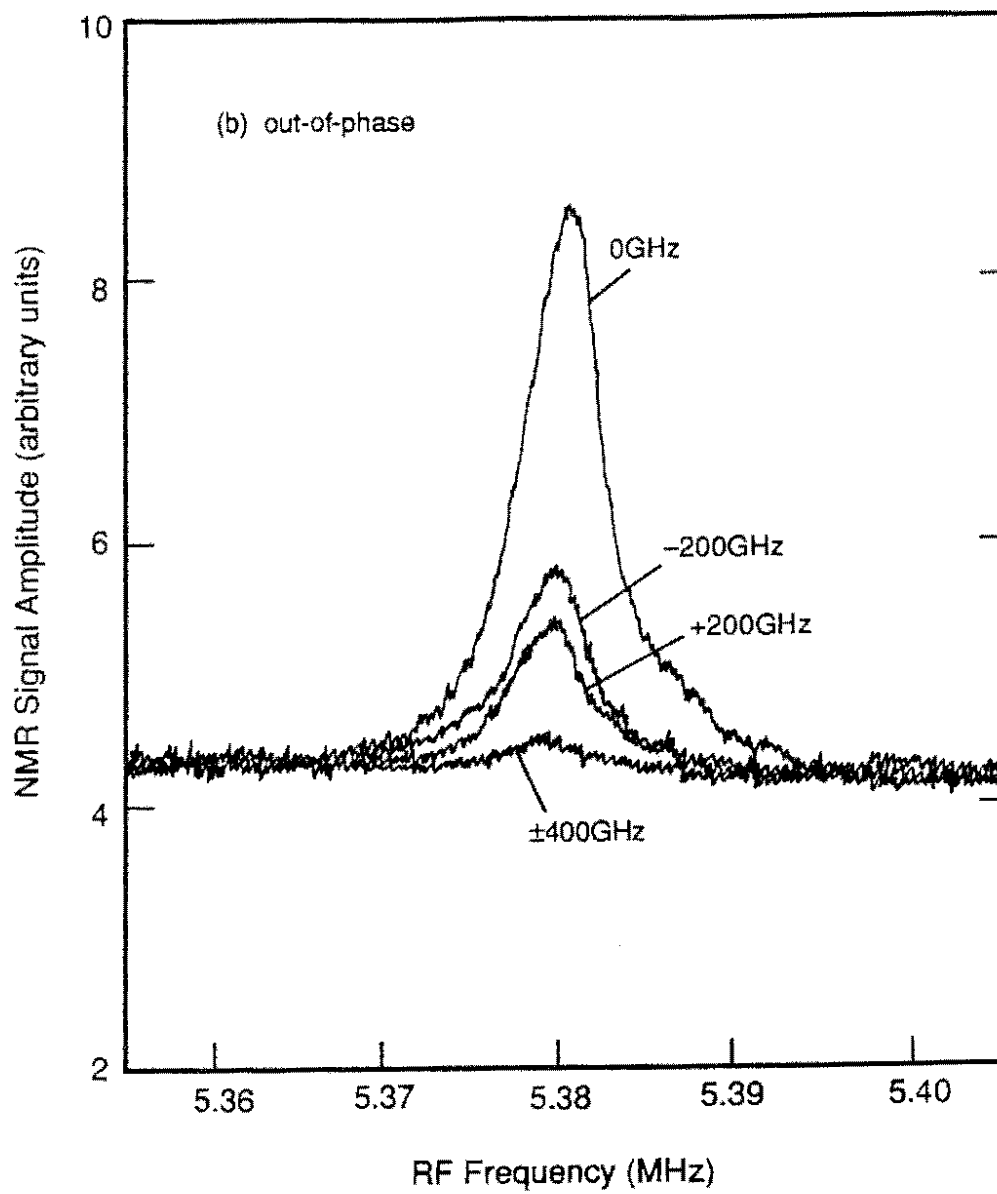


FIG. 4-13 (Continued)

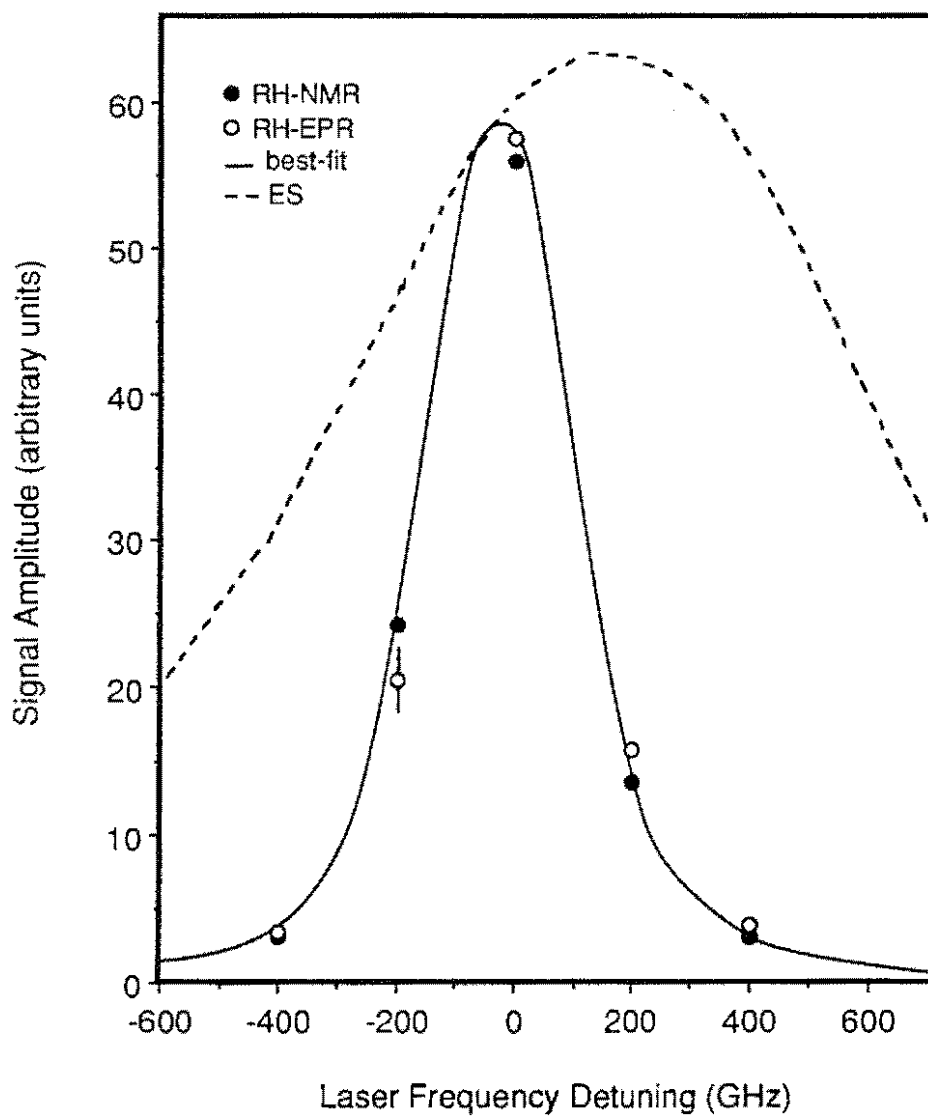


FIG.4-14 The Raman heterodyne NMR and EPR signal amplitude as a function of laser detuning within the 6380 \AA zero-phonon line. A Gaussian profile of the best-fit is plotted (solid line). The zero-phonon line measured by excitation spectroscopy (ES) is also illustrated (dashed line) all for same sample.

the line (Holliday 1989). It was also found (Reddy 1989) that the optical hole burnt in the zero-phonon line became broader as the laser was detuned from the line centre. These phenomena imply that the relaxation processes in the optical transition may change with the laser frequency. As a result, the NMR or EPR signal with the laser being in the wings may be reduced even more and the linewidth of the Raman heterodyne signal envelope is then smaller.

In a recent experiment, van Oort *et al.* (1991) observed that the ODMR signal of the N-V centre detected using optical excitation was enhanced by the application of a microwave at 2.88 GHz when the laser frequency was detuned in the "red" wing of the 6380Å zero-phonon line while the signal was reduced when the laser was in the "blue" wing. We found, however, that the Raman heterodyne signals were detectable only when the laser frequency was in the low frequency parts of the optical line, as can be seen in Fig.4-14. This phenomenon is possibly due to fast relaxations from the higher frequency components to the lower ones in the 3E state. As a result, the lifetime of an energy level in the higher frequency parts of the excited state is not long enough to maintain a population difference over a desirable period of time and therefore no Raman heterodyne signal is detectable.

4-5. CONCLUSIONS

The Raman heterodyne detected NMR and EPR lineshapes in the 3A ground state of the N-V centre have been measured at various RF powers, laser intensities and laser frequencies and compared with theory. At low RF powers, the lineshapes were found to have profiles of Eqs.(2-10a) and (2-10b) as predicted by theory (Wong *et al.* 1983). The NMR signal with a linewidth (FWHM) as narrow as 3.4 kHz was obtained. In the EPR experiments three hyperfine components were clearly resolved either by sweeping the RF frequency or by sweeping the magnetic field.

When the RF power was increased, the NMR and EPR transitions were broadened and saturated. The lineshapes measured with intense RF fields were found to be reasonably well

described by the theoretical model developed by Fisk *et al.* (1990). Both the signal size and the linewidth at arbitrary RF powers were also found to be consistent with the theoretical predictions. Because of the different saturation characteristics for the in-phase and the 90° out-of-phase components, their signal magnitude differs as power increases. This results in the anomalous lineshapes at high powers using amplitude detection.

The Raman heterodyne signal was found to increase linearly with the laser intensity in the low laser power regime, being in agreement with theory, but tended to be saturated at higher intensities.

Laser detuning within the 6380Å zero-phonon line did not alter the spectral profiles except for a change of the signal size. The Raman heterodyne signals were found to be detectable only when the laser frequency was in the low frequency components of the optical line and the linewidth determined from the NMR or EPR signal envelope as the laser was detuned within the zero-phonon line was found to be much narrower (~320GHz) than that determined by optical excitation technique (~1000GHz).

Chapter 5

ENDOR AND DOUBLE NMR SPECTRA

Magnetic double resonance measurements (see *e.g.* Slichter 1990) can be achieved by introducing a second RF field to drive an additional spin transition while monitoring the change in a Raman heterodyne EPR or NMR signal (Fig.5-1) (Manson *et al.* 1990). For example, in electron-nuclear double resonance (ENDOR) (Feher 1957) measurements, the transition between any two nuclear spin levels in the 3A ground state can be measured by monitoring the amplitude of the EPR signal while scanning a second RF in the range of 0~8 MHz. Similarly, nuclear-nuclear double resonance (double NMR) (Hartmann and Hahn 1962) can be obtained if an appropriate NMR line is monitored.

This chapter deals with the ENDOR and double NMR lineshapes measured using Raman heterodyne techniques. Attention is paid here to the analysis of their spectral profiles, *e.g.*, how they depend on the RF power, the EPR resonance, and the detection scheme. The application of ENDOR measurements to the studies of hyperfine and nuclear quadrupole interactions in the 3A state will be discussed elsewhere (Chapter 7).

The coherence processes involved in the double resonances are shown in Fig.5-1. In ENDOR measurements, the EPR transition is driven by an RF field, ω_{RF} , while the 6380Å optical transition is driven by a laser field, ω_L . A second RF, ω'_{RF} , is used to drive an additional spin transition and it in fact alters the spin population within the hyperfine sub-levels. The EPR signal amplitude is changed each time when ω'_{RF} is in resonance with a nuclear transition. Likewise, the second RF affects the magnitude of the NMR signals and an equivalent

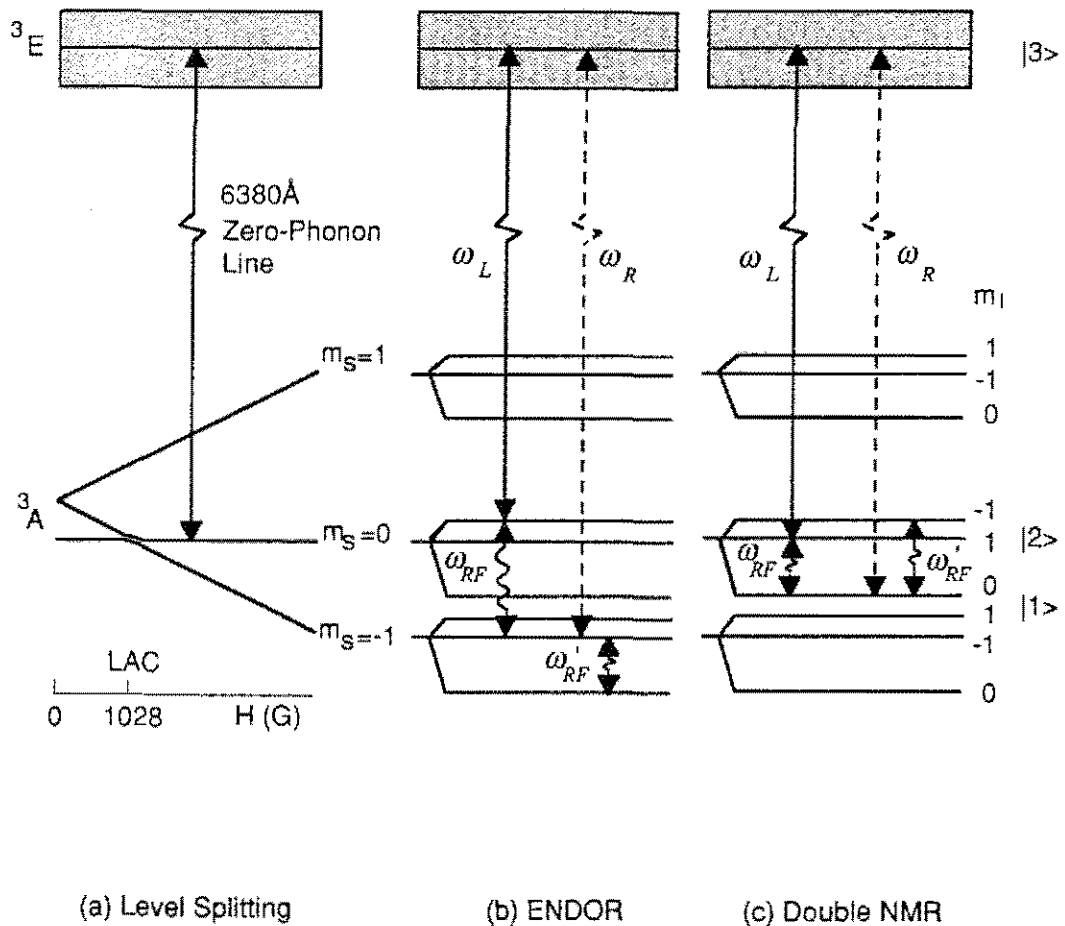


FIG. 5-1 (a) The level splitting in the magnetic field and the energy levels and coherence processes involved in the Raman heterodyne detected ENDOR (b) and double NMR (c) in the 3A ground state of the N-V centre. The schemes are similar to the EPR and NMR measurements except the application of a second RF field, ω'_{RF} , which drives an additional spin transition. The double resonance spectra are obtained by monitoring the Raman heterodyne signal at ω_{RF} as a function of ω'_{RF} .

spectrum - double NMR - can be generated by monitoring an NMR signal as a function of the second RF frequency ω'_{RF} .

5-1. ENDOR: DEPENDENCE ON RF POWER

Figure 5-2 shows several ENDOR spectra measured at various power levels of the swept RF. In the experiment, the first peak in the EPR amplitude spectrum at 98MHz was monitored as a function of the second RF frequency. The RF driving the EPR transition was set in the low power regime and the measured spectra represent the change in the total EPR signal amplitude.

At the -30dB power level, only the $m_f=0 \leftrightarrow 1 (m_s=0)$ and $m_f=0 \leftrightarrow -1 (m_s=0)$ transitions were detectable. The $m_f=0 \leftrightarrow -1 (m_s=0)$ transition at 5.3 MHz has a linewidth (FWHM) of 40 kHz at this power level, compared with the NMR linewidth of ~5kHz (Chapter 4). As ENDOR is measured by monitoring an EPR signal, the EPR processes can cause additional broadening to the observed linewidth (Abragam and Bleaney 1970), such as the inhomogeneous broadening of the EPR line, and the cross relaxation within the electron spin system, where nearby centres whose resonance frequencies coincide may exchange a quantum energy and undergo a flip-flop transition.

The swept RF power level affects the spin populations and hence the associated ENDOR signals. The other four transitions were observed at the power level of -10dB. At this high power, the ENDOR lineshapes become complicated, an example of which is the 7.0 MHz line, which has a dispersive profile due to interference effects.

At the highest power level (-10dB), all nuclear transitions within the $m_s=0, -1$ states appear. Their resonances are at 0.7, 3.2, 3.8, 4.8, 5.3 and 7.0 MHz, corresponding to the transitions indicated in the figure. The first and third lines are "forbidden" transitions and found to appear only in the ENDOR measurements. The other four allowed transitions are in agreement

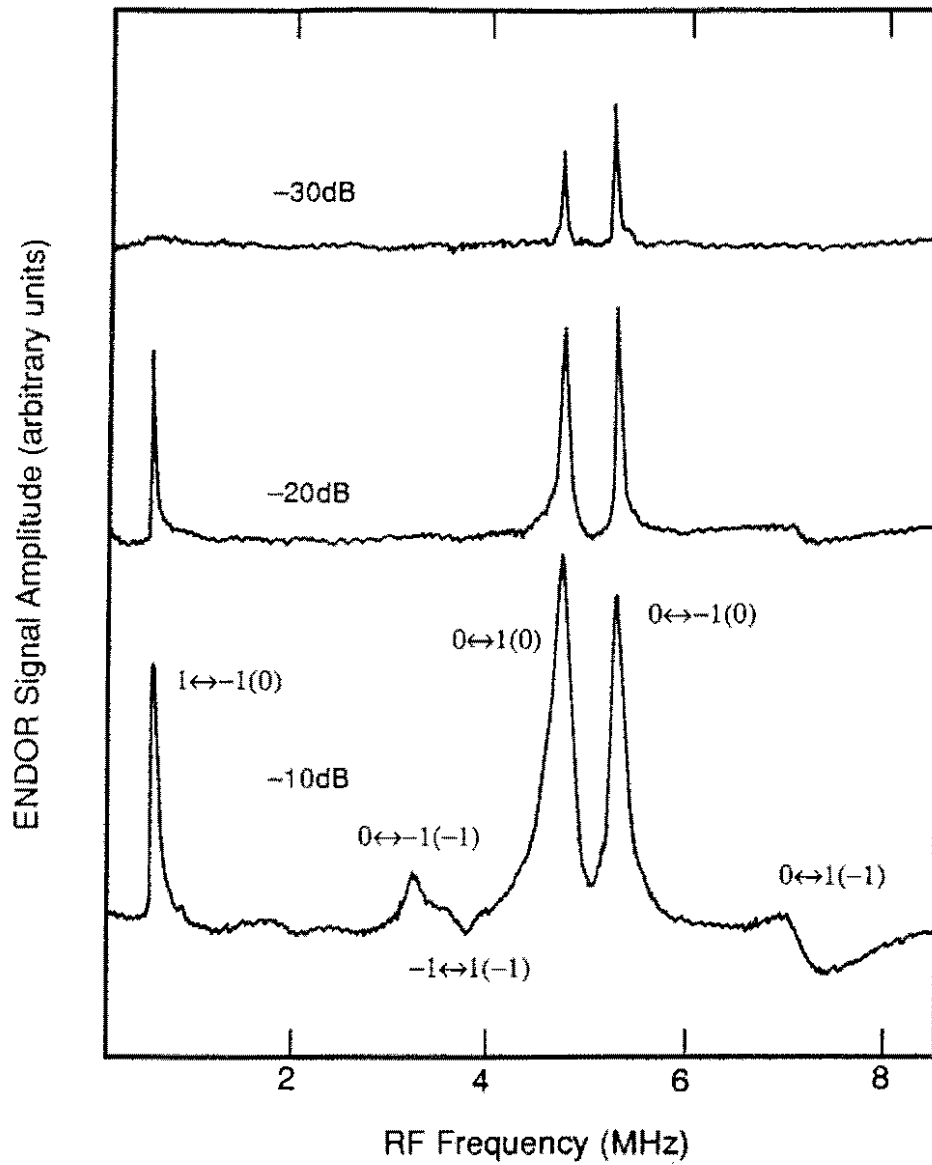


FIG.5-2 The ENDOR lineshapes measured by monitoring a 98 MHz EPR resonance at various power levels of the swept RF field.

with those observed in the NMR (Chapter 7). Relaxation proceeds between all the hyperfine sub-levels at a rate $\sim 1/T_1$, where T_1 is the spin-lattice relaxation time, so that the spin populations of all levels are indirectly affected by the swept RF after a time of order T_1 . The population re-adjustments within the spin levels due to the spin-lattice relaxation processes leads to the observation of all nuclear spin transitions although only one single EPR resonance is monitored (Abragam and Bleaney 1970).

5-2. ENDOR MEASURED IN DIFFERENT EPR PHASE COMPONENTS

Figure 5-3 plots two typical ENDOR traces measured in different EPR phase components at a magnetic field of 995 G. The absorptive and dispersive EPR lineshapes were obtained first as described in Chapters 3 and 4. The second RF source was then applied and swept from 0-8 MHz. Its power level was adjusted such that all the six transitions were observed.

The traces (1) and (2) in Fig.5-3 were measured by monitoring the two EPR phase components, respectively, where the spectral positions being monitored are indicated by arrows. As the sign of the ENDOR signal relies on the EPR signal level with respect to the reference RF magnitude, traces (1) and (2) are of opposite signs. Physically, the ENDOR spectra are the same by monitoring either the in-phase or the out-of-phase component.

5-3. ENDOR MEASURED AT DIFFERENT EPR RESONANCES

Since three hyperfine components as well as other forbidden transitions appear in the EPR spectra, the ENDOR signals can be obtained by monitoring different EPR resonances, *e.g.* at each of the three hyperfine components. Figure 5-4 illustrates the results measured at the three allowed resonances in the absorptive EPR spectra. Traces (1), (2) and (3) were obtained,

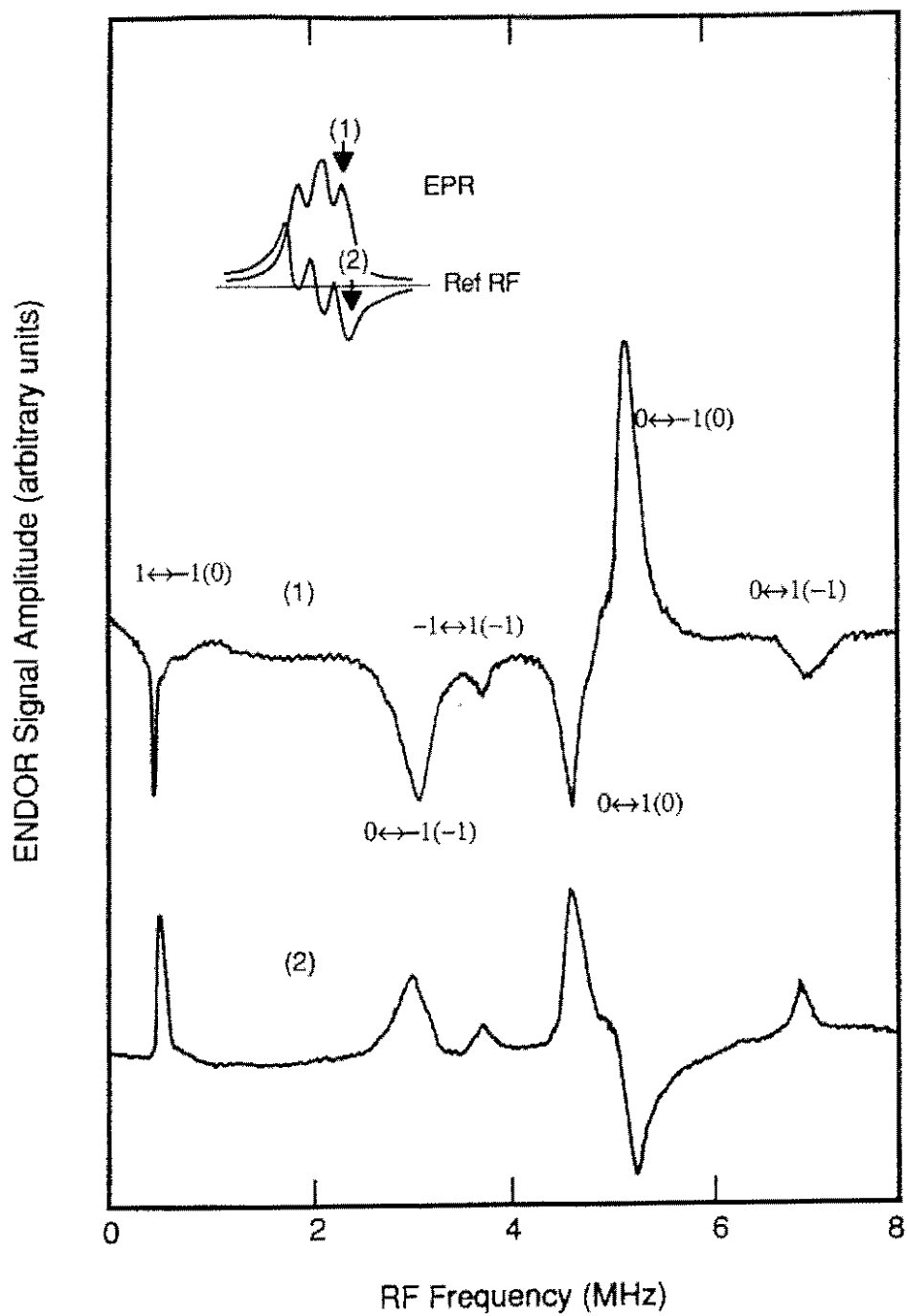


FIG.5-3 The ENDOR lineshapes obtained by monitoring the absorptive (1) and dispersive (2) EPR phase components. The spectral positions being monitored are indicated by arrows.

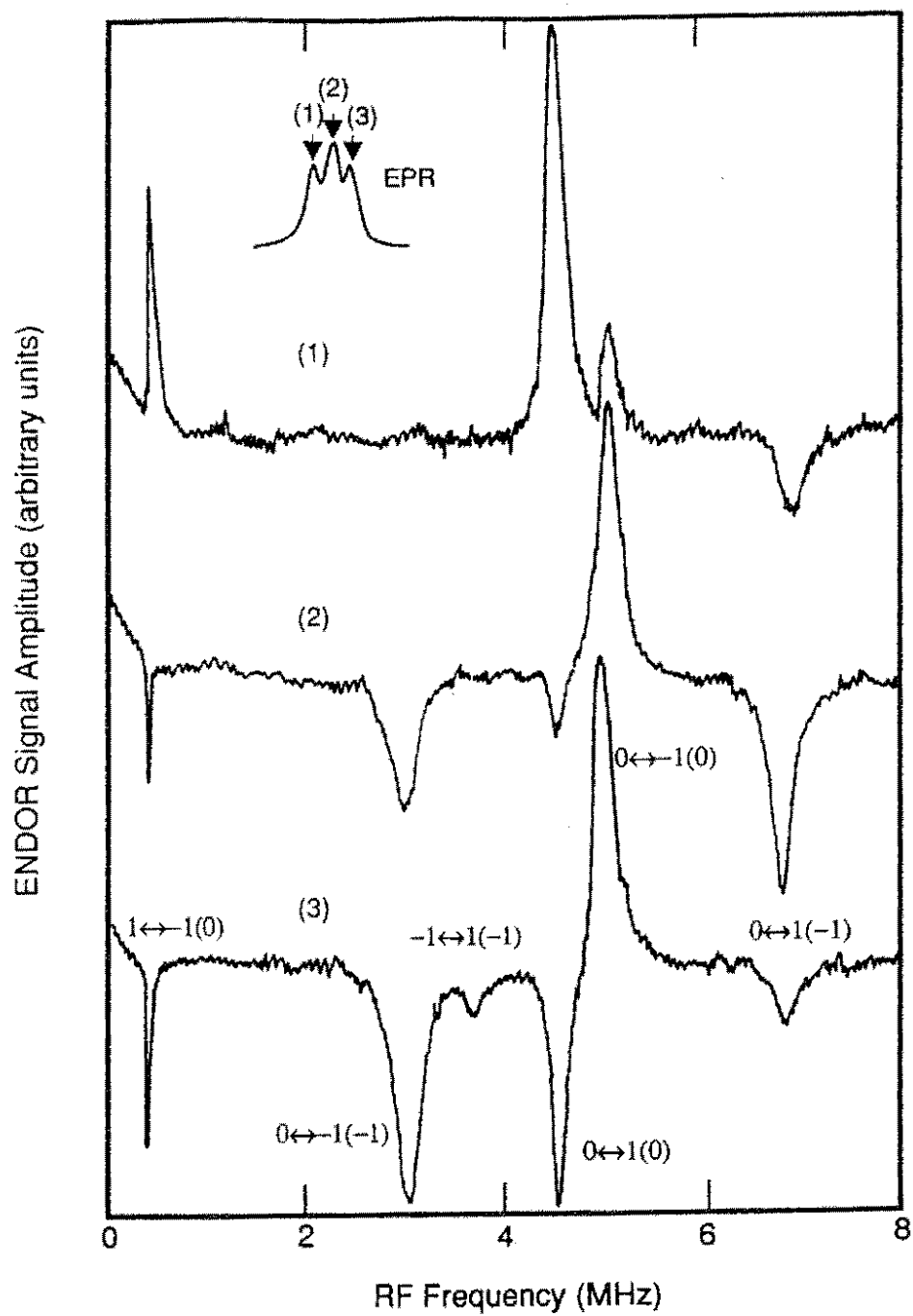


FIG.5-4 The ENDOR signals measured at different EPR resonances in the absorptive spectrum. Traces (1), (2) and (3) were obtained by monitoring the three allowed transitions indicated by arrows.

respectively, by monitoring the first, the second and the third EPR lines, *i.e.* the $m_s=0 \leftrightarrow -1$ ($m_f=-1, 0, +1$) allowed transitions.

In the ENDOR measurement, the effect of the swept RF field is different when different EPR resonance is monitored and this reflects in the different sign and/or size in the measured traces. With the application of the second RF source, a prediction for the ENDOR signal sign and/or size needs a consideration of both the two RF and the laser fields. This has not been modeled because optical pumping effects on the spin population distribution in the 3A state have not been quantitatively determined.

5-4. DOUBLE NMR

When an NMR transition is monitored while the second RF field is swept in the range of 0~8 MHz, one may obtain a double NMR spectrum. Figure 5-5 shows a typical double NMR spectrum obtained at a magnetic field of 1039 G by monitoring the 5.3 MHz line. All six transitions clearly appear, which is a one-to-one correspondence to the ENDOR spectra. In the NMR measurements, normally only two transitions, $m_f=0 \rightarrow 1$ ($m_s=0$) and $m_f=0 \rightarrow -1$ ($m_s=0$), or at most four transitions, $m_f=0 \rightarrow -1$ ($m_s=-1$), $m_f=0 \rightarrow 1$ ($m_s=0$), $m_f=0 \rightarrow -1$ ($m_s=0$) and $m_f=0 \rightarrow 1$ ($m_s=-1$) transitions were detectable (see Chapter 7), depending on the experimental settings. Using the double NMR detection scheme, however, all six nuclear transitions are observed. This is again due to the relaxation and population re-adjustment within all the spin levels caused by the second RF source.

The technique is superior to the NMR measurement in that it overcomes spurious RF pickup, particularly in the low frequency regime (≤ 1 MHz), where noise arises from the laser instability. In addition, the double NMR has sharper lines compared with the ENDOR spectra. This is because the nuclear spin is less affected by the surrounding lattice and therefore the

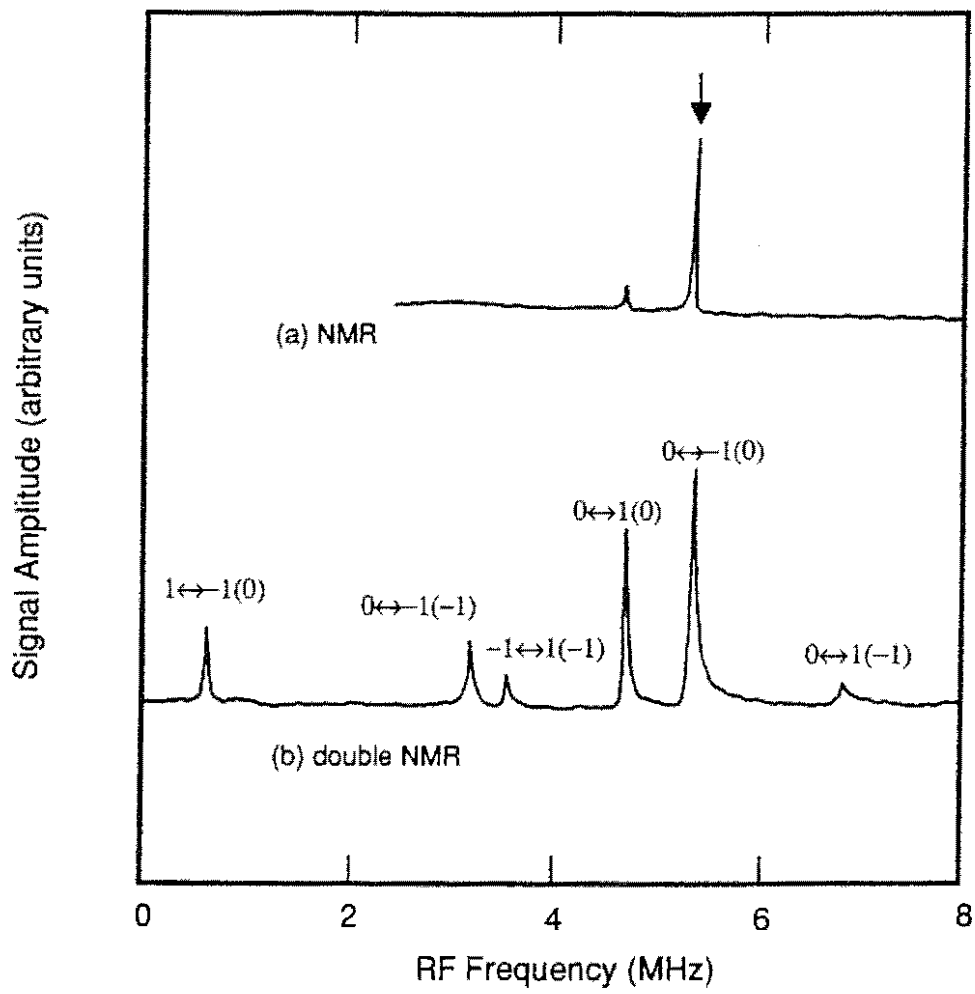


FIG.5-5 The NMR (a) and double NMR (b) spectra. The latter was measured by monitoring the 5.3 MHz NMR transition indicated by an arrow while sweeping the second RF field.

resonance has a much narrower inhomogeneous linewidth. The double NMR technique provides complementary information on the magnetic interactions in the 3A ground state.

5-5. CONCLUSIONS

By applying an additional RF field, the ENDOR signals in the 3A state were obtained using Raman heterodyne techniques. The ENDOR lineshapes have been measured and analyzed at various swept RF powers and EPR resonances with different EPR detection schemes. Increasing the RF power enhanced and broadened the ENDOR signals significantly. Due to the spin-lattice relaxation within the spin levels, all six nuclear transitions in the $m_S=0$ and $m_S=-1$ states of the triplet were observed at high RF powers. Different signs were also observed when the ENDOR was probed at different EPR resonances, depending on whether an increase or a decrease in the population factor was caused by the second RF field.

The double NMR spectra were measured similarly, showing a one-to-one correspondence to the ENDOR signals, but with much sharper lines. This provides a complementary technique for the double resonance measurements.

Chapter 6

LEVEL ANTICROSSING STUDY

As discussed earlier, when an external magnetic field is aligned along the [111] crystallographic direction, it lifts the degeneracy of the $m_s = \pm 1$ states of the triplet and causes the $m_s = 0$ and $m_s = -1$ levels to approach the same energy at 1028 G. Owing to the hyperfine interaction and slight misalignment of the crystal in the experiment, the two levels do not cross. This is generally referred to as level anticrossing (LAC). By studying the resonances near the level anticrossing (He *et al.* 1991a) useful information can be obtained about the strengths of various interactions, in particular those associated with the off-diagonal terms in the Hamiltonian.

6-1. EPR LINESHAPE AND SPIN ALIGNMENT

Loubser and van Wyk (1977) have reported the EPR of the N-V centre using conventional techniques. One of the interesting observations about the N-V centre is that the EPR line at low field is in absorption while the one at high field is in emission. The reason for the reverse of signal sign is associated with spin alignment under optical pumping. However, the details of this effect are not completely clear, though similar inversion has been observed in other systems, such as and the Si-G9 centre (Watkins 1967) and the Si-S centre (Brower 1971).

We have observed such an effect in the Raman heterodyne detected EPR signals, as shown in Fig.6-1. In the experiment, the RF was fixed at 64 MHz and the magnetic field was swept

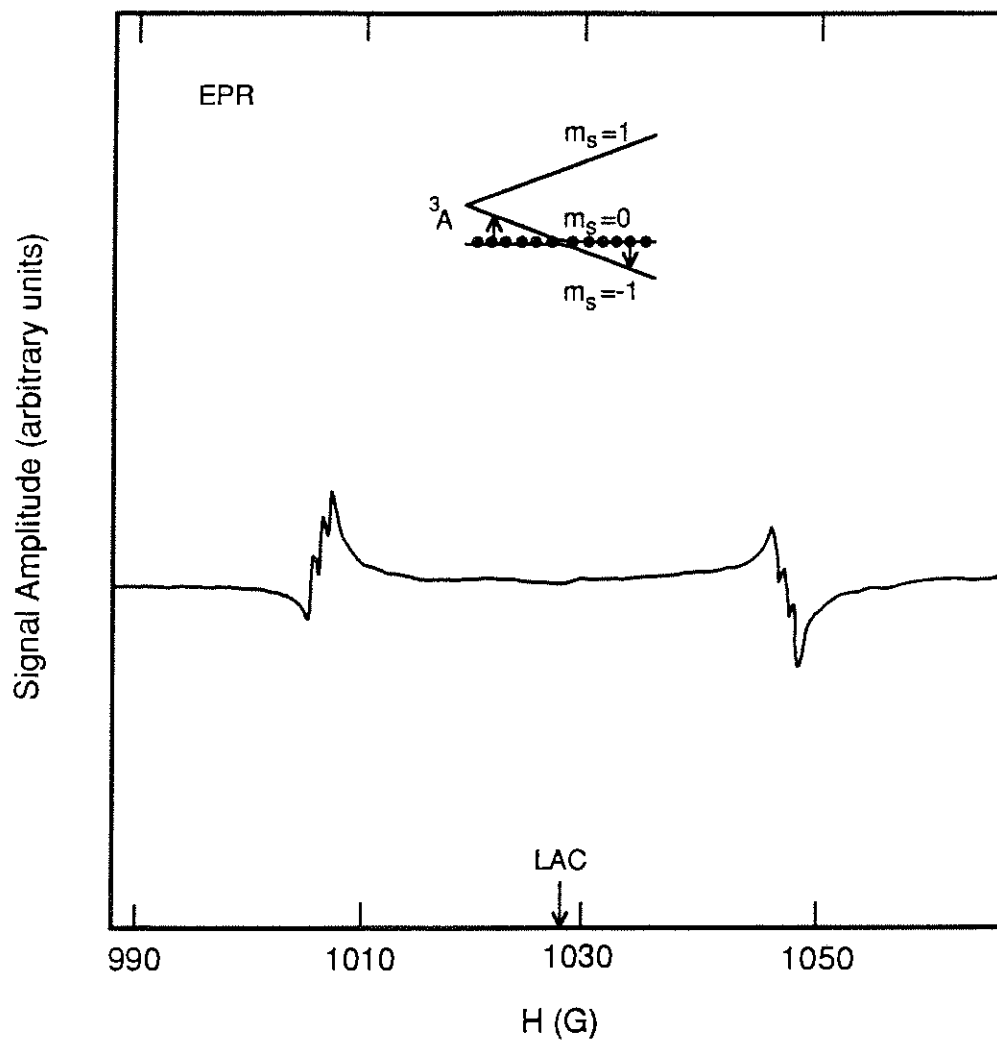


FIG. 6-1 Raman heterodyne detected EPR lineshapes at low and high field sides of the level anticrossing using dispersive phase detection. The 180° phase difference of the two signals is attributed to spin alignment indicated in the inset.

from 988 to 1068 G. Dispersive-phase detection was used and low RF power levels were employed. As can be seen, the EPR signal sign reverses when the field goes through the anticrossing value.

Owing to the spin alignment, the sign of the population factor, $P_2 - P_1$, (see Chapter 2) where P_1 and P_2 denote the populations in the higher and lower EPR levels respectively, will change when the magnetic field goes through 1028 G. In consequence, the EPR signals at high and low fields reverse sign (180° out of phase). The inversion of phase in the EPR signals is consistent with the previous observation by Loubser and van Wyk (1977). However, the Raman heterodyne technique is not capable of directly determining which is the preferentially populated state.

To illustrate the populations in the levels involved in the EPR transition, it is helpful to calculate the amount of $m_s=0$ state in the lower and higher EPR levels. Let,

$$W_1(m_s=0) = \frac{1}{3} \sum_{n=1}^3 \sum_{m_I} a_n^2(m_s=0, m_I) \quad (6-1a)$$

$$W_2(m_s=0) = \frac{1}{3} \sum_{n=4}^6 \sum_{m_I} a_n^2(m_s=0, m_I) , \quad (6-1b)$$

where $W_1(m_s=0)$ and $W_2(m_s=0)$ are, respectively, the normalized amount of $m_s=0$ state in the lower eigenstates $|n\rangle$ ($n=1,2,3$) and higher eigenstates $|n\rangle$ ($n=4,5,6$). If we assume that the spins totally reside in the $m_s=0$ state (see discussions below) the population factor is then,

$$P_2 - P_1 = W_2(m_s=0) - W_1(m_s=0).$$

Table 6-1 lists some calculated results at different magnetic field strengths near the anticrossing. The wave functions were obtained by diagonalizing the Hamiltonian matrix of

Eq.(1-11), where the field misalignment to the [111] axis was taken to be 0.25° . The parameters used in the calculations were $D=2.88$ GHz, $|A_{||}|=2.30$ MHz $|A_{\perp}|=2.10$ MHz and $|P|=5.04$ MHz (see Chapter 7). As can be seen, at 980 G the the amount of $m_s=0$ state in the higher EPR level is zero whereas at 1028 G (LAC) it reaches 50 %. At a field of 1080 G, the higher EPR level is dominated by the $m_s=0$ state (100 %). If electron spins tend to reside in the $m_s=0$ state, the population difference between the two EPR levels vanishes at the level anticrossing and reverses sign when the field goes through 1028G.

TABLE 6-1 Amount of state mixing and population difference in the EPR levels near the level anticrossing.

	Magnetic Field Strength H (G)				
	980	1010	1028	1050	1080
$W_1 (m_s = 0)$	1.00	0.97	0.50	0.02	0.00
$W_2 (m_s = 0)$	0.00	0.03	0.50	0.98	1.00
$P_2 - P_1$	-1.00	-0.94	0.00	0.96	1.00

6-2. EPR IN THE LEVEL ANTICROSSING REGION

6-2-1. Lineshape: Dependence on Magnetic Field Strength

Figure 6-2 shows a few EPR signals for various magnetic field strengths near the level anticrossing, where the RF frequencies used in the experiments are indicated in the figure. Amplitude detection was employed and therefore no phase information is included. Low RF

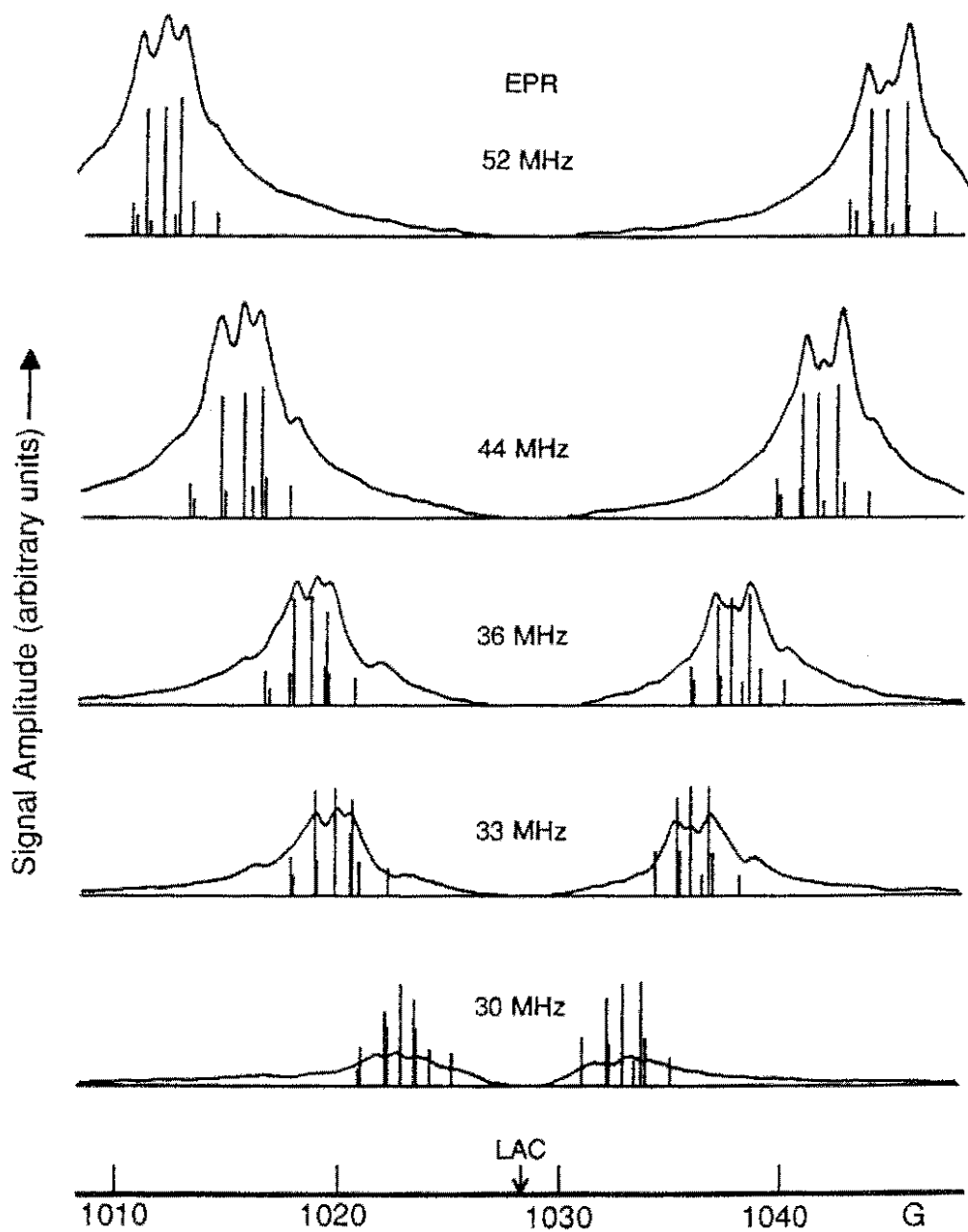


FIG. 6-2 EPR lineshapes (curves) for various magnetic field strengths near the level anticrossing, where amplitude detection was employed. The corresponding transition matrix elements are shown by vertical lines.

power levels were used to avoid power broadening effects.

Holliday *et al.* (1990) have reported the EPR at frequencies up to 1GHz and have confirmed the signals as arising from the $m_s=0$ and $m_s=-1$ level splitting of a 3A state. The results presented here are restricted to those close to the level anticrossing with the intention of studying the structure of Raman heterodyne signals. Because of the state mixing, some "forbidden" transitions ($\Delta m_s=1, \Delta m_l \neq 0$) appear in addition to the three allowed transitions ($\Delta m_s=1, \Delta m_l=0$). The forbidden transition clearly gains intensity at fields close to the level anticrossing.

In Raman heterodyne measurements, the dipole moments and the population factor of the two EPR levels involved determine the signal intensity, *i.e.*

$$I_S \sim \mu_{12} \mu_{13} \mu_{23} (P_2 - P_1). \quad (6-2)$$

The EPR transition matrix element, $\mu_{12} = \langle 1 | \mu_H | 2 \rangle$, where μ_H is the Y-axis component of magnetic dipole moment, and $|1\rangle$ and $|2\rangle$ are the wave functions of lower and higher EPR level, respectively, can be calculated by transforming the matrix of Eq.(1-14) into the representation in which the Hamiltonian of Eq.(1-11) becomes diagonal. The theoretical spectra were calculated by fixing the resonance at a particular RF frequency corresponding to the experimental value while finding the field strengths for which all the EPR resonances match that frequency. The results are shown by vertical lines in Fig. 6-2, which reflect the normalized magnetic coupling strengths. As optical pumping effects can significantly change the equilibrium populations, the measured signal intensities do not fit well to the calculated results of μ_{12} . Near the level anticrossing, the signal was found to disappear and this will be discussed in Section 6-3.

6-2-2. Lineshape: Dependence on Magnetic Field Orientation

The EPR spectra near the level anticrossing at different field orientations with respect to the

[111] axis were also measured in the range of -0.8° to 0.8° . Some of the results are shown in Fig. 6-3, where the magnetic field strength was fixed at 1019 G (9 G less than LAC), while the RF field was swept from 15 to 65 MHz. Only amplitude detection was employed and the RF field again was set in the low power regime.

As can be seen in Fig. 6-3, forbidden transitions are almost as significant as three allowed components because of the state mixing. When the field was aligned approaching the [111] axis from $\pm 0.8^\circ$, the EPR signal size was found to increase initially. At about $\pm 0.2^\circ$ the three allowed transitions were most clearly resolved and the signal magnitude was at a maximum. Then, further approaching the [111] axis caused a drop of the signal size associated with the $m_S = -1 \leftrightarrow 0$ ($m_I = -1, 0, +1$) transitions, and finally all three resonances collapsed when the field was exactly along the [111] axis.

The transition matrix elements μ_{12} were also calculated at various field misalignments and compared with the experimental traces. The results are plotted in Fig. 6-3 again using vertical lines. Some agreement is apparent but clearly it is not exact. For example, for misalignments greater than $\pm 0.2^\circ$, the middle line of the three allowed transitions is much weaker than the other two, while the calculated result shows that it is expected to be of equivalent to the other two allowed transitions. This again suggests that the population factor plays a role in the magnitude of Raman heterodyne signal and the details of the population distribution is not fully understood.

Figure 6-4 shows the EPR frequencies of three allowed resonances measured at different field orientations compared with the calculated results using the triplet Hamiltonian of Eq. (1-11). The parameters used were the same as those given above. A good correlation is evident between theory and experiment. This again confirms that the signals indeed arise from a 3A state.

6-3. COLLAPSE OF EPR AT THE LEVEL ANTICROSSING

The EPR signal was observed to decrease appreciably as the magnetic field closed to the

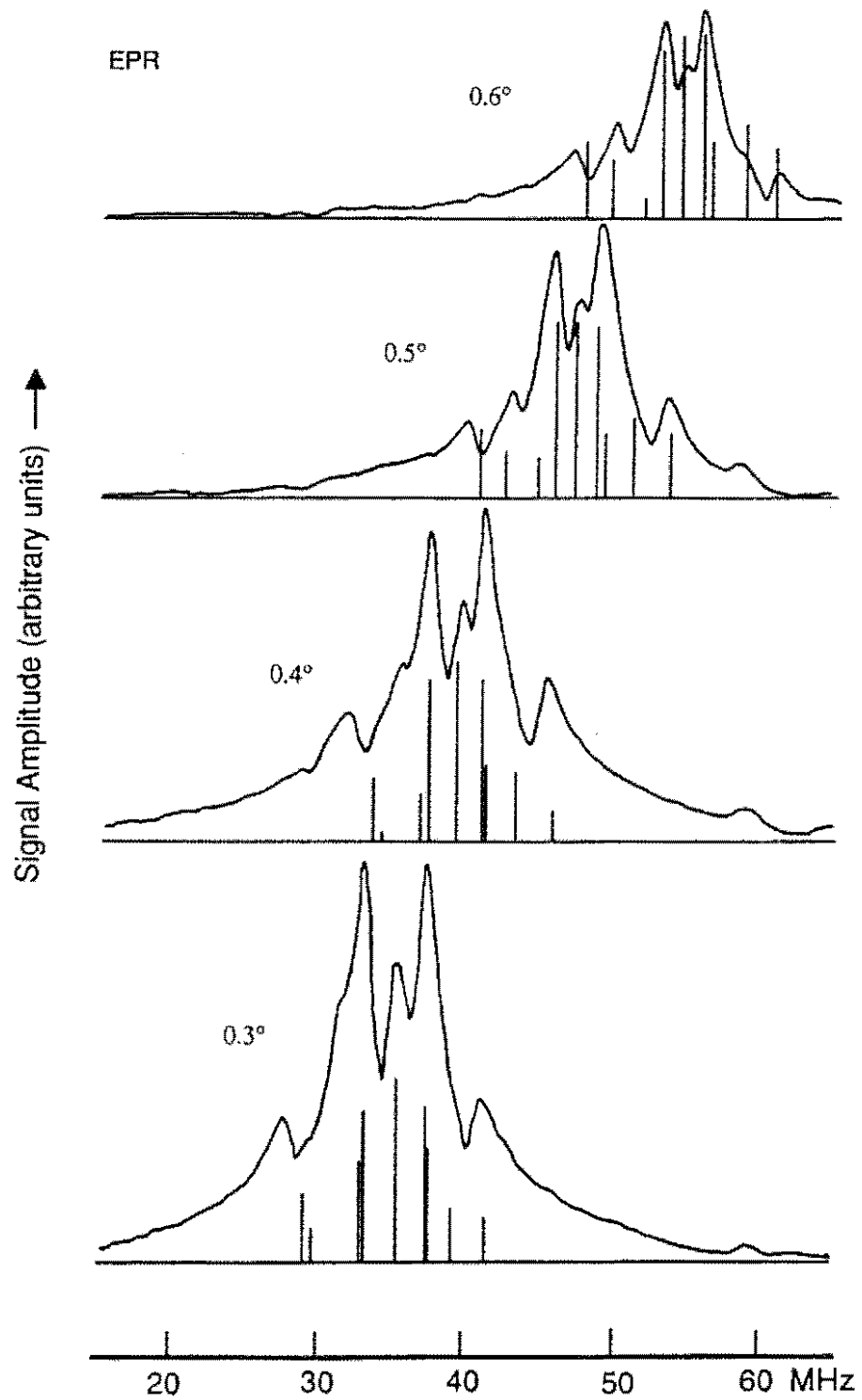


FIG. 6-3 EPR lineshapes measured at various field orientations relative to the [111] axis (curves) compared with the calculated transition matrix elements (vertical lines).

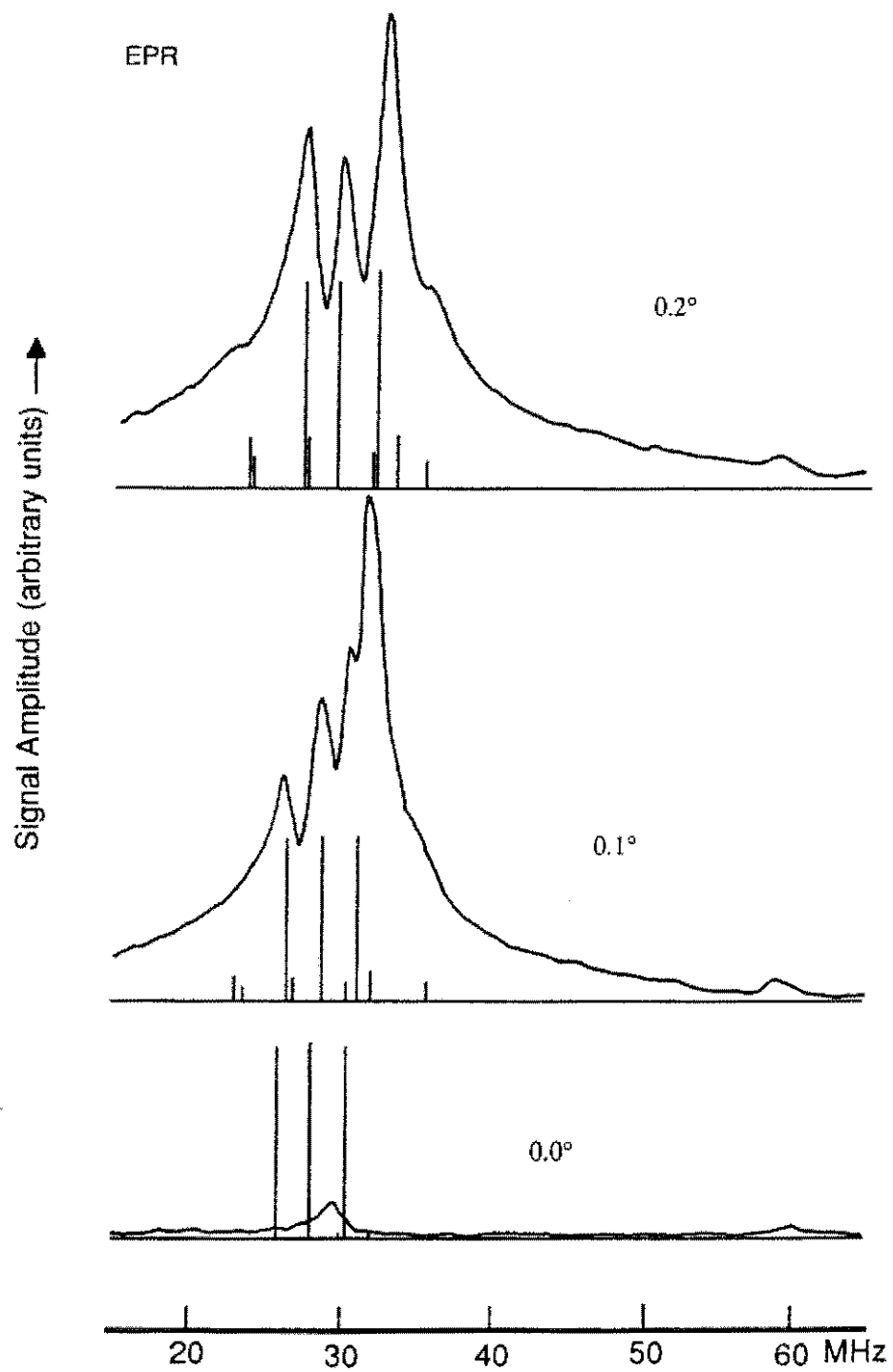


FIG. 6-3 (Continued)

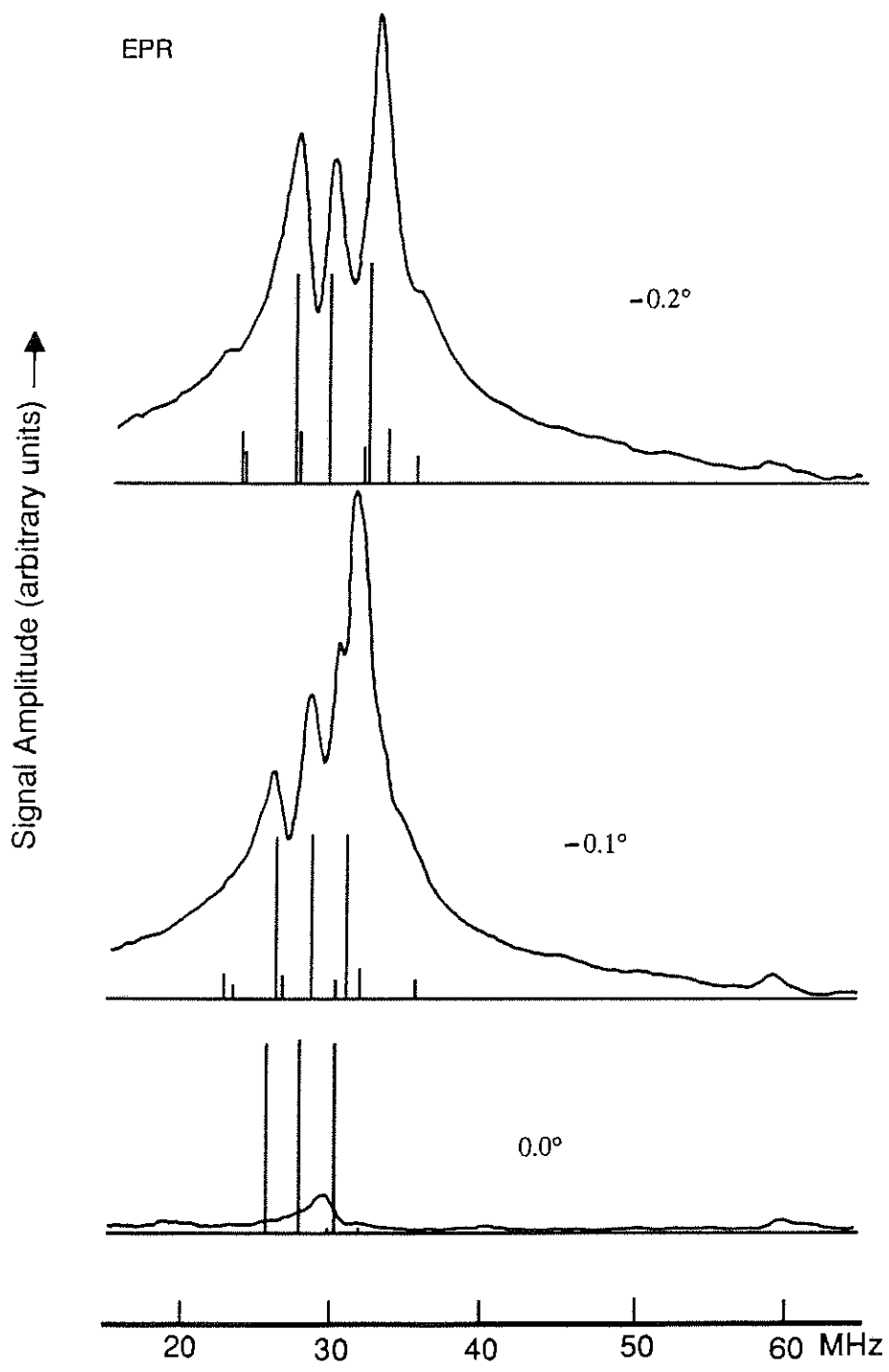


FIG. 6-3 (Continued)

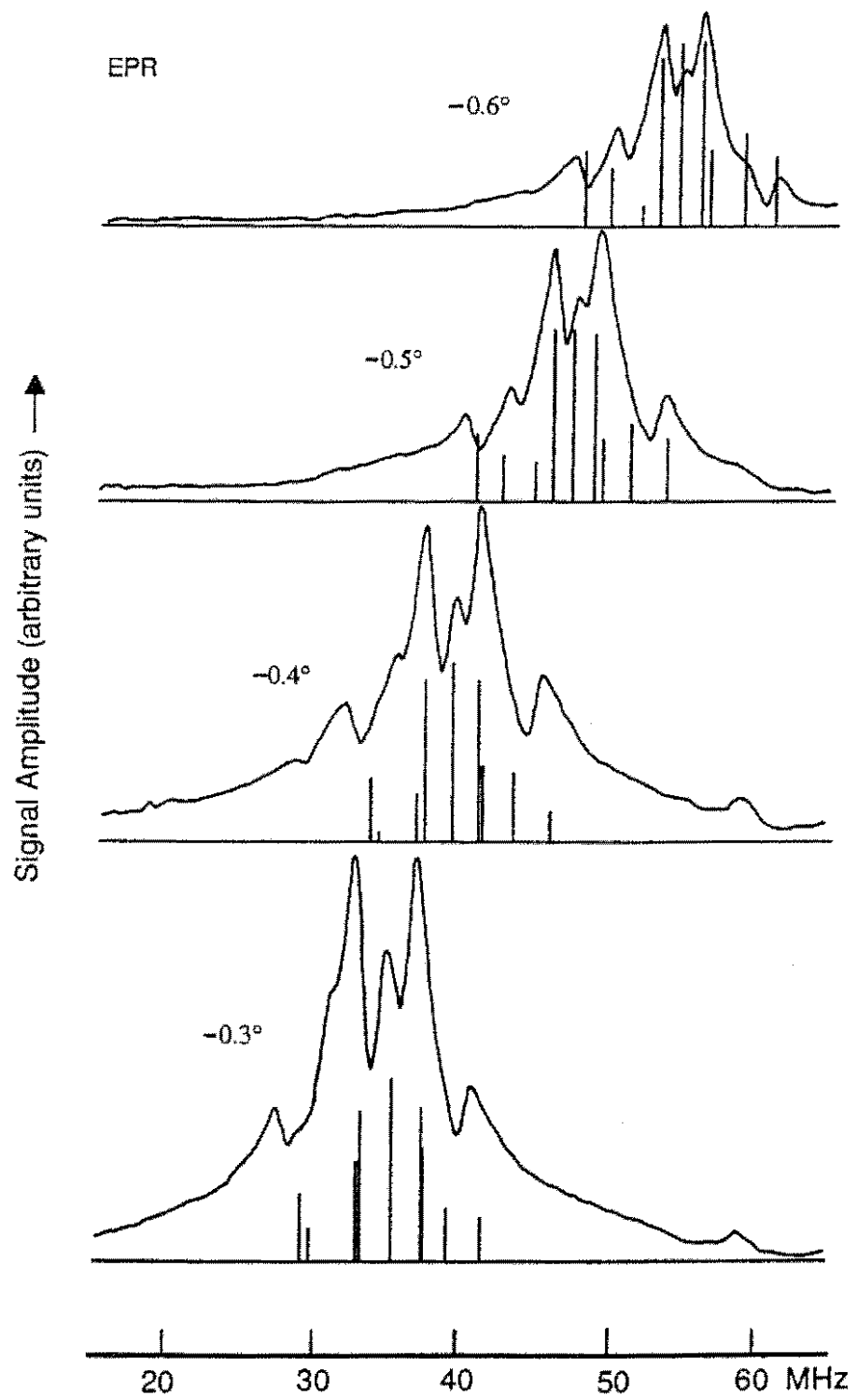


FIG.6-3 (Continued)

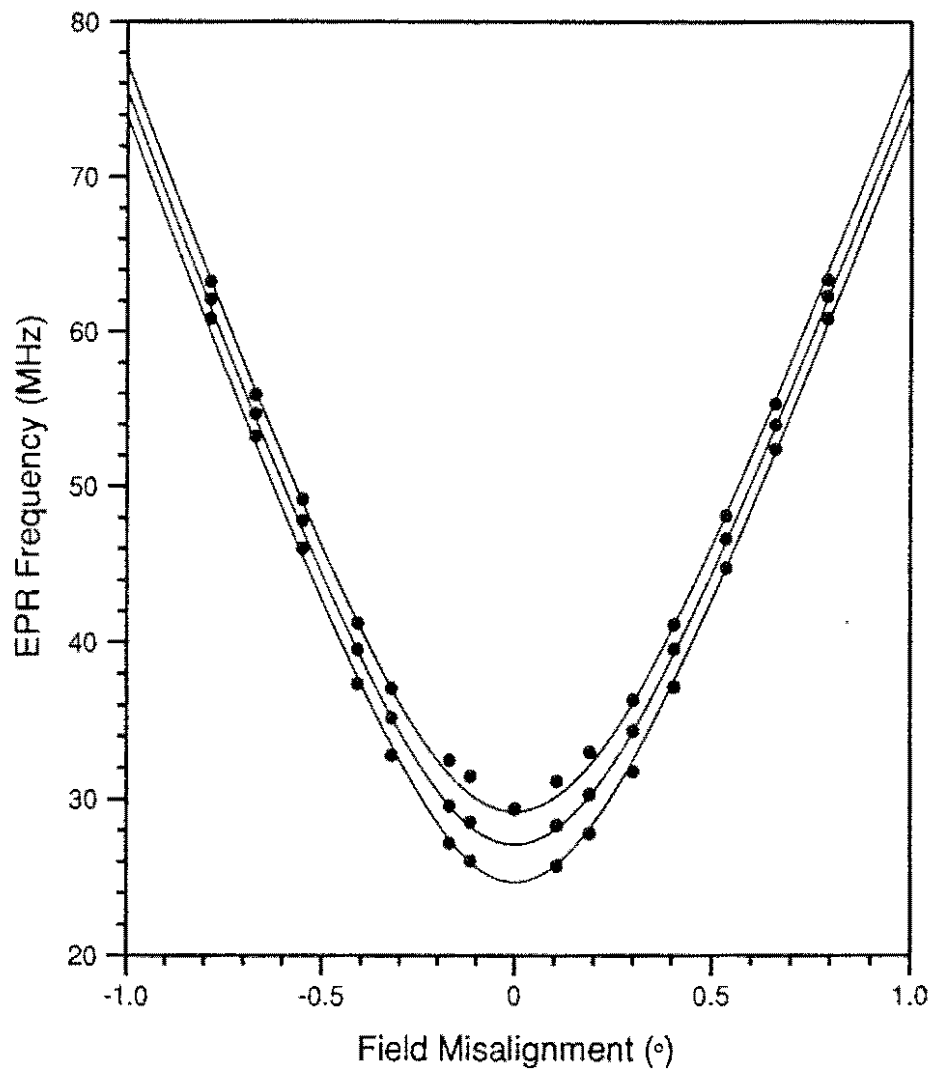


FIG. 6-4 Three EPR allowed transition frequencies (dots) measured at various field orientations with respect to the [111] axis compared with the results of a triplet Hamiltonian (solid curves).

level anticrossing (Fig.6-2). For RF frequencies from 30 to 52 MHz, theoretical values of the transition matrix elements only change by approximately 10% for the three allowed transitions. However, the signals were found to be greatly reduced at 30MHz and almost to disappear for RF frequencies less than 30 MHz. The EPR signal size as a function of magnetic field strength is plotted in Fig.6-5. For a magnetic field direction aligned to within a few degrees of the [111] axis, the EPR signal was found to disappear at the level anticrossing. As two EPR levels do not cross, the spin populations in the two levels will become equal due to state mixing and spin alignment when the static magnetic field approaches 1028 G. As a result, the population factor $P_2 - P_1$ vanishes (Table 6-1). This is likely to be the reason why the Raman heterodyne EPR signal always collapses at the anticrossing.

Observation of the RF power broadened lineshapes (Chapter 4) and Rabi oscillation (Chapter 9) have shown that the magnetic dipole moment of the EPR transition does not vanish at the anticrossing, being in agreement with the theoretical calculations of matrix elements. Spin echo measurements (Chapter 9) also indicated no evidence of change in the dephasing process near the anticrossing. In addition, no appreciable change was found in the optical transition at the level anticrossing. All of these factors suggest the population factor as being responsible for the collapse of the EPR signal.

From conventional EPR measurements, Loubser and van Wyk (1977) found that the spin alignment was independent of the magnetic field orientation. As a result, aligning the external field direction approaching to the [111] axis at a field strength other than 1028G will increase the population difference as well as the Raman heterodyne signal, as a consequence of decreasing the mixing between the $m_S=0$ and $m_S=-1$ states. This seems to be consistent with the experimental traces for the angles greater than $\pm 0.2^\circ$ as shown in Fig.6-3. The decrease of the Raman heterodyne signal for angles less than $\pm 0.2^\circ$ suggests that there exists a lower frequency limit, below which the signal collapses. Aligning the field approaching to the [111] axis locates the signal in such a range. This range is possibly due to spin fluctuations and a further investigation is desirable.

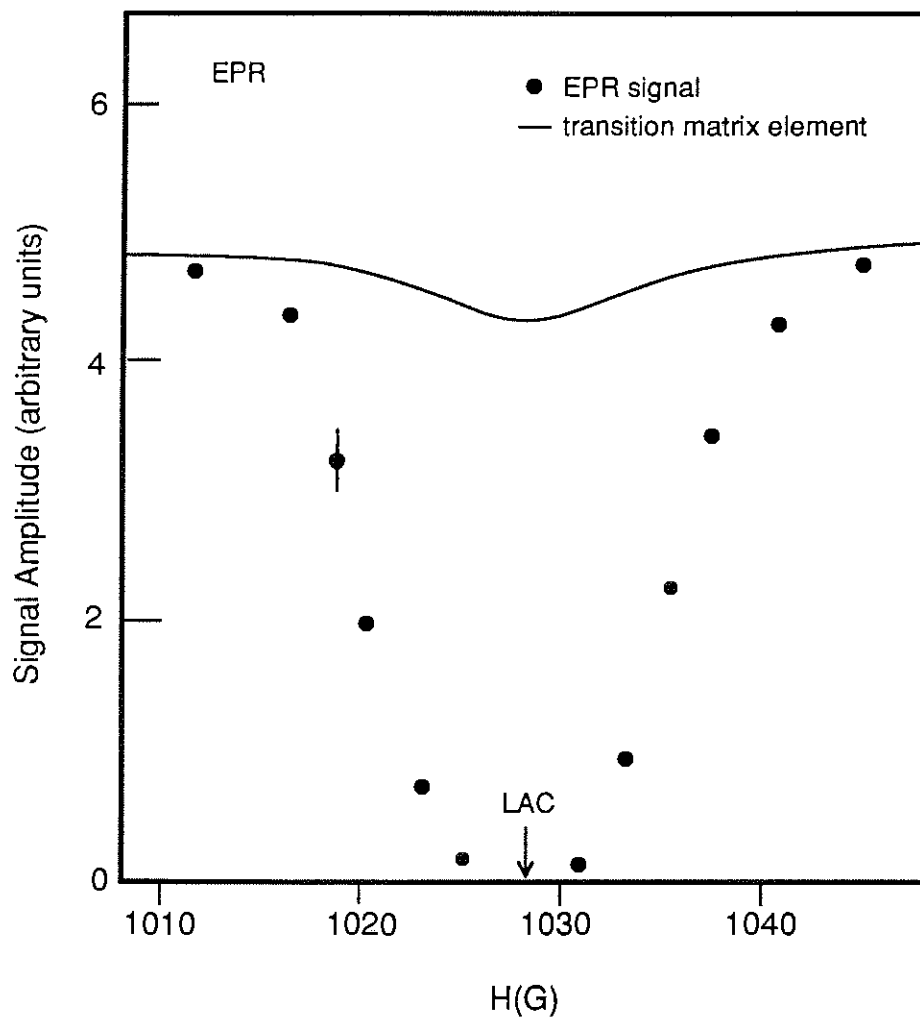


FIG. 6-5 The measured EPR signal amplitude as a function of magnetic field strength compared with the calculated transition matrix elements near the level anticrossing, showing the collapse of EPR signal at 1028 G. The range over which the EPR signal disappears depends on the crystal orientation.

6-4. ZERO-FIELD SPLITTING D

If the hyperfine structure is ignored, the Hamiltonian associated with the EPR interactions is given simply by the electronic Zeeman and crystal field interactions,

$$\mathcal{H}_0 = \mathcal{H}_Z + \mathcal{H}_{CF} . \quad (6-3)$$

When the magnetic field is along the $[111]$ axis, the Hamiltonian becomes,

$$\mathcal{H}_0 = (\gamma/2\pi)H S_z + D [S_z^2 - S(S+1)/3] . \quad (6-4)$$

For $D > 0$ the $m_s = \pm 1$ levels lie above the $m_s = 0$ level at the zero field and for $D < 0$ the $m_s = \pm 1$ levels lie below.

From the NMR and ENDOR measurements (Chapter 7), it is noted that the resonances associated with the $m_s = 0$ levels are stronger than those associated with the $m_s = -1$ levels. The greater strength of the resonances associated with the $m_s = 0$ levels is attributed to optical pumping which gives a greater population in the $m_s = 0$ levels than in the $m_s = -1$ levels. Taking this information into account with the observed absorptive and emissive EPR signals at low and high fields (Loubser and van Wyk 1977), it can be concluded that the $m_s = \pm 1$ levels lie above the $m_s = 0$ level at the zero field (Manson *et al.* 1990). That is the crystal field splitting D is positive,

$$D = +2.88 \text{ GHz.}$$

The energy levels of the triplet in the cases of $D > 0$ and $D < 0$, and the EPR spectra measured at 9.4 GHz corresponding to the experiment by Loubser and van Wyk (1977) are shown schematically in Fig.6-6, where the $m_s = 0$ level has a greater population than the other two levels.

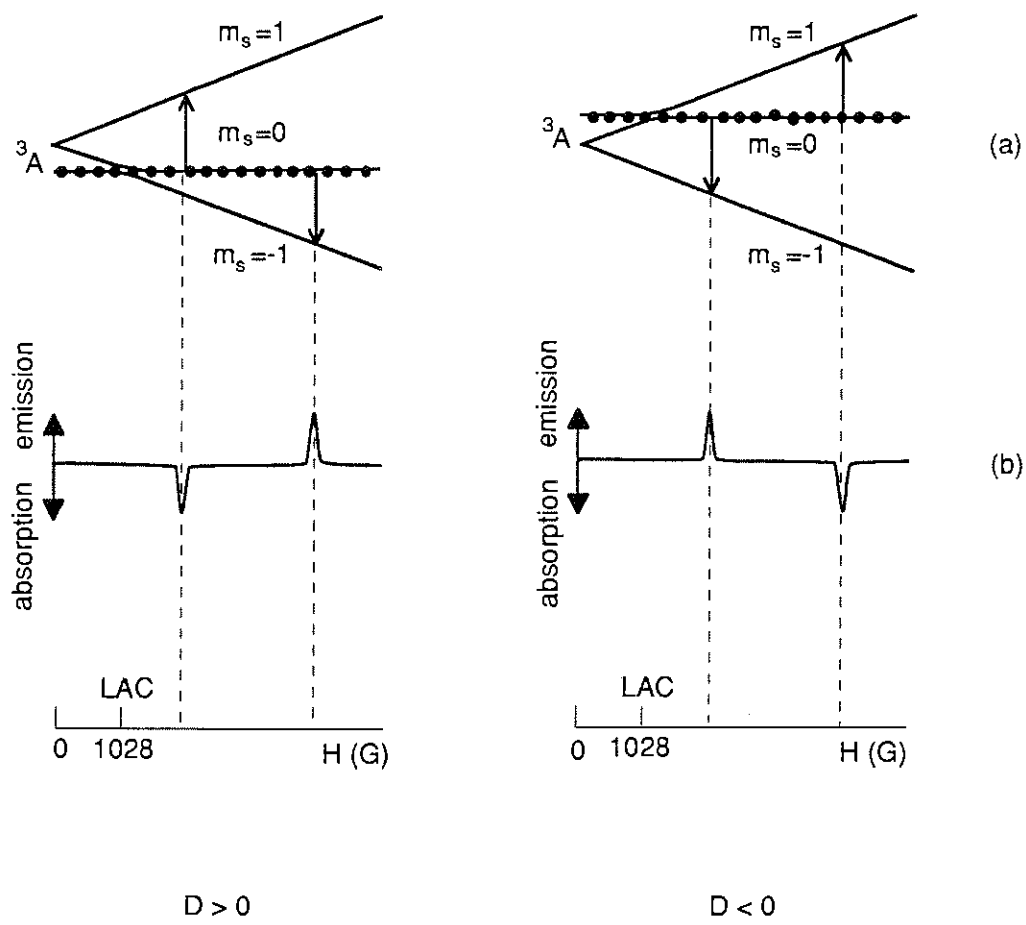


FIG. 6-6 Energy levels of the 3A ground state (a) and the corresponding EPR lineshapes measured at 9.4 GHz (Loubser and van Wyk 1977) (b) in the cases of $D > 0$ and $D < 0$, where the hyperfine interaction is not shown.

The origin of the zero-field splitting D is the purely direct electron spin-spin interaction and it has a value of (Lomer and Wild 1973),

$$D = \frac{3}{2} g^2 \beta^2 \frac{1}{r^3} \quad , \quad (6-5)$$

where r is the average separation of the components of the dipole-dipole interaction. Equation (6-5) then suggests that the two electrons are localized in the N-V centre with a separation of $r=3\text{\AA}$.

6-5. CONCLUSIONS

Raman heterodyne detected EPR signals at low and high field sides of the level anticrossing have shown a 180° phase difference. This is attributed to spin alignment in the ground state resulting from optical pumping. The result is consistent with the conventional EPR measurements by Loubser and van Wyk (1977). Taking into account the observation of NMR and ENDOR intensities (Chapter 7) with the result of absorptive and emissive EPR signals, it is concluded that the crystal field splitting D is positive ($D=+2.88$ GHz).

In level anticrossing studies, the EPR signals were measured at various field strengths and misalignments to the [111] axis. Calculations using a triplet Hamiltonian confirm that the signals arise from a 3A state. The theoretical transition matrix elements compared with the measured EPR signal intensities shows that optical pumping plays an important role in determining the Raman heterodyne signal magnitude.

The EPR signal was found to collapse at the level anticrossing (1028 G), which is interpreted in terms of equal populations in the two EPR levels due to the state mixing and spin alignment. This is substantiated by the RF power broadened lineshape (Chapter 4), Rabi oscillation and spin echo (Chapter 9) measurements. More detailed measurements in the

anticrossing regime suggest that there exists a range of the level separations within which the EPR signal disappears. Such a range is assumed to occur due to spin fluctuations.

Chapter 7

HYPERFINE AND NUCLEAR QUADRUPOLE INTERACTIONS

Raman heterodyne techniques provide a sensitive and precise method to investigate the magnetic hyperfine and nuclear electric quadrupole interactions in the 3A ground state of the N-V centre. The NMR and ENDOR measurements that have been demonstrated (He *et al.* 1991a, Manson *et al.* 1990) were used to probe the magnetic resonances within the triplet at various magnetic field strengths and orientations. Consequently, the hyperfine and quadrupole parameters in the Hamiltonian of Eq.(1-5) were determined. Interesting properties such as the spin density distribution in the N-V centre can be obtained from the hyperfine interaction parameters. On the other hand, because the signal intensity is associated with both the magnetic dipole moment and the population factor, optical pumping effects on the Raman heterodyne signals can be examined by comparing the signal intensity with the transition matrix element.

Hole burning techniques (Manson and Silversmith 1987) were also employed as a complement to study the hyperfine and quadrupole interactions. When an additional strong RF field is introduced into the Raman heterodyne EPR measurement, it saturates the absorption of a subgroup of N-V centres in the magnetically inhomogeneous distribution. In consequence, one observes holes and/or antiholes in the EPR spectra. The hole or antihole structure is helpful for a further understanding of the nuclear spin levels and their population distribution.

The Hamiltonian associated with the nuclear spin transitions is given by the magnetic hyperfine, nuclear Zeeman and nuclear electric quadrupole interactions (Chapter 1),

$$\mathcal{H}_0 = \mathcal{H}_{\text{HF}} + \mathcal{H}_{\text{Zn}} + \mathcal{H}_{\text{Q}} \quad (7-1)$$

If the magnetic field is aligned along the [111] axis, Eq.(7-1) becomes,

$$\mathcal{H}_0 = A_{\parallel} S_z I_z + A_{\perp} (S^+ I^- + S^- I^+) / 2 - (\gamma_n / 2\pi) H I_z + P [I_z^2 - I(I+1)/3] \quad (7-2)$$

When the field magnitude is set far away from the level anticrossing, the states are less mixed and the eigenvalues of Eq.(7-2) can be calculated analytically. In this case, the magnetic transition frequencies are given by,

$$\omega / 2\pi = \pm (\gamma_n / 2\pi) H + |P| (\pm A_{\parallel}) \quad \Delta m_I = \pm 1, \quad (7-3a)$$

$$\omega / 2\pi = 2(\gamma_n / 2\pi) H (+ 2 |A_{\parallel}|) \quad \Delta m_I = \pm 2, \quad (7-3b)$$

where the parentheses apply only to the $m_S = -1$ multiplet. Therefore, the measurements of NMR or ENDOR frequencies give the hyperfine and quadrupole parameters A_{\parallel} , A_{\perp} and P . When the magnetic field is close to the level anticrossing, however, the states are strongly mixed and the transition frequencies can only be obtained numerically by diagonalizing the matrix of Eq.(1-11).

7-1. NMR AND ENDOR MEASUREMENTS

By scanning the RF frequency in the range of 0~8 MHz, in which all NMR lines are expected to be located, one can observe several nuclear spin transitions within the $m_S = 0$ and the $m_S = -1$ states (He *et al.* 1991a, Manson *et al.* 1990). The results are shown in Figs.7-1 and 7-2, which were obtained at various field strengths and directions with respect to the [111] axis. In order to

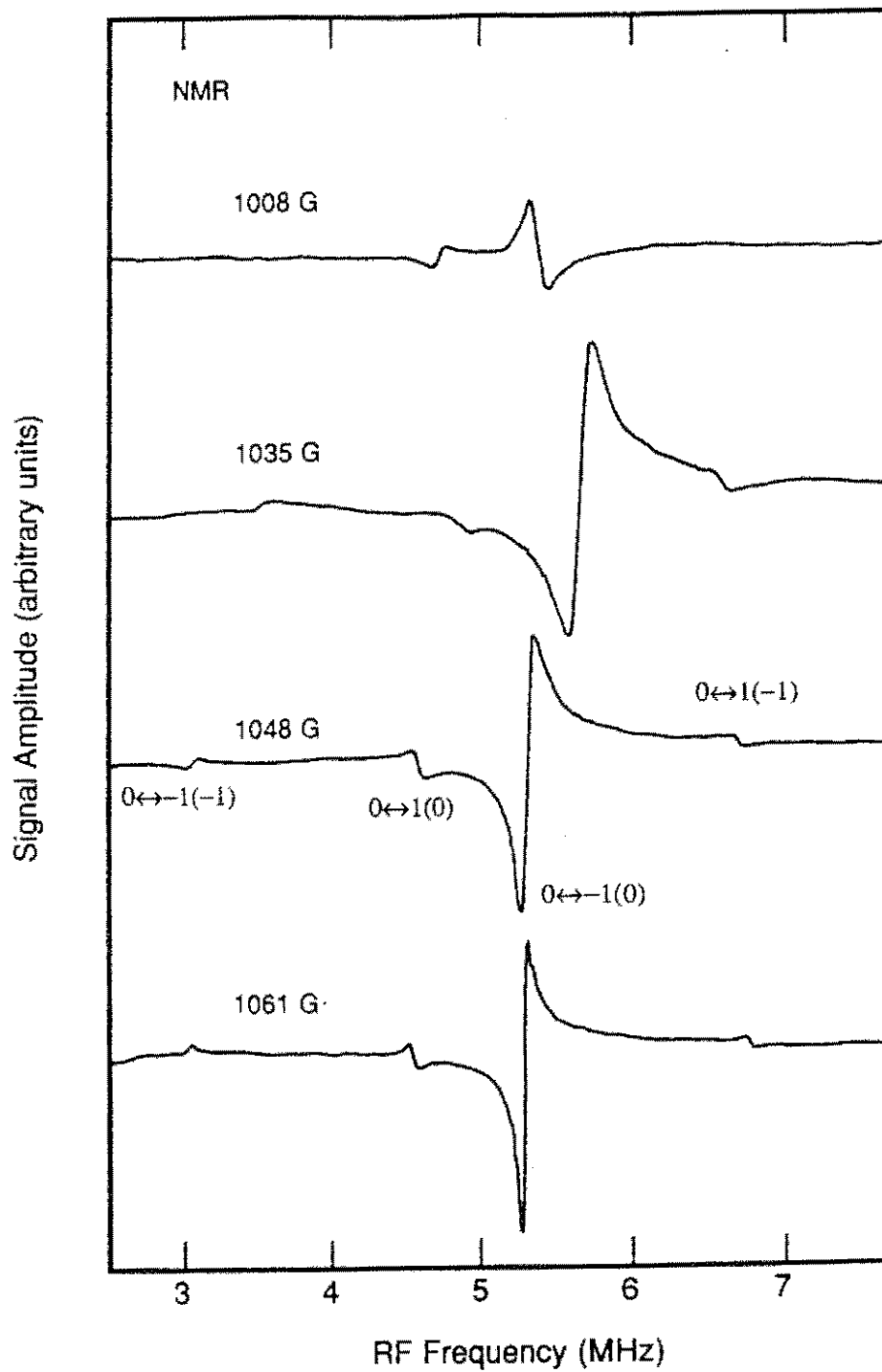


FIG. 7-1 The NMR spectra showing four allowed transitions in the $m_s=0$ and $m_s=-1$ states of the 3A measured at various magnetic field strengths.

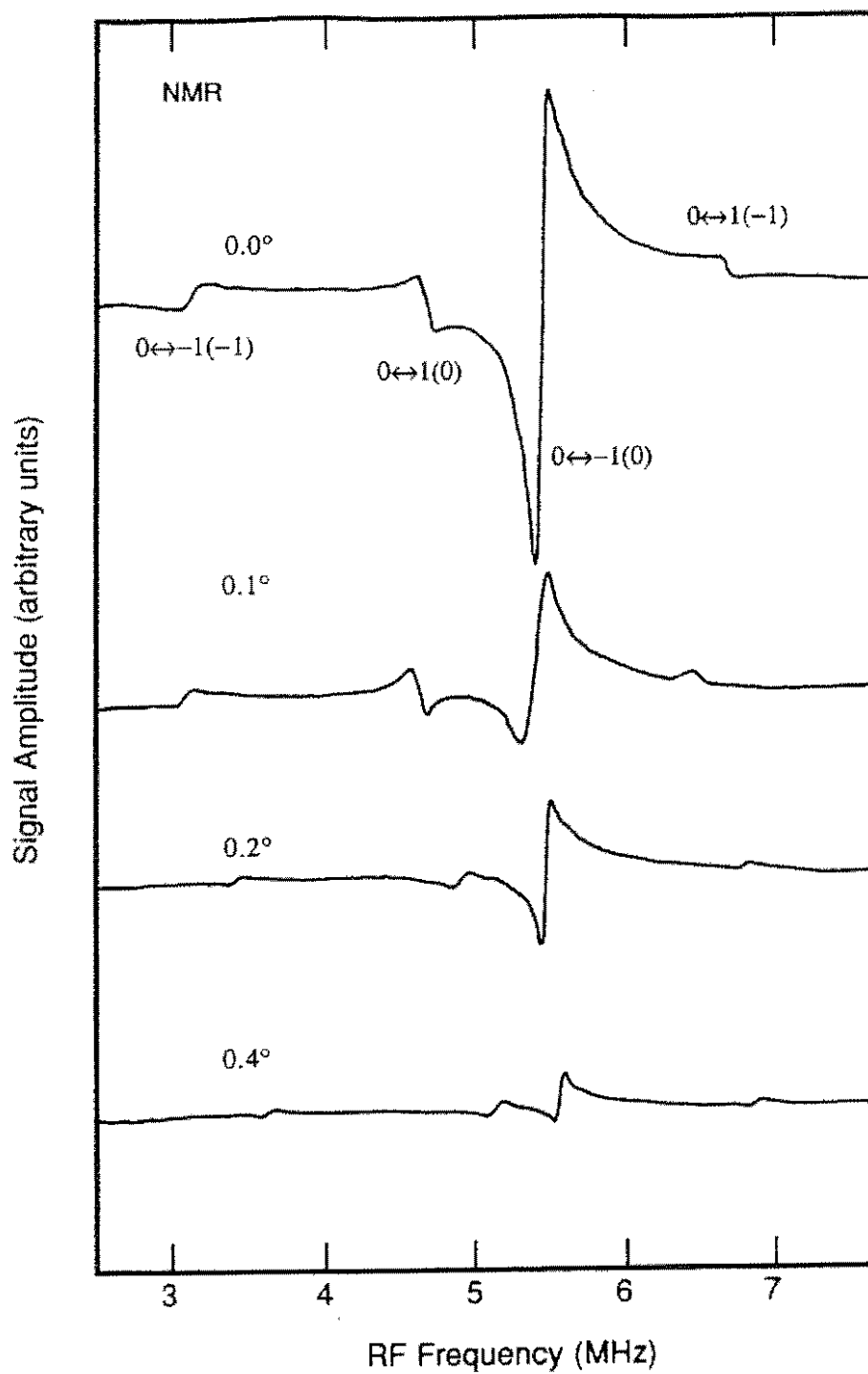


FIG. 7-2 The NMR spectra measured at various magnetic field directions with respect to the [111] axis at a field of 1042 G.

bring out the weak structure, a strong RF was used. Line broadening is not a concern in this situation for we are interested only in the NMR frequencies and the resonance frequencies are found not to be affected by the RF power. For the sake of easy measurements, dispersive phase detection was employed. There are four observable NMR lines, all being allowed transitions. The strongest one at 5.56 MHz is due to the $m_I=0 \leftrightarrow -1$ ($m_S=0$) transition, which has been analyzed and discussed in detail in Chapter 4.

The ENDOR measurements were carried out by introducing an additional RF, which was swept in the range of 0-8 MHz while monitoring an EPR line (see Chapter 5). Figures 7-3 and 7-4 illustrate some of the ENDOR traces measured at various magnetic field strengths and directions with respect to the [111] crystallographic axis. In the measurements, the signals were obtained by monitoring the second peak of the EPR spectra, *i.e.* the $m_S=0 \leftrightarrow -1$ ($m_I=0$) transition.

In contrast to the NMR case, the two forbidden transitions appear in the ENDOR spectra in most cases in addition to the four allowed transitions. Because of the overlap of EPR signals, it is not possible to monitor a single electronic spin transition and the ENDOR signal arises from the RF affecting several overlapping EPR lines. We found that the ENDOR signals were observable in a much larger range of field strengths around the level anticrossing than the NMR signals. This is simply due to the larger range where the EPR signal is detectable.

The resonances observed in the experiments are listed in Table 7-1 and the corresponding magnetic transitions within the 3A state are illustrated in Fig. 7-5 with resonance frequencies at a field of 1048 G. The two forbidden transitions were not observed in the NMR, while they were found to be detectable in both ENDOR and hole burning experiments, the latter of which will be discussed in Section 7-2.

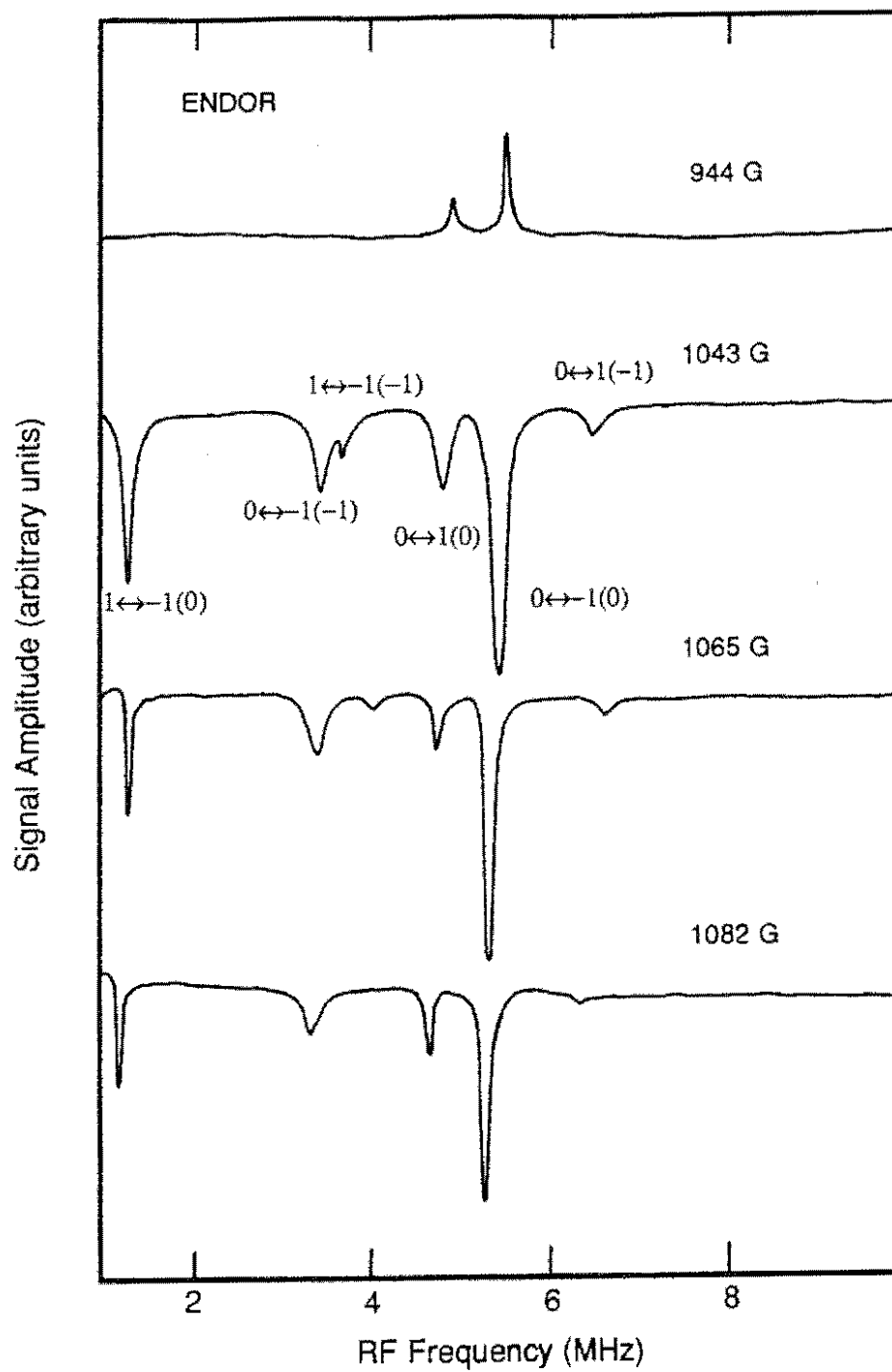


FIG. 7-3 The ENDOR spectra measured at various magnetic field strengths, where all six nuclear spin transitions in the $m_s=0$ and $m_s=-1$ states are observed.

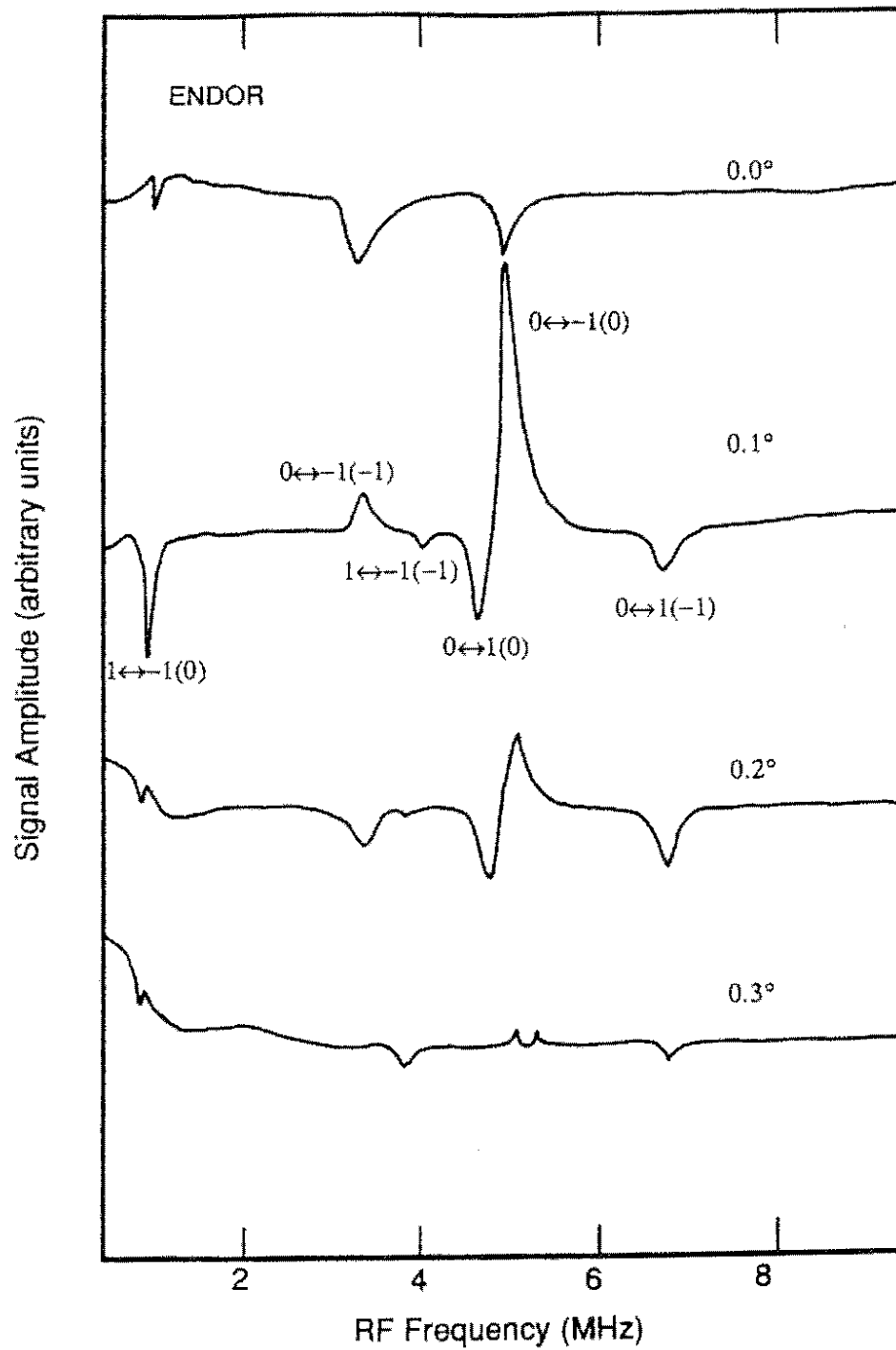


FIG. 7-4 The ENDOR spectra obtained at various magnetic field directions with respect to the [111] axis, where the magnetic field strength is 1019 G.

TABLE 7-1 Nuclear spin transitions in the 3A ground state observed using the Raman heterodyne measurements.

Transition	Frequency at 1048 G (MHz)	Observation
$m_I=1 \leftrightarrow -1$ ($m_S=0$) ^a	0.6	ENDOR, HB ^b
$m_I=0 \leftrightarrow -1$ ($m_S=-1$)	3.2	ENDOR, HB, NMR
$m_I=-1 \leftrightarrow 1$ ($m_S=-1$) ^a	3.8	ENDOR, HB
$m_I=0 \leftrightarrow 1$ ($m_S=0$)	4.7	ENDOR, HB, NMR
$m_I=0 \leftrightarrow -1$ ($m_S=0$)	5.3	ENDOR, HB, NMR
$m_I=0 \leftrightarrow 1$ ($m_S=-1$)	7.0	ENDOR, HB, NMR

^a Forbidden transitions

^b HB: hole burning

7-1-1. Determination of Hyperfine and Quadrupole Parameters

Figures 7-6 and 7-7 plot the NMR frequencies as a function of magnetic field strength and direction with respect to the [111] axis. The dots are experimental data and the curves are the best-fits calculated using the Hamiltonian of Eq.(1-11). For field strengths less than 1028 G (LAC) only two NMR transitions were observed.

The ENDOR frequencies as a function of magnetic field strength and orientation are shown in Fig.7-8 and 7-9, again compared with the calculated results using a 3A Hamiltonian. As can be seen in Figs. 7-6 to 7-9, the experimental data are in good agreement with the triplet Hamiltonian. This is additional evidence that the 3A is indeed the ground state of the N-V centre.

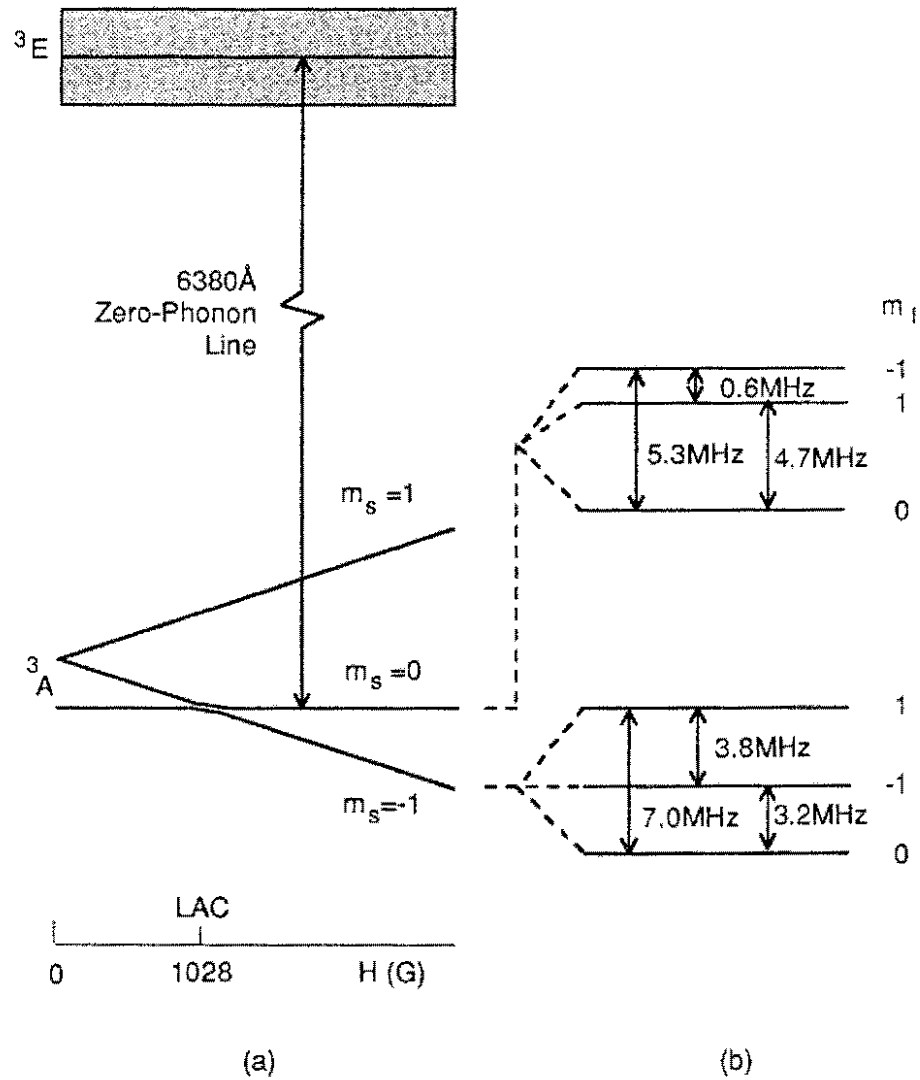


FIG. 7-5 All nuclear spin transitions in the $m_s=0$, and -1 states of the triplet. (a) Energy level splitting in the magnetic field where the hyperfine sub-levels are not shown. (b) Hyperfine levels and associated transitions with resonance frequencies at 1048 G.

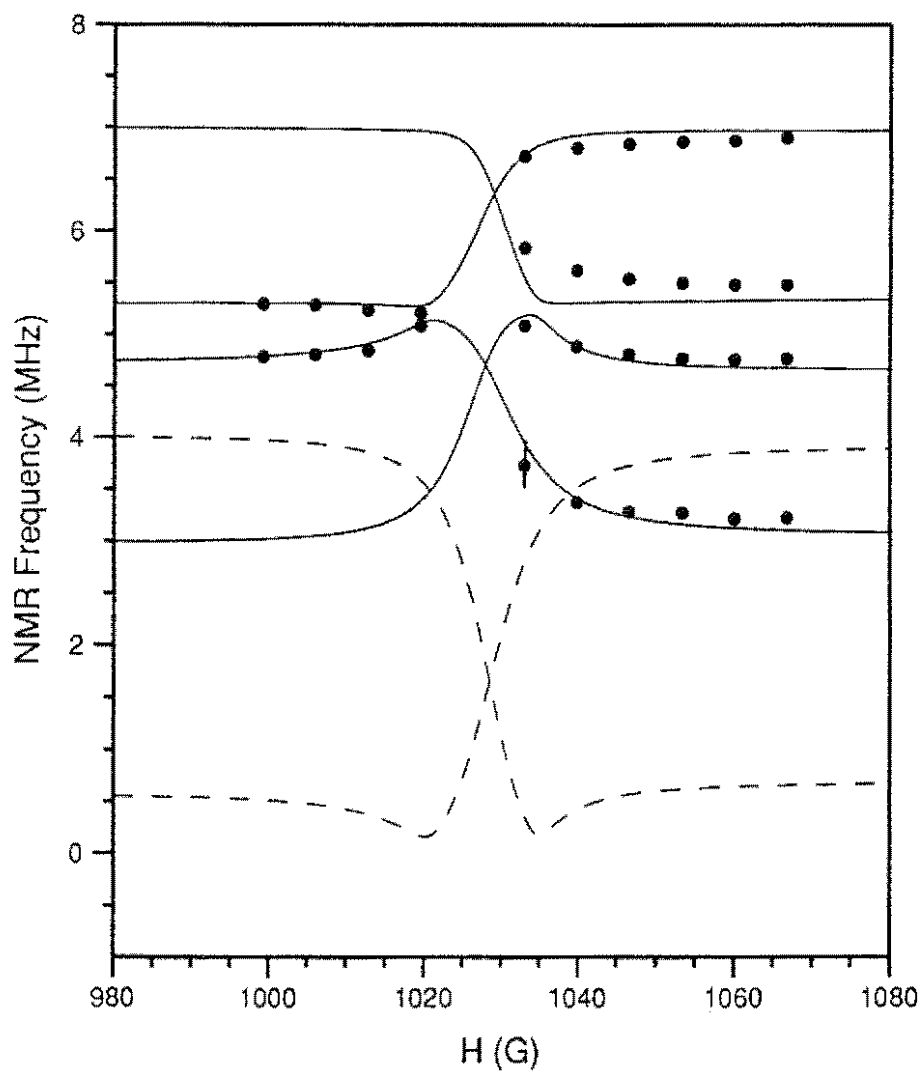


FIG. 7-6 Experimental NMR frequencies (dots) compared with theoretical calculations (curves) at various magnetic field strengths. Solid curves: allowed transitions. Dashed curves: forbidden transitions.

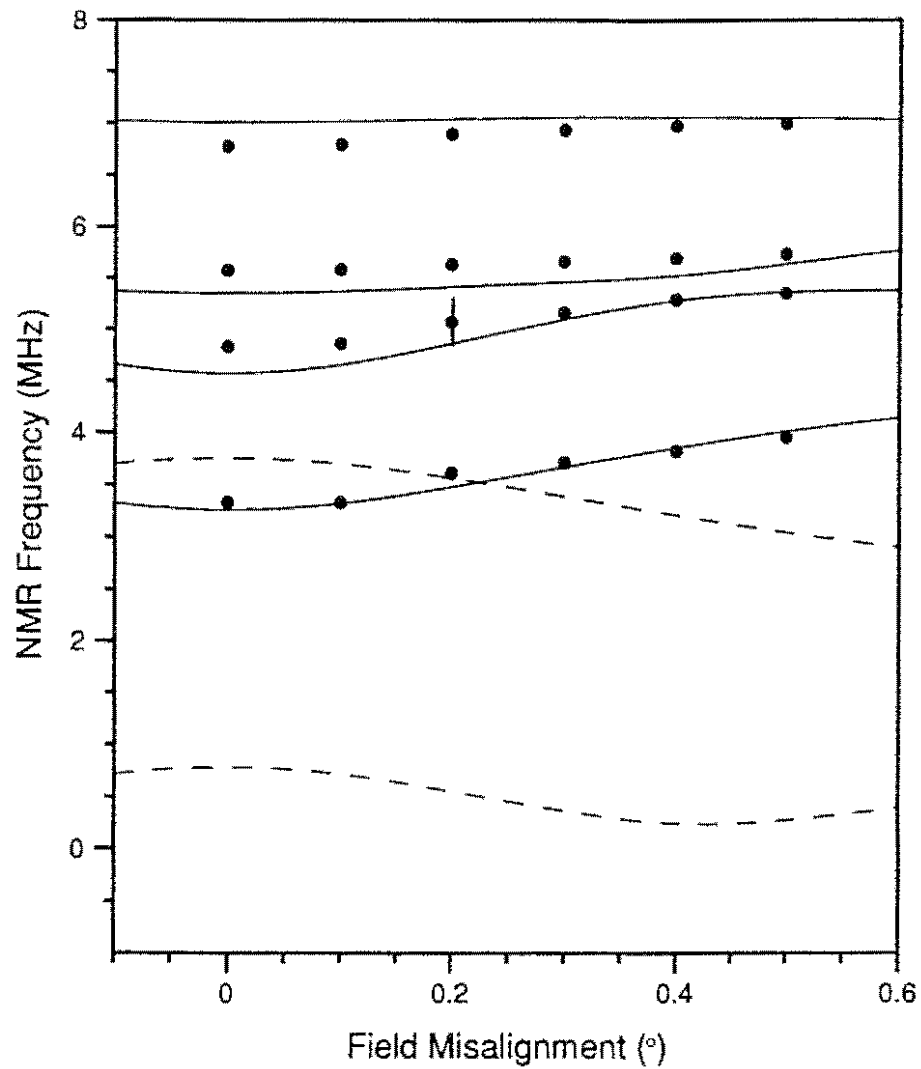


FIG. 7-7 Experimental NMR frequencies (dots) compared with theoretical results (curves) at various magnetic field directions with respect to the [111] axis at a magnetic field of 1042G. Solid curves: allowed transitions. Dashed curves: forbidden transitions.

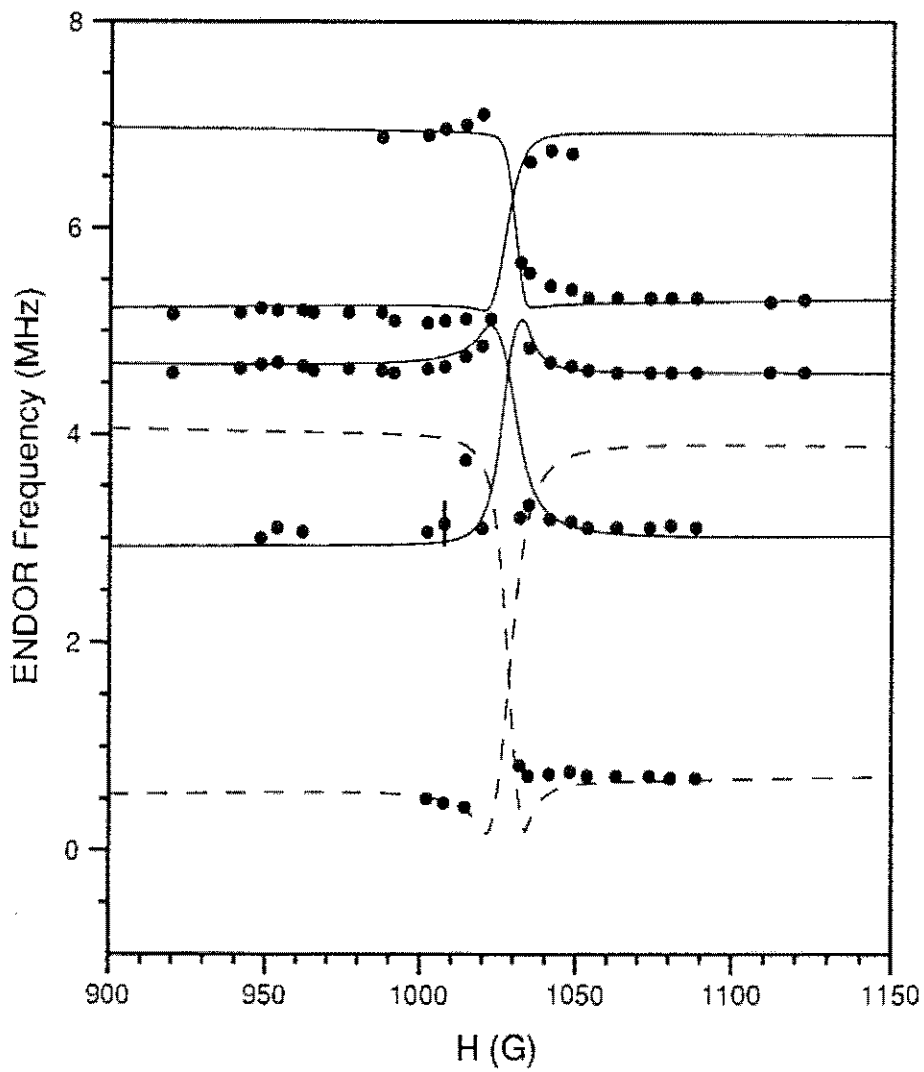


FIG. 7-8 Experimental ENDOR frequencies (dots) compared with theoretical results (curves) as a function of magnetic field strength. Solid curves: allowed transitions. Dashed curves: forbidden transitions.

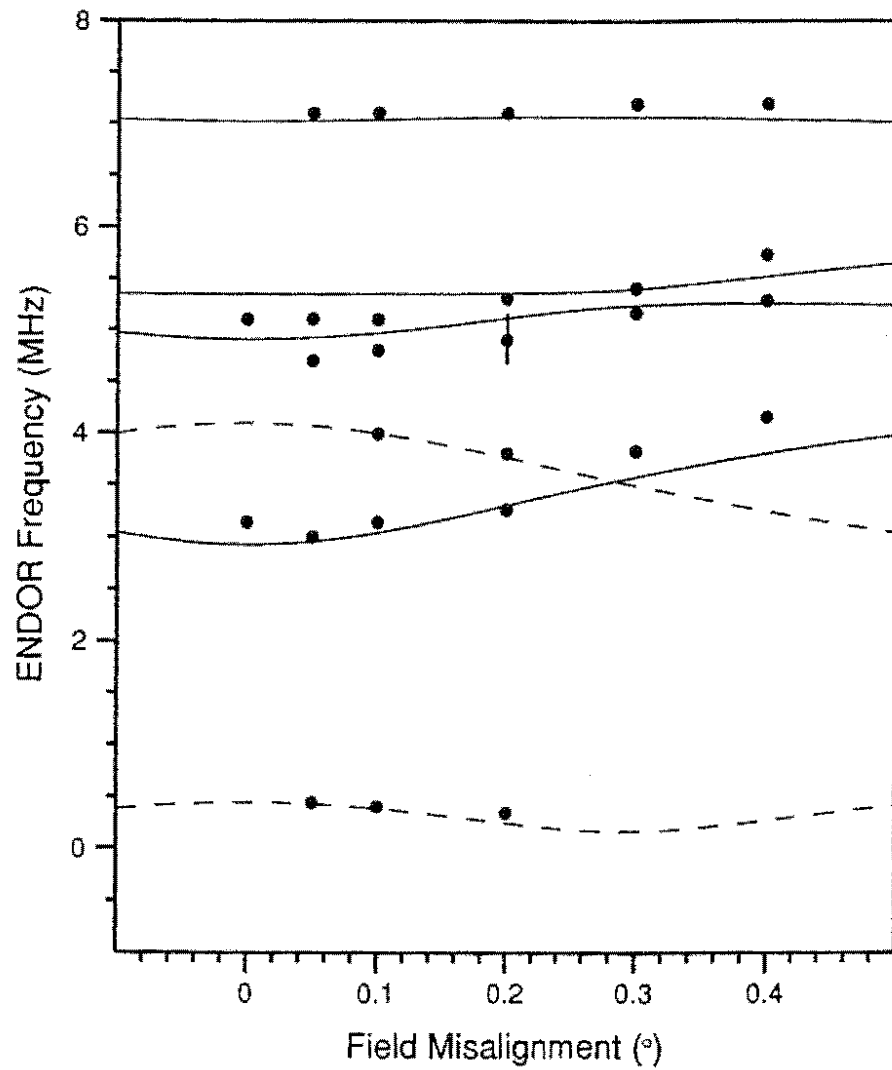


FIG. 7-9 Experimental ENDOR frequencies (dots) compared with theoretical calculations (curves) at a magnetic field of 1019 G at various field misalignments to the [111] axis. Solid curves: allowed transitions. Dashed curves: forbidden transitions.

The calculations were performed by diagonalizing the Hamiltonian matrix of Eq.(1-11) with corresponding experimental values of the magnetic field strengths and directions. By adjusting the parameters $A_{//}$, A_{\perp} and P (the values of D , γ and γ_n were fixed in the calculations) the best-fit traces were obtained. In Table 7-2 the hyperfine and quadrupole parameters determined from the experiments are listed and compared with previous results. The sign of D has been determined to be positive as discussed in Chapter 6.

TABLE 7-2 Zero-field splitting, hyperfine and quadrupole parameters of the 3A ground state determined from experiments.

	D (GHz)	$ A_{//} $ (MHz)	$ A_{\perp} $ (MHz)	$ P $ (MHz)
This Study	$+2.880 \pm 0.005^a$	2.30 ± 0.02	2.10 ± 0.10	5.04 ± 0.05
Previous Results	$\pm 2.880 \pm 0.005^{b,c,d}$	2.30 ± 0.03	—	—

^a Only sign determined in this study

^b Loubser and van Wyk (1977)

^c Bloch *et al.* (1985)

^d Reddy *et al.* (1987)

The magnitude of zero-field splitting D was first determined using conventional EPR spectroscopy (Loubser and van Wyk 1977), and later confirmed by RF-optical excitation (Bloch *et al.* 1985b) and two laser hole burning (Reddy *et al.* 1987) experiments. The magnitude of $A_{//}$ was also measured by Loubser and van Wyk (1977) from the hyperfine splittings in the EPR spectra. However, A_{\perp} and P were not previously determined. For our experimental setups, the NMR and ENDOR spectra were relatively insensitive to A_{\perp} , therefore it has lower accuracy.

7-1-2. Transition Intensity

In the NMR spectra, it was found that the $m_I=0 \leftrightarrow -1 (m_S=0)$ transition was much stronger than the others, particularly compared to the $m_I=0 \leftrightarrow 1 (m_S=0)$ transition within the same $m_S=0$ state. As has been already noted in Chapter 6, the Raman heterodyne intensity does not depend only on the dipole moment. Instead, the signal magnitude in the low RF power regime is linear in the triple factors, $\mu_{12}\mu_{23}\mu_{31}$, and the population difference, P_1-P_2 , between two levels involved (see Eq.(6-2)), and the latter can be disturbed significantly by optical pumping effects.

By transforming the magnetic dipole moment matrix of Eq.(1-14) into the representation in which the Hamiltonian is diagonal, the matrix elements for NMR transitions can also be obtained. The calculations show that the magnitudes of μ_{12} for the four allowed transitions ($\Delta m_I = \pm 1$) are the same at most field strengths within an error of $\sim 10\%$.

The magnitude of a matrix element can be quantitatively measured using the Autler-Townes effect (see Chapter 8). The Autler-Townes splitting occurs when one of the levels involved in a transition is coupled to a third level by a second (perturbing) RF field. The splitting is equal to the Rabi frequency of the transition driven by the second RF. Therefore, by introducing an additional RF field, one not only can distinguish the levels involved in an NMR transition but also can establish the dipole moment of a particular transition by measuring the amount of splitting. Using this technique in Chapter 8, we have confirmed the labelling of the four NMR lines, as indicated in Table 7-1. Keeping the perturbing RF power unchanged, we found that the $m_I=0 \leftrightarrow -1 (m_S=0)$ and $m_I=0 \leftrightarrow 1 (m_S=0)$ transitions had the same amount of splitting. This indicates that their dipole moments μ_{12} are the same, being in agreement with the calculations. In the NMR measurements, however, the former was observed with a much greater strength (by a factor of 5~20) compared with the latter. As no appreciable change in the dipole moments associated with the optical transitions is expected, the varying Raman heterodyne signal size can thus be attributed to the population factor.

The transitions associated with the $m_s = 0$ state were found to be stronger than those within the $m_s = -1$ state in most cases, as can be seen in Figs. 7-1 to 7-4. In addition, for field strengths less than 1028 G only the two allowed transitions in the $m_s = 0$ state were observed in the NMR. This is attributed to the spin alignment in the 3A state and therefore the $m_s = 0$ levels are more highly populated than the $m_s = -1$ levels, resulting in the greater transition intensities.

It was also noted that when the field was exactly aligned along the [111] axis at a field of 1019 G, the ENDOR signals were still detectable (Fig. 7-4), whereas the Raman heterodyne EPR signal almost disappeared (Fig. 6-3). This phenomenon supports the interpretation for the collapse of EPR signal as a consequence of equal populations in the two electron spin levels. The application of the second RF field altered the populations within the hyperfine sub-levels so that the EPR signal was greatly modified and became detectable in the ENDOR measurements.

7-2. HOLE BURNING

When an additional strong RF is introduced into the EPR measurement, it selects a subgroup of N-V centres within the inhomogeneous distribution and saturates its absorption. This results in holes or antiholes in the EPR spectra probed by sweeping the first RF of a relatively low power (Manson and Silversmith 1987).

Figure 7-10 shows two typical hole burning spectra in the EPR, where the second RF was tuned to 42 MHz and 50 MHz respectively, indicated by arrows, and the first RF was swept from 40 to 50 MHz. The holes are 4.9 and 5.2 MHz away from the burning RF in both cases, giving the hyperfine level separations in the $m_s = 0$ state.

The population hole burning processes corresponding to Fig. 7-10 are illustrated in Fig. 7-11. Due to the state mixing, the saturating RF field could drive a forbidden EPR transition. In trace (b) of Fig. 7-10, the second RF at 42 MHz depleted the population in the $m_f = -1 (m_s = -1)$ level

Hole Burning in EPR

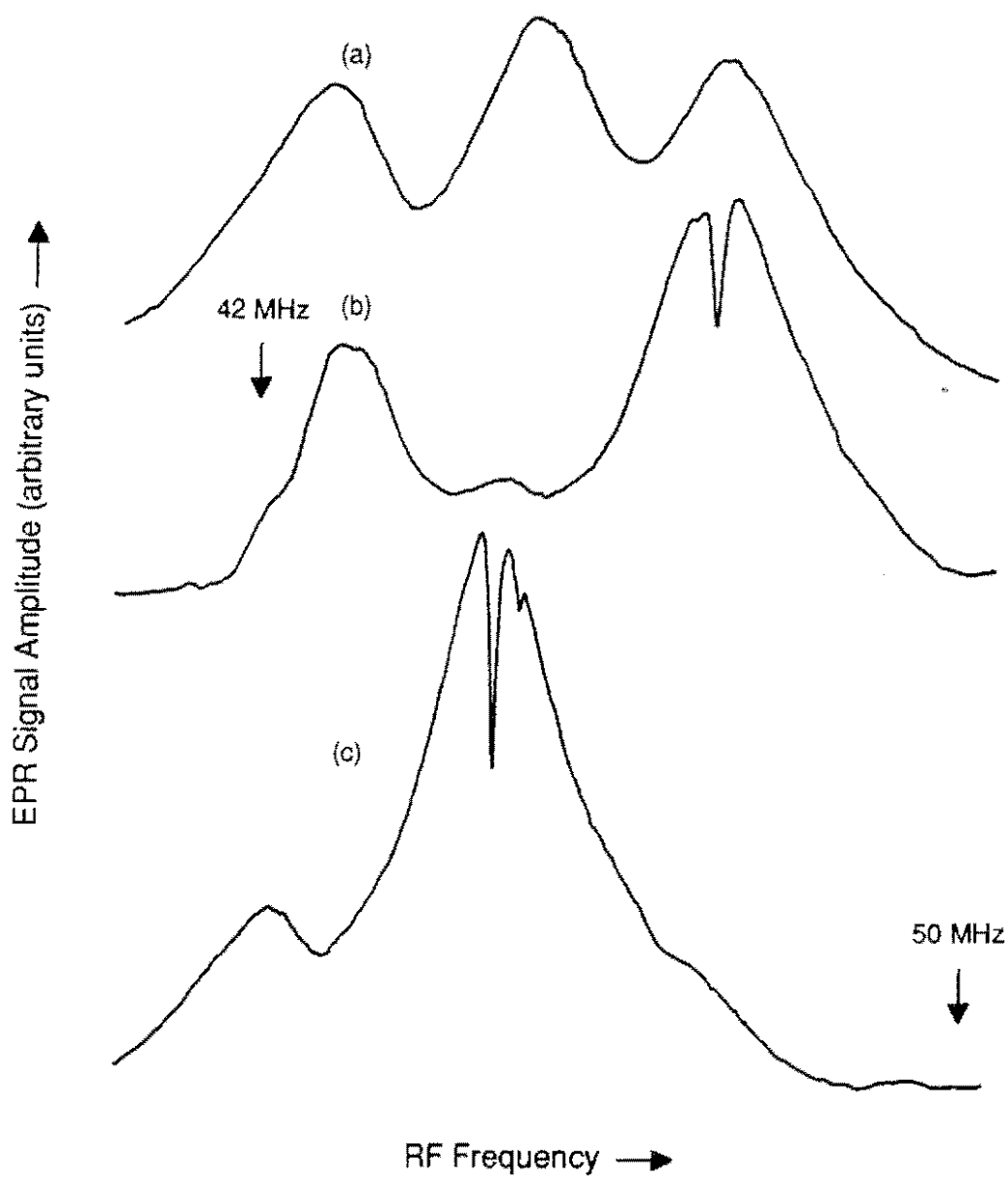


FIG. 7-10 The unperturbed EPR signals (a) and the hole burning effects in the Raman heterodyne detected EPR spectra with a second RF field (arrows) at 42 MHz (b) and 50 MHz (c), respectively.

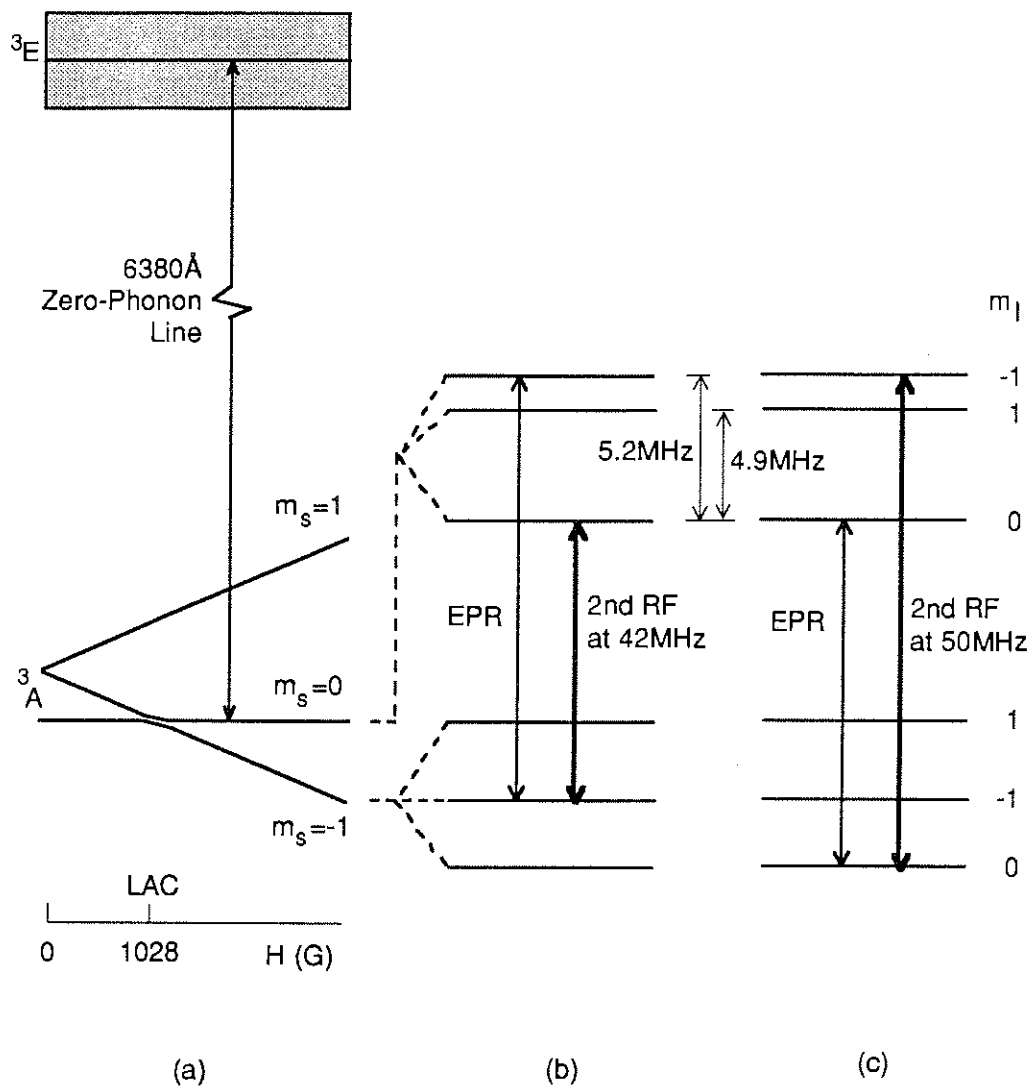


FIG. 7-11 Energy levels and hole burning processes corresponding to Fig. 7-10. (a) Level splitting where the hyperfine interaction is not shown. (b) and (c) The hole burning processes corresponding to the trace (b) and (c) in Fig. 7-10.

and a hole appeared, at 5.2 MHz relative to the saturating RF frequency, when the first RF was swept through the $m_s=-1 \leftrightarrow 0 (m_f=-1)$ transition. Similarly, in trace (c), the second RF at 50 MHz drove an $m_f=0 (m_s=-1) \leftrightarrow m_f=-1 (m_s=0)$ transition and depleted the population in the $m_f=0 (m_s=-1)$ level, resulting in a hole when the first RF was swept through the $m_s=-1 \leftrightarrow 0 (m_f=0)$ transition. Both of the holes at 5.2 MHz have a linewidth (FWHM) of 70 kHz.

Figure 7-12 illustrates some of the differential EPR spectra showing hole burning effects at various saturating RF powers. The signals were obtained by applying a second RF field driving the $m_s=-1 \leftrightarrow 0 (m_f=0)$ transition at 74 MHz. At the lowest power (-35 dB), two holes, separated by 3.25 and 7.0 MHz, and an antihole, separated by 5.2 MHz, clearly appear. Increasing power level deepened and widened the holes and antiholes. In addition, two sharp holes at 4.95 and 5.3 MHz were observed to appear as superimposed in the broadened 5.2 MHz antihole at the power of -15 dB. Another antihole at 5.0 MHz turned out on the other side at a power of 5 dB. The superposition of holes on the antiholes is a consequence of optical pumping and spin-lattice relaxations within the 3A state. Similar hole burning spectra were also obtained with the saturating RF field tuned to the other EPR resonances.

Figure 7-13 plots the hole and antihole frequencies measured when the saturating RF field was tuned to different EPR lines. The results are compared with the energy level separations calculated using the Hamiltonian of Eq.(1-11), where a good agreement is found.

7-3. INTERFERENCE EFFECTS

Application of a second RF field also has prominent effects on the NMR signals. In the NMR measurements, the 5.5 MHz line was found to be much stronger than the 4.7 MHz line in most cases. By introducing an additional RF at 5.5 MHz, the relative size of the NMR lines was found to vary with different power levels of the second RF field (Fig. 7-14). It is clear that

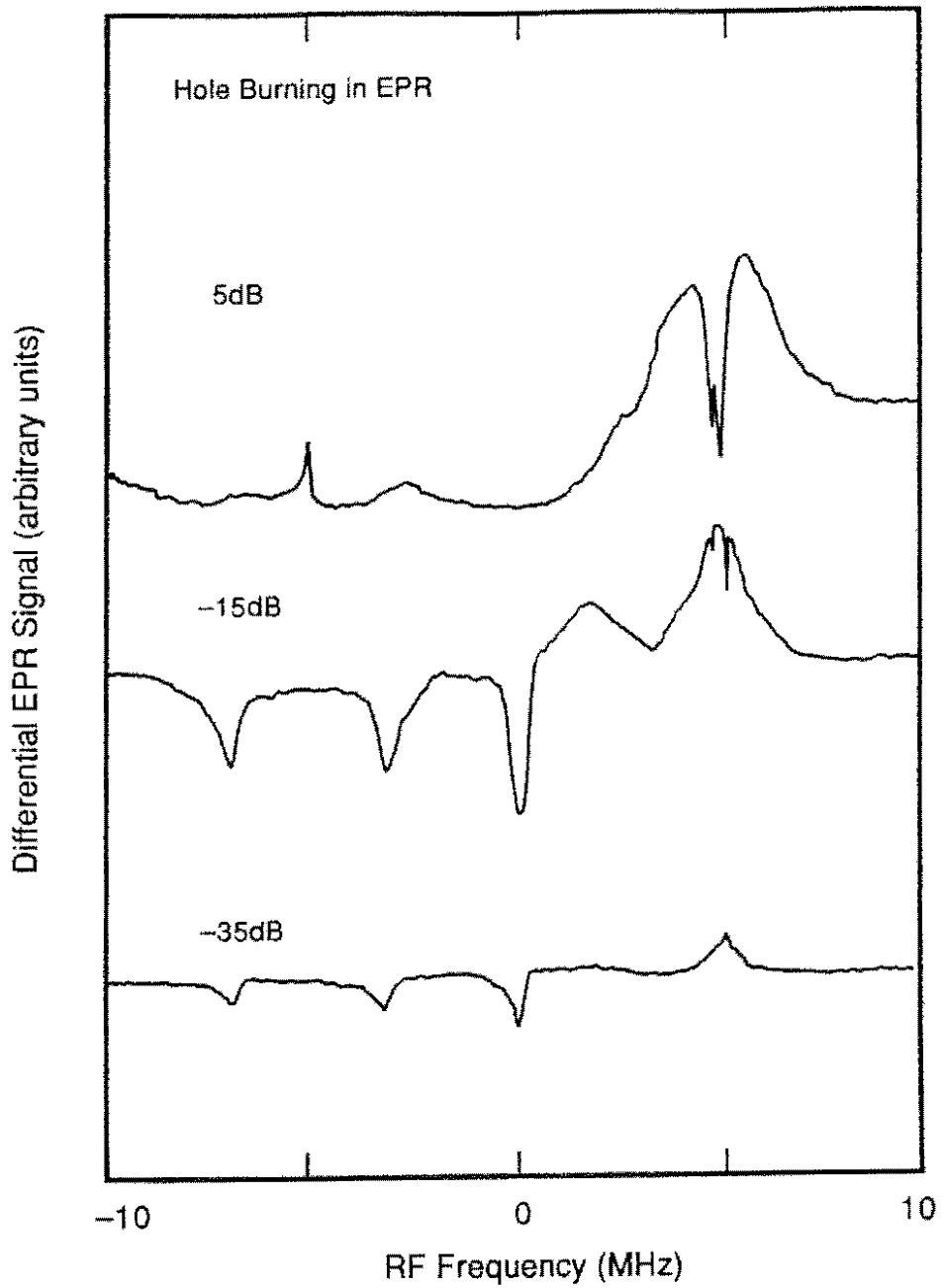


FIG. 7-12 Differential EPR spectra showing holes and antiholes at various saturating RF power levels. The RF field had a frequency of 74MHz (0MHz) and the magnetic field was 1006G.

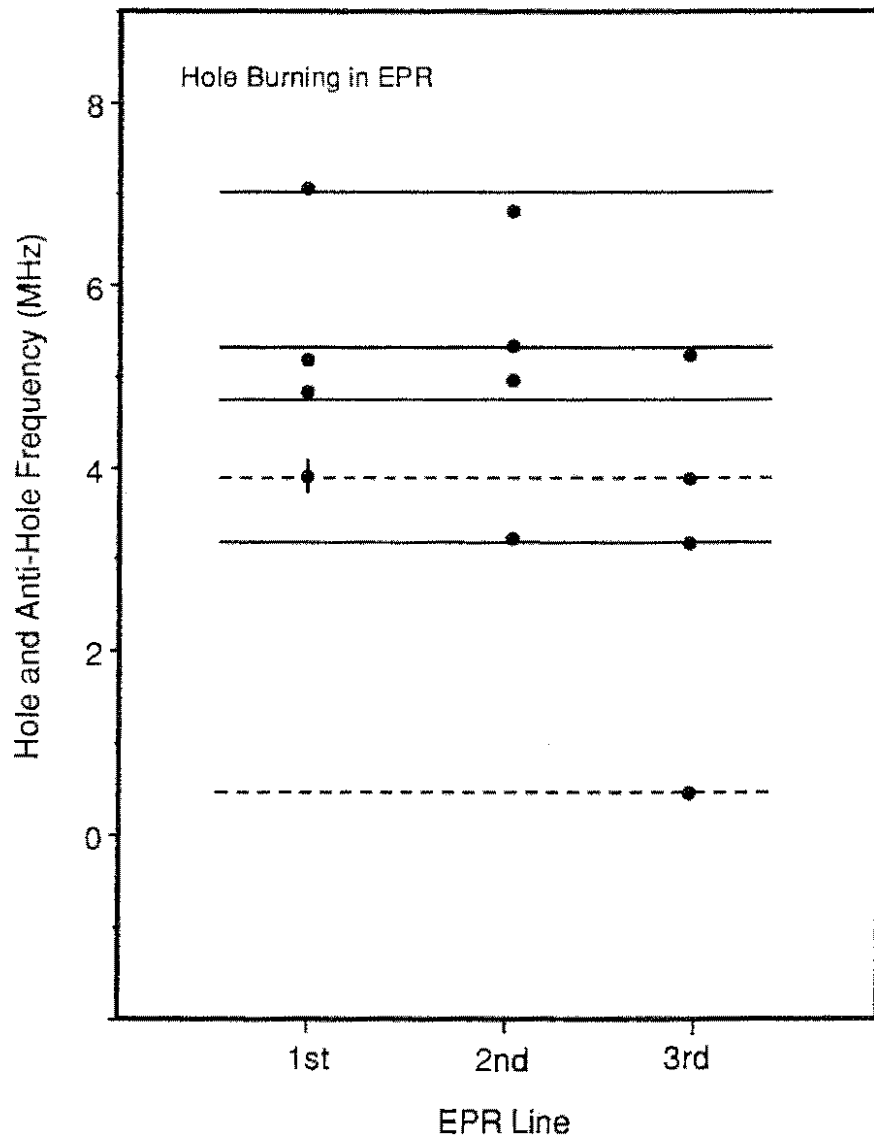


FIG. 7-13 Hole and antihole frequencies (dots) relative to the saturating RF frequency tuned to the three allowed EPR transitions compared with energy level separations (lines) in the triplet at a magnetic field of 1006 G. Solid lines: allowed transitions, dashed lines: forbidden the transitions.

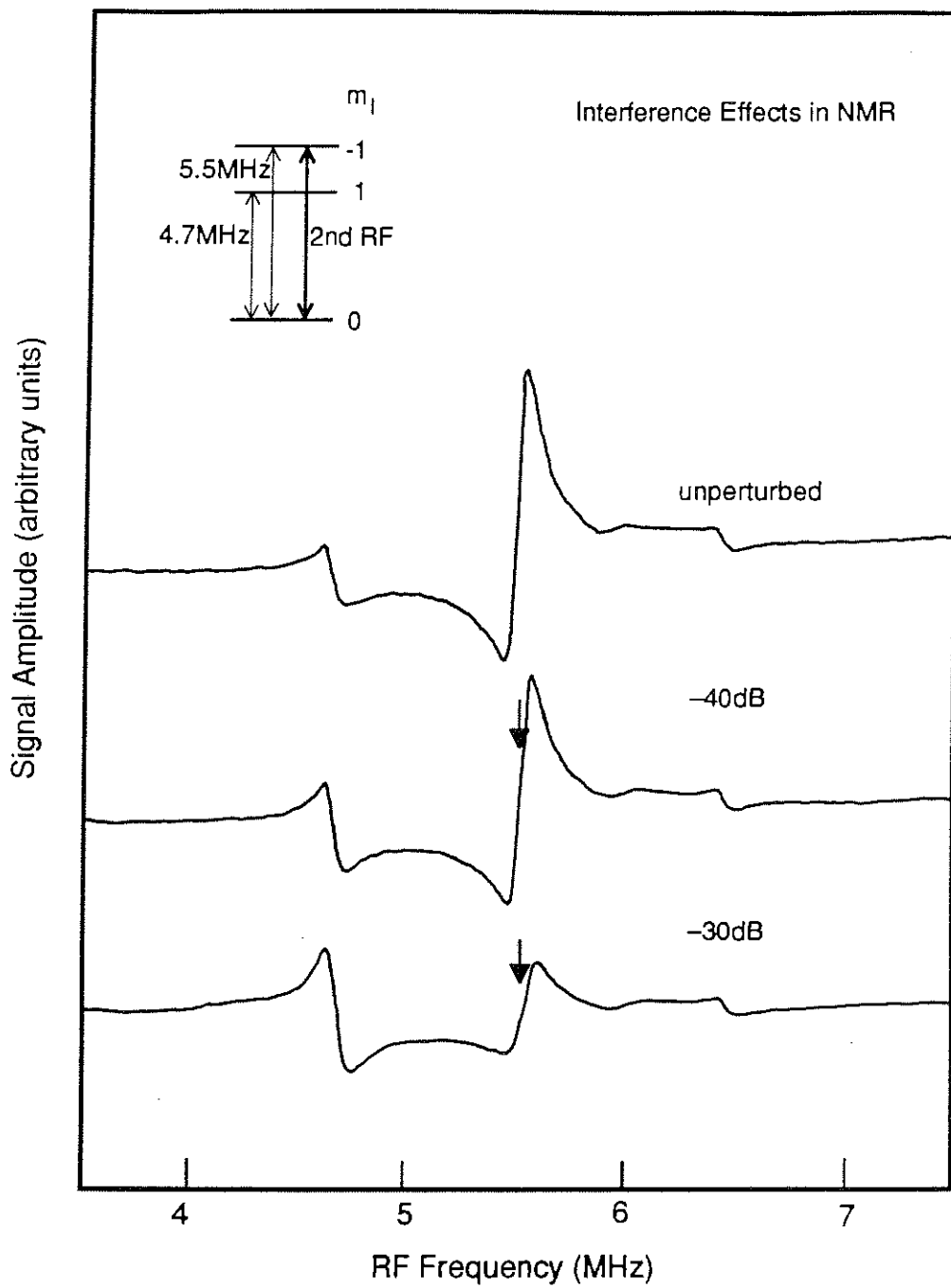


FIG. 7-14 Interference effects on the NMR spectra by an additional RF field tuned to 5.5MHz indicated by arrows. The corresponding energy levels and transitions are illustrated in the inset.

increasing power of the second RF field increases (decreases) the 4.7 MHz (5.5 MHz) line appreciably. This indicates that the second RF field increases the population difference between the $m_f=0$ and $m_f=1$ levels, but tends to equalize the populations in $m_f=0$ and $m_f=-1$ levels in the $m_s=0$ states. The effect supports the interpretation that the difference in the Raman heterodyne NMR signal size is due to the population factor. When the second RF power was increased to a higher value, the 4.7 MHz line was observed to be split into a doublet, *i.e.* Autler-Townes splitting, which will be discussed in detail in Chapter 8.

7-4. SPIN DENSITY DISTRIBUTION

For axial symmetry, the hyperfine parameters can be expressed as (Smith *et al.* 1959),

$$|A_{||}| = \gamma\gamma_n \hbar^2 (O + 2T) \quad (7-4a)$$

$$|A_{\perp}| = \gamma\gamma_n \hbar^2 (O - T), \quad (7-4b)$$

where O represents the isotropic or contact interaction, *i.e.* the s orbital contribution and T is the anisotropic interaction due to the p , d or f orbital contributions. The contact interaction is related to the density of ^{the} unpaired s electron at the nucleus by (Abragam 1961),

$$O = (8\pi/3) |\psi(r_n)|^2, \quad (7-5)$$

where $\psi(r)$ is the wave function of the electrons and r_n is the position of the nucleus.

Suppose all except the s and p orbital contributions can be neglected. This is valid for diamond as the carbon atom bonds have s and p atomic orbitals easily available, while the d orbital is very high in energy. Let the normalized molecule orbital be,

$$\psi = \sum_i c_i \psi_i + c_p \psi_p, \quad (7-6)$$

where summation is over the non neighbours.

where ψ_s and ψ_p are the s and p orbitals, and c_s and c_p are two coefficients. The amount of the unpaired electron in the s and p states are given respectively by (Loubser and van Wyk 1978),

$$c_s^2 = O/O^* \quad (7-7a)$$

$$c_p^2 = T/T^* \quad (7-7b)$$

where O^* and T^* are respectively the isotropic splitting for an s electron and the anisotropic splitting for a p electron in the free atom. The values of O^* and T^* can be calculated *e.g.* from self-consistent-field wave functions (Ramsey 1953, Watson and Freeman 1961a, b, Atkins and Symons 1967).

Using the experimental data $|A_{||}|=2.30$ MHz and $|A_{\perp}|=2.10$ MHz for the ^{14}N hyperfine interaction in the N-V centre, one has,

$$O_N = 0.38 \times 10^{24} \text{ cm}^{-3} = 0.056 \text{ atomic unit}$$

$$T_N = 0.012 \times 10^{24} \text{ cm}^{-3} = 0.0018 \text{ atomic unit,}$$

where the atomic unit is in a_0^{-3} , where $a_0=0.5292\text{\AA}$ is the Bohr radius. The value of O_N implies a finite density of the unpaired electron at the nitrogen nucleus $|\psi(r_n)|^2 = 0.045 \times 10^{24} \text{ cm}^{-3}$.

Using the theoretical results for the free nitrogen atom (Brown *et al.* 1933, Torrance 1934, Barnes and Smith 1954), we have

$$O_N^* = 38.0 \text{ atomic units}$$

$$T_N^* = 1.01 \text{ atomic units.}$$

One thus has the coefficients for the nitrogen, $c_s^2 = 0.0015$ and $c_p^2 = 0.0018$. This gives a ratio of p to s orbital for the nitrogen, $(p/s)_N = 1.2$.

Likewise, one can obtain the results for the carbon. Using the hyperfine parameters for the ^{13}C , $|A_{\parallel}|=2204.9 \text{ kHz}$ and $|A_{\perp}|=2123.3 \text{ kHz}$ determined by Loubser and van Wyk (1977, 1978), the isotropic and anisotropic terms for the carbon are (neglecting overlap effects)

$$O_C = 7.6 \times 10^{24} \text{ cm}^{-3} = 1.1 \text{ atomic units}$$

$$T_C = 1.4 \times 10^{24} \text{ cm}^{-3} = 0.21 \text{ atomic unit.}$$

For the free carbon atom (Brown *et al.* 1933, Torrance 1934, Barnes and Smith 1954),

$$O_C^* = 24.6 \text{ atomic units}$$

$$T_C^* = 0.48 \text{ atomic unit.}$$

These give the coefficients for the carbon, $c_s^2 = 0.045$ and $c_p^2 = 0.44$, and the orbital ratio, $(p/s)_C = 9.8$.

The spin population of one unpaired electron localized in the nitrogen is therefore 0.002 and that localized on the three equivalent carbons is 0.73. This shows that the unpaired electron spend most of time on the three carbons and very little time on the nitrogen.

7-5. QUADRUPOLE INTERACTION AND LOCAL ELECTRIC FIELD

The quadrupole parameter P is related to the nuclear quadrupole moment Q and the electric field gradient eq arising from other nuclei and electrons (*e.g.* Cohen and Reif 1957),

$$P = \frac{3e^2qQ}{4I(2I-1)} \quad (7-8)$$

The field gradient is given by,

$$eQ = \frac{\partial^2 V(\mathbf{r}_n)}{\partial z^2} = -\frac{\partial E(\mathbf{r}_n)}{\partial z}, \quad (7-9)$$

where $E(\mathbf{r})$ and $V(\mathbf{r})$ are the electric field and potential, respectively, due to the surroundings and z is the coordinate axis along the N-C pair. For the ^{14}N nucleus, $Q \approx 0.01 \times 10^{-24} \text{ cm}^2$ (Cook and Whiffen 1966).

For the P1 centre (substitutional nitrogen) in diamond, the nuclear quadrupole parameter associated with the ^{14}N has been measured using conventional ENDOR techniques (Cook and Whiffen 1966), $|P| = 3.97 \text{ MHz}$. Compared with the P1 centre, the quadrupole parameter associated with the ^{14}N in the N-V centre, $|P| = 5.04 \text{ MHz}$, is about 25% larger. If there is no distortion in the defects, the difference in the electric field gradient is, to a large extent, due to the carbon vacancy next to the nitrogen as the vacancy is the dominant factor that could disturb the local electric field. However, Smith *et al.* (1959) argued that the P1 centre probably experiences the Jahn-Teller effect (Jahn and Teller 1937) where the length of the N-C bond is likely to be 10~14% longer than the usual N-C bond length. On the other hand, the N-V centre does not show any evidence of Jahn-Teller effect (Loubser and van Wyk 1978) and therefore the role the vacancy plays in determining the local electric field needs further examination.

7-6. ENERGY LEVELS AND WAVE FUNCTIONS OF THE ^3A STATE

As all the parameters in the Hamiltonian have been fully determined, the energy levels and wave functions of the triplet can be obtained. Figures 7-15 and 7-16 show the eigenvalues of the ^3A ground state ($m_s = 1$ state is not included) calculated using Eq.(1-11) as a function of magnetic field strength and direction with respect to the [111] axis near the anticrossing. The zero-field splitting, hyperfine and quadrupole parameters listed in Table 7-2 were used in the calculations. As shown in Fig. 7-15 the $m_s = 0$ and $m_s = -1$ levels anticross at 1028 G, in this region the state

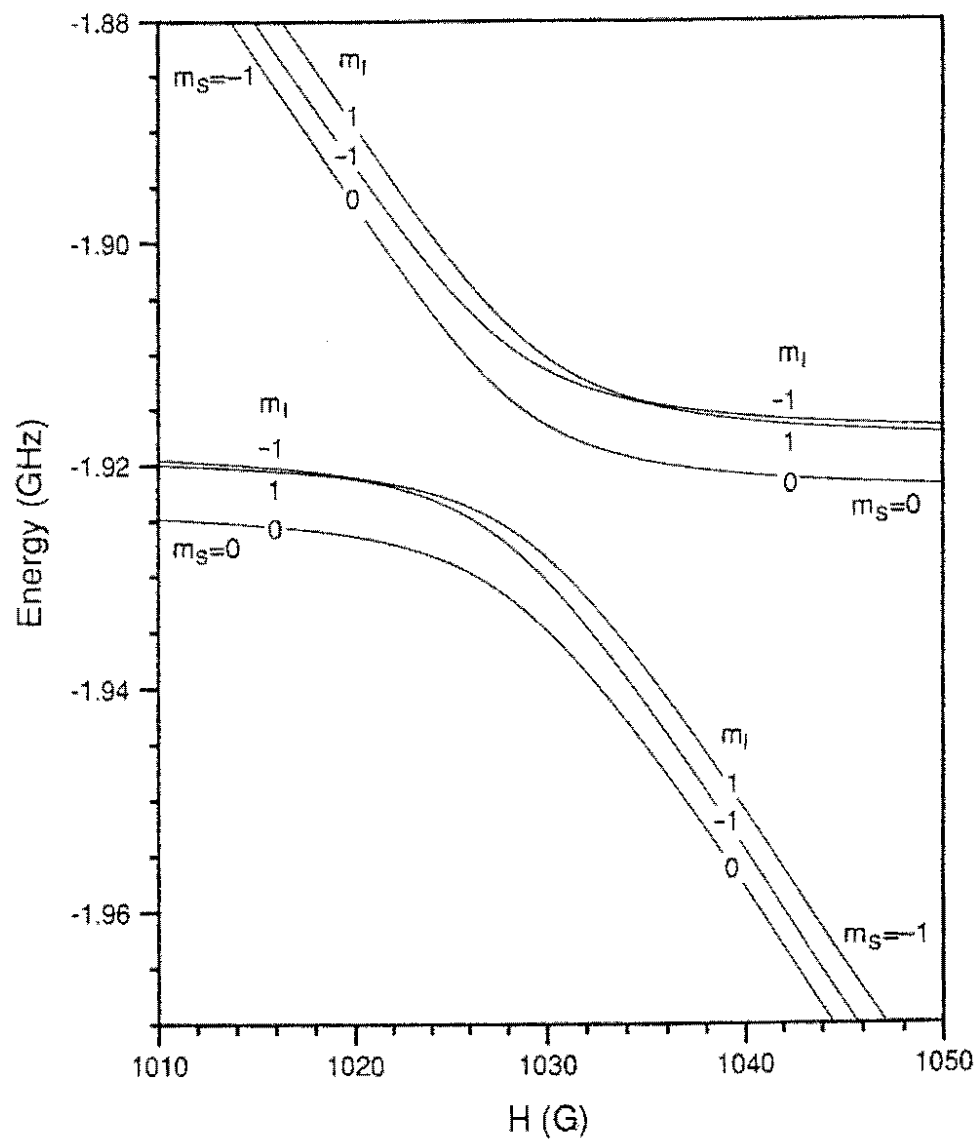


FIG. 7-15 Energy levels of the 3A ground state (the $m_s=1$ state is not shown) in the level anticrossing region as a function of magnetic field strength.

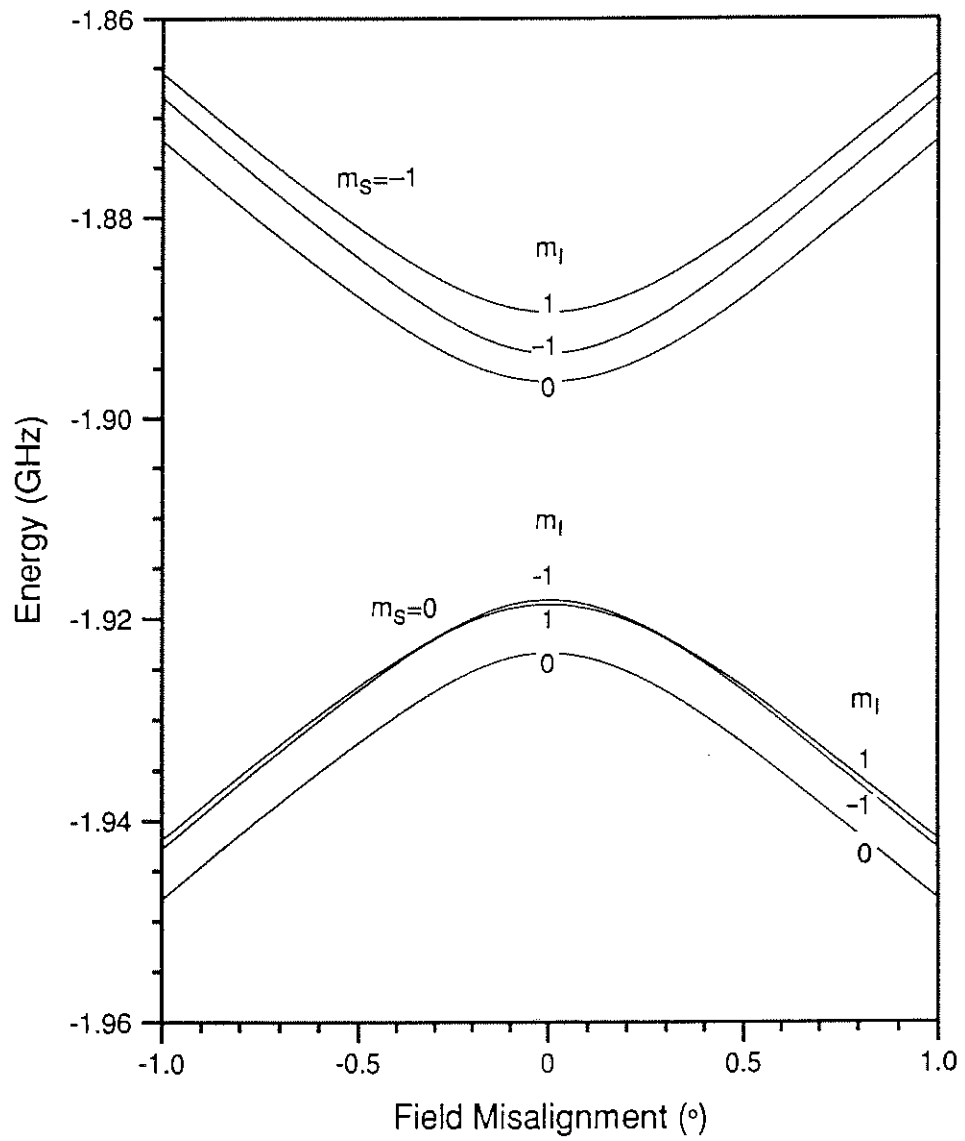


FIG. 7-16 Energy levels of the triplet as a function of field orientations with respect to the [111] axis at a field of 1019 G.

are an admixture of $|m_S m_I\rangle$. In addition, the hyperfine sub-levels $m_I = \pm 1$ anticross as well at about 1019 and 1035 G. In Fig.7-16, two sub-levels ($m_I = \pm 1$) in the $m_S = 0$ state also anticross at approximately $\pm 0.3^\circ$.

Table 7-3 lists the normalized and orthogonal wave functions, $|n\rangle$ ($n=1,2,\dots,6$) in terms of $|m_S m_I\rangle$ basis at various magnetic field strengths. In the calculations the field misalignment to the [111] axis was taken to be 0.25° and other parameters were the same as those used above. As can be seen in Table 7-3, for field strengths less than 980 G and greater than 1080 G, one of the $|m_S m_I\rangle$ components dominates (>99.6%). At 1010 and 1050 G, the state mixing is about 98% to 2%, while at 1028 G (LAC), the states are almost equally mixed.

TABLE 7-3 Wave functions of the 3A ground state ($m_S = 1$ state is not included) in terms of $|m_S m_I\rangle$ in the level anticrossing region.

(a) H=980 G

$ n\rangle$	$ m_S m_I\rangle$					
	$ -\rightarrow$	$ -\ 0\rangle$	$ -\ +\rangle$	$ 0\rightarrow$	$ 0\ 0\rangle$	$ 0\ +\rangle$
$ 1\rangle$	0.0016	-0.0623	0.0176	-0.2266	0.9972	-0.0282
$ 2\rangle$	-0.0005	0.0020	0.0604	0.0078	-0.0289	-0.9977
$ 3\rangle$	0.0629	-0.0157	-0.0000	-0.9975	-0.0279	-0.0071
$ 4\rangle$	-0.0497	-0.9966	-0.0204	0.0143	-0.0614	-0.0013
$ 5\rangle$	0.9968	-0.0486	-0.0017	0.0637	-0.0029	-0.0001
$ 6\rangle$	0.0007	-0.0194	0.9978	0.0004	-0.0171	0.0608

TABLE 7-3 (Continued)

(b) $H=1010$ G

$ n\rangle$	$ m_s m_l\rangle$					
	$ -\rightarrow$	$ -\ 0\rangle$	$ -\ +\rangle$	$ 0-\rightarrow$	$ 0\ 0\rangle$	$ 0+\rangle$
$ 1\rangle$	0.0104	-0.1627	0.0466	-0.0676	0.9811	-0.0650
$ 2\rangle$	-0.0118	0.0149	0.1515	0.0698	-0.0649	-0.9837
$ 3\rangle$	0.1668	-0.0323	0.0071	-0.9800	-0.0794	-0.0658
$ 4\rangle$	-0.1303	-0.9773	-0.0511	0.0231	-0.1573	-0.0091
$ 5\rangle$	0.9772	-0.1227	-0.0109	0.1719	-0.0185	-0.0018
$ 6\rangle$	0.0042	-0.0464	0.9860	0.0026	-0.0442	0.1542

(c) $H=1028$ G

$ n\rangle$	$ m_s m_l\rangle$					
	$ -\rightarrow$	$ -\ 0\rangle$	$ -\ +\rangle$	$ 0-\rightarrow$	$ 0\ 0\rangle$	$ 0+\rangle$
$ 1\rangle$	-0.1241	0.6506	-0.1427	0.1859	-0.7053	0.0950
$ 2\rangle$	-0.6915	-0.0488	0.1454	0.6595	0.2007	-0.1517
$ 3\rangle$	-0.1413	-0.1814	-0.5932	0.1102	0.1084	0.7559
$ 4\rangle$	-0.2374	-0.6951	-0.0910	-0.1261	-0.6375	-0.1728
$ 5\rangle$	-0.6534	0.2096	0.0998	-0.7052	0.1148	0.0929
$ 6\rangle$	0.0556	-0.1197	0.7670	0.0716	-0.1760	0.5984

TABLE 7-3 (Continued)

(d) H=1050 G

$ n\rangle$	$ m_s m_l\rangle$					
	$ -\rightarrow$	$ -\ 0\rangle$	$ -\ +\rangle$	$ 0\rightarrow$	$ 0\ 0\rangle$	$ 0\ +\rangle$
$ 1\rangle$	0.0941	-0.9824	0.0468	-0.0466	0.1468	-0.0064
$ 2\rangle$	0.9855	0.0981	-0.0092	-0.1372	-0.0156	0.0013
$ 3\rangle$	-0.0048	-0.0533	-0.9865	-0.0013	-0.0328	0.1513
$ 4\rangle$	0.0096	0.1432	-0.0285	0.0618	0.9842	0.0788
$ 5\rangle$	0.0053	0.0085	-0.1540	0.0367	0.0708	-0.9848
$ 6\rangle$	0.1406	-0.0421	0.0071	0.9868	-0.0595	0.0317

(e) H=1080 G

$ n\rangle$	$ m_s m_l\rangle$					
	$ -\rightarrow$	$ -\ 0\rangle$	$ -\ +\rangle$	$ 0\rightarrow$	$ 0\ 0\rangle$	$ 0\ +\rangle$
$ 1\rangle$	0.0457	-0.9965	0.0210	-0.0181	0.0646	-0.0013
$ 2\rangle$	0.9969	0.0466	-0.0018	-0.0626	-0.0031	0.0001
$ 3\rangle$	-0.0009	-0.0221	-0.9975	-0.0003	-0.0152	0.0654
$ 4\rangle$	0.0018	0.0639	-0.0144	0.0278	0.9969	0.0335
$ 5\rangle$	0.0004	0.0019	-0.0659	0.0069	0.0323	-0.9973
$ 6\rangle$	0.0634	-0.0170	0.0008	0.9975	-0.0271	0.0060

7-7. CONCLUSIONS

In the NMR experiments, four allowed transitions were observed, whereas in the ENDOR experiments, all six nuclear spin transitions were detectable. The NMR and ENDOR frequencies measured using Raman heterodyne spectroscopy have been well accounted for by the Hamiltonian of a 3A state. The hyperfine and quadrupole parameters were obtained from the NMR and ENDOR spectra measured at various magnetic field strengths and orientations with respect to the [111] axis and all the parameters in the Hamiltonian of Eq.(1-5) have been fully determined. Holes and antiholes have also been observed by introducing an additional RF field into the EPR experiment, which saturates a subgroup of N-V centres within the inhomogeneous distribution. Their spectral positions were found to be in good agreement with the energy levels calculated using the 3A Hamiltonian.

The isotropic and anisotropic hyperfine interactions due to the s and p orbital contributions in the N-V centre have been calculated for the nitrogen as well as the carbon. On comparing with the theoretical results for the free nitrogen and carbon atoms, it is concluded that the unpaired electrons in the N-V centre are localized mainly in the three equivalent carbons.

Although the NMR and ENDOR frequencies were accounted for, optical pumping effects on the Raman heterodyne signals are far less understood quantitatively. The optical pumping transfers the population of a hyperfine level to another level in the 3A ground state via optical excitation to the 3E levels with subsequent relaxations. This action creates a non-thermal equilibrium spin population distribution that determines the NMR as well as the ENDOR signal intensity. Such effects have not been included in the theoretical model of Raman heterodyne spectroscopy because of its complexity. Both theoretically and experimentally, we have demonstrated that optical pumping effects substantially change the signal magnitudes, which differ from those expected from the magnetic coupling strengths.

It was found that the resonances associated with the $m_s=0$ levels are stronger than those associated with the $m_s=-1$ levels. This effect is attributed to the spin alignment as observed in the

EPR experiment. It was also found that the ENDOR signals were detectable close to the level anticrossing, where the EPR signal almost disappeared. This supports the interpretation for the collapse of EPR as a consequence of equal populations in the two EPR levels.

Chapter 8

THE AUTLER-TOWNES EFFECT

When a monochromatic electromagnetic field of high power at frequency ω_1 is tuned to a resonance $|a\rangle \leftrightarrow |b\rangle$ (Fig.8-1), the states involved in the transition are strongly mixed. This causes each of the levels to be split into two components by the dynamic Stark effect (Autler and Townes 1955). If a weak field ω_2 is scanned, which connects one of the levels $|b\rangle$ to a third level $|c\rangle$, the splitting may be observed in the $|b\rangle \leftrightarrow |c\rangle$ transition. The phenomenon is the well known Autler-Townes effect and has been observed both in the RF range (*e.g.* Autler and Townes 1955) and in the optical range (*e.g.* Schabert *et al.* 1975, Picque and Pinard 1976, Fisk *et al.* 1986a, b, c).

This chapter deals with the Raman heterodyne detection of the Autler-Townes effect in the 3A state of the N-V centre. The splitting was measured at various perturbing RF powers with different detection schemes and compared with theory (Autler and Townes 1955, Whitley and Stroud 1976). Using the Autler-Townes effect, the spin levels involved in a magnetic transition can be conveniently identified by introducing an additional RF source in Raman heterodyne measurements. For instance, in Fig.8-1, the resonance associated with the $|b\rangle \leftrightarrow |c\rangle$ transition probed by the weak field ω_2 is observed to be split when the strong RF field ω_1 couples one of the levels to another level $|a\rangle$. As they share a common level, if the former transition is known, the latter can be identified, and *vice versa*. In addition, the matrix elements of dipole moments for magnetic transitions can be examined and their magnitudes can be easily compared as they are related to the amount of splitting. This is helpful for a better understanding of the Raman heterodyne signal intensity, as discussed earlier (see Chapter 7).

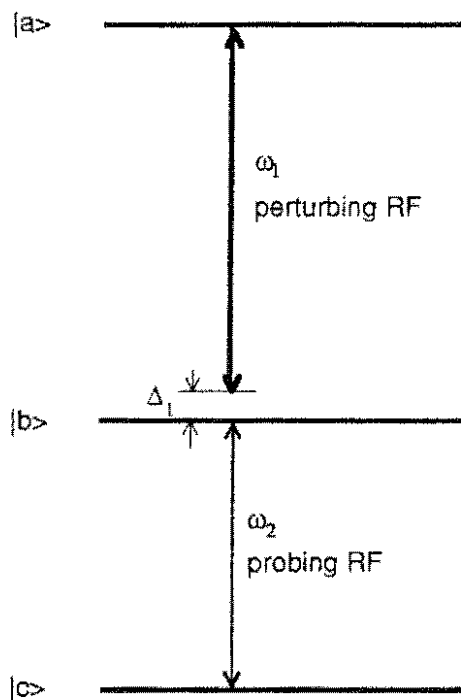


FIG. 8-1 An energy level diagram and characteristics of the RF fields in the Autler-Townes splitting measurements. A strong RF ω_1 drives the $|a\rangle \leftrightarrow |b\rangle$ transition and causes the levels to be split. The splitting is then probed by a weak field ω_2 which couples another transition $|b\rangle \leftrightarrow |c\rangle$ sharing a common level.

The Raman heterodyne measurement of Autler-Townes splitting utilizes the same techniques as for measuring the NMR and EPR except there is an additional (perturbing) RF field. The probing RF field ω_2 scans in frequency and monitors an NMR transition $|b\rangle \leftrightarrow |c\rangle$ in the 3A state, which is displayed by the spectrum analyzer. The perturbing RF field ω_1 is then applied, which couples one of the NMR levels $|b\rangle$ to another level $|a\rangle$. This strong perturbing RF field drives an additional magnetic transition $|a\rangle \leftrightarrow |b\rangle$, either another NMR or an EPR in the 3A state, and causes the $|b\rangle \leftrightarrow |c\rangle$ NMR line to be split.

8-1. THE AUTLER-TOWNES EFFECT IN NMR AND EPR TRANSITIONS

The Autler-Townes effect observed in the 3A ground state is shown in Figs. 8-2 and 8-3, where the spectra were obtained by scanning the probing RF through the $m_I=0 \leftrightarrow -1$ ($m_S=0$) transition centred at 5.5 MHz. Both phase and amplitude detections were used. In the experiment, the probing RF power was set in the low power regime and therefore no power broadening is expected. In each figure, the splittings are presented for at various perturbing RF powers as indicated.

The energy levels and transitions corresponding to the measurements are shown in Fig. 8-4. In the measurement of Fig.8-2, the strong perturbing RF field was tuned to 4.6MHz associated with the $m_I=0 \leftrightarrow 1$ ($m_S=0$) NMR transition. This is an $m_I = -1 \leftrightarrow 0 \leftrightarrow 1$ ($m_S=0$) three level system, where both transitions are NMR. In the measurement of Fig.8-3, the perturbing RF drove the $m_S=0 \leftrightarrow -1$ ($m_I=-1$) EPR transition and the Autler-Townes effect occurred in an $m_I=-1$ ($m_S=-1$) \leftrightarrow $m_I=-1$ ($m_S=0$) \leftrightarrow $m_I=0$ ($m_S=0$) three level system involving both NMR and EPR. In both cases, the splittings appear clearly using either phase or amplitude detection.

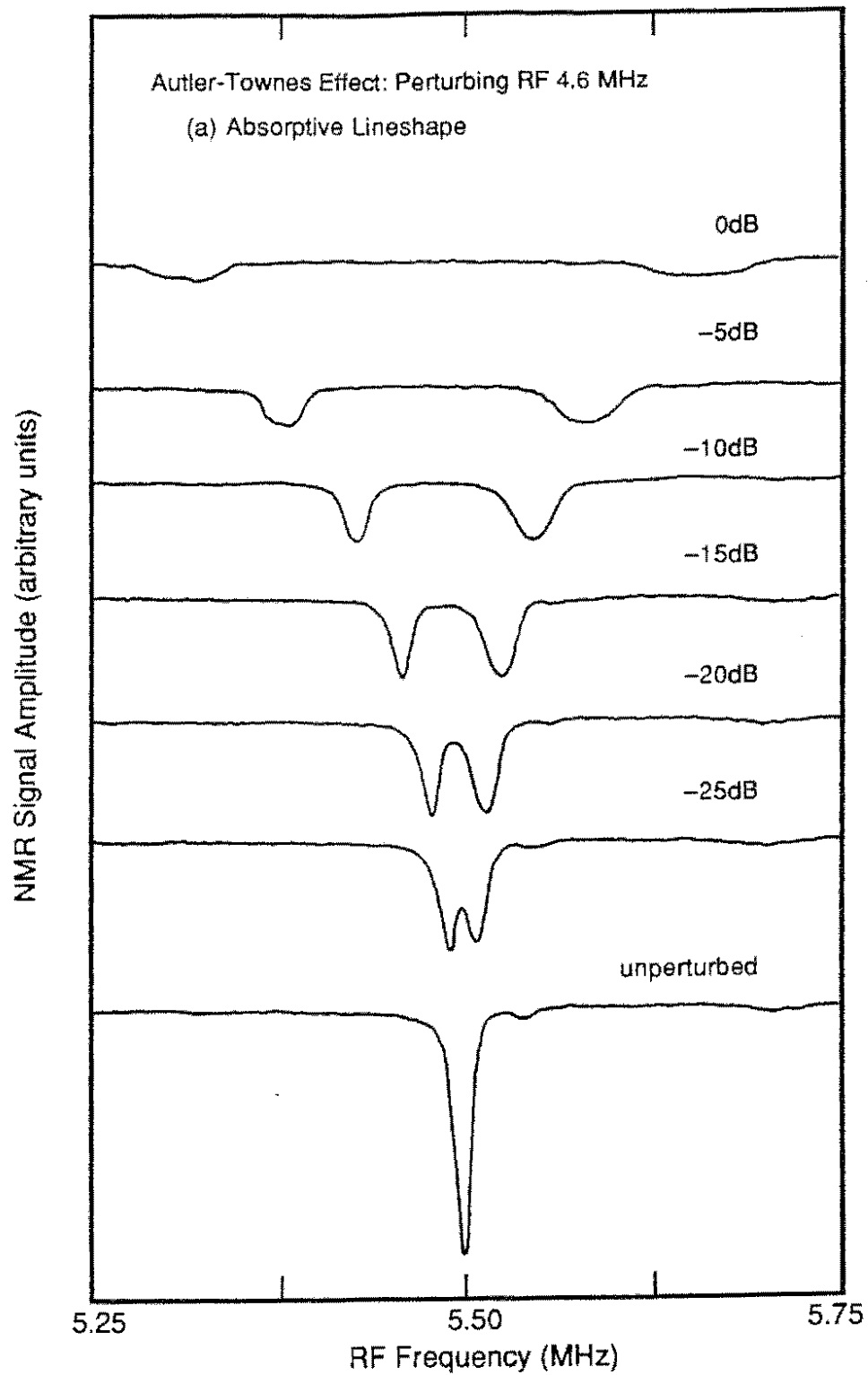


FIG. 8-2 Autler-Townes effects in the 5.5MHz NMR line with a perturbing RF at 4.6MHz. (a) Absorptive, (b) dispersive and (c) amplitude lineshapes.

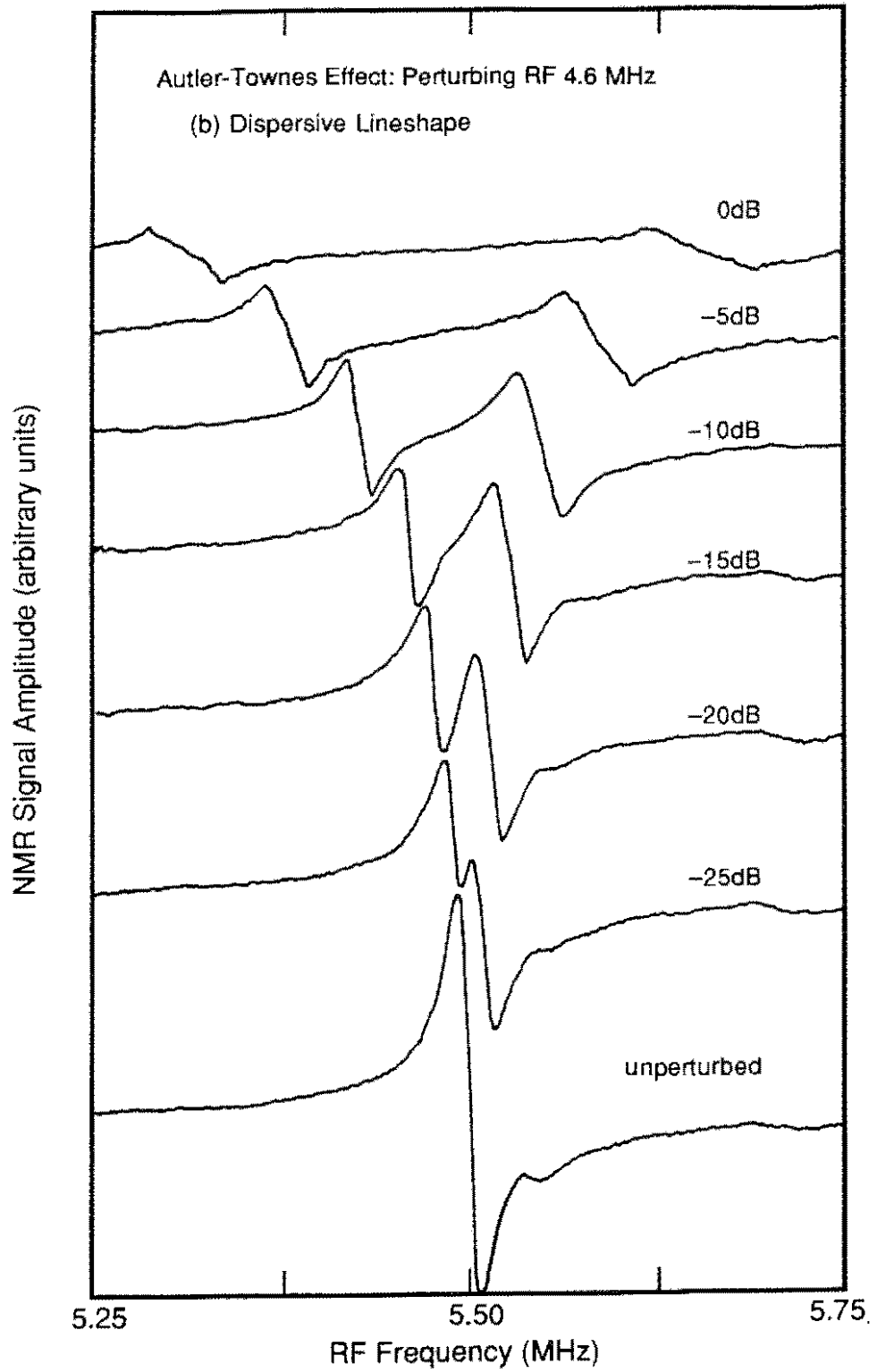


FIG. 8-2 (Continued)

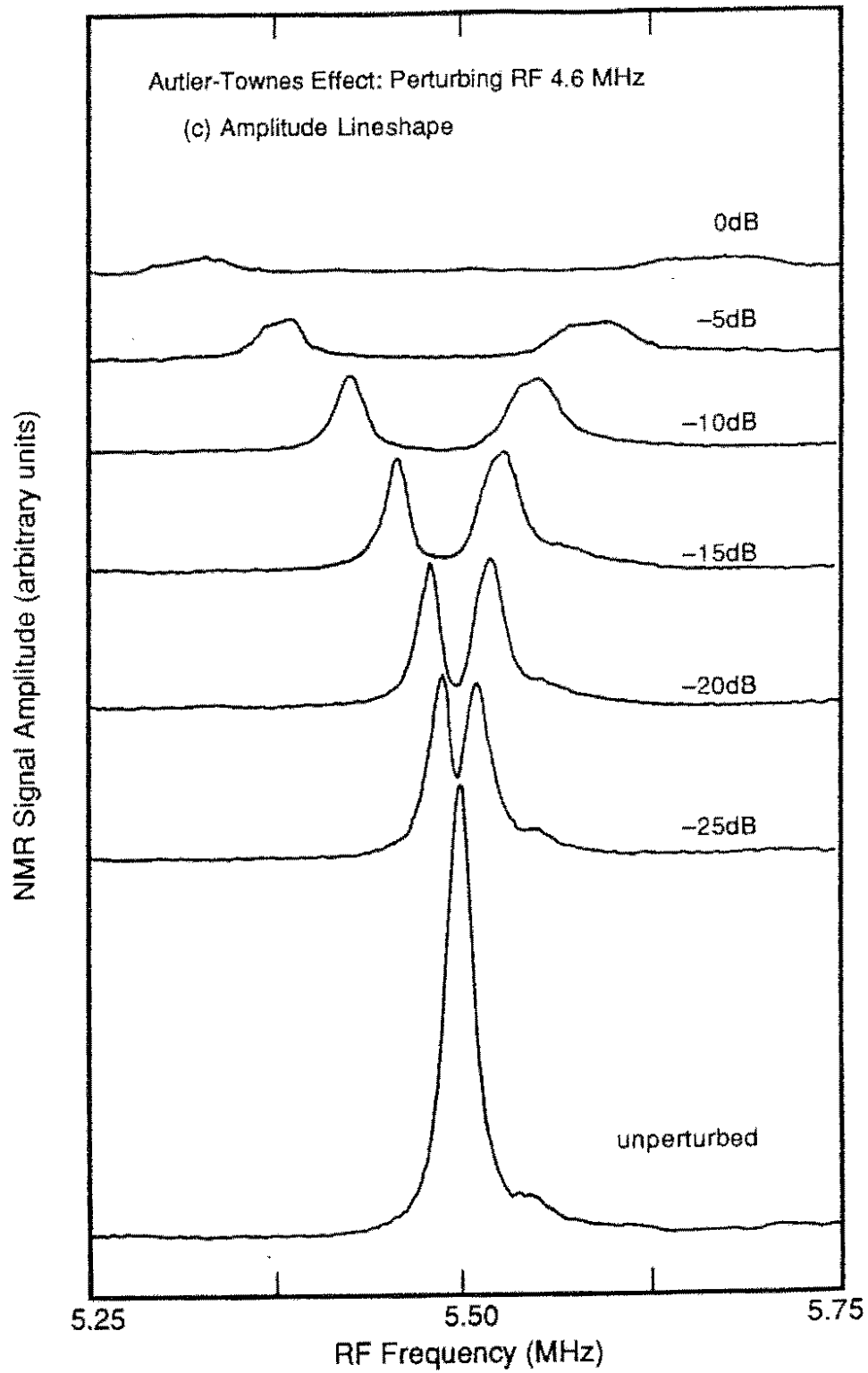


FIG. 8-2 (Continued)

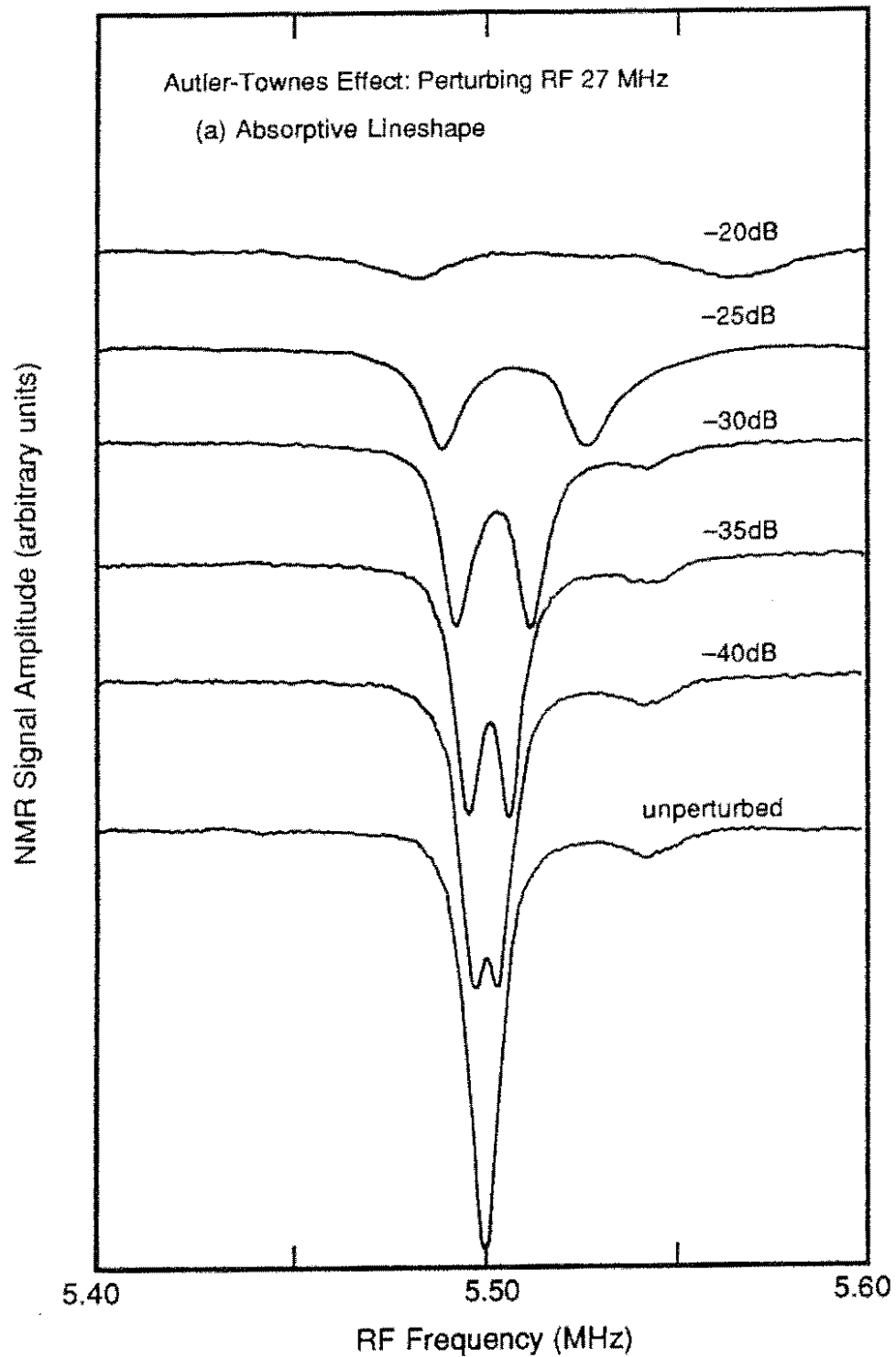


FIG. 8-3 Autler-Townes effects in the 5.5MHz NMR line with a perturbing RF at 27MHz.

(a) Absorptive, (b) dispersive and (c) amplitude lineshapes.

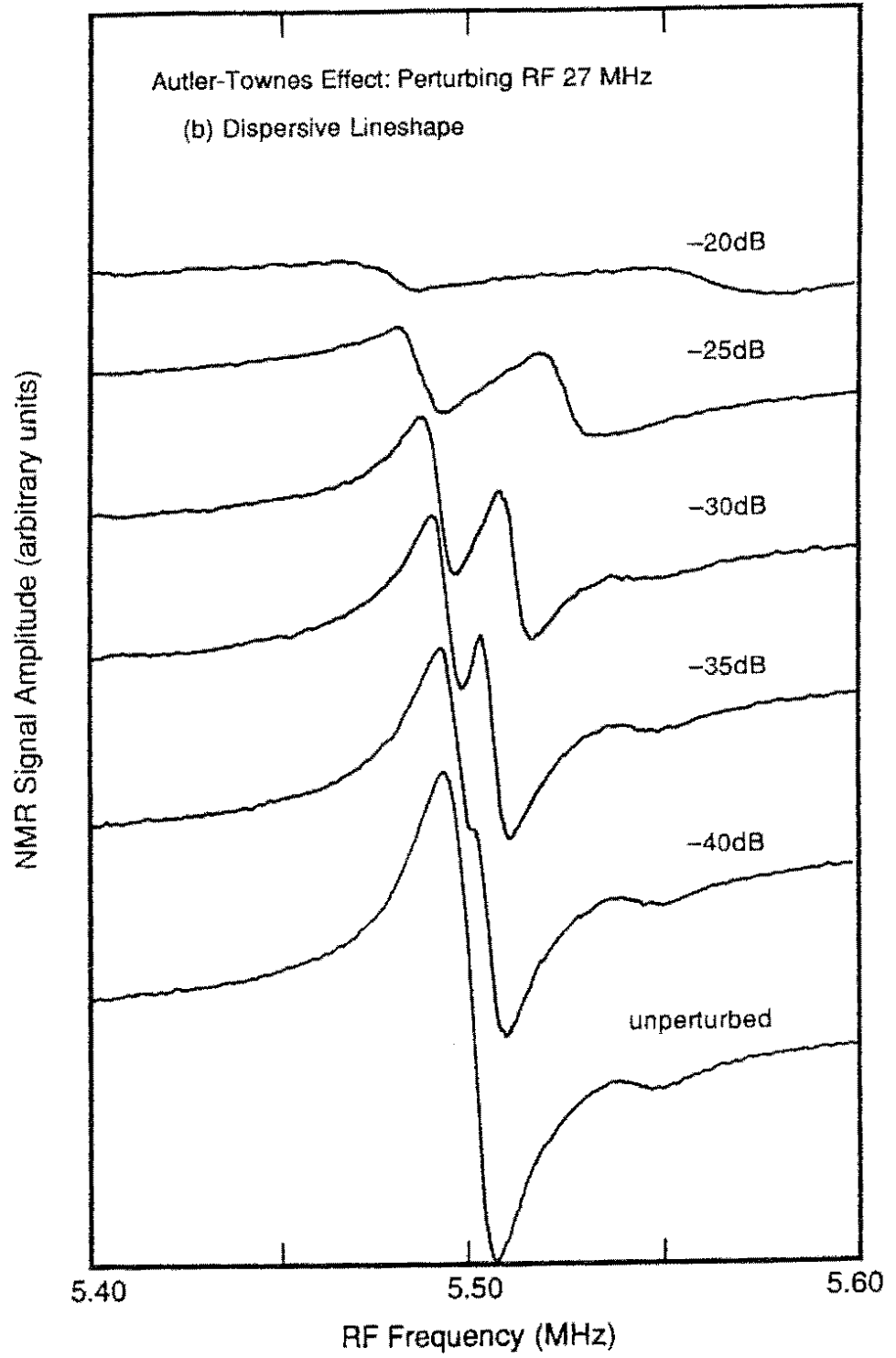


FIG. 8-3 (Continued)

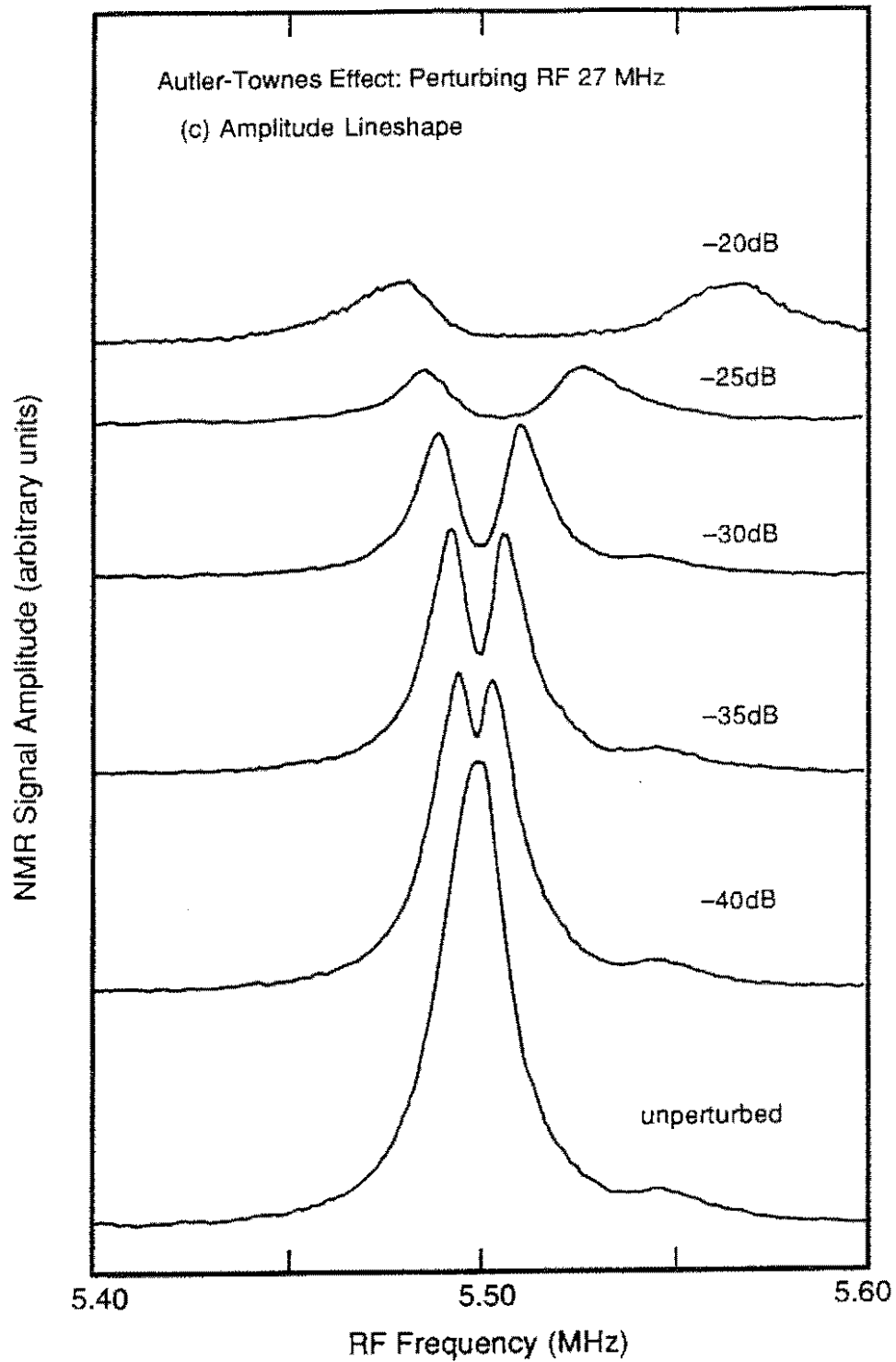


FIG. 8-3 (Continued)

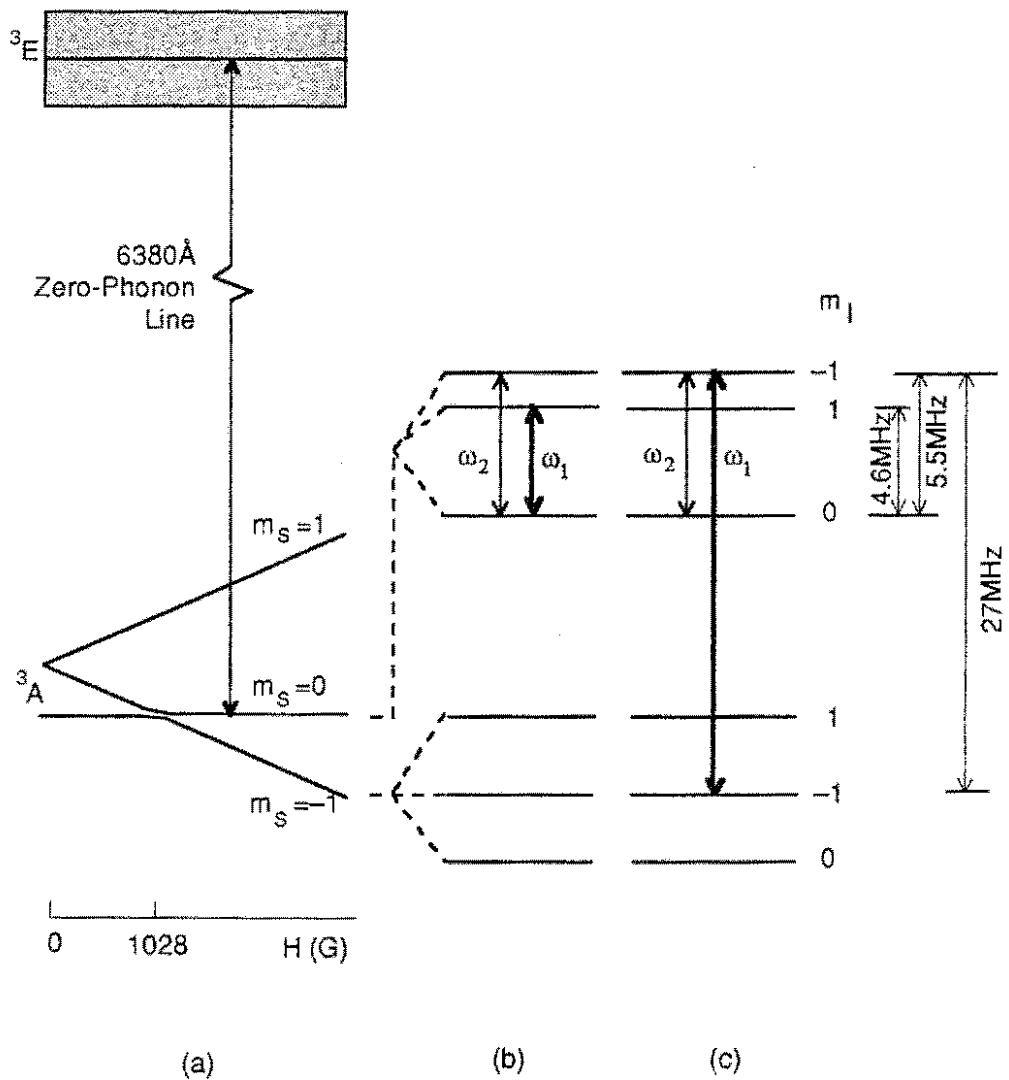


FIG. 8-4 (a) Level splitting in the static magnetic field, where the hyperfine interaction is not shown, and the hyperfine sub-levels and magnetic transitions in the 3A ground state corresponding to the Autler-Townes splitting measurements in (b) Fig. 8-2 and (c) Fig. 8-3, where ω_1 is the perturbing RF field and ω_2 is the probing RF field.

8-2. DOUBLET SPLITTING

For a simple three level system shown in Fig.8-1, the Autler-Townes doublet frequencies depend on the perturbing RF detuning, Δ_I , and the Rabi frequency of the magnetic transition coupled by ω_I , $\beta_I = \mu_{ab}H_I/\hbar$, where μ_{ab} is the dipole moment matrix element of the transition $|a\rangle \leftrightarrow |b\rangle$ and H_I is the magnetic field strength of ω_I (Autler and Townes 1955, Whitley and Stroud 1976),

$$\omega_{\pm} = \omega_0 - \frac{\Delta_I}{2} \pm \frac{1}{2} \left[\Delta_I^2 + \beta_I^2 \right]^{1/2}, \quad (8-1)$$

where ω_- and ω_+ denote, respectively, the frequencies of the low and high energy components of the doublet, and ω_0 is the unperturbed NMR frequency of the transition $|b\rangle \leftrightarrow |c\rangle$. The amount of splitting,

$$\omega_+ - \omega_- = \left[\Delta_I^2 + \beta_I^2 \right]^{1/2}, \quad (8-2)$$

is equal to the Rabi flopping frequency. If the detuning of the perturbing RF is negligible ($\Delta_I=0$), the doublet is symmetric with respect to ω_0 and their separation is equal to the Rabi frequency β_I .

Figures 8-5 and 8-6 plot the Autler-Townes doublet frequencies measured at various perturbing RF powers compared with Eq.(8-1). In the calculations, the relative magnitudes of the Rabi frequencies were set according to the experimental values of RF powers but their absolute values were adjusted to obtain the best-fits. The Rabi frequencies were $\beta_I/2\pi=1\sim 600$ kHz for Fig. 8-5 and $\beta_I/2\pi=0.2\sim 200$ kHz for Fig. 8-6. The detunings Δ_I were measured from the centre frequencies of the doublets. In Figs. 8-5 and 8-6, the results are found to be in good agreement with Eq.(8-1) except at the highest power level of the perturbing RF field tuned to

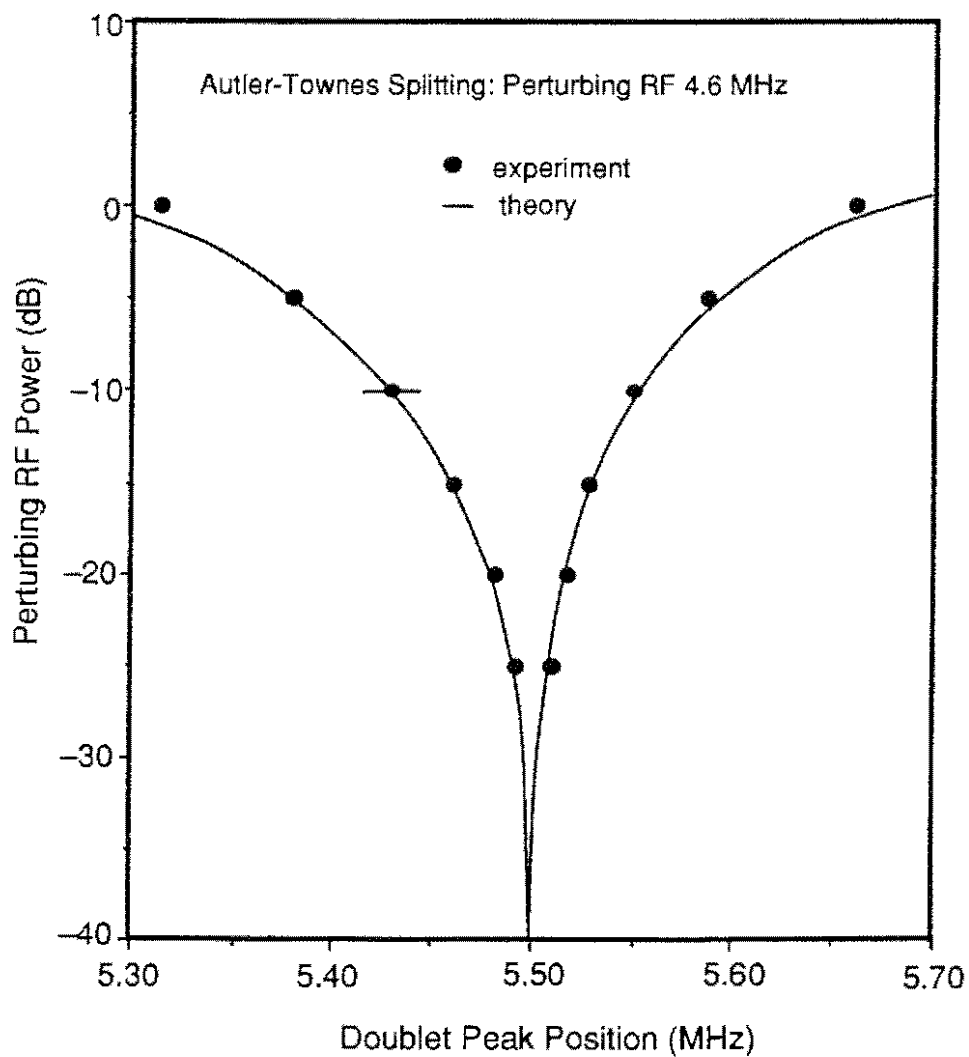


FIG. 8-5 The measured Autler-Townes splittings in the 5.5MHz NMR line (dots) compared with theoretical results (solid lines), where the perturbing RF field connects another NMR at 4.6MHz.

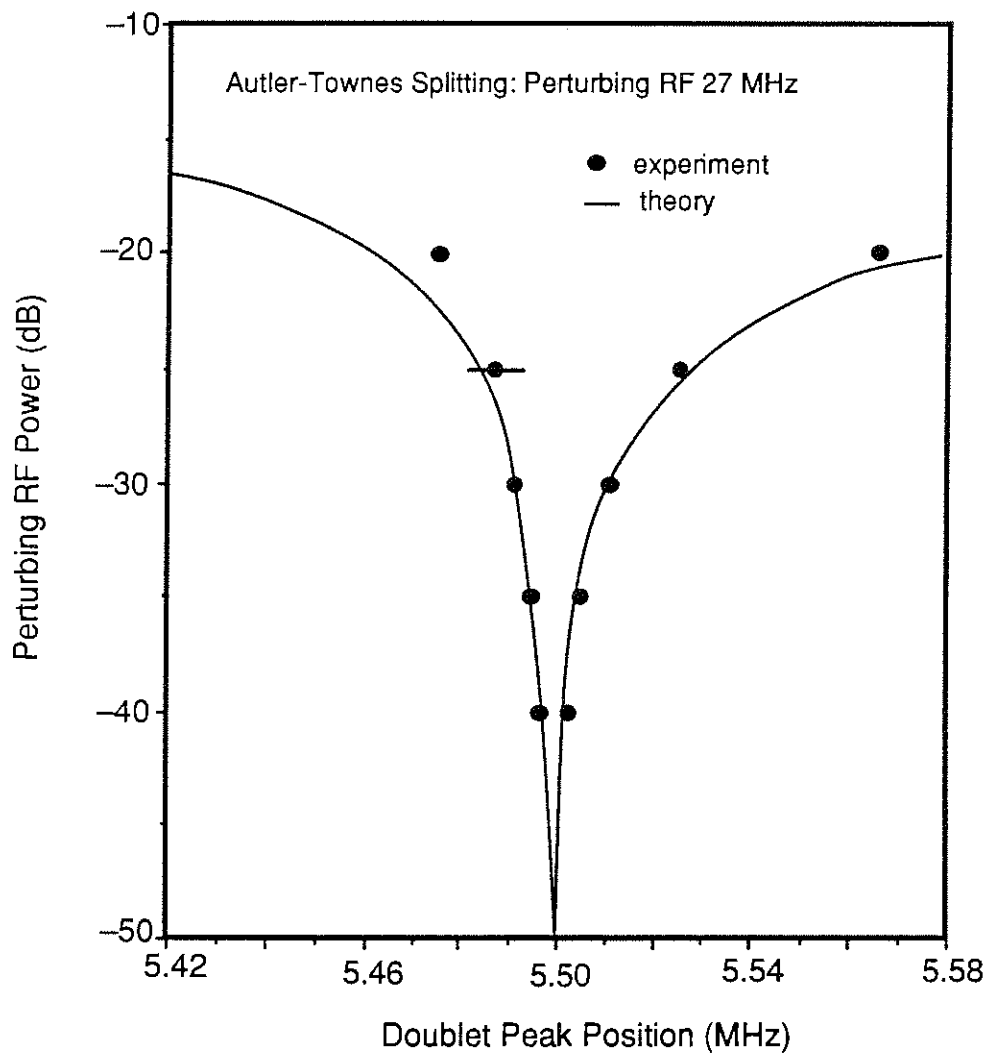


FIG. 8-6 The measured Autler-Townes splittings in the 5.5MHz NMR line (dots) compared with theoretical results (solid lines), where the perturbing RF field connects an EPR at 27MHz.

27MHz, where there is a significant discrepancy. This is due to the fact that at this high power there are several contributing EPR signals and all the transitions have to be considered. In this case, the levels involved in the Autler-Townes splitting measurement can no longer be described as a simple three-level system.

In Fig.8-7, the doublet splittings are plotted against the perturbing RF power on a logarithmic scale, where the square root dependency is also plotted for comparison. The results are again in good agreement with the theoretical dependence $\sim(\text{RF power})^{1/2}$ except at the highest power of the perturbing field, which connects the EPR.

It is clear in Figs.8-2 and 8-3 that the width of each component increases with the increasing RF power. Theoretically, the width of the doublet should not be affected by the power level. This phenomenon is possibly due to the inhomogeneity of the RF field strength inside the sample produced by the five-turn coil. Being described by Eq.(3-6), the field inhomogeneity increases with the RF power. As the Autler-Townes splitting of a centre is proportional to the RF field strength at the site where it is located, any spatial inhomogeneity of the field strength may result in additional inhomogeneous broadening of the doublet.

The amplitude of the doublet was found to decrease with the increasing perturbing RF power. This is attributed to the change of population in one of the NMR levels coupled by the strong perturbing field (Whitley and Stroud 1976). Consequently, the Raman heterodyne signal size is modified by the change in the population factor.

8-3. MATRIX ELEMENTS OF THE $m_I=0 \leftrightarrow \pm 1 (m_S=0)$ TRANSITIONS

In the Raman heterodyne NMR measurements (see Chapter 7), we observed that the $m_I=0 \leftrightarrow -1 (m_S=0)$ transition is much stronger than the $m_I=0 \leftrightarrow 1 (m_S=0)$ transition in most cases. This is an interesting observation upon which we wish to comment here. The Raman

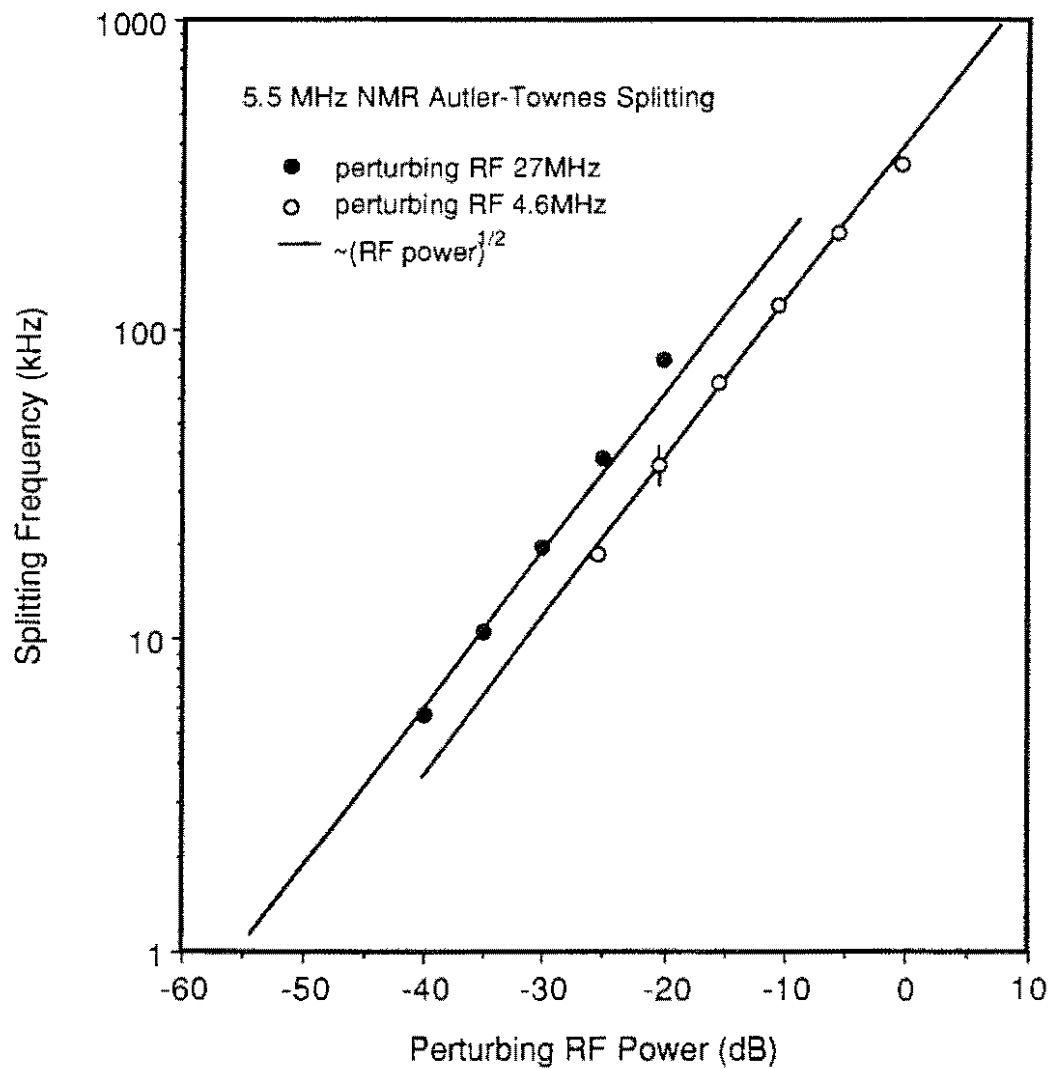


FIG. 8-7 The measured splittings of the 5.5MHz NMR line (dots) compared with the square root dependency on the RF power (solid lines).

heterodyne signal is proportional to both the magnetic dipole moment and the population factor, (see Eq.(6-2)). However, it is not at all clear why one line should appear stronger than the other using Raman heterodyne detection. The problem can be examined by measuring the Autler-Townes splitting, from which one can establish the magnitude of a matrix element. The amount of splitting is proportional to the Rabi frequency, $\beta_I = \mu_{ab}H_I/\hbar$, when the perturbing field is at resonance, and consequently a quantitative comparison of matrix elements (μ_{ab}) can be made if the perturbing RF power ($\sim H_I^2$) is kept unchanged in the measurements.

We have measured the splittings in both the 4.6MHz line associated with the $m_I=0 \leftrightarrow 1$ ($m_S=0$) transition and the 5.5MHz line with the $m_I=0 \leftrightarrow -1$ ($m_S=0$) transition. Two of the traces are shown in Fig. 8-8, where amplitude detection was employed. The dispersive-like lineshapes in the 4.6MHz line are due to the interference effect between the NMR and the background EPR signal. In the measurements, the perturbing RF was tuned to 4.6 and 5.5MHz, respectively, with the same power level and the NMR signals were measured by scanning the weak RF in the range of 4~6 MHz. As can be seen in Fig.8-8, the splittings in both the NMR lines are found to be the same.

In Fig.8-9, the splittings of the 4.6 and 5.5MHz NMR lines obtained with various perturbing RF powers are plotted. The RF voltage here is the RMS voltage across the terminals of a 50Ω load, which is connected in series to the RF coil. It is therefore proportional to the magnetic field magnitude of the perturbing field. The splittings of both lines are found to be very close to a linear dependence. This establishes that, within an error of ~5%, the matrix element has the same magnitude for both the 4.6 and 5.5 MHz NMR transitions, whereas in the NMR measurements we observed that the latter is stronger than the former by a factor of 5~20 (Fig. 8-8). We have thus experimentally demonstrated that the Raman heterodyne signal magnitude not only depends on the transition matrix element but also is affected greatly by the population factor.

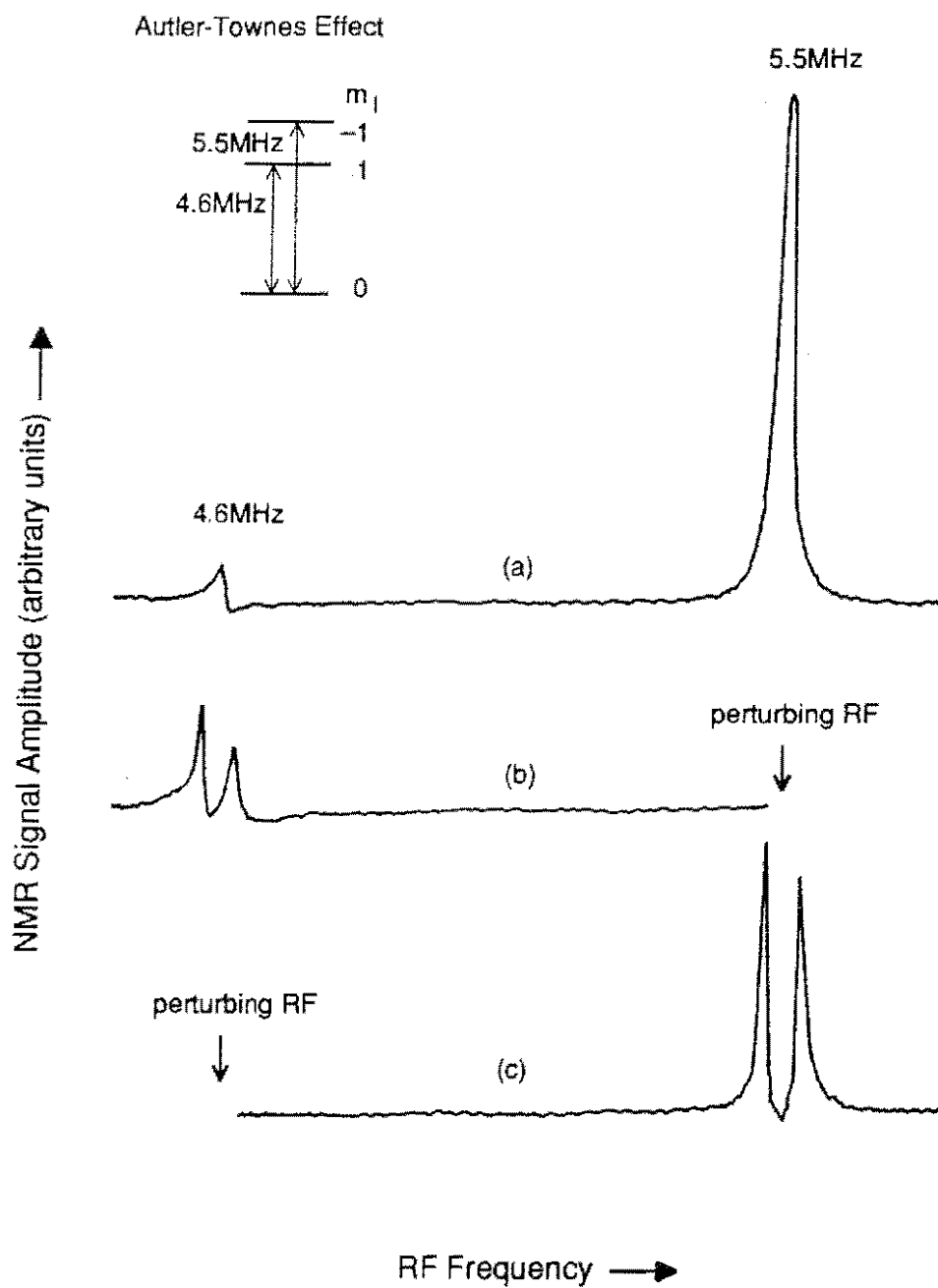


FIG. 8-8 (a) The unperturbed NMR signals and the Autler-Townes splittings (b) in the 4.6MHz line with the perturbing field at 5.5MHz and (c) in the 5.5MHz line with the perturbing field at 4.6MHz.

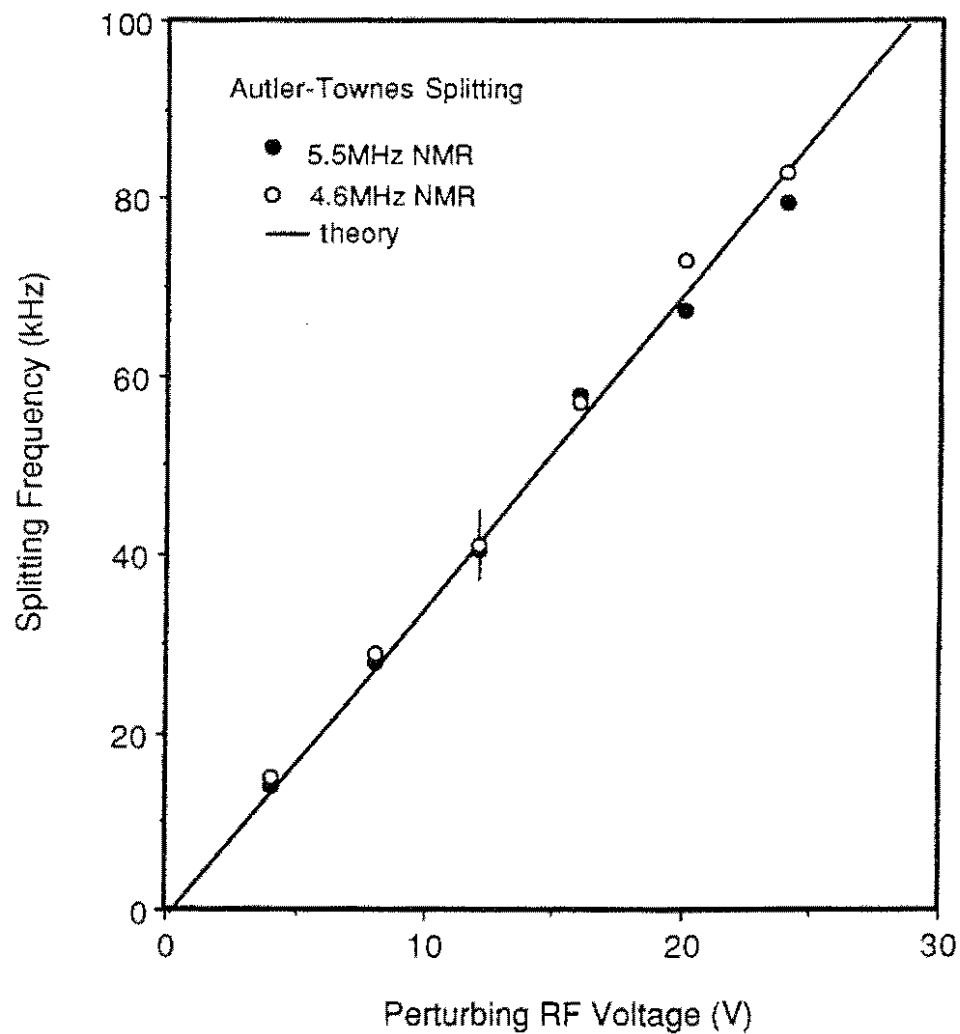


FIG. 8-9 The Autler-Townes splittings of the 4.6 and 5.5 MHz NMR lines measured with the perturbing RF field tuned to the alternative transitions (dots) compared with theoretical prediction (solid line).

8-4. CONCLUSIONS

By introducing a perturbing RF field into Raman heterodyne measurements, the Autler-Townes splitting has been observed. The splittings in the 5.5MHz NMR have been measured with the perturbing RF field of various powers tuned to either another NMR or an EPR transition in the 3A state. The measured doublet frequencies were found to be in good agreement with the theoretical results for a three-level system except in the case of the EPR transition being driven by a very strong perturbing RF field. At this power level, several EPR transitions have to be considered and therefore the simple three-level system does not apply.

As they share a common level, both of the $m_f=0 \leftrightarrow \pm 1$ ($m_s=0$) transitions were observed to be split when a perturbing field was tuned at the alternative transitions. The magnitudes of the dipole moment matrix elements for the $m_f=0 \leftrightarrow \pm 1$ ($m_s=0$) transitions were compared by measuring the amounts of Autler-Townes splittings with the same perturbing RF power level. The measurements confirm that their matrix element magnitudes are the same within the experimental error. Comparison of this result with the NMR signal size indicates that the Raman heterodyne signal intensity is affected greatly by the population factor.

Chapter 9

COHERENT SPIN TRANSIENTS

This chapter deals with the coherent spin transients in the 3A ground state of the N-V centre measured using Raman heterodyne techniques. In the experiments, the RF field was pulsed while the laser was kept in the CW mode. After the RF pulse or pulses excited a particular magnetic transition, the associated Raman heterodyne signal was recorded as a function of time. Coherence properties in the time domain provide useful information about spin relaxation behaviour (see, *e.g.* Farrar and Becker 1971, Poole and Farach 1971, Steinfeld 1978) and important parameters such as the homogeneous linewidth of a magnetic transition can be determined.

Using Raman heterodyne techniques we have measured nutations and echoes in the NMR and EPR transitions. The homogeneous linewidths associated with both the NMR and EPR transitions were determined from echo measurements. Spin coherence transfer was also observed in the ENDOR measurement by pulsing the RF field which drove the NMR transition while monitoring the change of the EPR signal driven by a CW RF field. In addition, Zeeman beating in the nuclear quadrupole resonance (NQR) was observed. The beat signal arises from the interference between the $m_I=0 \leftrightarrow \pm 1$ ($m_S=0$) transitions, which were excited by an RF pulse whose Fourier linewidth was larger than the Zeeman splitting of the $m_I=\pm 1$ levels.

9-1. NUTATION

Nutation occurs when a strong RF field tuned to or close to a magnetic resonance is suddenly applied to a system at thermal equilibrium (Torrey 1949, Ferretti and Freeman 1966). The signal arises from the alternating absorption and stimulated emission of the radiation between the two levels involved until the population reaches an equilibrium state. The observed signal oscillates at the Rabi flopping frequency (Farrar and Becker 1971),

$$\chi_{RF} = \left[\Delta_{RF}^2 + \beta_{RF}^2 \right]^{1/2}, \quad (9-1)$$

with an exponential decay characterized by a relaxation time related to both T_1 and T_2 , where Δ_{RF} is the RF detuning from the resonance centre frequency and β_{RF} is the Rabi frequency. If the detuning is negligible ($\Delta_{RF}=0$), the system "flops" at the Rabi frequency β_{RF} .

One of the nutation signals associated with the $m_I=0 \leftrightarrow -1 (m_S=0)$ transition at 5.5 MHz measured by the Raman heterodyne technique is shown in Fig. 9-1. In the experiment, the magnetic field was 1040G and phase detection was employed. The RF field was applied at the time $t=0$.

At higher RF powers, we observed modulation patterns in the nutation signals. One of the experimental traces is shown in Fig. 9-2. The phenomenon became more evident when the RF power level was increased further. This is almost certainly due to the involvement of the adjacent 4.6 MHz NMR transition. When the RF power is increased, the NMR transitions are broadened such that the 4.6MHz line becomes coupled to the 5.5MHz line. The fast Fourier transform (FFT) analysis clearly shows two peaks, corresponding to the two nutation frequencies associated with the 4.6 and 5.5 MHz NMR transitions.

5.5MHz NMR Nutation

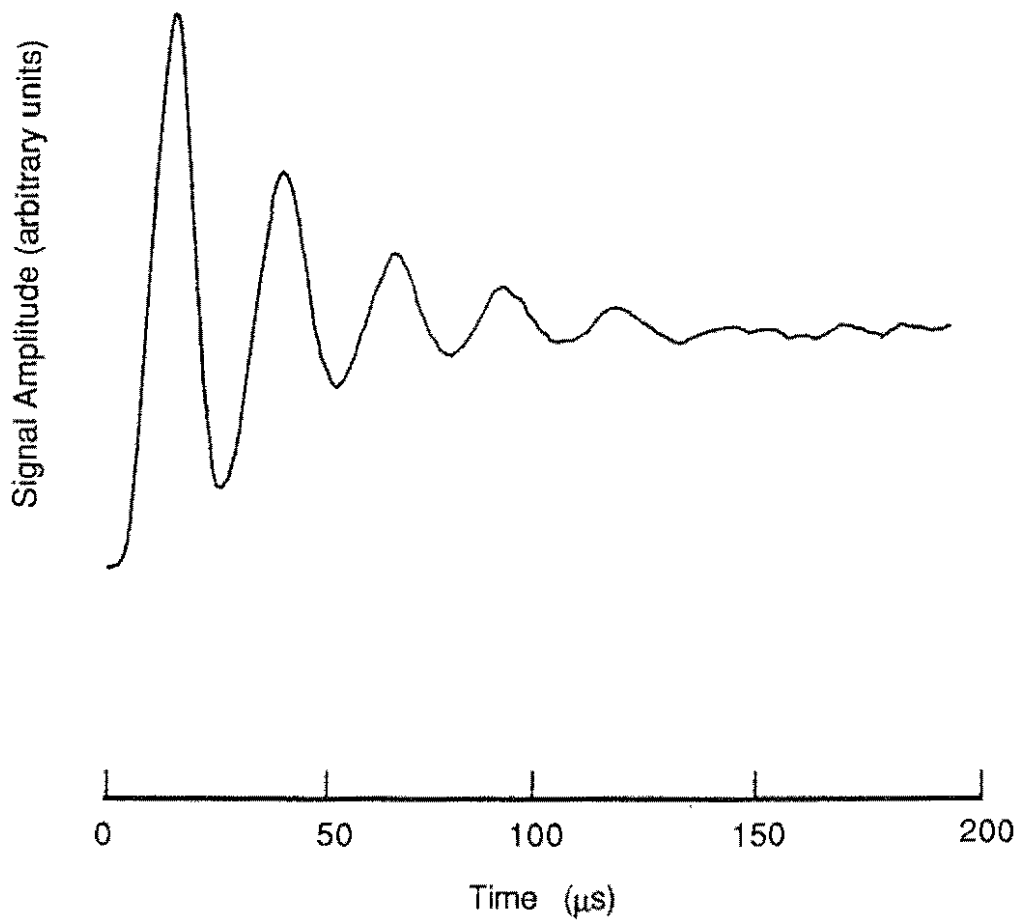


FIG. 9-1 The 5.5 MHz NMR nutation measured using Raman heterodyne techniques.

5.5MHz NMR Nutation

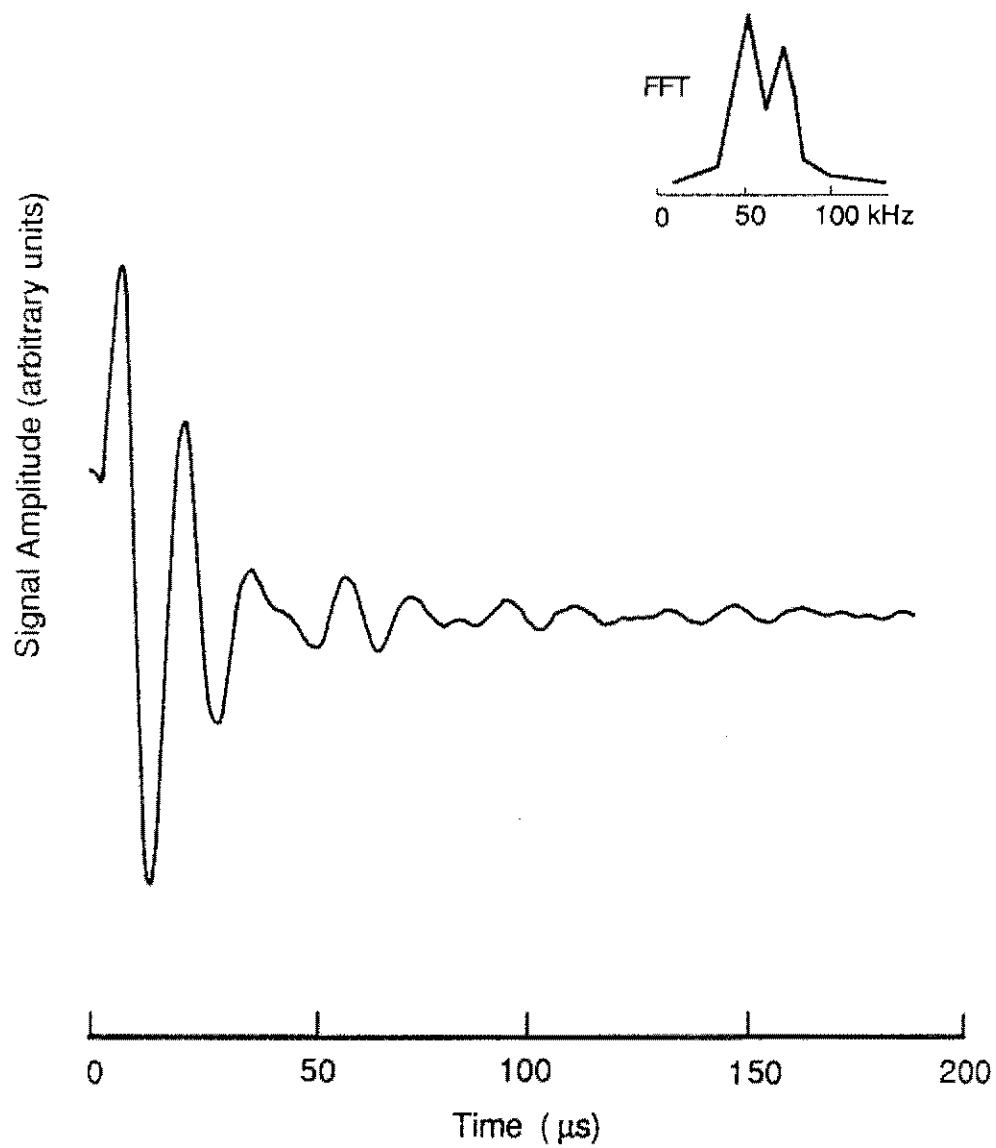


FIG. 9-2 An NMR nutation signal with the modulation pattern arising from the interference between the 5.5 and 4.6 MHz NMR transitions. The inset is its fast Fourier transform (FFT) spectrum.

The Rabi frequencies and the Rabi flopping frequencies measured from the NMR nutations are plotted in Figs. 9-3 and 9-4 as a function of RF power and detuning. The signals are again associated with the $m_I = 0 \leftrightarrow -1$ ($m_S = 0$) transition at 5.5 MHz. In Fig.9-3, the RF detuning is negligible ($\Delta_{RF} \approx 0$), and the signal oscillates at the Rabi frequency β_{RF} , which increases with $\sim(\text{RF power})^{1/2}$. In both Figs.9-3 and 9-4, very good agreement is found between the experiment and Eq.(9-1).

Nutation signals associated with the other NMR and the EPR transitions were also observed. One of the EPR nutations measured at a magnetic field of 1036G is shown in Fig. 9-5. Due to the hyperfine interaction, both the allowed and forbidden transitions appear in the EPR spectra, resulting in a non-exponential pattern similar to those observed in the NMR.

9-2. SPIN ECHO AND HOMOGENEOUS LINEWIDTH

When a magnetic transition is excited by a $\pi/2$ pulse and a following π pulse separated by a delay time τ , the system may emit an echo pulse delayed from the second incident pulse by a time equal to τ (Hahn 1950). The echo signal appears even in an inhomogeneously broadened system as the rephasing of magnetic moments is independent of the inhomogeneous broadening. As a consequence, this technique enables one to probe the dephasing process or the homogeneous linewidth embedded within an inhomogeneous transition. It has been shown (Farrar and Becker 1971) that the echo amplitude varies with an exponential decay,

$$A(t_{echo}) = A_0 \exp(-2\tau / T_2) , \quad (9-2)$$

where $t_{echo} = 2\tau$ and T_2 is the spin-spin relaxation time. The dephasing time T_2 can therefore be mapped out by measuring the echo amplitudes with a series of delay times τ . The homogeneous linewidth (FWHM) of a transition Δf_H is related to T_2 by,

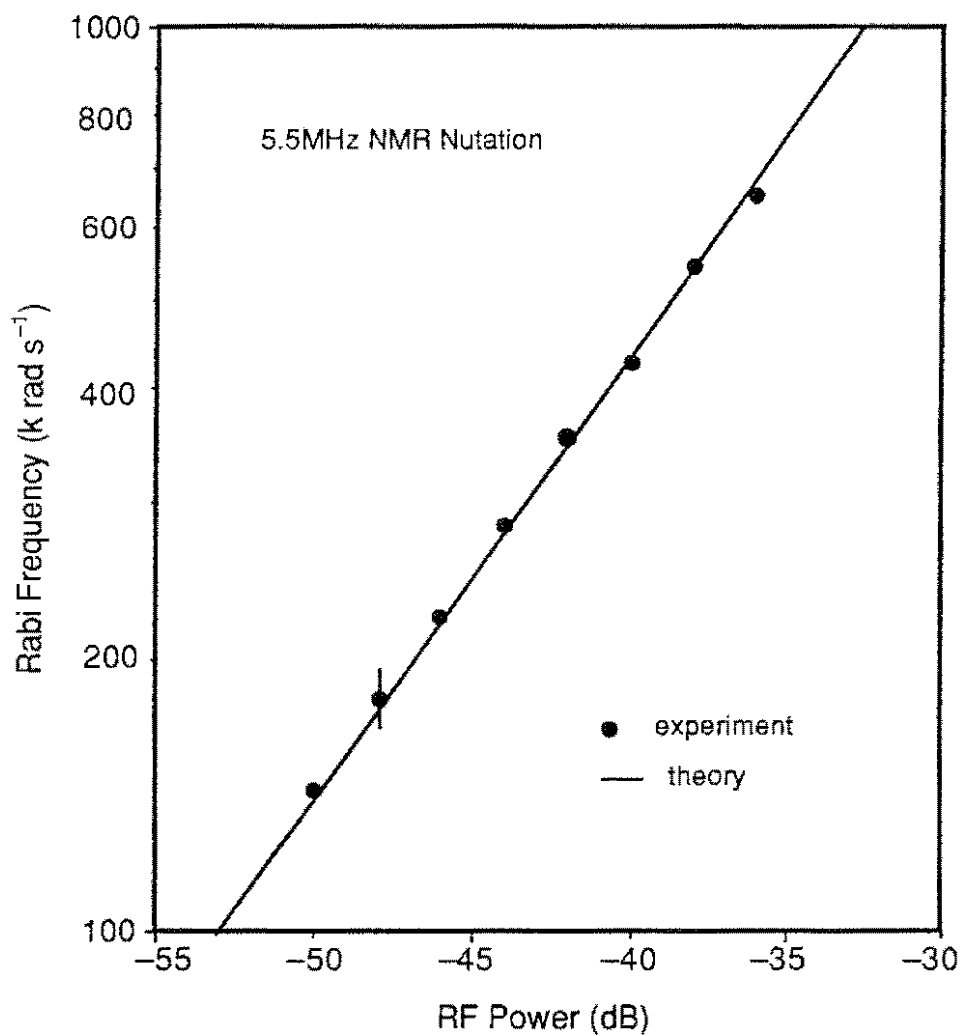


FIG. 9-3 The Rabi frequencies measured from the 5.5 MHz NMR nutations at various RF powers (dots) compared with the square root dependence (solid line).

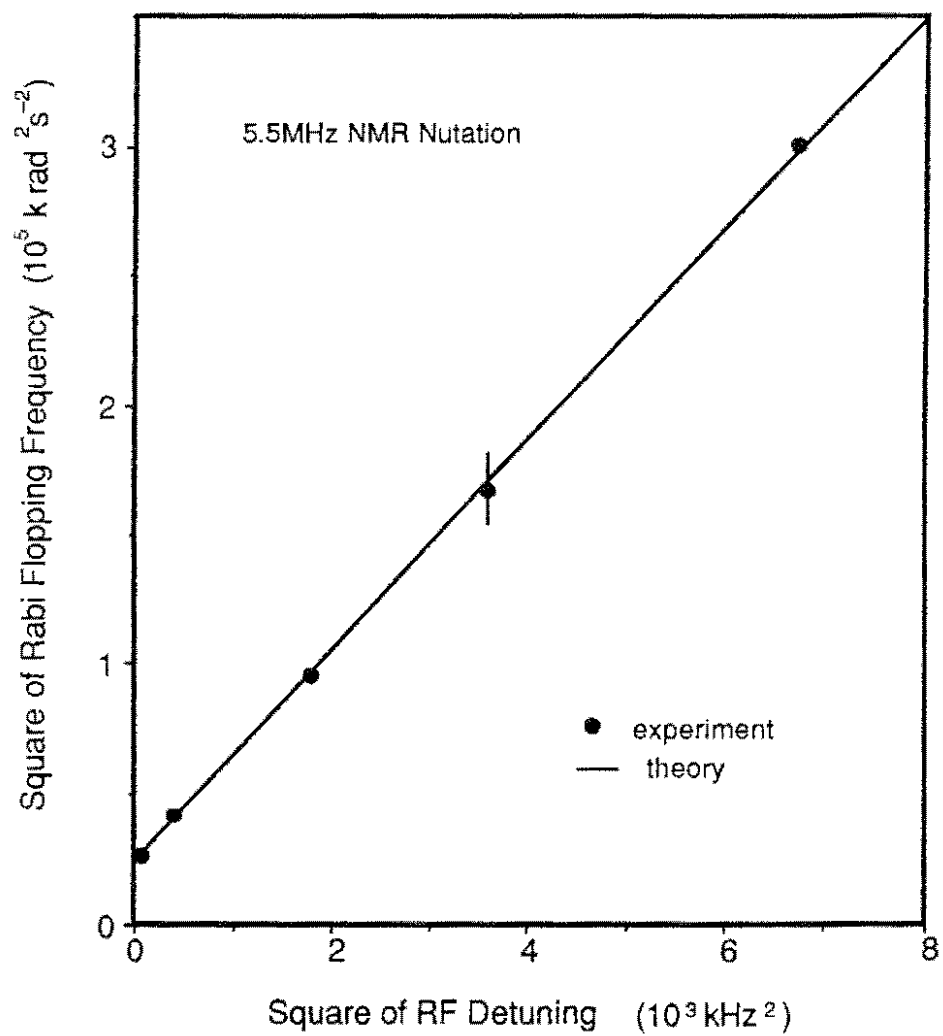


FIG. 9-4 The Rabi flopping frequencies measured from the 5.5 MHz NMR nutations at various RF detunings (dots) compared with theoretical prediction (solid line).

29MHz EPR Nutation

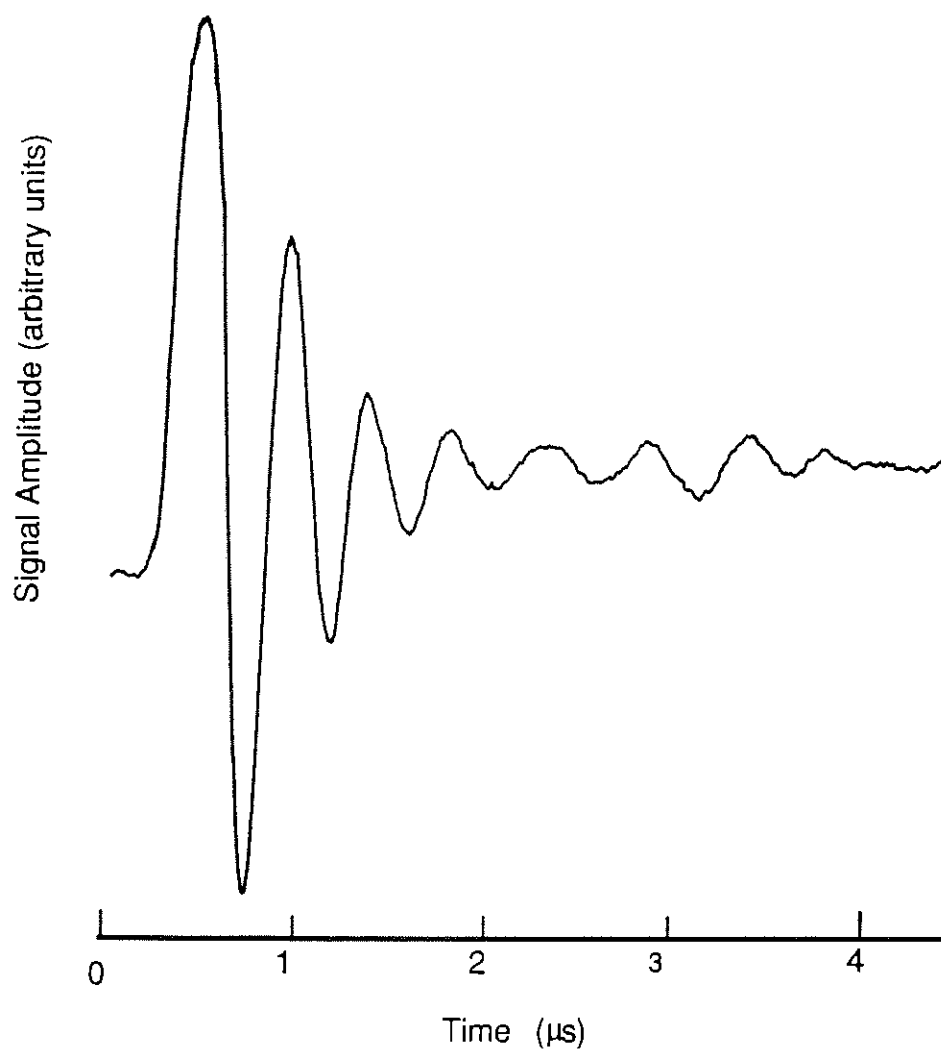


FIG. 9-5 An EPR nutation signal measured at 29 MHz. The modulation pattern clearly appears due to the hyperfine interaction.

$$\Delta f_H = 1/\pi T_2 \quad (9-3)$$

and is obtained straightforwardly from T_2 . In the echo measurements, the durations of $\pi/2$ and π pulses are initially determined from the corresponding nutation signal for a particular RF power level. Similar to the other transient experiments, phase detection was used.

9-2-1. NMR Transition

A typical echo signal associated with the $m_I=0 \leftrightarrow -1$ ($m_S=0$) transition at 5.5 MHz is shown in Fig.9-6, where the magnetic field was 1040 G. In the experiment, the $\pi/2$ -pulse width was 7.3 μ s and the separation between the $\pi/2$ and π pulses was 300 μ s.

The echo amplitudes associated with the $m_I=0 \leftrightarrow -1$ ($m_S=0$) transition at various delay times have been measured and plotted in Fig. 9-7, where the data were found to be in good agreement with an exponential decay. The dephasing time and the homogeneous linewidth (FWHM) for the $m_I=0 \leftrightarrow -1$ ($m_S=0$) transition were then determined to be,

$$T_2 = 260 \pm 6 \mu\text{s}$$

$$\Delta f_H = 1.20 \pm 0.03 \text{ kHz.}$$

The dipole-dipole interaction (van Vleck 1948, Bloembergen 1961) is expected to be one of the important mechanisms that determine the homogeneous linewidth of the NMR transitions associated with the N-V centre. In the sample each ^{14}N nucleus has neighbouring nuclei and the spread in precession rates is produced by the local magnetic field that one nucleus produces at another. As a result, if all the nuclei were precessing in phase at time $t=0$, they would get out of step in a time T_2 such that, $\gamma_n H_{loc} T_2 \sim 1$, where H_{loc} is the magnitude of the local field a

5.5MHz NMR Echo

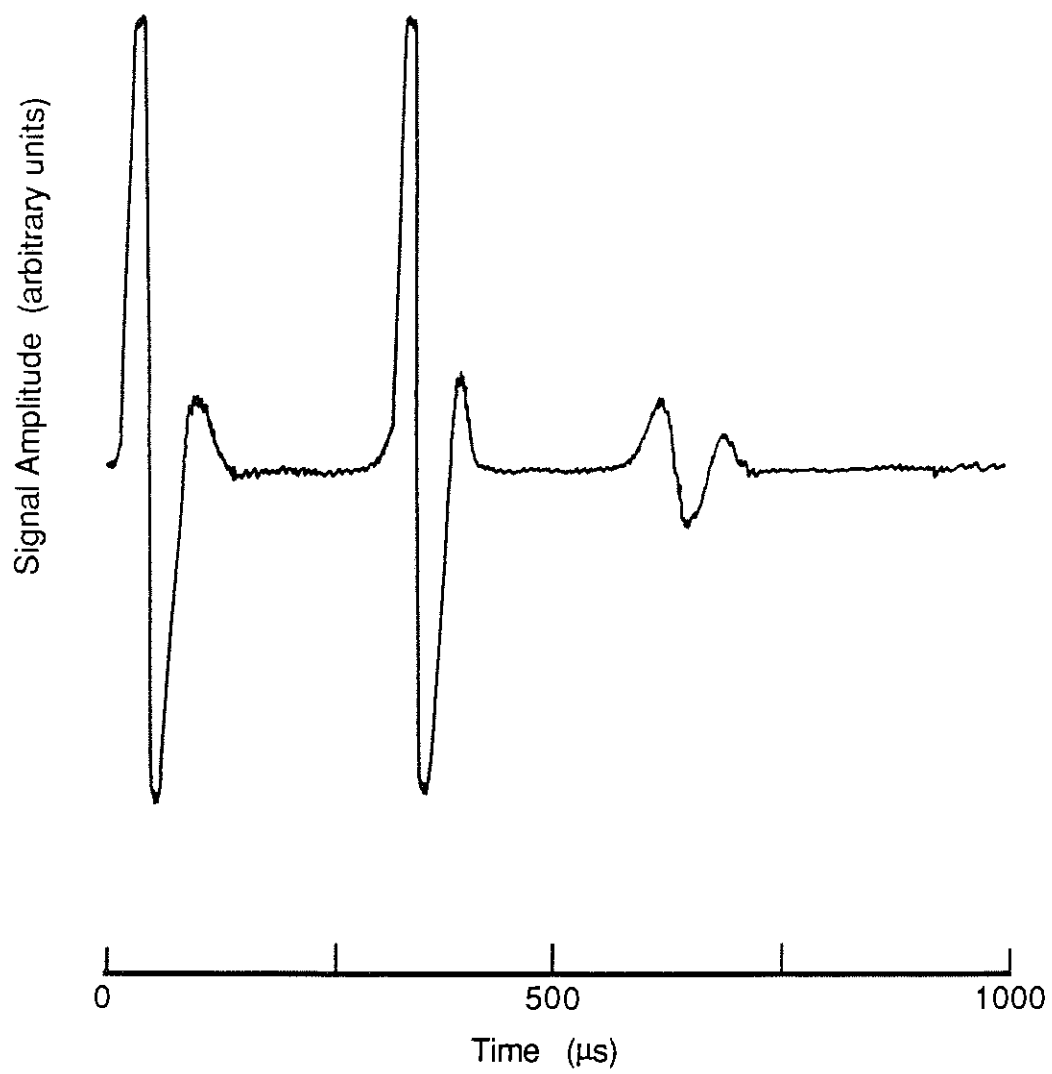


FIG. 9-6 The 5.5MHz NMR echo measured using Raman heterodyne techniques.

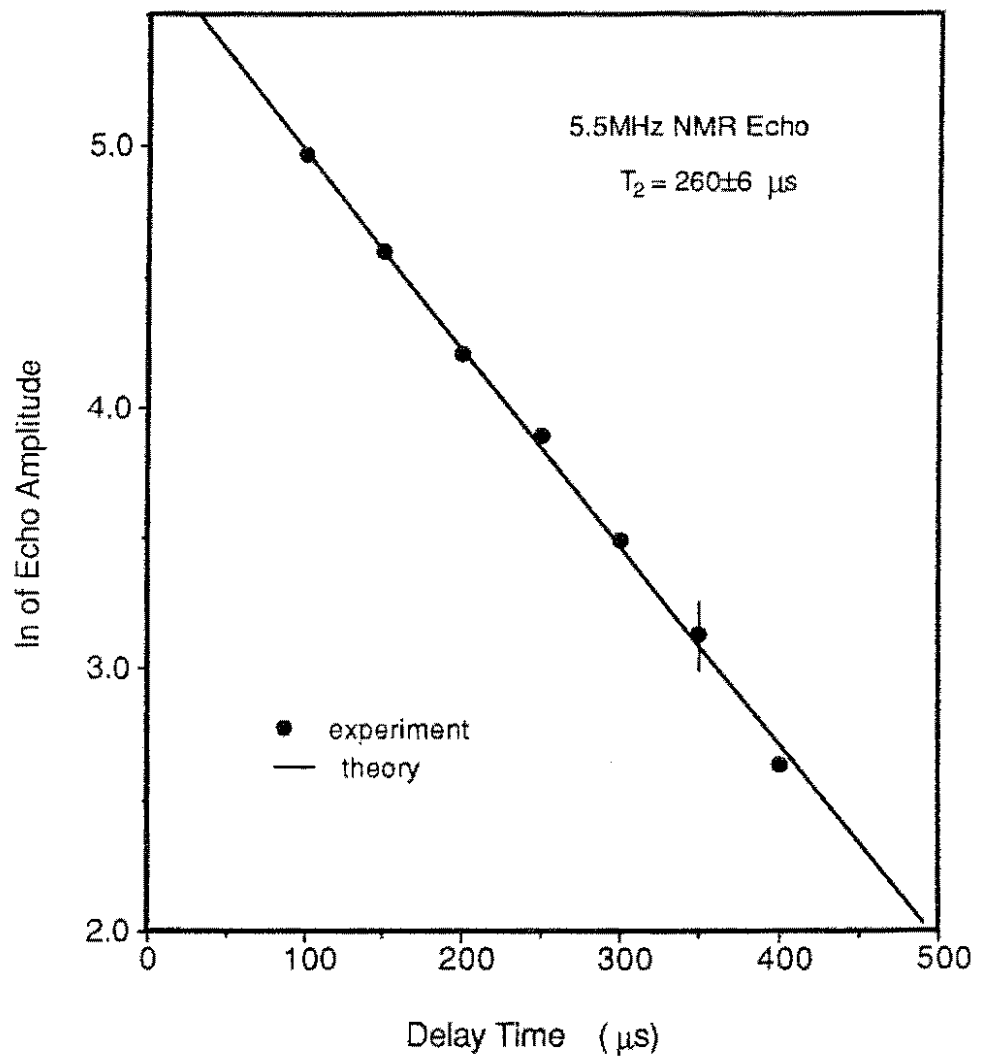


FIG. 9-7 The 5.5MHz NMR echo amplitudes as a function of delay time. The results are found in good agreement with an exponential decay, from which the dephasing time is determined.

typical ^{14}N nucleus experiences, and the vector sum of the moments would have thus diminished significantly. Another relaxation mechanism may arise from the interaction between the ^{14}N nuclear spin and the electric field gradient at the nucleus (Cohen and Reif 1957). As the spin re-orientates, the components of the quadrupole coupling tensor \mathbf{P} become a random function of time and provide a relaxation. A further study is needed to establish which relaxation mechanism is dominant in the N-V centre.

We were not able to measure the echo signals associated with the other NMR transitions because of their weak Raman heterodyne signals.

9-2-2. EPR Transition

Figure 9-8 shows a typical trace of the EPR echoes associated with the $m_s=0 \leftrightarrow -1 (m_I=0)$ transition at 81 MHz and at a magnetic field of 1046 G. The $\pi/2$ pulse width was $0.2 \mu\text{s}$ and the separation between the $\pi/2$ and π pulses was $8 \mu\text{s}$.

Interference effects due to the hyperfine interaction leads to the non-exponential decay in the EPR echo signals. However, the total signals measured at various magnetic field strengths are still consistent with an exponential law, as shown in Fig.9-9. The dephasing time and the homogeneous linewidth (FWHM) for the $m_s=0 \leftrightarrow -1 (m_I=0)$ transition were determined from the best-fit to be,

$$T_2 = 8.0 \pm 1.5 \mu\text{s}$$

$$\Delta f_H = 40 \pm 7 \text{ kHz},$$

where the large error arises from the modulation patterns.

81MHz EPR Echo

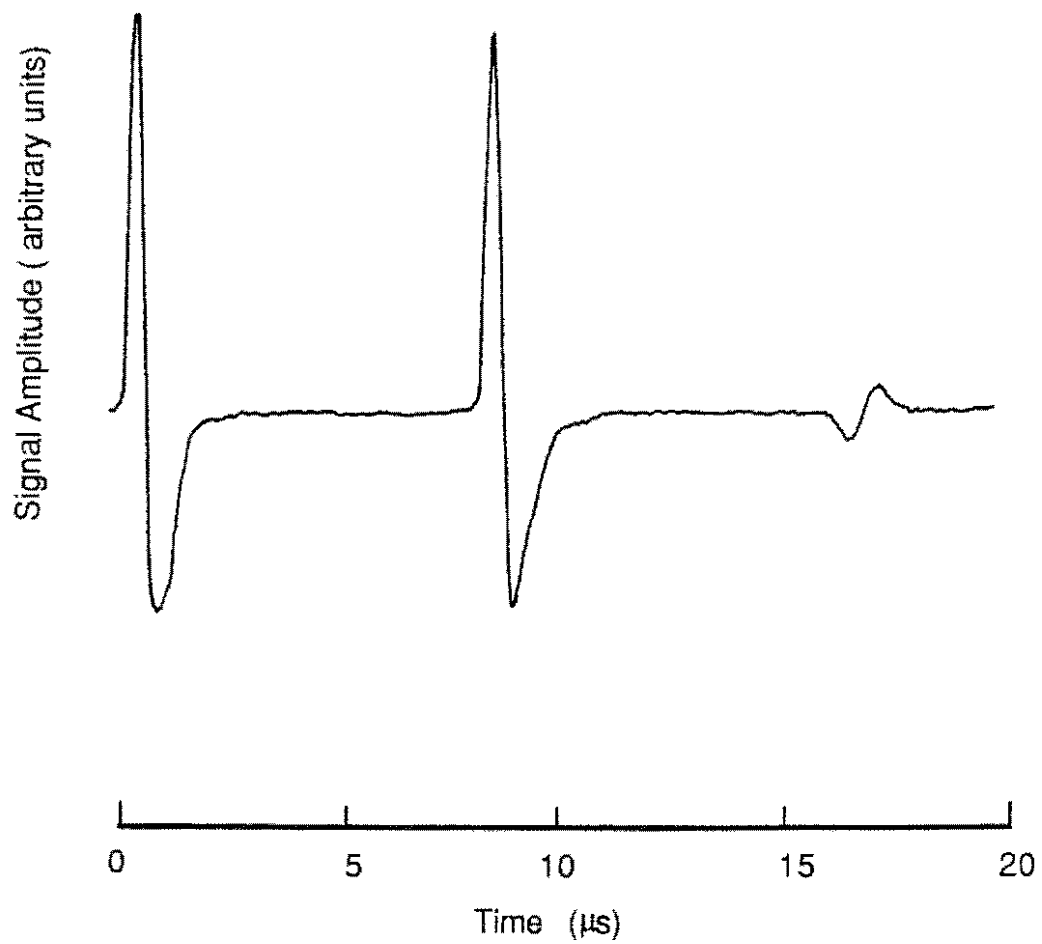


FIG. 9-8 An EPR echo signal measured at an RF frequency of 81MHz .

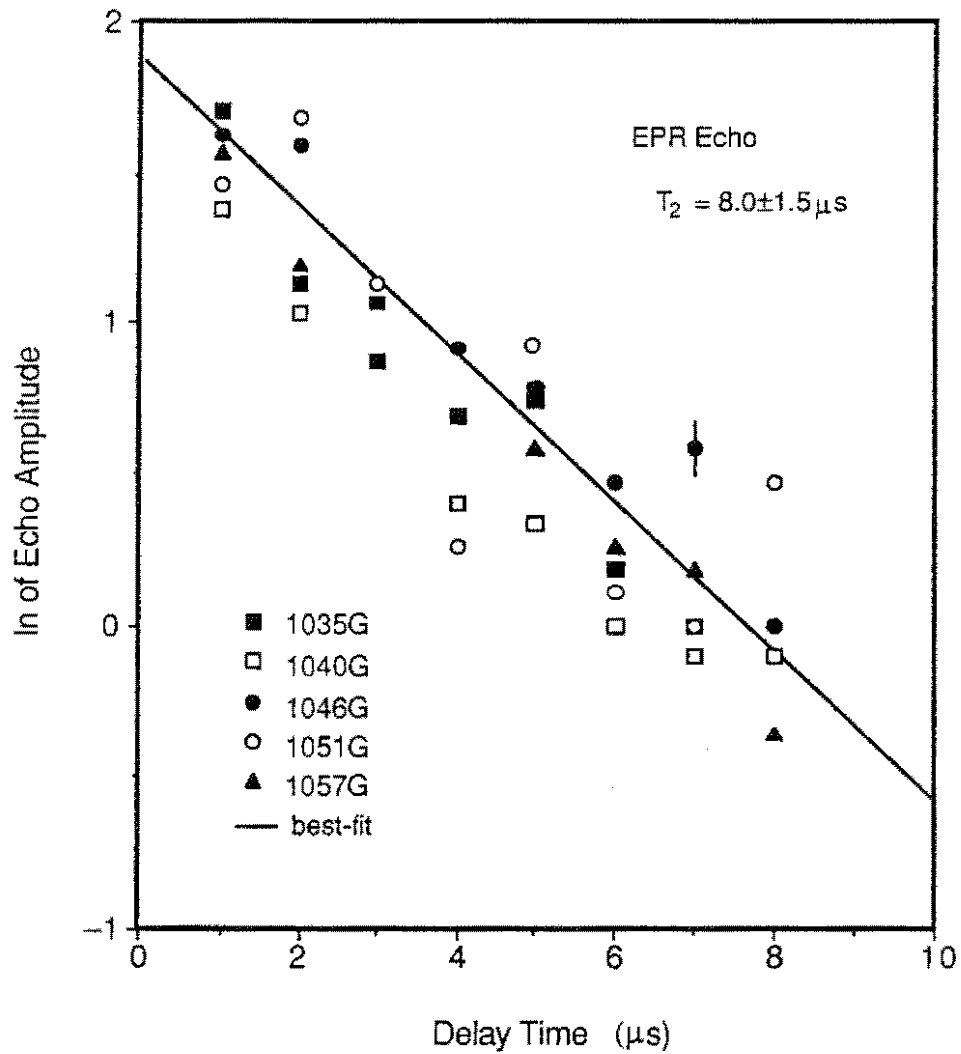


FIG. 9-9 The EPR echo amplitudes as a function of delay time measured at various magnetic field strengths near the level anticrossing. Despite the scattering of data due to the hyperfine interaction, the total result is in agreement with an exponential decay.

As can be seen in Fig.9-9, although the data points are somewhat scattered due to the hyperfine interaction, the EPR dephasing time seems unchanged when the magnetic field approaches 1028 G. This result rules out the mechanism for the collapse of EPR signal as being associated with any change in the dephasing process at the level anticrossing (see Chapter 6).

9-3. COHERENCE TRANSFER IN ENDOR

In ENDOR measurements, when the RF driving an NMR transition is pulsed, the transient variation of the populations in the NMR levels causes a corresponding change in the EPR signal monitored by a CW RF field. By recording the EPR signal amplitude as a function of time after the RF field driving the NMR is applied, one can investigate the spin polarization and/or spin coherence transfer from the nuclei to the electrons.

Figure 9-10 illustrates an NMR nutation and the corresponding transient EPR signal measured at a magnetic field of 1050 G. The RF step pulse at 5.4 MHz was applied at time $t=0$ to drive the $m_I=0 \leftrightarrow -1 (m_S=0)$ transition and, as a consequence, the nutation appeared in the NMR. The transient EPR was obtained by monitoring the signal amplitude associated with the $m_S=0 \leftrightarrow -1 (m_I=0)$ transition driven by a CW RF field at 59 MHz. As can be seen, the EPR signal oscillates in a similar way to the NMR nutation.

The oscillation frequency in the EPR signal depends on the power levels of both the RF fields (Whitley and Stroud 1976). In the experiment, the power of the RF field driving the EPR transition could be adjusted such that the Rabi frequency in the transient EPR was the same as that of the NMR nutation. Figure 9-11 shows the Rabi flopping frequencies measured from the transient EPR at various detunings of the pulsed RF field from the NMR line centre (5.40 MHz). The square of Rabi flopping frequency was plotted against the square of RF detuning and compared with the theoretical dependency,

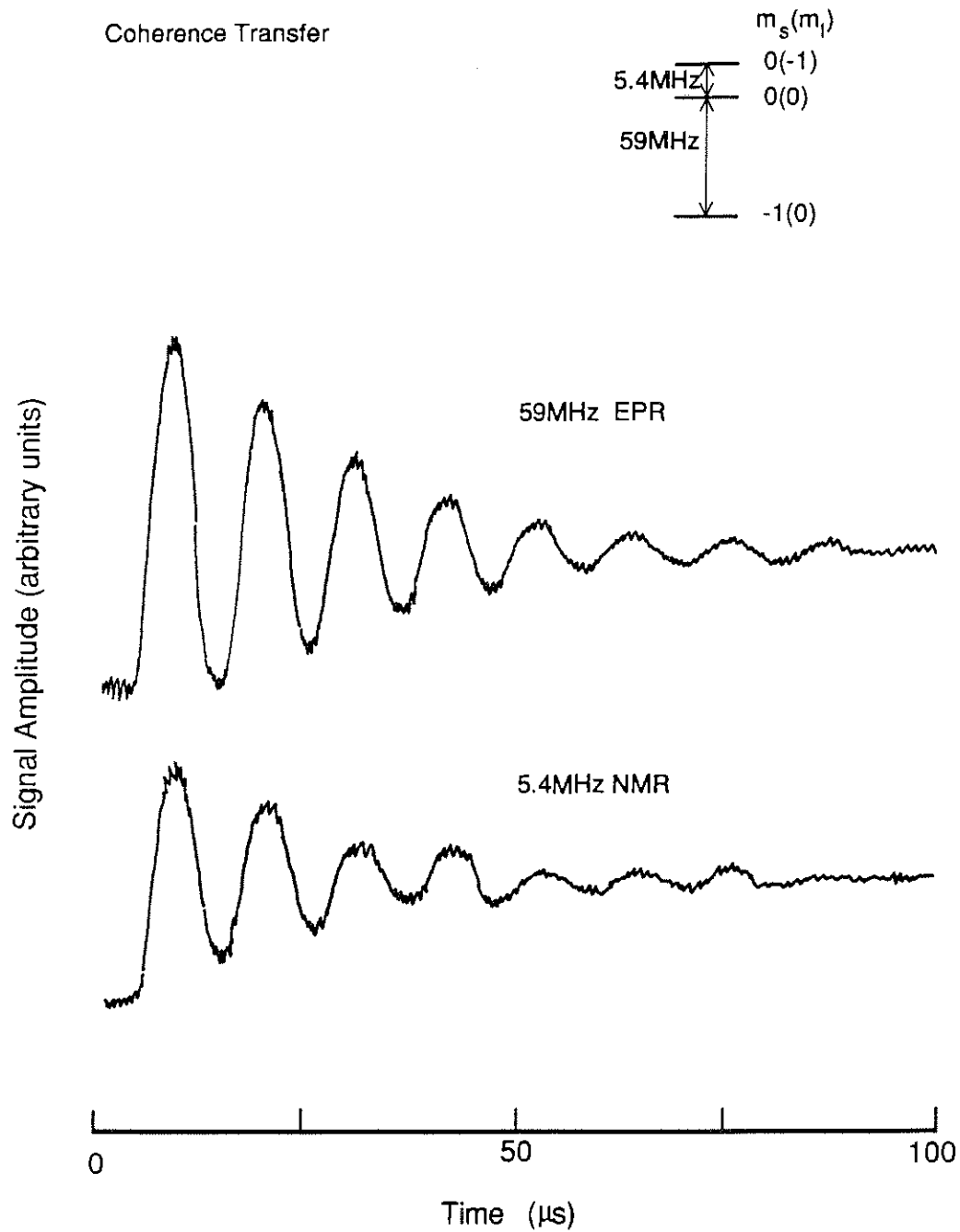


FIG. 9-10 An NMR nutation and the corresponding transient EPR signal monitored by a CW RF field after a step pulse was applied at time $t=0$ to the NMR transition.

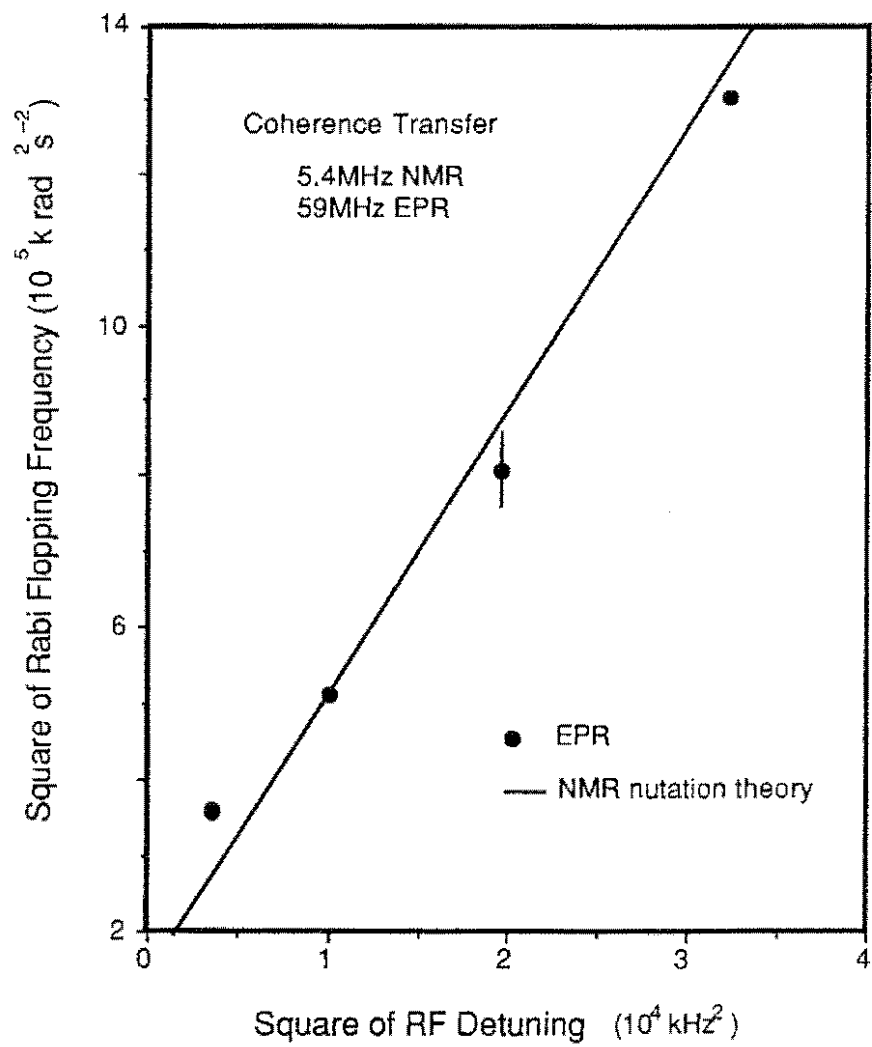


FIG. 9-11 The Rabi flopping frequencies measured from the transient EPR signals (dots) compared with the theoretical prediction for the NMR nutation (solid line) at various RF detunings from the NMR line centre.

$$\chi_{RF}^2 = \Delta_{RF}^2 + \beta_{RF}^2, \quad (9-4)$$

predicted for the NMR nutation. The experimental data are found to be in agreement with the above relation.

The method of polarization transfer has been used to enhance the NMR transitions with small dipole moments, such as selective population transfer (SPT) and insensitive nucleus enhanced by polarization transfer (INEPT) experiments (Pachler and Wessels 1973, Morris and Freeman 1979). In a system where a weak NMR transition and a relatively strong transition are coupled, the weak NMR signal can be significantly enhanced if the populations in the energy levels involved in the strong transition are inverted. Such a scheme of polarization transfer was used for transferring electron magnetization to nuclei, or for transferring large γ_n nuclear magnetization to lower γ_n nuclei (Feher 1956, 1957, Feher and Gere 1956). In the present experiment, however, the nuclear magnetization was able to be transferred to the electrons. The state mixing in the level anticrossing region greatly enhances the NMR transitions and consequently leads to such a transfer being detectable.

9-4. ZEEMAN QUANTUM BEAT

When two closely spaced levels $|a\rangle$ and $|b\rangle$ with the respective transition frequencies ω_a and ω_b to a third level $|c\rangle$ (Fig.9-12) are excited simultaneously by a short pulse, a beat at frequency $|\omega_a - \omega_b|$ may appear in the detected emission signals after the end of the pulse. This phenomenon is generally referred to as a quantum beat, which is a result of the interference between the decaying signal amplitudes of the coherently prepared excited states (*e.g.* Haroche *et al.* 1973, Demtroder 1982).

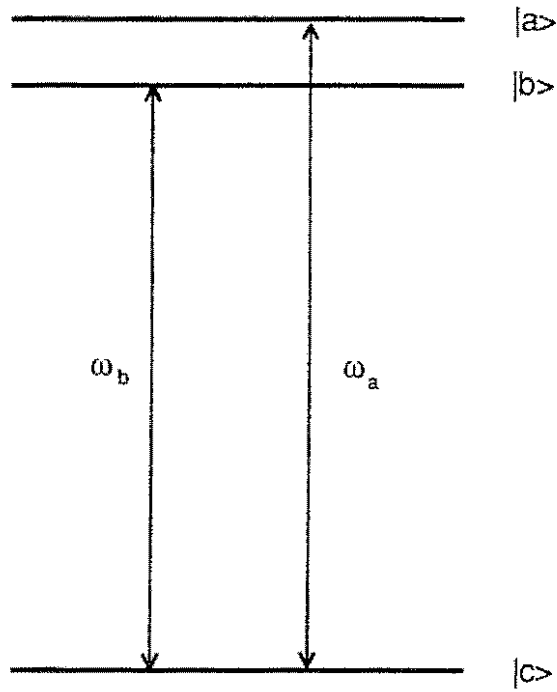


FIG.9-12 An energy level diagram for the quantum beat detection in a three-level system. The coherence processes involved in the Raman heterodyne measurements are not shown.

The quantum beat phenomenon can be treated with the semi-classical theory described below (Corney and Series 1964). Suppose the Fourier linewidth of the exciting pulse is larger than the separation of the $|a\rangle$ and $|b\rangle$ levels such that both of them are excited simultaneously. The system at the end of the exciting pulse ($t=0$) is in a coherent superposition of the two states $|a\rangle$ and $|b\rangle$, which can be written as,

$$|\psi(0)\rangle = A_a |a\rangle + A_b |b\rangle, \quad (9-5)$$

where A_a and A_b are two coefficients, which determine respectively the populations in the $|a\rangle$ and $|b\rangle$ levels. The system will decay at a time $t>0$, when the wave function is,

$$|\psi(t)\rangle = A_a e^{i(\omega_a+i\gamma_a/2)t} |a\rangle + A_b e^{i(\omega_b+i\gamma_b/2)t} |b\rangle, \quad (9-6)$$

where γ_a and γ_b are respectively the spontaneous decay rates of the $|a\rangle$ and $|b\rangle$ states to the third state $|c\rangle$. The detected emission intensity depends on the polarization,

$$P(t) = |\langle c | \boldsymbol{\mu}_H \cdot \mathbf{H}_{RF} | \psi(t) \rangle|^2, \quad (9-7)$$

where the transitions have been assumed to be magnetic dipole transitions. Substituting Eq.(9-6) into Eq.(9-7) gives,

$$P(t) = \hbar^2 \beta_{RF}^2 e^{-\gamma t} \left[|A_a|^2 + |A_b|^2 + 2 \operatorname{Re} (A_a^* A_b) e^{i\Delta\omega t} \right], \quad (9-8)$$

where $\Delta\omega = |\omega_a - \omega_b|$, and the decay rate γ and the Rabi frequency β_{RF} are assumed to be the same for both the $|a\rangle \leftrightarrow |c\rangle$ and $|b\rangle \leftrightarrow |c\rangle$ transitions. This assumption is valid for the $m_f=0 \leftrightarrow \pm 1$ ($m_s=0$) transitions in the 3A state of the N-V centre (see Chapter 8). As described by Eq.(9-8), the beat signal at frequency $\Delta\omega$ is superimposed on the exponential signal with a decay rate γ .

Using Raman heterodyne techniques, we have observed the beating in the $m_I=0 \leftrightarrow \pm 1$ ($m_S=0$) transitions, which arises from the nuclear Zeeman splitting of the $m_I=\pm 1$ ($m_S=0$) levels. The experimental results measured at 1016 G are shown in Fig. 9-13. At a field of 1016G, the two transition frequencies are 4.73 and 5.09 MHz, respectively, and the Zeeman splitting is 0.36MHz, which could be measured from the CW NMR spectra. In the experiments, the RF field had a pulse width of 1 μ s. The Fourier linewidth of the pulse was \sim 1MHz, which is larger than the Zeeman splitting. Amplitude detection was used and consequently the signal was solely due to the interference effect in the total emissions.

The beating was measured at various RF frequencies between 4.73 and 5.09 MHz, where the beat frequency was determined to be $\Delta\omega/2\pi=360\pm 5$ kHz and found to be unchanged at different RF frequencies. This is in excellent agreement with the Zeeman level splitting (0.36MHz). When the RF frequency was tuned to a value greater than 5.1MHz or less than 4.7MHz, the beating was observed to disappear.

Zeeman quantum beat was also observed at other magnetic field strengths. The splitting of the $m_I=\pm 1$ ($m_S=0$) levels changes with the magnetic field strength (see Chapter 7), and accordingly the beat frequency changed as well. For all the field strengths, the beat frequency was found to be equal to the level separation as determined from the CW NMR spectra.

Changing the RF power level changed the magnitude of beat signal but did not affect the beat frequency, as shown in Fig. 9-14.

9-5. CONCLUSIONS

Nutations in the NMR and EPR transitions of the 3A ground state have been measured using Raman heterodyne techniques. Modulation patterns in the nutation signals were observed at high RF powers due to the coupling of an adjacent transition, as confirmed by the fast Fourier transform analysis. The Rabi flopping frequencies of the $m_I=0 \leftrightarrow -1$ ($m_S=0$) transition measured at various RF powers and detunings were found to be in good agreement with theory.

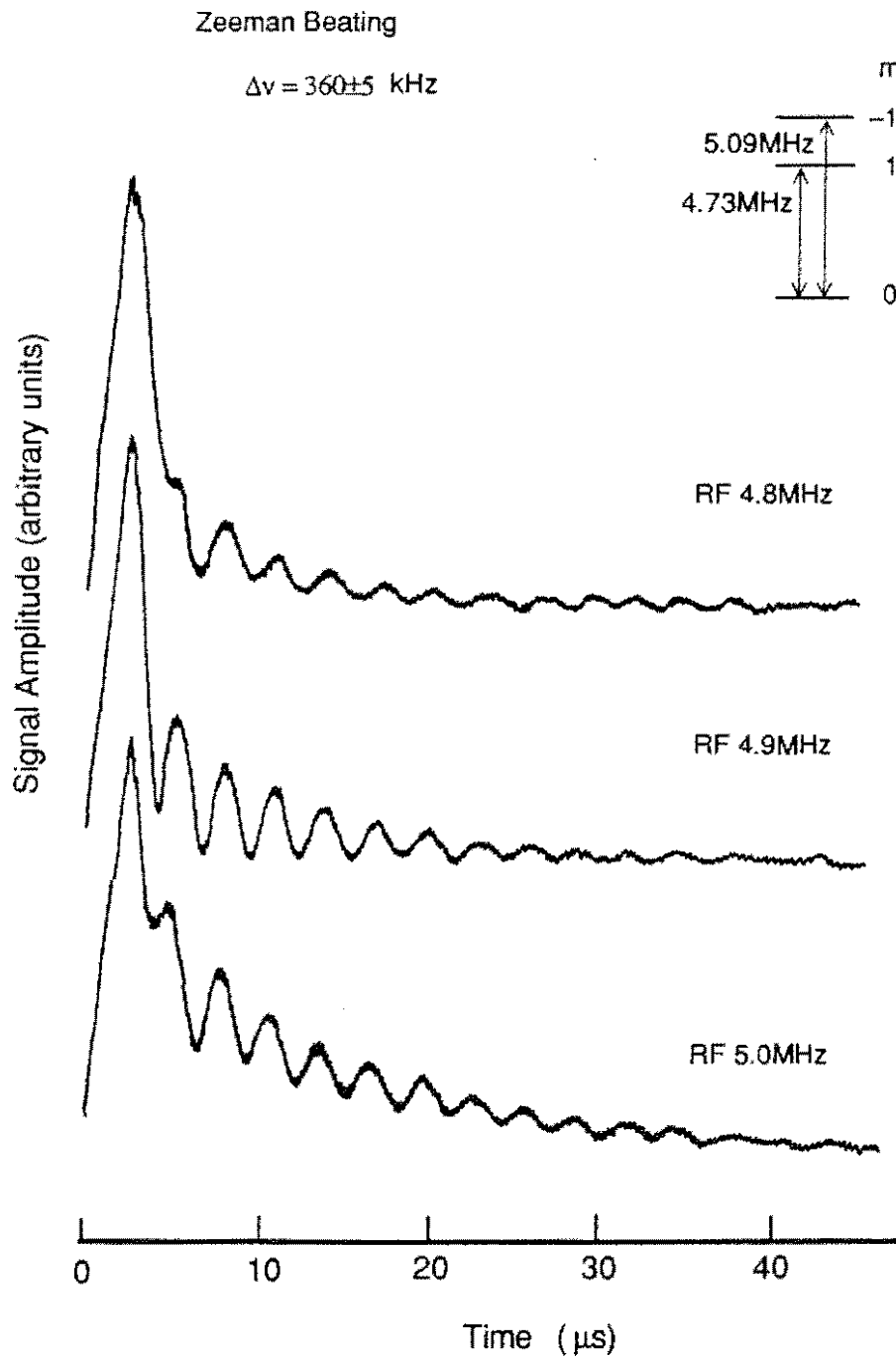


FIG. 9-13 The detected emission signals after a $1\mu\text{s}$ RF pulse tuned to various frequencies showing the Zeeman beating arising from the 4.73 and 5.09MHz NMR transitions.

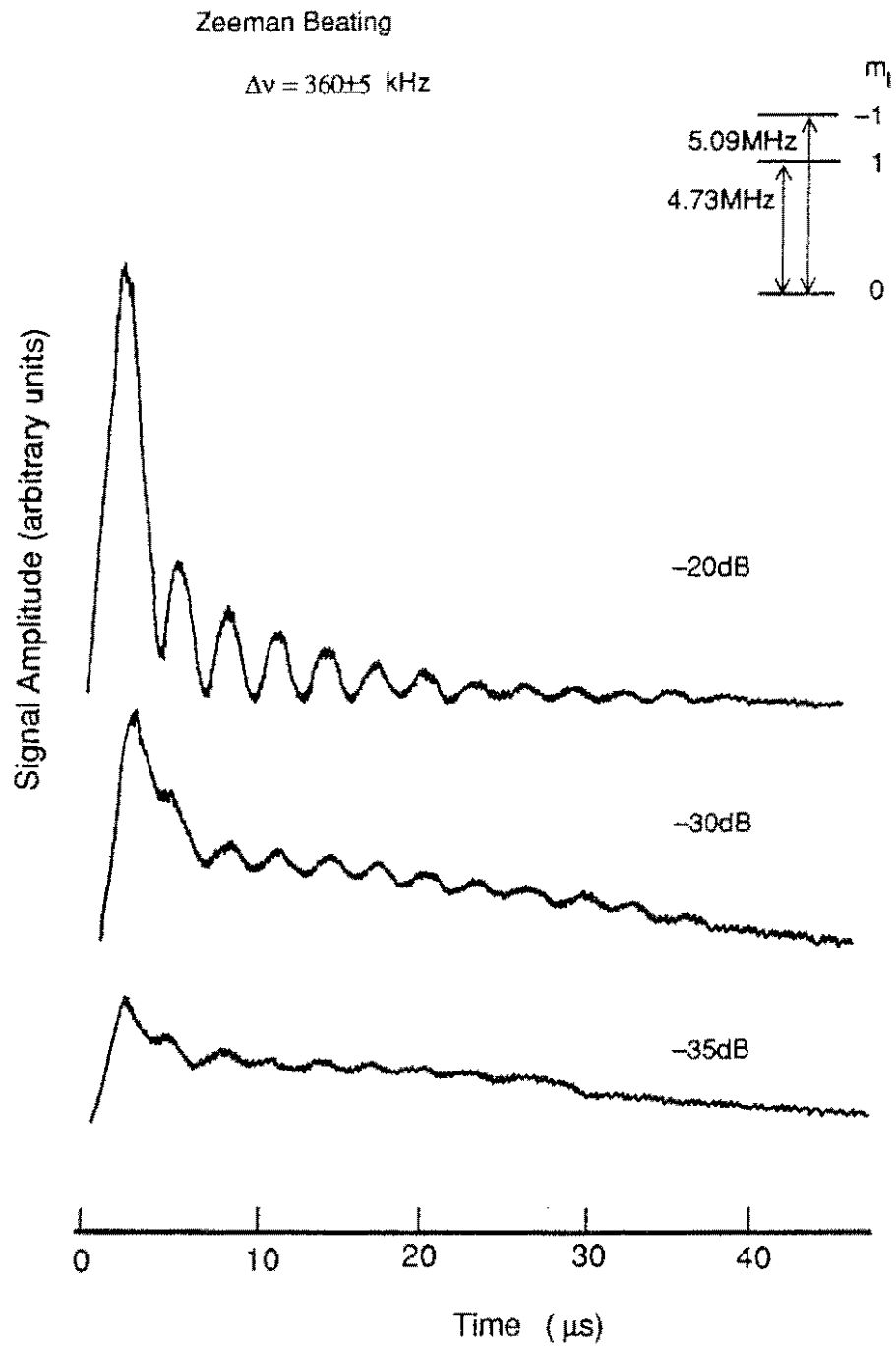


FIG. 9-14 The Zeeman beating signals after a 1μ s RF pulse tuned to 4.9MHz measured at various power levels.

The spin echoes associated with the $m_I=0 \leftrightarrow -1 (m_S=0)$ NMR transition have been measured and the homogeneous linewidth has thus been determined. The echoes associated with the other NMR transitions have not been successfully observed because of their weak Raman heterodyne signals. The EPR echoes associated with the $m_S=0 \leftrightarrow -1$ transition were also measured and the homogeneous linewidth has been determined as well. The echo measurements at various magnetic field strengths near the level anticrossing indicate that the dephasing time is unchanged when the field approaches 1028G. This suggests that the collapse of EPR signal at the level anticrossing is not related to the change of dephasing processes.

Spin coherence transfer was observed in the ENDOR experiment by pulsing the RF field connecting the NMR transition while monitoring the EPR signal coupled by a CW RF field. The EPR signal was found to oscillate in a similar way to the NMR nutation and the Rabi flopping frequencies measured from the EPR signal were found to be in agreement with the theoretical prediction for the NMR nutation. The state mixing in the level anticrossing region significantly enhances the NMR transition and leads to such a polarization transfer from the nuclei to the electrons being detectable.

With a short RF pulse, the Zeeman quantum beat in NQR has been observed using Raman heterodyne techniques, which arises from the splitting of the $m_I=\pm 1 (m_S=0)$ levels. The beat frequency was found to be in excellent agreement with the level separation at various magnetic field strengths.

Chapter 10

SUMMARY

The Raman heterodyne detected NMR and EPR signals in the 3A ground state of the N-V centre measured at lower RF powers were found to have lineshapes described by Eqs.(2-10a) and (2-10b) as predicted by theory in the low RF power regime (Wong *et al.* 1983). With intense RF fields, the spectral lineshapes were observed to be broadened and saturated. The saturation behaviour was found to be well described by the theoretical model developed by Fisk *et al.* (1990), which is based on the Bloch equations. We have found that the in-phase and out-of-phase components of the Raman heterodyne signal have totally different saturation characteristics, which result in anomalous lineshapes at high RF powers using amplitude detection.

Various measurements such as the EPR, NMR, ENDOR and hole burning have been used to study the 3A ground state using Raman heterodyne techniques. In the level anticrossing region, state mixing arising from the hyperfine interaction causes the NMR transitions to have comparable strengths to the EPR transitions. This facilitates the detection of nuclear spin resonances. The measured resonance frequencies were well accounted for by the Hamiltonian of a 3A state and all the parameters in the spin Hamiltonian have been fully determined. From the values of hyperfine interaction parameters, one can conclude that the unpaired electrons in the N-V defect are mainly localized in the three equivalent carbons.

Level anticrossing studies have shown the spin alignment in the 3A state under optical pumping, being in agreement with the previous observation using conventional EPR techniques (Loubser and van Wyk 1977). The Raman heterodyne detected EPR signal was found to

collapse at the level anticrossing, and this phenomenon is attributed to the equal populations in the two EPR levels due to the state mixing and spin alignment. The interpretation was substantiated by the RF power broadened lineshape, Rabi oscillation and spin echo measurements. Taking into account the observation of NMR and ENDOR intensities with the result of absorptive and emissive EPR signals at low and high fields, it is further claimed that the crystal field splitting D is positive, *i.e.* the $m_S=\pm 1$ levels lie above the $m_S=0$ level at zero field.

Interesting transient properties such as Zeeman quantum beat and coherence transfer have been observed using Raman heterodyne techniques. The state mixing near the level anticrossing significantly enhances the NMR transitions and leads to the spin polarization transfer from the nuclei to the electrons being detectable. Other coherent measurements such as spin echo experiments have yielded the homogeneous linewidths of the NMR and EPR transitions.

On the other hand, optical pumping effects in the Raman heterodyne experiments are far less fully understood. The Autler-Townes splitting measurements in the 3A state have shown that for the two NMR transitions which have vastly different Raman heterodyne signal intensities, their transition dipole moments are equal. It is thus concluded that the different Raman heterodyne signal magnitudes are because of different population factors and this can arise from optical pumping, which alters the spin population distribution in the 3A state through optical excitation to the 3E state with subsequent relaxations. However, the details of optical pumping effects have not been included in the theoretical models, and the consideration of such effects may require further work.

REFERENCES

- Abragam A 1961 *The Principles of Nuclear Magnetism* (Clarendon, Oxford)
- Abragam A and Bleaney B 1970 *Electron Paramagnetic Resonance of Transition Ions* (Dover, New York)
- Abramowitz M and Stegun I A 1972 *Handbook of Mathematical Functions* (Dover, New York)
- Anderson H L ed. 1989 *A Physicist's Desk Reference* (American Institute of Physics, New York)
- Atkins P W and Symons M C R 1967 *The Structure of Inorganic Radicals* (Elsevier, Amsterdam)
- Autler S H and Townes C H 1955 *Phys. Rev.* **100** 703
- Barnes R G and Smith W V 1954 *Phys. Rev.* **93** 95
- Bartola B D 1968 *Optical Interactions in Solids* (John Wiley & Sons, New York)
- Bloch F 1946 *Phys. Rev.* **70** 460
- Bloch P D, Brocklesby W S, Harley R T and Taylor D R 1985a *J. Phys. (Paris) C* **7** 523
- Bloch P D, Brocklesby W S, Harley R T and Henderson M J 1985b *J. Phys. (Paris) C* **7** 527
- Bloembergen N 1961 *Nuclear Magnetic Relaxation* (W A Benjamin, New York)
- Brower K L 1971 *Phys. Rev. B* **4** 1968
- Brown, Bartlett and Dunn 1933 *Phys. Rev.* **44** 296
- Clark C D and Norris C A 1971 *J. Phys. C: Sol. St. Phys.* **4** 2223
- Cohen M H and Reif F 1957 in *Solid State Physics* vol 5 eds Seitz F and Turnbull D (Academic, New York) p321
- Collins A T, Thomaz M F and Jorge M I B 1983 *J. Phys. C: Sol. St. Phys.* **16** 2177

- Cook R J and Whiffen D H 1966 *Proc. R. Soc. A* **295** 99
- Corney A and Series G W 1964 *Proc. Phys. Soc.* **83** 207
- Davies G and Hamer M F 1976 *Proc. R. Soc. Lond. A* **348** 285
- Demtroder W 1982 *Laser Spectroscopy Basic Concepts and Instrumentation* (Springer-Verlag, Berlin)
- du Preez L 1965 *PhD Thesis University of Witwatersrand*
- Erickson L E 1985 *Phys. Rev. B* **32** 1
- 1987 *J. Phys. C: Sol. St. Phys.* **20** 291
- 1989 *Phys. Rev. B* **39** 6342
- 1990 *Phys. Rev. B* **42** 3789
- Farrar T C and Becker E D 1971 *Pulse and Fourier Transform NMR* (Academic, New York)
- Feher G 1956 *Phys. Rev.* **103** 500
- Feher G 1957 *Phys. Rev.* **105** 1122
- Feher G and Gere E A 1956 *Phys. Rev.* **103** 501
- Ferretti J A and Freeman R 1966 *J. Chem. Phys.* **44** 2054
- Fisk P T H 1991 private communication
- Fisk P T H, Bachor H -A and Sandeman R J 1986a *Phys. Rev. A* **33** 2418
- 1986b *Phys. Rev. A* **33** 2424
- 1986c *Phys. Rev. A* **34** 4762
- Fisk P T H, He X -F, Holliday K and Manson N B 1990 *J. Lumin.* **45** 26
- Hahn E L 1950 *Phys. Rev.* **80** 580
- Harley R T, Henderson M J and Macfarlane R M 1984 *J. Phys. C: Sol. St. Phys.* **17** L233
- Haroche S, Paisner J A and Schawlow A L 1973 *Phys. Rev. Lett.* **30** 948
- Hartmann S R and Hahn E L 1962 *Phys. Rev.* **128** 2042
- He X -F, Manson N B and Fisk P T H 1991a in preparation

He X -F, Fisk P T H and Manson N B 1991b in preparation

Holliday K 1989 *PhD Thesis Australian National University*

Holliday K, He X -F, Fisk P T H and Manson N B 1990 *Opt. Lett.* **15** 983

Jackson J D 1975 *Classical Electrodynamics* (John Wiley & Sons, New York)

Jahn H A and Teller E 1937 *Proc. R Soc. A* **161** 220

Kintzer E S, Mitsunaga M and Brewer R G 1985 *Phys. Rev. B* **31** 6958

Levenson M D 1982 *Introduction to Nonlinear Laser Spectroscopy* (Academic, New York)

Lomer J N and Wild A M A 1973 *Radiat. Effe.* **17** 37

Loubser J H N and van Wyk J A 1977 *Diamond Research* **11**

——— 1978 *Rep. Prog. Phys.* **41** 1201

Manson N B, Fisk P T H and He X -F 1991 in preparation

Manson N B, He X -F and Fisk P T H 1990 *Opt. Lett.* **15** 1094

Manson N B and Silversmith A J 1983 *J. Phys. C: Sol. St. Phys.* **20** 1507

Mitsunaga M, Kintzer E S and Brewer R G 1984 *Phys. Rev. Lett.* **52** 1484

——— 1985 *Phys. Rev. B* **31** 6947

Mlynek J, Wong N C, DeVoe R G, Kintzer E S and Brewer R G 1983 *Phys. Rev. Lett.* **50** 993

Morris G A and Freeman R 1979 *J. Am. Chem. Soc.* **101** 760

Nisida Y, Mori K, Muro K, Mihara T, Demizu Y, Kato R, Asida M, Sato S and Yazu S 1989

reprint

Owen J 1965 *Physical Properties of Diamond* ed. Berman R (Clarendon, Oxford)

Pachler K G R and Wessels P L 1973 *J. Magn. Reson.* **12** 337

Picque J L and Pinard J 1976 *J. Phys. B: Atom. Molec. Phys.* **9** L77

- Poole C P and Farach H A 1971 *Relaxation in Magnetic Resonance* (Academic, New York)
—— 1972 *The Theory of Magnetic Resonance* (Wiley-Interscience, New York)
- Pople J A, Schneider W G and Bernstein H J 1959 *High-Resolution Nuclear Magnetic Resonance* (McGraw-Hill, New York)
- Ramsey N F 1953 *Nuclear Moments* (Wiley, New York)
- Reddy N R S 1989 *PhD Thesis Australian National University*
- Reddy N R S, Manson N B and Krausz E R 1987 *J. Lumin.* **38** 46
- Redfield A G 1955 *Phys. Rev.* **98** 1787
—— 1956 *Rev. Sci. Instrum.* **27** 230
- Schabert A, Keil R and Toschek P E 1975 *Appl. Phys.* **6** 181
- Schiff L I 1968 *Quantum Mechanics* (McGraw-Hill, New York)
- Slichter C P 1990 *Principles of Magnetic Resonance* (Springer-Verlag, Berlin)
- Smith W V, Sorokin P P, Gelles I L and Lasher G J 1959 *Phys. Rev.* **115** 1546
- Steinfeld J I ed. 1978 *Laser and Coherence Spectroscopy* (Plenum, New York)
- Stoneham A M 1975 *Theory of Defects in Solids* (Clarendon, Oxford)
- Szabo A, Muramoto T and Kaarli R 1988 *Opt. Lett.* **13** 1075
—— 1990 *Phys. Rev. B* **42** 7769
- Takahashi Y, Tanaka T, Hatanaka H, Fukuda Y and Hashi T 1987 *J. Lumin.* **38** 261
- Takahashi Y, Ishikawa K, Tanaka T, Fukuda Y, Hatanaka H and Hashi T 1988 *Phys. Rev. B* **38** 7121
- Taylor D R 1984 *Opt. Commun.* **52** 204
- Torrance C C 1934 *Phys. Rev.* **46** 388
- Torrey H C 1949 *Phys. Rev.* **76** 1059
- van Oort E and Glasbeek M 1989 *Phys. Rev. B* **40** 6509
—— 1990a *Chem. Phys. Lett.* **168** 529

- 1990b *Chem. Phys.* **143** 131
- van Oort E, Manson N B and Glasbeek M 1988 *J. Phys. C: Sol. St. Phys.* **21** 4385
- van Oort E, van der Kamp B, Sitters R and Glasbeek M 1991 *J. Lumin.* **48&49** 803
- van Vleck J H 1948 *Phys. Rev.* **74** 1168
- Walker J 1979 *Rep. Prog. Phys.* **42** 1605
- Watkins G D 1967 *Phys. Rev.* **155** 802
- 1975 *Point Defects in Solids* vol 2 ed Crawford J H and Slifkin L M (Plenum, New York)
- Watson R E and Freeman A J 1961a *Phys. Rev.* **123** 521
- 1961b *Phys. Rev.* **124** 1117
- Whitley R M and Stroud C R 1976 *Phys. Rev. A* **14** 1498
- Wong N C, Kintzer E S, Mlynec J, DeVoe R G and Brewer R G 1983 *Phys. Rev. B* **28** 4993
- Yariv A 1975 *Quantum Electronics* (John Wiley & Sons, New York)